

# **Copyright Undertaking**

This thesis is protected by copyright, with all rights reserved.

#### By reading and using the thesis, the reader understands and agrees to the following terms:

- 1. The reader will abide by the rules and legal ordinances governing copyright regarding the use of the thesis.
- 2. The reader will use the thesis for the purpose of research or private study only and not for distribution or further reproduction or any other purpose.
- 3. The reader agrees to indemnify and hold the University harmless from and against any loss, damage, cost, liability or expenses arising from copyright infringement or unauthorized usage.

#### **IMPORTANT**

If you have reasons to believe that any materials in this thesis are deemed not suitable to be distributed in this form, or a copyright owner having difficulty with the material being included in our database, please contact <a href="mailto:lbsys@polyu.edu.hk">lbsys@polyu.edu.hk</a> providing details. The Library will look into your claim and consider taking remedial action upon receipt of the written requests.

# TENSILE FATIGUE BEHAVIOR OF UHPECC AND APPLICATION OF FRPREINFORCED UHPECC FOR OFFSHORE STORAGE TANKS

**DENG FUHAO** 

**PhD** 

The Hong Kong Polytechnic University

2025

# The Hong Kong Polytechnic University Department of Civil and Environmental Engineering

# Tensile Fatigue Behavior of UHPECC and Application of FRP-Reinforced UHPECC for Offshore Storage Tanks

# **DENG** Fuhao

A thesis submitted in partial fulfillment of the requirements for the degree of Doctor of Philosophy

August 2024

# **CERTIFICATE OF ORIGINALITY**

I hereby declare that this thesis is my own work and that, to the best of my knowledge and belief, it reproduces no material previously published or written, nor material that has been accepted for the award of any other degree or diploma, except where due acknowledgment has been made in the text.

(Signed)

DENG Fuhao (Name of student)

# **ABSTRACT**

With climate change driving higher sea levels and more frequent extreme weather occurrences, coastal megacities are facing a growing scarcity of land. On the other hand, the demand for infrastructure to support urban economic development is increasing, intensifying the conflict between land supply and infrastructure needs. Developing and utilizing ocean space is emerging as a viable solution. The development of high-performance and durable marine infrastructure is of great significance to the economic advancement of coastal cities. However, marine environments present conditions that are much harsher than those on land. Structures are subjected to long-term effects from wind, waves, and currents while being exposed to a highly corrosive environment. Widely used steel-reinforced concrete and steel structures inevitably suffer from corrosion. The combined effects of loading and corrosion can significantly reduce the safety and durability of these structures, posing considerable challenges for the development and application of marine engineering.

To address the aforementioned issues, the development of marine infrastructures using high-performance materials has emerged as a significant field. This thesis aims to explore the feasibility of two emerging materials, Fiber Reinforced Polymer (FRP) and Engineered Cementitious Composites (ECC), for use in marine infrastructure applications. The research employs polyethylene (PE) fibers and a high-strength cement matrix to create ultra-high-performance Engineered Cementitious Composites (UHPECC) with high tensile strength and deformation capacity. Initially, the fatigue performance of UHPECC under different load conditions is investigated through experiments, considering variables such as stress levels and loading frequencies. The influence of initial static tensile strength is also introduced, and a probability of failure-stress level-fatigue life (P-S-N) model is established using data from

tensile fatigue tests. Subsequently, to account for the stress ratio, particularly the influence of stress reversal on fatigue life, an additional set of fatigue load tests under different stress ratio conditions was conducted. The adverse impact of a negative stress ratio on the fatigue life of ECC was examined. A cumulative fatigue damage model was developed based on the fatigue deformation history of the specimens to assess fatigue damage under various loading conditions.

At the component level, this study investigates the mechanical performance of flexural members made of UHPECC reinforced with FRP bars, which are particularly suitable for marine infrastructure. These novel structural members offer the following advantages over steel reinforced members: (1) steel corrosion is completely avoided by replacing steel bars with FRP bars; (2) the tensile strength of FRP reinforcement could be completely utilized due to the ultra-high strength of UHPECC; (3) UHPECC's high ductility and tensile toughness ensure excellent deformation compatibility with FRP bars; (4) using locally available sea sand dramatically reduces the transportation cost and energy consumption. To demonstrate the above advantages, FRP-reinforced UHPECC beams were fabricated and tested. The influences of FRP reinforcement ratio, fiber dosage of UHPECC, and loading scheme on the behaviors of the beam specimens were investigated in detail. The crack development in UHPECC, loaddisplacement responses, failure modes, energy dissipation capacities, deformation capacities, and strain evolutions were measured and discussed. The test findings demonstrated that the incorporating of fibers significantly reduces the relative slip between FRP and UHPECC, enhancing the deformation capacity of the specimens. However, cyclic loading damages the fibers' bridging effect, thereby reducing the performance of the specimens.

On the structural scale, this study proposes an offshore placement scheme for storage tanks, a widely used industrial structure, to achieve large-scale storage. The newly proposed offshore storage tank can remain stable in a marine environment, and its feasibility is verified under various potential failure scenarios. The research subsequently examines how hydrodynamic pressure is distributed across the cylindrical shell of the storage tank as a result of wave loads, and it determines the stresses induced in the shell by these wave loads. The findings reveal that the ultimate stress levels of the proposed structures fall within the range that the new materials can withstand. This preliminary evidence confirms the feasibility of using these emerging materials in marine infrastructure applications.

Finally, the conclusions are outlined and suggestions for future research are emphasized. Overall, the developed work provides a foundational exploration into the application of emerging materials in marine infrastructures.

# LIST OF PUBLICATIONS

#### Journal papers from the dissertation:

**DENG, Fuhao**; WANG, Zhao; WEI, Yuanhao. Effect of loading frequency on tensile fatigue behavior of ultra-high-strength engineered cementitious composites. *International Journal of Fatigue*, 2025, 191: 108701. (published)

**DENF, Fuhao** et al. Tensile fatigue behavior of ultra-high-performance engineered cementitious composites considering stress reversal. *Construction and Building Materials*. (submitted)

**DENF, Fuhao** et al. Experimental Investigation on GFRP-Reinforced UHPECC Beams Subjected to Various Cyclic Deformation Histories. *Journal of Structural Engineering*. (submitted)

**DENF, Fuhao** et al. Design and hydrodynamic response of cylindrical shell tank for shallow coastal placement. *Engineering Failure Analysis*. (submitted)

# **ACKNOWLEDGEMENT**

The journey of completing a PhD thesis is rarely a solitary one, and I am deeply grateful for the many individuals and institutions that have supported me along the way.

First and foremost, I would like to express my sincere gratitude to my supervisors, Professor You Dong and Professor Jian-fei Chen, for their invaluable guidance, insightful discussions, and continuous support. Their expertise in the field, encouragement to explore new ideas, constructive criticism that shaped this research has been invaluable throughout this research. I am also indebted to Professor Guan Lin, Dr. Yu Xiang and Dr. Jiayu Wu. Their valuable insights, critical feedback, and diverse perspectives have significantly enriched this thesis.

I would like to acknowledge the The Hong Kong Polytechnic University (PolyU) and the Southern University of Science and Technology (SUSTech) for providing a supportive research environment and the resources necessary to carry out this work.

I am particularly thankful to my friends and colleagues for their collaborative spirit, stimulating discussions, and technical assistance. Special thanks go to those from PolyU, including Dr. Peng Yuan, Dr. Hongyuan Guo, Dr. Yaohan Li, Dr. Demin Zhu, Dr. Jing Qian, Dr. Menghan Zhao, Dr. Qian Wu, Dr. Zhihao Hao, Dr. Lujia Yu, Mr. Jiaxin Zhang, and Ms. Chuying Cui, as well as those from SUSTech, including Professor Chao Hou, Dr. Xiaojie Zhang, Dr. Qiqi Zou, Dr. Dengshuo Chen, Dr. Zhenbo Yu, Mr. Zhao Wang, Mr. Huiheng Lian, and Ms. Jingyi Zhang.

On a more personal note, I want to express my deepest appreciation to my family, for their

unwavering love, encouragement, and understanding throughout this demanding journey. Their belief in me has been a constant source of strength. Finally, to Yeping, thank you for your incredible patience, support, and love.

# **CONTENTS**

ABSTRACT	I
CONTENTS	IV
LIST OF FIGURES	XI
LIST OF TABLES	XVII
LIST OF ABBREVIATIONS	XIX
CHAPTER 1 INTRODUCTION	1
1.1 BACKGROUND	1
1.2 FIBER-REINFORCED POLYMER (FRP)	4
1.3 ULTRA-HIGH PERFORMANCE ENGINEERED CEMENTITIOUS CO. (UHPECC)	
1.4 FRP-REINFORCED UHPECC STRUCTURE	9
1.5 OBJECTIVES, SCOPE, AND LAYOUT OF THE THESIS	10
CHAPTER 2 LITERATURE REVIEW	15
2.1 INTRODUCTION	15
2.2 FATIGUE PERFORMANCE OF CONCRETE/ECC	15
2.2.1 Fatigue behavior of normal concrete	15
2.2.2 Fatigue behavior of fiber-reinforced concrete	17
2.2.3 Fatigue model concrete	20
2.3 FLEXURAL PERFORMANCE OF ECC MEMBERS	22
2.3.1 Flexural performance of ECC beam reinforced with steel or FRP bars .	22
2.3.2 Effect of deformation history on reinforced concrete members	26
2.4 EXISTING METHODS OF STORAGE FACILITIES	31
2.4.1 Storing oil in sea space	31
2.4.2 Performance of above-ground tanks	39
2.5 CONCLUSIONS	42
CHAPTER 3 EFFECT OF LOADING FREQUENCY ON TENSILE FATIGUE BE OF ULTRA-HIGH-PERFORMANCE ENGINEERED CEMENTITIOUS COM	IPOSITES
3.1 INTRODUCTION	45
3.2 EXPERIMENTAL PROGRAM	47

3.2.1 Preparation of concrete test specimens	47
3.2.2 Test method	48
3.3 FATIGUE TEST RESULTS AND DISCUSSIONS	49
3.3.1 Failure mode	49
3.3.2 Fatigue life	51
3.3.3 Fatigue deformation	58
3.3.4 Secondary strain rate	61
3.4 FATIGUE LIFE AND P-S-N MODELS	63
3.4.1 Distribution of static tensile strength and fatigue life	64
3.4.2 P-S-N models	67
3.5 CONCLUSIONS	71
CHAPTER 4 TENSILE FATIGUE BEHAVIOR OF ULTRA-HIGH-PERFO ENGINEERED CEMENTITIOUS COMPOSITES CONSIDERING STRESS RI	EVERSAL
4.1 INTRODUCTION	73
4.2 EXPERIMENTAL PROGRAM	74
4.2.1 Material	74
4.2.2 Testing method	74
4.2.3 Experimental Phenomena	75
4.3 FATIGUE TEST RESULTS AND DISCUSSIONS	76
4.3.1 Fatigue life	76
4.3.2 S-N curves	84
4.3.3 Fatigue deformation	89
4.4 CUMULATIVE FATIGUE DAMAGE MODEL	94
4.4.1 Review of existing fatigue models	94
4.4.2 Cumulative fatigue damage model	99
4.4.3 Method for estimating fatigue life under multilevel fatigue loading	104
4.5 CONCLUSIONS	104
CHAPTER 5 CYCLIC FLEXURAL BEHAVIOR OF GFRP BAR-REINFORCED	UHPECC
BEAMS	106
5.1 INTRODUCTION	106
5.2 EYDEDIMENTAL DDOGDAM	108

5.2.1 Materials	108
5.2.2 Specimen design and test setup	110
5.3 EXPERIMENTAL RESULTS AND DISCUSSION	115
5.3.1 Crack patterns	115
5.3.2 Load-deflection curves	118
5.3.3 Skeleton curves and loading capacity	122
5.3.4 Energy dissipation	125
5.3.5 Deformation capacity	126
5.3.6 Strain development in FRP reinforcement	129
5.4 THEORETICAL ANALYSES	130
5.4.1 Prediction of strength	130
5.4.2 Strength difference under two loading directions	132
5.5 CONCLUSIONS	134
CHAPTER 6 EXPERIMENTAL INVESTIGATION ON GFRP-REINFORCED UH BEAMS SUBJECTED TO VARIOUS CYCLIC DEFORMATION HISTORIES	
6.1 INTRODUCTION	137
6.2 EXPERIMENTAL PROGRAM	140
6.2.1 Specimen geometry	140
6.2.2 Materials	141
6.2.3 Test setup and instrumentation	142
6.2.4 Applied deformation histories	143
6.3 EXPERIMENTAL RESULTS AND DISCUSSION	146
6.3.1 Failure mode	146
6.3.2 Crack width evolution	148
6.3.3 Hysteretic response	153
6.3.4 Reinforcement strain evolution	158
6.4 CONCLUSIONS	166
CHAPTER 7 OFFSHORE STORAGE TANK: STRUCTURAL CONCEPT FEASIBILITY	
7.1 INTRODUCTION	168
7.2 CONCERT DEVELORMENT	171

7.2.1 Types of offshore storage tanks	171
7.2.2 Offshore fixed storage tank	174
7.3 ASSESSMENT OF FAILURE MODES IN OFFSHORE STORAGE TANK	S176
7.3.1 Possible failure modes	176
7.3.2 Environmental conditions	178
7.3.3 Floatation	181
7.3.4 Sliding	182
7.3.5 Overturning	184
7.3.6 Buckling	185
7.3.7 Recommended geometry range based on the above failure modes	186
7.4 RESPONSE OF CYLINDRICAL TANKS UNDER WAVE LOAD	187
7.4.1 Regular wave-induced pressure distribution on a cylindrical shell	187
7.4.2 Methodology for calculating stress response spectra	192
7.4.3 Regular wave-induced stress on a cylindrical shell	194
7.4.4 Stress response spectra of a cylindrical shell under the given wave spectr	rum .200
7.4.5 Parametric analysis	204
7.4.5.1 Effects of diameter and diameter to shell thickness ratio	204
7.4.5.2 Effects of water depth	207
7.4.6 Discussions	208
7.5 CONCLUSIONS	209
CHAPTER 8 CONCLUSIONS AND FUTURE WORK	211
8.1 CONCLUSIONS	211
8.2 FUTURE WORK	215
References	218

# LIST OF FIGURES

Fig. 1.1 Satellite derived variation of global mean sea level: 1993 - present (source:
https://climate.copernicus.eu/climate-indicators/sea-
$level \#: \sim : text = Since \% 201993\% 2C\% 20 global\% 20 mean \% 20 sea, Antarctic\% 20 and \% 20 Green land \#in the property of t$
nd%20Ice%20Sheets.)
Fig. 1.2 Floating fuel base in Japan (Ueda 2014)
Fig. 1.3 Floating hydrocarbon storage facil(CHI 2020)
Fig. 1.4 Typical FRP structural diagram
Fig. 2.1. Deformation histories employed in cyclic testing of reinforced ECC components by
(a) Fischer and Li (2003), (b) Parra-Montesinos and Chompreda (2007), (c) Yuan et al. (2013)
28
Fig. 2.2 Sectional view of Khazzan No.1 (source: Curtis and Shepler 1970)32
Fig. 2.3 An illustration of Condeep oil storage platform (source: Galbraith et al. 1993)32
Fig. 2.4 Floating oil storage systems featuring a floating tank secured to fixed anchors (source:
Hirata 1973)
Fig. 2.5. N'Kossa floating prestressed concrete barge (Source: Oil&Gas Journal 2019)34
Fig. 2.6. 3D architectural view of FHSF (Source: Zhang et al. 2019)35
Fig. 2.7. Isometric view of hydrocarbon storage tank (Source: Dai et al. 2019)36
Fig. 3.1. Dimension of tensile specimen
Fig. 3.2. Test setup
Fig. 3.3. Fatigue crack development at different stress levels for specimen F04-S09-5 in50
Fig. 3.4. Typical crack patterns observed in specimens under static and fatigue loading
conditions51
Fig. 3.5. Main crack at fatigue specimen

Fig. 3.6. The S-N relation under different loading frequencies	55
Fig. 3.7 Modified S-N relation of all tested specimens	57
Fig. 3.8 Evolution curves of fatigue deformation of S-shape	59
Fig. 3.9. Evolution curve of fatigue deformation under high-stress level	61
Fig. 3.10 Secondary strain rate	62
Fig. 3.11 Secondary strain rate plotted against the fatigue life	63
Fig. 3.12 Distribution of tensile strength fitted with the experimental measurements	65
Fig. 3.13 Distribution of fatigue life under various loading conditions	70
Fig. 4.1 Fatigue life fitted curves at each stress level under stress ratio of -0.1	81
Fig. 4.2 Fatigue life fitted curves at each stress level under the stress ratio of -1	82
Fig. 4.3 Fatigue life versus experimental variables	84
Fig. 4.4 The relationship between S and lgN	85
Fig. 4.5 The S-N relation based on Aas-Jakobsen's equation	88
Fig. 4.6 Evolution curves of fatigue deformation with stress ratio of -0.1	90
Fig. 4.7 Evolution curves of fatigue deformation with stress ratio of -1	92
Fig. 4.8 Evolution curves of fatigue deformation with stress ratio of 0.1 (tested in chap	ter 4)
	93
Fig. 4.9 Damage evolution under various loading conditions	103
Fig. 5.1 Tensile stress-strain curves of ECC	110
Fig. 5.2 Specimen details (unit: mm)	111
Fig. 5.3 Test set up	112
Fig. 5.4 Cyclic loading scheme	114
Fig. 5.5 Final crack patterns observed in various specimens	118
Fig. 5.6 Load-midspan deflection curves for specimens subjected to monotonic loading	118

Fig. 5.7 Load versus midspan deflection curves for specimens subjected	to tension-
compression cyclic loading	122
Fig. 5.8 Load versus midspan deflection curves for specimens subjected to co	ompression-
compression cyclic loading	122
Fig. 5.9 Skeleton load-deflection curves of specimens	124
Fig. 5.10 Calculation of energy dissipation	125
Fig. 5.11 Accumulated energy dissipations of specimens subjected to tension-c	ompression
cyclic loading	126
Fig. 5.12 Schematic diagram for energy calculation	128
Fig. 5.13 Development of strains in FRP reinforcement with the deflection: a) S-p1	.88-V2-C2
b) S-ρ1.13-V2-C2, c) S-ρ1.88-V1-C2	130
Fig. 5.14 Strength prediction method for a) specimens failed with fiber bridging ma	intained, b
specimens failed after fiber bridging damaged	131
Fig. 5.15 Strength envelop compare of (a) S-p1.88-V2-C2, (b) S-p1.13-V2-C2, (	c) S-p1.88-
V1-C2	134
Fig. 6.1 Details of the specimens (unit: mm)	141
Fig. 6.2 Test set up.	143
Fig. 6.3 Cyclic loading protocol: (a) FEMA, (b) Small-pulse, and (c) Large-pulse of	deformation
histories	146
Fig. 6.4 Final crack patterns of different specimens	148
Fig. 6.5 Setup of DIC system	150
Fig. 6.6 Evolution of crack width	152
Fig. 6.7 Hysteresis curves of specimens with 1.88% reinforcement ratio	157
Fig. 6.8 Hystarseis curves of specimens with 1.13% rainforcement ratio	157

Fig. 6.9 Impact of the initial pulse amplitude on ultimate drift, categorized by reinforcement
ratio
Fig. 6.10 Strain envelops in the middle span of FRP reinforcement
Fig. 6.11 Strain variation along longitudinal direction in the FRP reinforcement
Fig. 7.1 Semi submerged tank with a floating roof
Fig. 7.2 Semi submerged tank with a conical roof
Fig. 7.3 Semi submerged tank supported by piers
Fig. 7.4 Semi submerged tank with anchorage
Fig. 7.5 Submerged tank - A
Fig. 7.6 Submerged tank - B
Fig. 7.7 The layout of the offshore storage tank
Fig. 7.8 Schematic of the load-resistance forces considered for offshore storage tank floatation.
Fig. 7.9 Schematic of the load-resistance forces considered for offshore storage tank sliding.
Fig. 7.10 Impact of aspect ratio on sliding failure
Fig. 7.11 Impact of aspect ratio on overturning failure
Fig. 7.12 Schematic of the hydrostatic pressure considered for offshore storage tank buckling.
Fig. 7.13 Schematic of wave diffraction around a bottom fixed cylinder
Fig. 7.14 Snapshots of hydrodynamic pressure distribution on a cylindrical tank with Diameter
= 80 m, water depth = 20 m, wave height = 1 m, and wavelength = 100 m191
Fig. 7.15 Methodology to derive stress response spectra
Fig. 7.16 Hoop stress amplitude distribution at regular wave load for a cylindrical shell with $D$
= 60  m. $H = 30  m$ , water depth $= 20  m$ , wavelength $= 100  m$ , and wave height $= 1  m$ . (a) Stress

amplitude along the cylindrical shell circumference at the height of 16.5 m; (b) Stress amplitude
along with the cylindrical shell height at different locations
Fig. 7.17 Hoop stress amplitude along the cylindrical shell circumference at the height of 16.5
m ( $D = 60$ m, $H = 30$ m, water depth = 20 m, wavelength = 100 m, and wave height = 1 m)
Fig. 7.18 Hoop stress amplitude along the cylindrical shell circumference at the height of 16.5
m ( $D = 60$ m, $H = 30$ m, water depth = 20 m, wavelength = 180 m, and wave height = 1 m)
196
Fig. 7.19 Hoop stress amplitude along the cylindrical shell circumference at the height of 16.5
m ( $D = 60$ m, $H = 30$ m, water depth = 20 m, wavelength = 30 m, and wave height = 1 m) 197
Fig. 7.20 Hoop stress amplitude of the cylindrical shell ( $D = 60 \text{ m}$ , $H = 30 \text{ m}$ , water depth = 20
m, shell thickness = 240 mm, and wave height = 1 m)
Fig. 7.21 Axial stress amplitude of the cylindrical shell ( $D = 60$ m, $H = 30$ m, water depth = 20
m, shell thickness = 240 mm, and wave height = 1 m)
Fig. 7.22 Max hoop stress RAOs of the cylindrical shell ( $D = 60 \text{ m}$ , $H = 30 \text{ m}$ , water depth =
20 m)
Fig. 7.23 Max axial stress RAOs of the cylindrical shell ( $D = 60 \text{ m}$ , $H = 30 \text{ m}$ , water depth =
20 m)
Fig. 7.24 Wave spectrum at the selected place
Fig. 7.25 Response spectrum of the cylindrical shell ( $D = 60 \text{ m}$ , $H = 30 \text{ m}$ , water depth = $20 \text{ m}$ )
Fig. 7.26 The cumulative distribution function for the hoop stress in the cylindrical shell ( $D =$
60 m, $H = 30$ m, water depth = 20 m, shell thickness = 240 mm)204
Fig. 7.27 Effect of diameter/shell thickness ratio ( $H = 30 \text{ m}$ , water depth = $20 \text{ m}$ )206

Fig. 7.28 Wave-induced pressure along circumferential of the tank at still water surface (Unit:
MPa, $D = 60$ m, water depth = 20 m, wavelength = 70 m, wave height = 1 m)206
Fig. 7.29 Effect of water depth ( $D = 80 \text{ m}$ )

# LIST OF TABLES

Table 3.1 Proposition of the UHPECC mixture by weight ratio	47
Table 3.2 Properties of PE fiber	48
Table 3.3 Results of fatigue tests under the loading frequency of 1 Hz	52
Table 3.4 Results of fatigue tests under the loading frequency of 4 Hz	53
Table 3.5 Results of fatigue tests under the loading frequency of 16 Hz	54
Table 3.6 Regression parameters of secondary strain rate	63
Table 3.7 Direct tensile test for static strength	64
Table 3.8 Parameters for fitting the Weibull distribution	66
Table 3.9 Fitting parameters of Weibull distribution based on Equation (3-19)	71
Table 4.1 Results of fatigue test with a stress ratio of -0.1	77
Table 4.2 Results of fatigue test with a stress ratio of -1	78
Table 4.3 The fatigue life at a failure probability of 0.5 under different loading condition	ns83
Table 4.4 S-N curve fitting expressions	84
Table 4.5 Fitted value of maximum strain evolution curve	101
Table 5.1 Proportions of the ECC mixtures by weight ratio	109
Table 5.2 Properties of PE fibers	109
Table 5.3 Test matrix	112
Table 5.4 Deformation capacity of the test beams	128
Table 5.5 Summary of test results and estimated load	132
Table 6.1 Tested specimens	141
Table 7.1Failure modes of above-ground tanks	177
Table 7.2 Possible failure modes for offshore storage tanks.	178
Table 7.3 Design wave factors for 50 years return period	181

Table 7.4 Tanks with different geometry parameters	Table	7.4	Tanks	with	different	geometry	parameters		193
--	-------	-----	-------	------	-----------	----------	------------	--	-----

# LIST OF ABBREVIATIONS

AST Above ground tank

CPP Clean petrochemical products

DIC digital image correlation

ECC Engineered cementitious composites

FHSF Floating Hydrocarbon Storage Facility

FPU floating production unit

FRP Fiber-reinforced polymer

GFRP Glass-Fiber-Reinforced

LVDT Variable Displacement Transducer

PE Ultra-high-molecular-weight polyethylene

PVA Polyvinyl alcohol

P-S-N Probability of failure-stress level-fatigue life

RAO Response amplitude operator

RPC Reactive powder concrete

SHCC Strain-hardening cementitious composites

UHPECC Ultra-high performance engineered cementitious composite

UHTCC Ultra-high toughness cementitious composites

VLFS Very large floating structures

# **CHAPTER 1 INTRODUCTION**

### 1.1 BACKGROUND

Over the past few decades, coastal cities such as Hong Kong, Singapore, and Tokyo have experienced rapid development. The land supply in these cities is becoming increasingly limited. However, the demand for developable land in these cities continues to grow, driven by various needs including industrial development, residential expansion, and logistical requirements. In addition, the sea level rise induced by climate change presents growing challenges to these cities. The globally averaged sea level height derived from satellite monitoring has exhibited a rising trend for over thirty years, as illustrated in Fig. 1.1. Furthermore, the global average sea level rise has increased from  $2.1 \pm 1.1$  mm/year between 1993 and 2003 to  $4.3 \pm 0.6$  mm/year between 2013 and 2023, representing a 105% increase (Cazenave et al. 2018; Dieng et al. 2017). Prolonged sea level rise is anticipated to intensify coastal erosion, flooding, and storm impacts (Cazenave and Cozannet 2014).

# Mean sea level globally

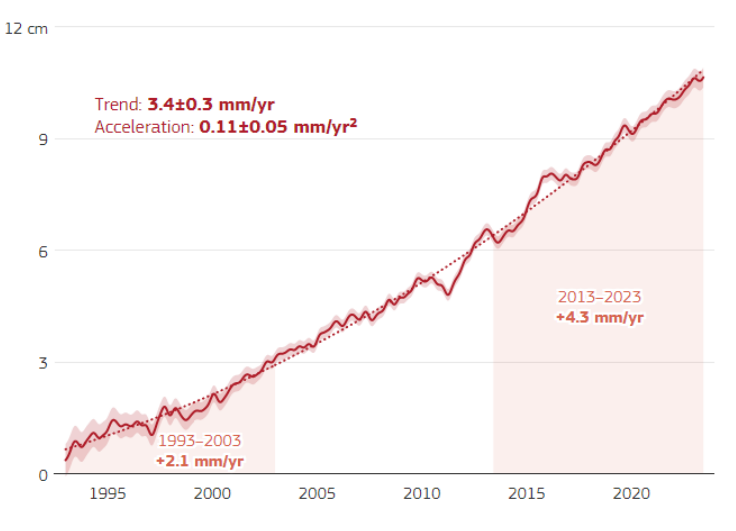


Fig. 1.1 Satellite derived variation of global mean sea level: 1993 - present (source:

#### https://climate.copernicus.eu/climate-indicators/sea-

level#:~:text=Since%201993%2C%20global%20mean%20sea,Antarctic%20and%20Greenland%20Ice%20Sheets.)

Against the above challenges, many coastal cities heavily rely on land reclamation to expand their land supply. However, such projects incur significant time and economic costs and can have negative impacts on ecosystems. Additionally, reclaimed areas are more susceptible to natural disasters (Watanabe et al. 2004). Rather than depending on land reclamation, an alternative strategy is to use sea space by installing marine structures, especially in nearshore waters. Coastal shallow waters typically experience mild sea state, making them well-suited for the construction of marine structures.

Recently, many researchers and companies have proposed various designs for offshore and marine structures. Considering residential preferences and transportation requirements, coastal and offshore marine structures are typically more suitable for industrial and public purposes, including airports, factories, ports, wind turbines, and other similar facilities. For example, Japan has adopted a steel-made floating oil storage system for strategic reserves as shown in Fig. 1.2 (Ueda 2014). A floating bridge operates in Norway (Wan et al. 2017; Eidem 2017). Benefiting from benign sea conditions, Singapore has undertaken many attempts in the field of marine structures. They placed a floating performance platform in reservoir condition (Sulaiman et al. 2013). They also proposed floating breakwaters (Jiang et al. 2018). A floating solar farm was also constructed in the coastal region (Zhang et al. 2022). Due to its proximity to one of the world's busiest shipping straits and its advanced petrochemical industry, Singapore has a substantial need for oil storage facilities. A collaborative team from Singapore

and Norway has developed an innovative concept called the Floating Hydrocarbon Storage Facility (FHSF), illustrated in Fig. 1.3. This novel FHSF concept features a modular design that allows for scalable construction to meet various capacity requirements, ranging from 5,000 m<sup>3</sup> to 35,000 m<sup>3</sup> (Zhang et al. 2019). The floating tanks are constructed using prestressed concrete, consisting of a central storage tank surrounded by four or eight empty floaters attached along the perimeter to provide additional buoyancy to the central tank. These floating tanks are of the single hull type, with skirts introduced at the tank's bottom to slow down motion response. The floating tank is housed within a frame-like structure barge with mooring systems connecting to the frame. The entire system is equipped with a station-keeping system to effectively respond to environmental forces.





(a) Shirashima

(b) Kamigoto

Fig. 1.2 Floating fuel base in Japan (Ueda 2014)

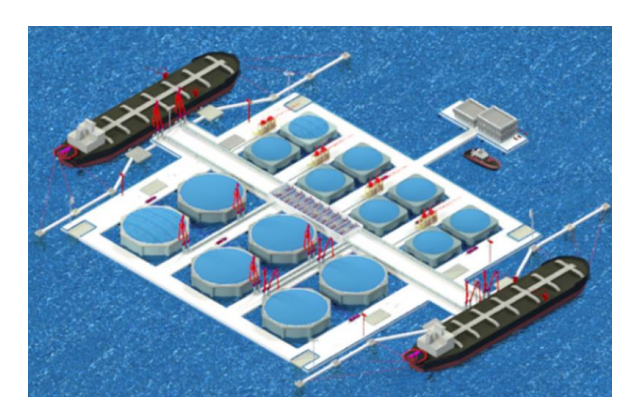


Fig. 1.3 Floating hydrocarbon storage facility (CHI 2020)

With the development of offshore engineering structures, some structures experience more complex loading conditions and severe environments, providing opportunities for the application of high-performance materials. Marine structures represent a significant and promising application for advanced materials, with engineered cementitious composites (ECC) and fiber reinforced polymer (FRP) being two notable examples. The integration of these high-performance materials can significantly minimize the overall dimensions of structural members, decrease self-weight, and enhance loading capacity and durability. This study aims to explore the feasibility of utilizing high-performance materials in marine engineering structures, considering the scales of materials, components, and entire structures.

#### 1.2 FIBER-REINFORCED POLYMER (FRP)

Corrosion of steel reinforcements is a major cause to the deterioration of concrete structures. Marine environments subject structures to more severe corrosion and cyclic loads over extended service periods compared to inland civil structures. Consequently, the corrosion and performance degradation of steel reinforcement in marine structures are significant concerns. Although some researchers have proposed methods such as electroplating protective coatings on steel surfaces or using epoxy resin coatings on steel surfaces to resist corrosion, these methods often fail to achieve ideal results in marine engineering structures. While some researchers have proposed methods such as electroplating protective coatings on steel surfaces or applying epoxy resin coatings to resist corrosion, these approaches often do not meet expectations in marine engineering structures. The utilization of fiber-reinforced polymer (FRP) reinforcement has become a promising method to overcome these shortcomings.

FRP is manufactured by combining fibers and resin matrix through a specific preparation process to achieve desired shapes and properties. The typical structure of FRP is shown in Fig. 1.4. Starting in the 1940s, material scientists began integrating high-strength, high-stiffness glass fibers as reinforcement into cost-effective, lightweight, and corrosion-resistant polymer resins. This process, typically achieved through pultrusion methods, achieves lightweight, high-strength composite materials known as glass fiber-reinforced polymers (Xue et al. 2016). Various types of FRP have emerged in the following decades, driving developments in defense and aerospace industries (Yang et al. 2020). With the production process of FRP matured the cost of products gradually decreased, leading to the gradual expansion of FRP materials into other industrial sectors, including civil engineering. The adoption of FRP in civil engineering has rapidly developed, with FRP material appearing more and more frequently in buildings, bridges, hydraulic structures, and port facilities.

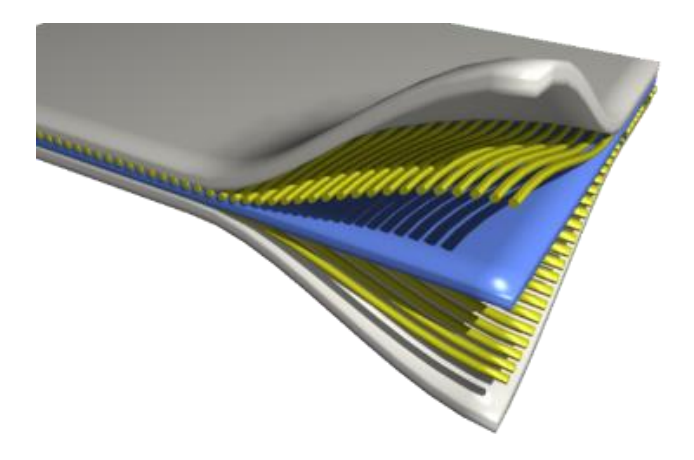


Fig. 1.4 Typical FRP structural diagram

FRP offers several advantages, including: (1) Lightweight and high strength. Utilizing FRP bars can considerably decrease the structure's self-weight while enhancing their loading capacity. (2) Excellent corrosion resistance. FRP bars can serve for a long time acidic, alkaline, chloride, and humid environment which is incomparable to steel. (3) Outstanding elastic

properties. Due to its linear elastic mechanical characteristics, FRP possesses strong recoverability upon unloading, making it suitable for structures subjected to dynamic, cyclic, or impact loads. (4) excellent design flexibility. FRP as a man-made material, FRP can be designed with various strength levels, elastic modulus, and cross-sectional forms by controlling parameters such as fiber type and content (Xiong et al. 2011; Liu et al. 2015).

FRP also has several notable disadvantages that need to be improved and avoided in design: FRP reinforcement is an elastic-brittle material, distinct from steel reinforcement in its tendency for brittle failure without a yield plateau (Peng and Xue 2018). The strength of FRP is primarily contributed by the fibers. In directions without fibers, the strength is determined by the properties of the matrix, resulting in reduced shear strength and interlaminar shear strength. FRP has a relatively low elastic modulus and its ultimate strain is significantly smaller than that of steel reinforcement (Hollaway and Teng 2008). Therefore, concrete structures reinforced with FRP may exhibit reduced stiffness and ductility. The matrix material of FRP reinforcement is epoxy resin, which tends to soften or even decompose at high temperatures. Therefore, FRP reinforcements are unsuitable for environments exceeding 60°C (Fang et al. 2020). Additionally, the material cost of FRP reinforcement remains high, with its unit mass price being approximately 8 to 12 times greater than that of steel reinforcement (Huang 2018a).

Although FRP provides promising durability and strength when used as reinforcement in concrete structures, its lower elastic modulus can result in a notable reduction in the stiffness of structural members. This reduction of stiffness may increase the risk of shear failure or premature concrete crushing. Meanwhile, strain in FRP reinforcement can develop unevenly: it tends to increase rapidly near crack locations, which can lead to early stress concentration

and potential fractures, while strain in other areas of the reinforcement may remain low until failure. These shortcomings limit its application in the field. To fully leverage the high strength of FRP and achieve a ductile failure structure, many approaches have been proposed (Grace et al. 2013; Zhao et al. 2016; Sonobe et al. 1997; Theriault and Benmokrane 1998). These methods can be summarized into two categories: the introduction of steel, which conflicts with the need for corrosion resistance in the marine environment, and the use of excess FRP reinforcement, which results in low utilization of materials.

# 1.3 ULTRA-HIGH PERFORMANCE ENGINEERED CEMENTITIOUS COMPOSITE (UHPECC)

In recent decades, the application of high-performance concrete presents as a potential solution for severe conditions. A category of high-performance engineered cementitious composites (ECC) has been developed to exhibit greater ductility in both compression and tension compared to normal concrete. By incorporating fibers, ECC can mitigate the quasi-brittle behavior of concrete and improve mechanical performance. The addition of fibers allows the material to sustain the tensile load even after cracking. As the load increases, multiple cracks will initialize and open to a certain width gradually (Lee and Barr 2004; Paskova and Meyer 1997; Grzybowski and Meyer 1993; Otter and Naaman 1988). The formation of multiple cracks prevents ECC from brittle fracture and exhibits strain-hardening behavior. Taking advantage of fibers, ECC can typically achieve an ultimate strain of over 3% before one particular localized crack grows wide enough followed by softening behavior (Zhang et al. 2011). Normal-strength ECC typically has a compressive strength ranging from 20 to 80 MPa, while high-strength ECC can achieve compressive strengths of 80 to 160 MPa (Huang et al. 2020). Compared to conventional concrete, ECC demonstrates superior performance under various

loading conditions, including monotonic, cyclic, fatigue, and impact loads. The formation of multiple fine cracks in the tensile zone contributes to ECC's notable ductility. The high spalling resistance with larger ultimate strain can prevent brittle failure due to crushing (Yuan et al. 2014). To ensure workability, the volume ratio of short fibers is lower than 2.5%. The micromechanics-based design theory for this material was initially introduced by Li and Leung (1992). ECC is also known as ultra-high toughness cementitious composites (UHTCCs) (Huang et al. 2020), or strain-hardening cementitious composites (SHCCs) (Peng et al. 2023). Due to its high performance, ECC has demonstrated potential for applications in structures under complex loading (Sahmaran et al. 2010; Leung et al. 2007; Zanuy et al. 2009; Ahlström et al. 2005; Wang et al. 1997). In structural applications, replacing normal concrete with ECC in the entire structure would result in significantly higher costs, mainly due to the expense of polymeric fibers compared to conventional cementitious materials and sands. To control costs, solutions include optimizing structural design, and using this material in critical loading areas (Takewaka et al. 2003; Matsumoto et al. 2004; Li et al. 2009).

The previous studies mainly focus on the normal strength ECC. However, in the complex long-term loading environment of marine applications, the application of ultra-high performance engineered cementitious composite (UHPECC) is expected to be more effective and suitable. Currently, research on the mechanical properties of UHPECC is still limited, and studies on UHPECC structural components are even rarer. In these cases, investigating the behavior of UHPECC is urgent and important for the design and application of structures utilizing this material.

#### 1.4 FRP-REINFORCED UHPECC STRUCTURE

The aforementioned offshore engineering structures must withstand significant marine environmental loads and meet durability requirements for long-term service. This imposes high demands on both their mechanical behavior and durability. The advancement of high-performance and durable marine infrastructure is crucial for the economic development of coastal cities. However, conventional marine infrastructure is constructed mainly of steel-reinforced concrete (RC) and thus faces a major challenge of deterioration due to steel corrosion (Rodrigues et al .2021). Due to their excellent corrosion resistance and high strength-to-weight ratios, fiber-reinforced polymer (FRP) composites (e.g., FRP bars and tubes) have emerged as a promising material in replacing steel in conventional steel RC structures in aggressive environments (Chen and Teng 2008). Typically, concrete structures reinforced with FRP bars (referred to as FRP-RC structures) are a promising form of structures for marine infrastructure.

Because FRP reinforcement is inherently brittle, structures reinforced with FRP exhibit significantly lower ductility compared to those reinforced with steel. To ensure a certain level of ductility, it is more desirable that the failure of an FRP-RC flexural member is governed by concrete crushing, by utilizing the inelastic behavior of concrete, although the failure mode of FRP bar rupture is also allowed in the current design codes/standards for FRP-RC flexural members (e.g., ACI 440.1R 2015). Note that in ACI code, a strength reduction factor of 0.55 is employed for FRP-RC flexural members governed by FRP bar rupture, which is smaller than that for members governed by concrete crushing (i.e., 0.65). However, for the members governed by concrete crushing, the strength of FRP reinforcement generally could not be fully utilized (i.e., the tensile strength of FRP bars is not reached when the member fails).

Furthermore, the energy dissipation capacity of an FRP-RC member is usually lower than that of a steel-RC counterpart, due to at least the following issues: (1) the linear elastic behavior of FRP reinforcement; (2) the inferior bond performance between FRP bar and concrete, especially under cyclic loading (Yan et al. 2016).

To address the above issues with FRP-RC flexural members, researchers have made plenty efforts in material and structural improvements. The present study adopted method from improve material performance, i.e. introduce ultra-high performance engineered cementitious composite (UHPECC). As a high performance material, the use of UHPECC with FRP bars leads to the following benefits of the reinforced members: (1) the tensile strength of FRP bars could be more easily fully utilized by capitalizing the ultra-high strength of UHPECC (commonly with a compressive strength of larger than 120 MPa); (2) good deformation compatibility between FRP bars and ECC due to the excellent ductility and toughness in tension caused by the presence of fibers; (3) better energy dissipation capacities of the members are anticipated due to the tensile toughness and multiple cracking behavior of ECC, as well as better bond performance between FRP and ECC compared with that between FRP and normal concrete. FRP and ECC, as high-performance materials, possess excellent mechanical and durability properties. With proper design, they can be combined to create high-performance components. These components can then be used to design marine infrastructure that meets long-term service requirements.

# 1.5 OBJECTIVES, SCOPE, AND LAYOUT OF THE THESIS

Against the above background, the main goal of this thesis is to assess the feasibility of using emerging materials in offshore infrastructures. The study began with an investigation at the

material scale, focusing on the fatigue performance of UHPECC. Subsequently, the research combined UHPECC with FRP at the component scale to examine the mechanical properties of structural members. Finally, using numerical methods, the research analyzed the structural performance of offshore storage tanks in marine environments to explore the potential applications of these emerging materials at the structural scale. More specifically, the thesis aims to:

- 1) Investigate the tensile fatigue behavior of UHPECC through experimental tests.
- 2) Develop a fatigue model to describe the degradation of UHPECC.
- 3) Examine the behavior of FRP-reinforced UHPECC flexural members under cyclic loading.
- 4) Explore the effect of cyclic deformation histories on FRP-reinforced UHPECC beams.
- 5) Propose an appropriate scheme for offshore storage tanks and assess their feasibility.

The thesis is structured into eight chapters, with a summary of each chapter as follows:

Chapter 2 begins with a comprehensive review of existing studies on material-scale investigations, focusing on the fatigue performance of ECC and the current models describing concrete fatigue degradation. Following this, to guide the structural-scale research of FRP-reinforced ECC members, the chapter reviews researches on the cyclic behavior of FRP/steel-reinforced ECC/concrete beams. Finally, it examines existing studies on the characteristics of above-ground tanks and floating storage tanks, along with their potential failure modes and application challenges.

Chapter 3 presents a material test on the tensile fatigue behavior of ultra-high-performance ECC using a direct tensile test set-up. This chapter focuses on the effects of stress levels and loading frequencies and on the fatigue performance of UHPECC. The test reveals that fatigue life increases with higher loading frequencies and decreases with higher stress levels. The analysis of the test results includes the examination of failure modes, fatigue life, deformation, and secondary strain rates. Using the fatigue life data, a probabilistic model for fatigue failure is proposed, incorporating the variability of initial tensile static strength. This model aligned well with the experimental results, offering important perspectives on the behavior of UHPECC under tensile fatigue conditions.

Chapter 4 further advances the foundation of Chapter 3 by introducing the stress ratio R and examining its impact on the fatigue life of ECC. Unlike most experimental investigations that set the stress ratio (the ratio of minimum to maximum stress during fatigue loading cycles) at 0.1, this study considers three different cases: 0.1, -0.1, and -1. Under a stress ratio of -0.1 and -1, it is evident that the stress experienced by the specimen has reversed. The experimental results indicate a significant reduction in the fatigue life of ECC when the stress ratio is less than zero. Building on the experiments from this and the previous chapter, and taking into account stress level, stress ratio, and loading frequency, a method for defining tensile fatigue damage in ECC is proposed. This method aims to predict ECC's fatigue life under random fatigue loading conditions.

Chapter 5 turns to the component level, studying the flexural performance of FRP-reinforced ECC members under cyclic loading. In this chapter, eight GFRP-reinforced ECC beams were

cast, along with two additional beams without fiber addition to serve as references. The beams were subjected to four-point bending tests to analyze factors such as the reinforcement ratio, the fiber volume ratio, and the loading methods affecting their flexural performance. By comparing the results of the tested beams, this research aims to provide a comprehensive understanding of how these factors affect the overall flexural performance of the beams subjected to cyclic loading conditions.

Chapter 6 investigates the impact of various loading histories on the cyclic performance of FRP-reinforced ECC members. In Chapter 6, all cyclic loading specimens employed a conventional loading protocol, where the applied loading displacement increased step by step. Based on this, Chapter 7 introduces two different loading histories, defined as cyclic loading with small initial pulses and large initial pulses. The cyclic performance of specimens under these different loading histories is compared, with a focus on hysteresis curves, crack development, and strain evolution.

Chapter 7 proposes an innovative storage tank designed for placement in coastal shallow waters. This scheme combines the advantages of both above-ground tanks and floating storage tanks, offering substantial storage capacity while maintaining stability in the sea. To substantiate the viability of this concept, the chapter outlines and examines the potential failure modes of the new structure. Given that wave load is the most critical factor for the overall design, an analytical method based on potential flow theory is adopted to determine the wave-induced hydrodynamic pressure on the cylindrical shell. Subsequently, numerical models of tanks are

constructed to evaluate and assess the feasibility of the proposed scheme. The results confirm the feasibility of the tank with a well-designed configuration.

The thesis concludes with Chapter 8, which reviews and summarizes the main findings drawn from the previous chapters. Additionally, it highlights several areas that warrant further investigation.

# CHAPTER 2 LITERATURE REVIEW

#### 2.1 INTRODUCTION

This chapter aims to offer a comprehensive literature review to support the following chapters in this dissertation. First, this chapter examines the fatigue characteristics of ECC, specifically emphasizing tensile fatigue and various fatigue modes, as ECC is the construction material used in this study. Next, existing studies on the cyclic performance of concrete flexural members, including both steel-reinforced and FRP-reinforced beams, are reviewed. Following this, different storage facilities are examined, including above-ground tanks and offshore floating tanks.

## 2.2 FATIGUE PERFORMANCE OF CONCRETE/ECC

The fatigue performance of concrete has been extensively studied due to its crucial impact on the durability and longevity of structures. Repeated loading over time can cause concrete to deteriorate, compromising the safety and functionality of the infrastructure. This section offers a concise review of the tensile fatigue behavior of concrete. According to literature reports, most researchers indicate that incorporating fibers can improve the fatigue performance of concrete.

## 2.2.1 Fatigue behavior of normal concrete

Early studies on the tensile fatigue performance of concrete were constrained by the limitations of loading equipment, leading scholars to primarily use bending and splitting test methods.

Around 1980, with improvements in equipment, researchers began to study the axial tensile fatigue performance of concrete.

In 1979, Tepfers (1979) performed axial tensile fatigue tests on 150mm cubic specimens with strengths of 40.8MPa and 56.7MPa, using stress ratios of 0.2, 0.3, and 0.4. A total of 60 specimens underwent testing. The findings revealed that the tensile fatigue performance of concrete could be accurately described using Wohler curves typically applied to compressive fatigue. Furthermore, the experimental data yielded predictive equations for the tensile fatigue life of both types of concrete. In 1983, Satiol (1983) employed custom-made friction fixtures to achieve direct tensile fatigue loading on concrete specimens. They derived the S-N curve equation for tensile fatigue in concrete. In 1993, Zhao et al. (1993) conducted comparative fatigue experiments on high-strength concrete using splitting, axial, and flexural loading. Their study revealed no notable difference in the fatigue performance of high-strength concrete under these loading conditions. Furthermore, they derived S-N curve equations for each loading condition and demonstrated a strong linear relationship between the growth rate of fatigue strain in the second stage and fatigue life. Lyu P.Y. (2002) investigated the axial tensile fatigue performance of concrete with a compressive strength of about 24.64 MPa using variable crosssection prismatic specimens. In the experiments, the minimum stress level was varied at 0, 0.15, and 0.30, while the maximum stress level ranged between 0.6 and 0.85. The study derived the S-N curve equation for axial tensile fatigue, taking into account the influence of both maximum and minimum stress levels. Feng and Song (2006), using data from axial tension-tension and tension-compression fatigue tests conducted under constant amplitude repeated loading on 76 concrete specimens from the literature (Lyu 2002), derived the correlation between the fatigue strength reduction factor of concrete after 2 million cycles and the minimum stress level. They

also provided fitting equations for the three-stage development patterns of fatigue strain and deformation modulus.

#### 2.2.2 Fatigue behavior of fiber-reinforced concrete

In the last twenty years, research on the fatigue performance of concrete with various added fibers has gradually increased. Behloul et al. (2005) conducted fatigue tests using a three-point bending setup on commercial steel fiber-reinforced reactive powder concrete known as Ductal. The specimens were initially exposed to quasi-static bending loads until the tensile strain at the bottom edge reached 0.30%. This was followed by bending fatigue tests with upper and lower stress limits set at 0.9 and 0.1 times the elastic limit strength, respectively. The results indicated that after 10 million fatigue cycles, the specimens exhibited only minor damage, with a corresponding fatigue limit of approximately 0.54 times the elastic limit strength. Lappa et al. (2006) performed four-point bending tests on another commercial ultra-high-performance concrete. Their findings revealed a linear relationship between the rate of deformation growth during the second stage and the number of cycles, and they provided the corresponding expression. However, due to variability in specimen strength, they did not provide the fatigue strength for 10 million cycles.

Parant et al. (2007) conducted bending tests of ultra-high-performance concrete reinforced with three different types of fibers. The findings revealed that fatigue strength after 2 million cycles was roughly 0.65 times of the static flexural strength. Shaheen and Shrive (2007) performed four-point bending fracture toughness tests as well as high and low cycle fatigue tests on Ductal commercial steel fiber reinforced concrete with a strength level of 150MPa. They derived a series of fracture mechanical parameters for Ductal commercial steel fiber-reinforced concrete.

The fatigue test results showed that reactive powder concrete (RPC) exhibited superior low and high cycle fatigue performance compared to ordinary concrete. This was due to the dense microstructure of RPC and the restraining effect of steel fibers, resulting in slower crack propagation.

Fitik et al. (2022) conducted uniaxial tension-compression fatigue tests on four different mixtures of ultra-high-performance concrete. They observed that the development of fatigue deformation in ultra-high-performance concrete followed a pattern similar to ordinary concrete, exhibiting three distinct stages. However, the presence of initial defects in the specimens resulted in significant variability in the test results and accelerated fatigue failure. Makita and Brühwiler (2014) in Switzerland conducted axial tensile fatigue tests on three groups of ultra-high-performance concrete, each containing 3% steel fiber by volume. The fatigue tests reached a maximum of 10 million cycles. Based on their experimental findings, they provided the S-N relationship curve for the axial tensile fatigue of ultra-high-performance concrete. Makita and Brühwiler (2015) introduced a bilinear form of the damage evolution equation for RPC, grounded in experimental findings. Furthermore, they developed a formula for the damage coefficient, which is indicated by the maximum total fatigue strain.

In recent decades, research on the fatigue properties of ECC has revealed that it exhibits a much longer fatigue life and greater ductility in deformation when subjected to flexural or compressive fatigue load, in contrast to conventional concrete (Müller and Mechtcherine 2017). Numerous researchers also have examined the fatigue property of ECC when subjected to tensile loads. Matsumoto et al. (2003) explored the tensile fatigue characteristics of ECC using a constant displacement amplitude. Huang et al. (2017) investigated the tensile fatigue crack

bridging in ECC. Matsumoto et al. (2010) also examined the uniaxial tension-compression fatigue properties of fiber-reinforced cementitious composites. Most prior studies on the fatigue behavior of ECC have employed polyvinyl alcohol (PVA) fibers with normal concrete strength. However, there is a scarcity of research on the fatigue behavior of high-strength ECC incorporating ultra-high-molecular-weight polyethylene (PE) fibers. To the author's knowledge, Zhou et al. (2020) investigated the impact of cyclic loading on the tensile fracture properties of ultra-high-performance ECC. Guo et al. (2020) examined the flexural fatigue performance of high-strength lightweight ECC. However, a more thorough understanding of the tensile fatigue behavior of high-strength ECC is needed.

Research has found that fatigue deformation under constant amplitude loading, regardless of whether the material is ordinary concrete, high-strength concrete, fiber-reinforced concrete, or other types of reinforced concrete, adheres to a three-stage deformation pattern that is unaffected by the stress ratio (Kou et al. 2018). The parameters explored in the fatigue tests include the stress level (S, the ratio of maximum loading stress to the ultimate strength), stress ratio (R, the ratio of minimum loading stress to the maximum loading stress), and loading frequency (f). The relationship established between fatigue life (N, the number of loading repetitions) and stress level is represented by the S-N curve. While the S-N curve is suitable for describing the fatigue behavior of steel, for concrete, other factors may also have an impact. The loading frequency can affect both fatigue life and the creep behavior of concrete (Nordby 1958). When examining the coupling effect of stress level and loading frequency, it was observed that for stress levels below 0.75, frequencies ranging from 1 to 15 Hz had minimal impact on fatigue life (Hanson et al. 1974). However, for stress levels exceeding 0.75, Sparks and Menzies (1973) found that the loading frequency demonstrated a notable impact on fatigue

life. Several researchers have proposed or adapted models to account for the influence of frequency (Zhang et al. 1996). Saucedo et al. (2013) investigated compressive fatigue behavior of fiber-reinforced concrete and developed a probabilistic model including loading frequency impact. Huang et al. (2017) investigated the loading frequency effect on the compressive fatigue behavior of ECC and also conducted a probabilistic analysis.

## 2.2.3 Fatigue model concrete

The primary reason for the gradual deterioration of mechanical properties during the fatigue loading of concrete is the internal accumulation of fatigue damage (Chen 2007). The incorporation of fibers can slow the accumulation of fatigue damage in concrete to some extent, thereby improving its fatigue performance. The most effective approach to studying the fatigue damage accumulation of fiber-reinforced concrete is to utilize microscopic quantities to reflect the deterioration of macroscopic mechanical properties. This involves treating fibers as a component and investigating the accumulation of damage in fiber-reinforced concrete from a microscopic level based on the fiber crack resistance mechanism. However, this method faces significant challenges due to the presence of numerous microcracks and micropores within the concrete itself, as well as the inherent randomness in fiber distribution (Batson et al. 1972). Therefore, it is crucial to develop a model that combines mechanical laws with characteristics observed through experimental research. This model should accurately depict the evolution of fatigue accumulation damage within fiber-reinforced concrete and its resulting deterioration in macroscopic mechanical properties (Bazant and Hubler 2014).

Numerous models describing the concrete fatigue damage process have been proposed. Whaley and Neville established an exponential function prediction model for fatigue inelastic

deformation in relation to loading stress and time based on fatigue tests of concrete prisms (Whaley and Neville 1973). Spark identified a strong linear relationship between the increasing rate of maximum fatigue strain in the second stage and fatigue life through uniaxial compression fatigue tests conducted on concrete specimens. Moreover, Sparks (1982) developed correlation equations in index form based on test data. Holmen conducted a study on the compressive fatigue behavior of concrete subjected to both constant and variable amplitude cyclic loads. From the test results, they established S-N-P fatigue life prediction curves that accounted for survival rate. Additionally, a segmented function form of the strain prediction method was derived from the fitted fatigue strain development curve. However, the complexity of this method limits its utility, as it does not provide corresponding prediction equations for strains beyond 80% of the cycle number (Holmen 1982). Maekawa introduced a fatigue constitutive model grounded in fracture micromechanics, assuming that the evolution of macroscopic deformation in concrete fatigue originates from the development of microcracks and defects (Maekawa et al. 2003). They further developed the nonlinear analysis software COM3, which can be employed to predict both low and high cycle fatigue performance in concrete structures (Maekawa et al. 2006a; Maekawa et al. 2006b; El-Kashif and Maekawa 2004). Bazant et al. (2014) proposed a fatigue fracture mechanics model for concrete, utilizing the Paris formula (Paris and Erdogan 1963). They calibrated the model parameters using experimental data and applied it to predict fatigue damage in real bridges. Kindrachuk et al. (2015) characterized the degradation of concrete materials under fatigue loading by evolving damage variables. They established a fatigue prediction model that includes yield surfaces, yield criteria, and rules for damage and hardening.

Recent years have seen substantial interest in examining the fatigue properties of fiber-reinforced concrete. Incorporating fibers into concrete can improve its fatigue performance, leading to an extended fatigue lifespan and increased deformation compared to conventional concrete (Zhang and Li 2002; Huang 2018b; Huang et al. 2018). Few models have been created and effectively predict the fatigue lifespan of fiber-reinforced concrete subjected to flexural loading. Qiu and Yang (2016) introduced a multiscale model to depict the fatigue behavior of the fiber-reinforced cementitious composites, focusing on the effects of fiber bridging. Li and Matsumoto (1998) developed a model to predict the fatigue life of brittle matrix composites reinforced with short fibers, relying on the phenomenon of fiber bridging during cyclic loading. Huang et al. (2019a) proposed an innovative model utilizing the three-parameter Weibull function to characterize the three-stage fatigue deformation behavior in both plain and fiber-reinforced concrete. Additionally, they presented a deformation-based approach for forecasting the fatigue life.

In summary, research on concrete fatigue mainly focuses on compressive and flexural fatigue, proposing various models. However, there is a noticeable gap in the exploration of concrete tensile fatigue, particularly concerning the tensile fatigue performance of fiber-reinforced concrete. Therefore, further investigation in this area is necessary.

## 2.3 FLEXURAL PERFORMANCE OF ECC MEMBERS

#### 2.3.1 Flexural performance of ECC beam reinforced with steel or FRP bars

Due to its crack control capabilities and outstanding ductility, ECC has seen extensive use in building, transportation, and hydraulic engineering over the past two decades. Reinforced ECC beams, when using either steel or FRP reinforcement bars, is well-suited for structural applications demanding high tensile strength. In the current study, the term "reinforced" denotes concrete reinforced with either steel bars or FRP bars. The fiber reinforcement effect within the ECC is implied. The presence of reinforcement bars complicates the analysis of structural responses due to their interaction with the composite material. Consequently, research on ECC members has been steadily emerging in recent years, though it remains relatively limited compared to studies on normal concrete members. This section, therefore, reviews ECC components reinforced with either steel or FRP, with a focus on their flexural cyclic behavior.

Reinforced ECC members are becoming more prevalent in construction, especially in elements subjected to severe conditions such as significant deformations or high shear stresses. These structures demand materials with exceptional damage tolerance, energy dissipation capacity, and ductility to withstand large cyclic deformations effectively. ECC possesses properties that align closely with these structural requirements. Its high ductility and ability to absorb energy make it suitable for flexural elements that must endure substantial cyclic forces. By incorporating these advanced materials into construction practices, infrastructure performance can be significantly enhanced in various severe conditions.

Several studies have examined the flexural performance of ECC members reinforced with FRP. By incorporating fibers in concrete, the compatible deformation between ECC and FRP reinforcement can reduce interfacial bond stresses and relative slip which can mitigate bond splitting cracks development and surface spalling (Li and Wang 2002; Maalej and Leong 2005). Another benefit of using ECC is a notable enhancement in ultimate compressive strain which reduces the risk of premature crushing of concrete. The ultimate compressive strain of concrete

with the incorporation of fibers ranged from 4000 to 5000 microstrains, compared with 2700 to 3000 microstrains for concrete without fibers (Wang and Belarbi 2011). Given that FRP is a high-strength material, employing high-strength ECC is more favorable for using the material properties of FRP. This can be evident in both improved cross-sectional bearing capacity and enhanced bonding reliability. Meanwhile, ECC is anticipated to develop multiple cracks on the tensile side. The tension stiffening characteristic of ECC allows it to continue carrying load even after cracking. These micro-cracks help distribute the stress, thereby increasing the stiffness of the cracked section. In contrast to normal concrete, which typically undergoes a sudden reduction in stiffness post-cracking, this behavior differs significantly. Moreover, the presence of multiple cracks in ECC aids in evenly distributing strain and delaying stress concentration on FRP reinforcement in the longitudinal direction. Consequently, tension stiffening in ECC significantly enhances structural performance under various loading conditions.

A series of static behaviors of FRP-reinforced ECC flexural members have been reported as mentioned before, but there is a notable gap in research concerning their cyclic behavior, particularly for FRP-reinforced high-strength ECC under cyclic loading. Fischer and Li (2003) investigate the cyclic performance of ECC columns reinforced with FRP, which are of normal strength. Peng et al. (2023) tested the cyclic behavior of normal strength concrete beams reinforced with polypropylene fibers, utilizing both prestressed CFRP tendons and nonprestressed steel bars. Xue et al. (2008) investigated the cyclic performance of prestressed fiber-reinforced concrete beams compared to prestressed conventional concrete beams. They found that incorporating polypropylene fibers greatly enhances the energy dissipation and ductility of steel prestressed concrete beams.

Although research on the cyclic behavior of FRP-reinforced ECC members is limited, studies on steel-reinforced ECC members can be reviewed for reference. Fischer and Li (2002b) demonstrate that integrating ECC with steel reinforcement leads to compatible deformations when subjected to uniaxial tension. This combination mitigates interfacial bond stresses and helps to prevent bond-splitting cracks as well as cover splitting. They later explored how the ductile deformation characteristics of ECC influence the performance of steel-reinforced flexural members subjected to lateral load reversals. Their research revealed that integrating a ductile cementitious matrix with steel reinforcement improves energy dissipation capacity, lessens the necessity for transverse steel reinforcement, and encourages damage-tolerant inelastic deformation characteristics (Fischer and Li 2002a). Canbolat et al. performed extensive tests to assess the damage tolerance and stiffness retention ability of ECC coupling beams. Thanks to the confinement provided by the ECC material, they were able to eliminate the transverse reinforcement around the diagonal bars (Canbolat et al. 2005). Kesner and Billington (2005) employed ECC for producing precast panels as substitutes for conventional reinforced concrete or masonry. They conducted FEM and structural scale examinations, demonstrating that modifying the ECC material composition and the quantity of reinforcement in the panels can achieve different degrees of panel strength and rigidity. Billington and Yoon (2004) proposed system utilizes unbonded post-tensioning to join precast segments, facilitating the incorporation of ECC in segments that may experience plastic hinging. Research revealed that incorporating ECC enabled the system to dissipate a greater amount of hysteretic energy compared to conventional concrete, particularly at drift levels ranging from 3% to 6%. Furthermore, ECC demonstrated superior structural integrity compared to reinforced concrete when subjected to high cyclic tensile-compressive loads. Yuan et al. (2014) carried out experiments on several RC/ECC composite beam-column joints subjected to reversed cyclic loading. They aimed to investigate how replacing conventional concrete with ECC in the joint area impacts the seismic performance of composite structures. Their results indicate that ECC can notably enhance both the load-bearing capacity and ductility of the beam-column joints, as well as enhances energy dissipation, owing to the material's high ductility and shear strength. Prior research consistently validates that substituting concrete with ECC enhances energy dissipation capacity and ensures better structural integrity. ECC, with its distinctive characteristics, can synergize with steel reinforcement to enhance the ductility of steel-reinforced elements.

## 2.3.2 Effect of deformation history on reinforced concrete members

The deformation history describes the sequence, magnitude, and frequency of deformation cycles undergone by a test specimen during testing or by an engineering structure throughout its service life. When analyzing structures subjected to loads such as waves, earthquakes, etc., it becomes essential to conduct a statistical analysis of the structure's response under numerous random loading conditions. In experimental studies, structural deformation history is typically controlled by applying controlled displacements or forces. However, due to constraints such as time and cost, experiments can only explore the response of test specimens under several types of loading histories. To calibrate structural analysis based on the results from limited experimental loading histories to real random loading histories, it becomes crucial to choose loading histories and understand their impact on the loading capacity (Krawinkler 2009).

A deformation history that encompasses the hazardous conditions experienced by the structure under actual loading conditions would be considered appropriate. Identifying hazardous

conditions can be challenging in most cases. Therefore, during experimental testing, it is often necessary to rearrange the cycling periods so that the smallest amplitude occurs first, followed by a monotonically increasing amplitude of cycles (Hutchinson and Wood 2013).

Certain deformation histories are specifically associated with construction materials, such as wood (ISO/TC 165 2003), whereas others are suggested for application to components regardless of the material used (FEMA 2007). Due to the complexity of deformation histories, researchers often resort to alternative deformation histories. So far, there is presently no deformation history specifically designed for ECC. Previous researchers have utilized alternative deformation histories to study ECC components as depicted in Fig. 2.1. The varying number of cycles for each amplitude level and the growth rate between successive amplitude levels make it challenging to compare different loading histories. Nevertheless, the amplitudes of these loading histories all demonstrate a monotonic increase. Consequently, deformation histories that include initial impulses are usually not taken into consideration. However, in practical engineering, structures may be impacted by initial impulses at an early stage. For instance, when subjected to seismic loads, the comparable speeds of rupture and shear waves cause most of the seismic energy reaching the structure in a single pulse (Krawinkler et al. 2001), or when, marine structures may encounter focusing waves (Chen et al. 2022). The susceptibility of FRP-reinforced ECC members to initial deformation pulses, which might cause crack localization, remains uncertain. In other words, it remains uncertain whether the results from an FRP-reinforced ECC component experience a monotonically increasing amplitude deformation history can be used to predict the behavior of the same component under a variety of unpredictable deformation histories.

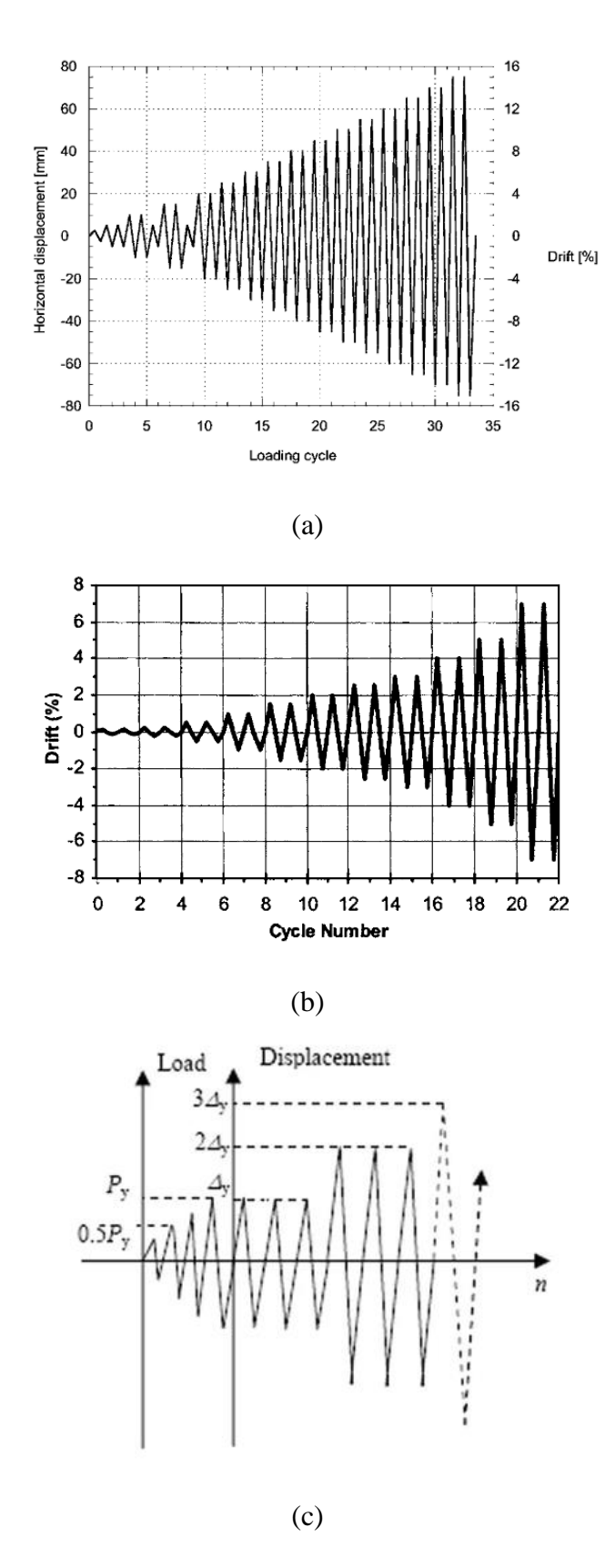


Fig. 2.1. Deformation histories employed in cyclic testing of reinforced ECC components by

(a) Fischer and Li (2003), (b) Parra-Montesinos and Chompreda (2007), (c) Yuan et al.

Although there have been no reported studies specifically on the effect of deformation history on FRP-reinforced beams, existing research on the deformation history effects on steel-reinforced concrete and steel-reinforced ECC can provide valuable guidance for the present study.

Hwang and Scribner investigated how different sequences and magnitudes of displacement history influence the flexural cyclic behavior of reinforced concrete elements. The findings showed that the amplitude of the maximum displacement experienced by the specimen had a considerable effect on the reduction in strength and stiffness, while the order of loading cycles had minimal impact (Hwang and Scribner 1984). Kawashima and Koyama (1988) conducted a series of tests using large-scale reinforced concrete piers with dynamic loading. This study primarily focused on the number of cycles required for each displacement amplitude step, varying from 3 to 10. The results showed that a higher number of cycles per displacement amplitude step led to increased buckling and fracture occurrences in the steel reinforcement. Lukkunaprasit and Thepmangkorn (2004) studied the influence of two typical loading histories on the ductility and energy dissipation capacity of concrete columns. The findings indicated that an increased rate of loading amplitude between two steps was positively correlated with the ultimate drift. For a specific level of drift, the accumulated plastic deformation in steel decreased as the rate of amplitude increase rose, leading to reduced overall deterioration in the concrete. The delaying concrete deterioration proved advantageous in achieving the specimen's ultimate drift capacity.

Several researchers have investigated how deformation history impacts steel-reinforced ECC members. Lignos et al. (2014) developed an innovative system for retrofitting existing steel moment-resisting frames after earthquakes, employing high-performance fiber-reinforced cement-based composite infill panels. This system aims to enhance dissipated energy during cyclic loading. Their findings indicate that the concrete's cracking pattern under recorded ground motions notably differs from that observed under gradually increasing deformation histories. Frank et al. (2018) tested eighteen steel-reinforced ECC flexural members under cyclic loading with three different loading histories. The results indicate that the deformation history has a wide range of effects on cracking patterns, strain accumulation in steel reinforcement, and fiber damage while having minimal impact on specimen ductility and failure modes. The monotonic increasing amplitude loading protocol may serve as a conservative method for testing steel-reinforced ECC members.

Compared to steel-reinforced concrete components, steel-reinforced ECC components exhibit distinct responses to various cyclic deformation histories. ECC demonstrates strain compatibility beyond steel yield, unlike their counterparts in normal concrete (Moreno et al. 2014). The enhanced bond strength in ECC contributes to this strain compatibility by limiting splitting cracks and mitigating or minimizing debonding from the steel bars. Conversely, ECC components reinforced with FRP might exhibit differences compared to those reinforced with steel, primarily due to FRP's linear elastic nature, which lacks a yield plateau. Consequently, the evolution of energy dissipation capability differs significantly between FRP reinforcement and steel reinforcement. Additionally, the bond between FRP and ECC is typically weaker compared to that between steel reinforcement and ECC. These differences necessitate further study to understand their respective impacts fully (Bandelt and Billington 2016a).

Under cyclic loading, the early stages often see initial pulses that can quickly lead to crack localization and fiber pull-out in the deformation process. This phenomenon alters the behavior of reinforced ECC specimens compared to those experiencing deformation histories with steadily increasing cycle amplitudes. The magnitude of the initial pulse can indicate occurrences such as splitting, debonding, crack localization, and fiber failures. After crack localization, the quantity and intensity of cycles in the deformation history are anticipated to influence residual stiffness, energy dissipation, strain localization, and strain accumulation in the FRP reinforcement. These response traits could play a crucial role in determining failure during random hazard events and guide decisions on post-failure repairs.

#### 2.4 EXISTING METHODS OF STORAGE FACILITIES

#### 2.4.1 Storing oil in sea space

Storing oil in the ocean offers a compelling option for oil storage, especially for coastal cities. This idea has captured the interest of the oil and gas industry for many years. In 1969, Dubai constructed an underwater fuel storage installation known as Khazzan No.1, depicted in Fig. 2.2. This storage tank, designed with a bottomless, inverted funnel shape, was intended for the storage of cured oil by employing the water displacement principle (Curtis and Shepler 1970). Galbraith et al. (1993) later applied the same principle in designing the gravity-based Condeep oil storage platforms as shown in Fig. 2.3.

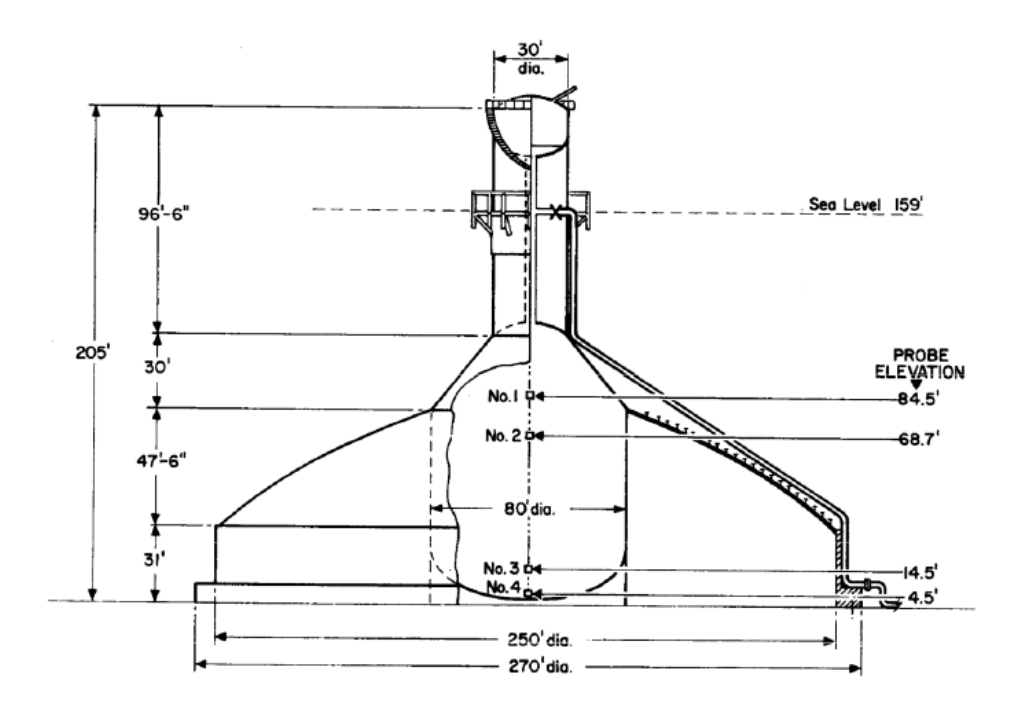


Fig. 2.2 Sectional view of Khazzan No.1 (source: Curtis and Shepler 1970)



Fig. 2.3 An illustration of Condeep oil storage platform (source: Galbraith et al. 1993)

While gravity-based offshore oil storage facilities are stable in severe environmental conditions, their use is considerably restricted by the conditions of the seabed. To enable fuel storage in calm waters, Hirata (1973) introduced the idea of floating bottomless tanks, referred to as the "Floating oil storage installation", depicted in Fig. 2.4. The principle of water displacement ensures floating ability, with the roof providing buoyancy when the oil level is low. However, one major issue with using the water displacement principle is the potential for contaminating both the marine environment and petrochemical products, making it unsuitable for storing clean petrochemical products (CPP).

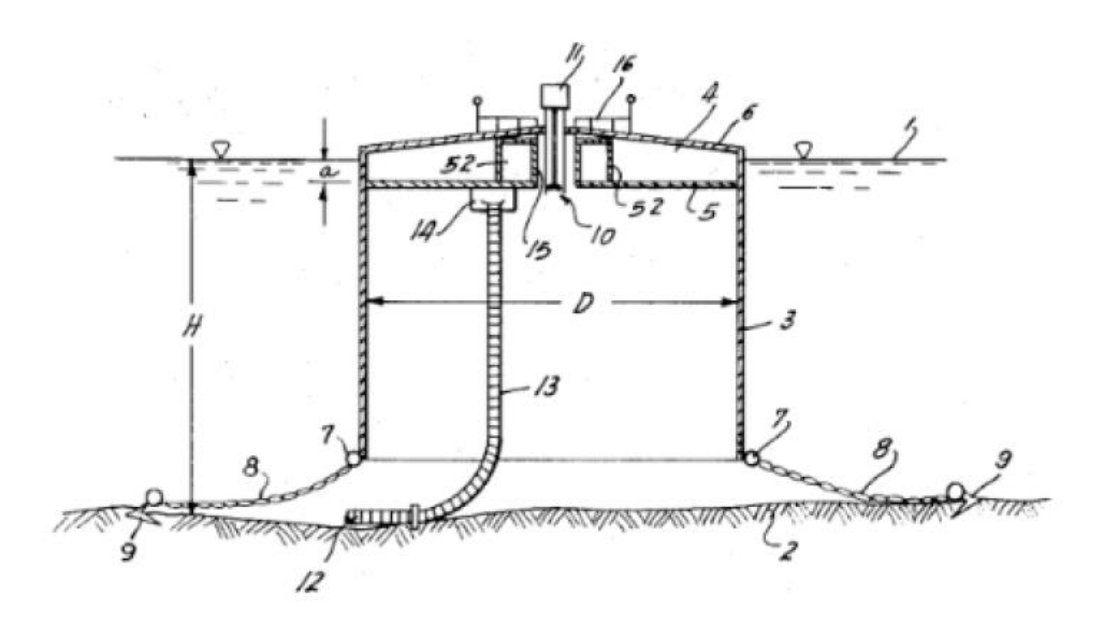


Fig. 2.4 Floating oil storage systems featuring a floating tank secured to fixed anchors (source: Hirata 1973).

Technology involving very large floating structures (VLFS) has also been utilized in the oil and gas sector. Japanese deployed two floating fuel storage facilities: the Kamigoto Oil Storage Base and the Shirashima Oil Storage Base (Fig. 1.2). These facilities are made up of several large, box-like steel storage modules, each divided into several oil tanks (Bhattacharya et al. 2006). Additionally, a comparable large prestressed concrete floating production unit (FPU)

for crude oil storage is deployed at the N'Kossa field in Congo, as illustrated in Fig. 2.5 (Collet et al. 2014).



Fig. 2.5. N'Kossa floating prestressed concrete barge (Source: Oil&Gas Journal 2019)

The VLFS storage facilities previously mentioned offer a robust method for both long-term and emergency oil storage at sea. However, these facilities are intended to support onshore oil fields and are not equipped for regular processing and trading activities. Maintaining the full capabilities of a land-based oil terminal remains highly advantageous. To tackle this issue, researchers in Singapore have introduced a novel design known as the "Floating Hydrocarbon Storage Facility" (Zhang et al. 2019). An overview of the scheme is presented in Fig. 2.6.

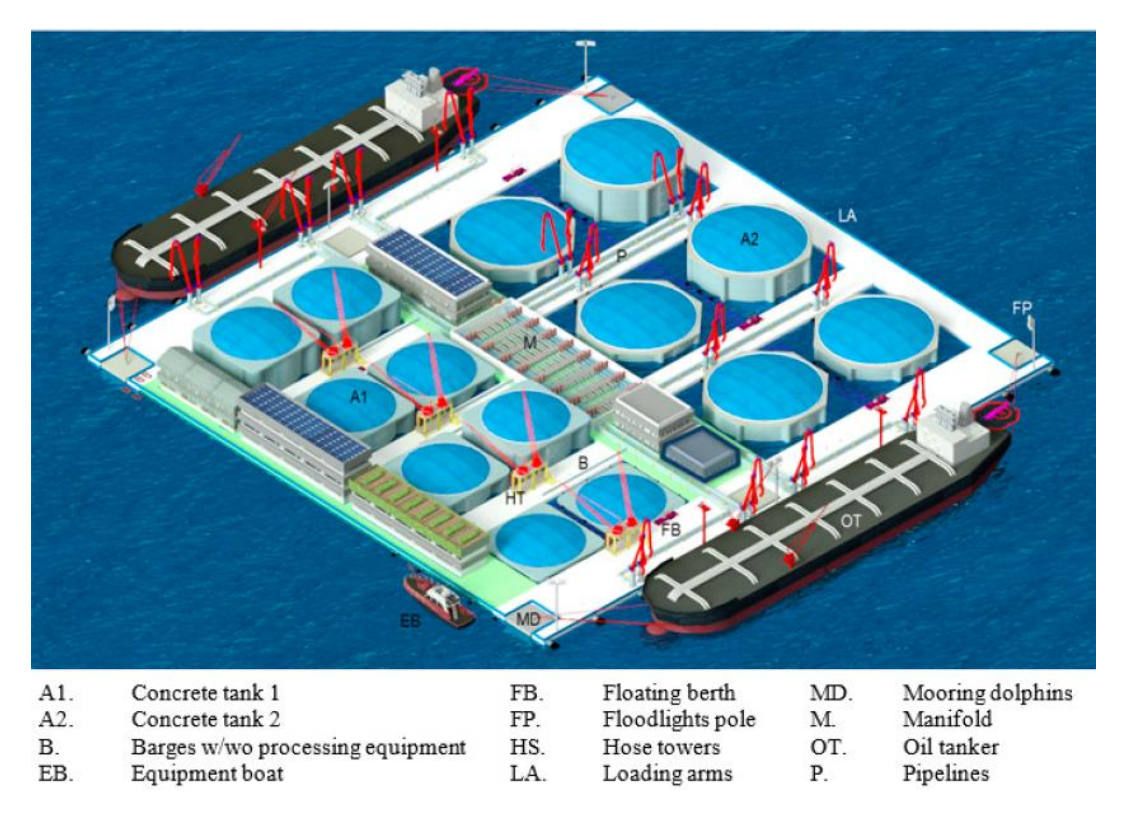


Fig. 2.6. 3D architectural view of FHSF (Source: Zhang et al. 2019)

This concept is comprehensive and includes all necessary facilities, including a power generation plant, control room, warehouse, and worker accommodations, all situated on the floating offshore base. Additionally, it features floating berths on the sides for oil tanker to load/unload hydrocarbon products. These floating berths and barges also help protect the storage tanks from wave action and the forces exerted during ship berthing. The dimensions can be modified based on local design standards, the size of the tank, environmental conditions, and other relevant factors.

In the scheme proposed by Singapore researchers, the FHSF system spans roughly 300 meters in length and 310 meters in width, with a total storage capacity of  $300,000 \, m^3$ . The FHSF system consists of floating storage tanks and floating barges. There are two proposed types of FHSTs: smaller tanks with storage capacities between 5,000 and  $15,000 \, m^3$ , and larger tanks

with capacities between 30,000 to 35,000  $m^3$  as shown in Fig. 2.7. The smaller FHST features a central cylinder, referred to as the central tank, which is used for hydrocarbon storage, surrounded by four side cylinders, or floaters, which provide additional buoyancy, enhance hydrostatic stability, and protect the central tank. The larger FHST follows a similar design but has an octagonal outer shape. Both variants of FHSTs are constructed as single-hull concrete structures, with a design lifespan of 60 years. The single-hull design allows for balanced hydrostatic pressure both inside and outside the tank, thereby minimizing the necessary wall thickness. The FHSTs are secured using a mooring system, including mooring fenders or hawsers, which are connected to the floating barges. These barges serve multiple purposes: they provide anchor points, protect the FHSTs from potential ship collisions, act as breakwaters, and support the daily operational access. The floating tanks are contained within the floating berths, allowing each tank to float freely and self-stabilize in the sea. These tanks could be built in conventional dockyards and deployed to their service position via tugboats. Each tank can operate independently for loading or unloading without affecting the others. The tank is designed to float freely on the water surface under any circumstances.

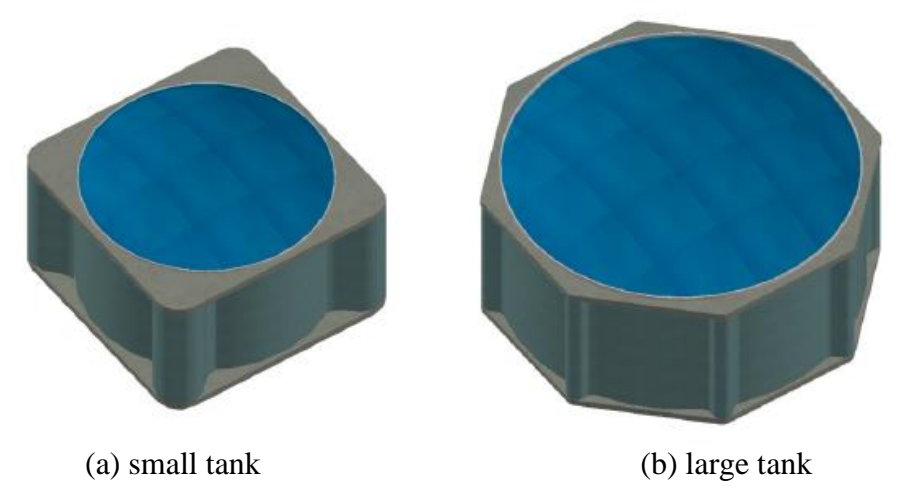


Fig. 2.7. Isometric view of hydrocarbon storage tank (Source: Dai et al. 2019)

The floating barges are constructed from concrete, but their very flat and wide structure—approximately 310 meters in length and 6 to 8 meters in depth—faces challenges from wave bending. To address this, the barge design incorporates a modular approach, with the modules connected by flexible connectors. These flexible connectors are anticipated to greatly reduce the sectional bending moments on the barges, thereby decreasing stress on both the deck and the bottom. The floating barges will be secured using mooring dolphins anchored to the seafloor, which will restrain the horizontal movement of the entire barge system. The system can move freely in the vertical direction, effectively accommodating tidal influences. Although initially intended for shielded coastal environments, this concept is adaptable for open sea applications and various other uses with only slight modifications, demonstrating its versatility as a modular compliant structure.

As the FHSF is a newly proposed concept, the research team at NUS has conducted extensive efforts on it. They began by studying the hydrodynamic response of a single floating tank induced by hydrodynamic loads. To verify the feasibility of a single FHSF, the research team designed scaled model tests for two different bottom plate shapes of the FHST, one of which featured a bottom skirt. They conducted decay tests, as well as regular and irregular wave tests, under the designed sea conditions. The motion of the rigid body in six degrees of freedom and the total reaction force of the skirts were measured. Then, a numerical model of the single FHST was developed and subjected to both frequency-domain and time-domain analyses (Wan et al. 2018a). Then, they focused on the mooring system between the barge and the storage tank. Starting with a single tank, they considered both empty and fully loaded conditions, designing various mooring fender configurations. They investigated the dynamic performance of storage tanks by changing the parameters of the fender mooring system across different

regular wave scenarios (Wan et al 2018b). In addition to fenders, another proposed mooring system involves multiple mooring ropes. These mooring ropes are elastic and capable of bearing mooring loads under all loading and environmental conditions. The research investigated the motion response of a single floating tank under linear and nonlinear mooring constraints, while also considering the scenario of one mooring cable failure (Wan et al. 2018c).

Their research expanded from analyzing a single tank to examining the entire modular system, which includes multiple tanks and barges while considering their interactions under wave load. They established a simplified model to verify the hydrodynamic response of the entire system. They acquired both the free surface elevations within the moonpool/gaps, as well as the hydrodynamic performance of the three floating structures (Zhang et al. 2020a). Additionally, the study examined various scenarios, including systems with two, three, and four barges, to analyze fluid dynamics interactions between different objects and optimize their configurations. They assessed the dynamic response of the storage tanks, considering both scenarios with and without fluid dynamics interactions (Amaechi et al. 2022).

Of course, there are still some issues with this newly proposed structure that require further study. For example, the coupling between liquid sloshing in the tanks and wave loads needs to be examined, especially given the potential for varying storage levels during the operation of oil tanks. In the above research, this issue has been simplified. Additionally, the detailed structural design and stress analysis of the tanks which are made of prestressed concrete, also require further exploration. In summary, they have conducted meaningful explorations in the utilization of ocean space.

#### 2.4.2 Performance of above-ground tanks

Above-ground storage tanks (ASTs) are the most commonly utilized facilities for storing oil, petrochemical products, and other hazardous materials. Due to economic and logistical considerations, ASTs are typically placed in coastal areas. Given the catastrophic consequences of the leakage of storage tanks, ensuring the safety of these tanks under various disaster scenarios is of particular importance. Against this background, several studies have addressed safety problems associated with ASTs in relation to different extreme events, including earthquakes, hurricanes, and floods.

For instance, Haroun and Housner (1981) performed a numerical analysis of flexible aboveground storage tanks (ASTs) employing finite element methods and boundary solution techniques. Niwa and Clough (1982) performed experimental study on the performance of ASTs subjected to seismic excitation. Barton and Parker (1987) conducted a finite element analysis to evaluate the seismic behavior of both anchored and unanchored storage tanks. Sakai et al. (1984) investigated the issue of sloshing in ASTs equipped with floating roofs. These studies aid in the creation of guidelines for the seismic design and assessment of ASTs (ASCE 2011; API 2013). Additionally, several seismic risk assessment studies have been conducted on ASTs (Fabbrocino et al. 2005; Salzano et al. 2003), utilizing historical earthquake performance data of ASTs to create empirical fragility curves through probabilistic analysis. These fragility curves are subsequently integrated with seismic hazard curves to evaluate risk.

While the seismic behavior of ASTs is well-documented, their response to various hurricaneinduced hazards remains relatively limited. Attention was drawn to this issue following hurricanes Katrina and Rita, as numerous tanks situated in coastal areas experienced severe failures. The most commonly observed failure modes were tank flotation and shell buckling caused by excessive wind pressure (Qin et al. 2020). A large storage tank at the Murphy Oil Refinery experienced flotation, causing the release of approximately 4,000 cubic meters of crude oil. This incident made around 1,800 homes uninhabitable across an area of roughly 2.6 square kilometers (Bernier and Padgett 2018). In 2017, Hurricane Harvey caused 47 instances of tank damage, leading to the release of two million liters of oil and other chemicals. Cozzani et al. (2010) investigated more than 272 industrial accidents related to flooding and found that ASTs were among the most vulnerable components. They attributed tank failures to flotation, debris impact, tank collapse caused by water pressure (i.e., buckling), and floating roof collapse. During Hurricanes Katrina and Rita, ASTs failed, leading to the discharge of over seven million gallons of petroleum products into the surrounding area (Maki 1991). These spills have detrimental impacts on the environment and natural habitats, both in the short and long term (Kingston 2002). Beyond environmental harm, Oil spills not only cause environmental damage but can also negatively impact the mental and physical health of nearby communities (Palinkas et al. 1993) and entail expensive cleanup efforts. For instance, the Murphy oil spill during Hurricane Katrina resulted from the failure of one large AST, released over one million gallons of crude oil and affected approximately 1,700 homes. Furthermore, the costs associated with cleaning, lawsuits, and economic loss following such disasters are also substantial.

Several studies have already identified the significant impact of hurricanes and their accompanying storm surges on ASTs. Kameshwar and Padgett (2015) conducted a fragility assessment of a case study tank subjected to storm surge conditions, examining both flotation and buckling failure. During Hurricane Katrina, numerous ASTs were noted to have suffered damage from wind-induced buckling (Godoy 2007). This damage impairs the operational

capability of these structures following the event, and in extreme situations, the rupture of the tank shells can result in catastrophic spills. The buckling performance of storage tanks often becomes a critical factor (Godoy et al. 2002; Chen and Rotter 2012; Flores and Godoy 1998) due to the heightened external pressure from wind and waves, which can easily induce buckling failure. Khakzad and Van Gelder (2017) revealed that storage tanks that are empty or have low liquid levels have been found to be more vulnerable to damage from wind, floods, and rain due to the large net pressure from external forces. Recommendations propose filling storage tanks with water before hurricanes to lessen their susceptibility. Nonetheless, this approach could compromise the quality of the stored chemicals and lead to extra expenses for water removal and treatment post-hurricane. Research on this aspect remains limited. At the same time, as thin-walled structures, the buckling performance of tanks can be easily affected by imperfections. Previous research relies on eigen or buckling mode configurations to illustrate imperfections (Portela and Godoy 2005a; Portela and Godoy 2005b), which tend to underestimate the buckling resistance of ASTs (Greiner and Derler 1995). Alternative approaches for imperfection modeling in buckling analyses are available beyond eigenmode shapes. For instance, one alternative method involves utilizing the Fourier representation of imperfections, as proposed by Teng et al. (2005) and Hornung and Saal (2002). Nevertheless, these representations introduce a degree of bias in imperfection modeling since factors such as imperfection amplitudes are still manually selected.

Additionally, many design guidelines, such as API 650 (2013), primarily focus on preventing wind-induced buckling of tank shells and mitigating tank tipping during earthquakes by recommending the use of anchors. Tank owners are generally given the responsibility to implement measures for preventing flotation failure caused by storm surges and floods, as per

these guidelines. The previous research has deepened our comprehension of the behavior of above-ground tanks when exposed to various hazards. The proposed offshore storage tanks are expected to experience similar loading conditions in coastal shallow water areas, particularly considering that the types of loads from wave action and hurricane-induced storm surges are similar.

#### 2.5 CONCLUSIONS

As previously described, the FHSF involves a complex soft-connected multibody system that demands substantial effort to control the motion of the floating tanks. Even in relatively calm sea states in Singapore, various hydrodynamic challenges must be thoroughly studied and experimentally verified. These challenges include multi-body interactions, sloshing effects within the floating tank, and the effectiveness of the mooring systems. The research team in Singapore has devoted significant effort to addressing these areas of study. While the situation differs for other countries. Higher latitude regions like China and the USA, inevitably face the impact of typhoons or hurricanes during the summer, resulting in significantly larger surges or storms along coastal areas compared to tropical regions like Singapore. Additionally, countries in East Asia have a huge demand for oil imports. The supply chain of crude oil is of vital importance to national security. Importing and storing large amounts of crude oil has become an essential choice for these countries. However, floating tanks encounter greater design challenges, economic constraints, and limitations on storage capacity in these scenarios.

Furthermore, it should be emphasized that storage facilities have particularly stringent safety requirements (Sengul et al. 2012). At industrial locations like petrochemical and oil & gas facilities, storage tanks are commonly employed to hold large quantities of hazardous

substances, including a range of fuels and chemicals. Above-ground tanks are essential for the functioning of oil refineries, petrochemical plants, and other industrial sites, as they are used to store both raw and processed materials. Typically, these tanks are made from thin steel plates that are welded together to create a vertical cylindrical structure, capable of storing millions of liters of chemicals. They are the most widely used equipment for storage in the industry. For economic and logistical reasons, these facilities are typically situated in coastal areas. The consequences of crude oil leakage resulting from overturning or damage can be extremely serious. For example, following Hurricanes Katrina and Rita, around 5 million liters of oil remained unrecovered, leading to contamination of wetlands and marshes, as well as affecting wild animals. Federal agencies spent over \$175 million, along with an additional \$150 million from the private sector, to address cleanup costs, lawsuits, disruptions to port activities, and product losses (Pine 2006; Davis 2006). Based on these reasons, the difficulties encountered in researching and field application of floating tanks in these countries will significantly increase.

Therefore, the authors believe that designing an emerging offshore oil storage tank based on UHPECC and FRP, which can be stably deployed in coastal areas for large-scale oil storage, holds significant application potential. Oil storage tanks made of FRP and ECC will be capable of maintaining stability in marine environments, withstanding long-term loads such as wind, waves, and currents, and ensuring durability. To achieve this, it is essential to investigate the performance of the materials and components of this structure. Structures in marine environments will inevitably be subjected to long-term cyclic loads, and there is currently very limited research on the tensile fatigue performance of UHPECC in the literature. Additionally, the cooperative working mechanism and mechanical properties of flexural components formed by UHPECC and FRP are rarely studied. Furthermore, as a large cylindrical shell, the possible

failure modes, optimal structural dimensions, and mechanical performance of the oil storage tank under wave loads in marine environments also need to be investigated. The following studies aims to address all this research gaps.

CHAPTER 3 EFFECT OF LOADING FREQUENCY ON
TENSILE FATIGUE BEHAVIOR OF ULTRA-HIGHPERFORMANCE ENGINEERED CEMENTITIOUS
COMPOSITES

## 3.1 INTRODUCTION

Concrete is extensively utilized as a construction material worldwide. Interest in the fatigue behavior of concrete materials dates back over a century, originating with the construction of reinforced concrete bridges (Huang et al. 2018). Since the 1960s, researchers have begun focusing on concrete structures exposed to earthquakes (Sinha et al. 1964). These structures can experience cyclic loads that vary from a few cycles to several thousand cycles. As infrastructure development progresses, concrete structures are increasingly exposed to numerous cycles of repeated loading, including vehicle loads, wave loads, etc. To distinguish different cyclic behaviors, cycles fewer than 1000 times are defined as low-cycle fatigue, while high-cycle fatigue is defined as cycles ranging from 1000 to 10,000,000 times (Hsu 1981).

The quasi-brittle behavior stands as a major limitation for concrete, with this shortcoming being more pronounced in tension. Tensile stress in concrete induced by fatigue loads can result in premature cracking, deterioration of mechanical properties, and a decrease in the structure's durability and safety. To address this issue, enhancing material characteristics becomes imperative. Utilizing high ductility fiber-reinforced cementitious composite proves to be an effective solution for mitigating fatigue problems, given its combination of high strength, ductility, and excellent fatigue resistance.

In recent decades, research on the fatigue performance of ECC has revealed that it exhibits a much longer fatigue life and greater ductile deformation under flexural or compressive fatigue loads compared with plain concrete. A better understanding of tensile fatigue performance of high-strength ECC is required. Studies have found that, whether it is normal concrete, fiber-reinforced concrete, or other reinforced concrete materials, the fatigue deformation under constant amplitude loading follows a three-stage deformation pattern that is independent of the stress ratio (Kou et al. 2018). The fatigue test examined parameters such as the stress level (S), defined as the ratio of maximum loading stress to ultimate strength, the stress ratio (R), which is the ratio of minimum to maximum loading stress, and the loading frequency (f). The relationship established between fatigue life (N, representing the number of loading repetitions) and stress level is referred to as the S-N curve. Although the S-N curve effectively describes the fatigue behavior of steel, concrete's fatigue behavior can be influenced by additional factors.

In the laboratory, we often use higher loading frequencies to shorten testing time. Examining the impact of loading frequency on fatigue behavior is essential, especially for ECC, where the utilization of its tensile performance is crucial. Meanwhile, tensile strength in concrete shows greater variability compared to compressive strength, making it necessary to incorporate the discrete distribution of tensile strength into the fatigue model. In this study, PE fiber and ultrahigh-strength cement matrix were chosen. The matrix, initially developed by Huang et al. (2020), was slightly modified to align with the characteristics of locally available raw materials. A series of fatigue tests were performed under varying stress levels and loading frequencies to assess how frequency affects the fatigue behavior of UHPECC. The analysis includes the examination of failure modes, fatigue lifespan, deformation, and secondary strain rates.

Furthermore, P-S-N (probability of failure-stress level-fatigue life) models are introduced, taking into account the effects of loading frequency and the initial static strength distribution to ensure the material's reliable application. Finally, the study concludes with pertinent findings.

# 3.2 EXPERIMENTAL PROGRAM

## 3.2.1 Preparation of concrete test specimens

The specimens utilized in the experiments were prepared with identical mix proportions. The specific mix proportions by weight for the ECC employed in this research are outlined in Table 3.1. Furthermore, a 2% volume ratio of polyethylene (PE) fiber was incorporated, and the properties of the PE fiber can be found in Table 3.2. The mixing process proceeded as follows: an initial 3-minute dry blending of all powders and sands, succeeded by the addition of water and superplasticizer, and an ensuing 5 minutes of mixing. Subsequently, PE fibers were gradually introduced and mixed for an additional 10 minutes. The resulting freshly mixed concrete was poured methodically into 50 mm cube steel molds and steel molds shaped like dog bones (dimensions specified in Fig. 3.1). To eliminate air voids, each specimen underwent 2 minutes of vibration. Following 24 hours within the molds, the specimens were removed and subsequently immersed in water for curing until reaching 28 days. Before the testing, aluminum plates were affixed to both ends of the specimens to forestall failure induced by stress concentration.

Table 3.1 Proposition of the UHPECC mixture by weight ratio

Cement	Silica fume	Sea sand	Water	Superplasticizer	PE
$(kg/m^3)$	$(kg/m^3)$	$(kg/m^3)$	$(kg/m^3)$	$(kg/m^3)$	(Vol.)
1210	303	454	303	20.5	2%

Table 3.2 Properties of PE fiber

Tensile strength	Modulus	Length	Diameter	Density (g/
(GPa)	(GPa)	(mm)	(µm)	$cm^3$ )
3	116	12	24	0.97

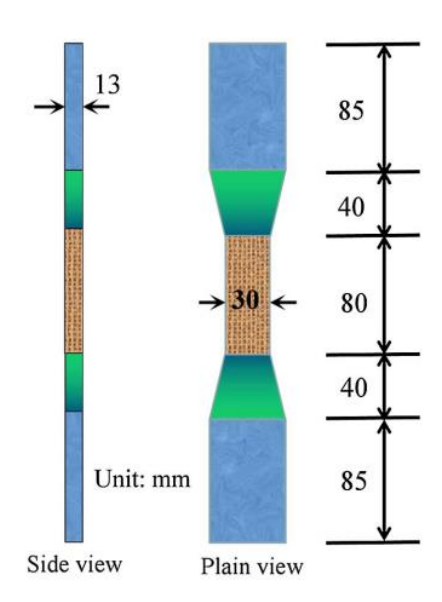


Fig. 3.1. Dimension of tensile specimen

#### 3.2.2 Test method

The tests were conducted using a servo-hydraulic control machine, with the setup illustrated in Fig. 3.2 employed for static and fatigue testing. The specimen's deformation during the test was measured using two extensometers attached to the specimen, with a net spacing of 80 mm between them. Two linear variable differential transformers (LVDTs) were installed on a fixed steel frame. The relative displacement of the specimen's central part, with a gauge length of 80 mm, was measured in real-time. Each batch of tests contains 10 specimens including 3 for static tests and the rest for fatigue tests. The static tests were conducted first, using displacement control at a steady rate of 0.20 mm/min. The tensile strength of different batches of concrete

ranged from 5.72 to 7.25 MPa. Standard concrete cube tests were performed following ASTM C109/C109M-16a (2016). For each batch, three specimens underwent testing at a loading rate of 1 MPa/s, resulting in an average compressive strength between 133.1 and 140.8 MPa. For the fatigue tests, a sinusoidal waveform with constant amplitude was used to apply the fatigue load. Three different loading frequencies (i.e., 1, 4, and 16 Hz) and three different stress levels (i.e., 0.9, 0.8, and 0.7) were examined in this study. The stress ratio, defined as the ratio of minimum stress to maximum stress, was set at 0.1. Load control was employed in the fatigue test, and to monitor the specimen's real-time deformation, the sampling frequency of the LVDTs was set to eight times the loading frequency. Each fatigue test condition was repeated with five specimens.



Fig. 3.2. Test setup

#### 3.3 FATIGUE TEST RESULTS AND DISCUSSIONS

## 3.3.1 Failure mode

Fig. 3.3 and Fig. 3.4 depict typical crack patterns observed in the specimen under static and fatigue loads in various states. When subjected to static loads, multiple visible cracks appear

in the necked region of each specimen. In contrast, specimens under fatigue loads initially develop parallel hairline cracks, which subsequently widen over time. One of these cracks evolves into the main crack, ultimately leading to fracture. Notably, the specimens under fatigue load exhibit fewer visible cracks compared to static specimens. This phenomenon can be illustrated by the mode of crack development. During the static test, the specimen demonstrates strain-hardening behavior owing to the fiber bridging effect. As stress and strain develop in the strain-hardening stage, multiple cracks gradually widen and become visible. In contrast, under fatigue loading, the maximum stress, determined by the stress level, is lower than the tensile strength. Consequently, the maximum stress may not reach the stage of strain hardening. Instead, microcracks occur, and fibers are gradually ruptured or pulled out under the fatigue load at the weakest section. The main crack in Fig. 3.5 shows the fiber pull out process of the specimen under fatigue loading.

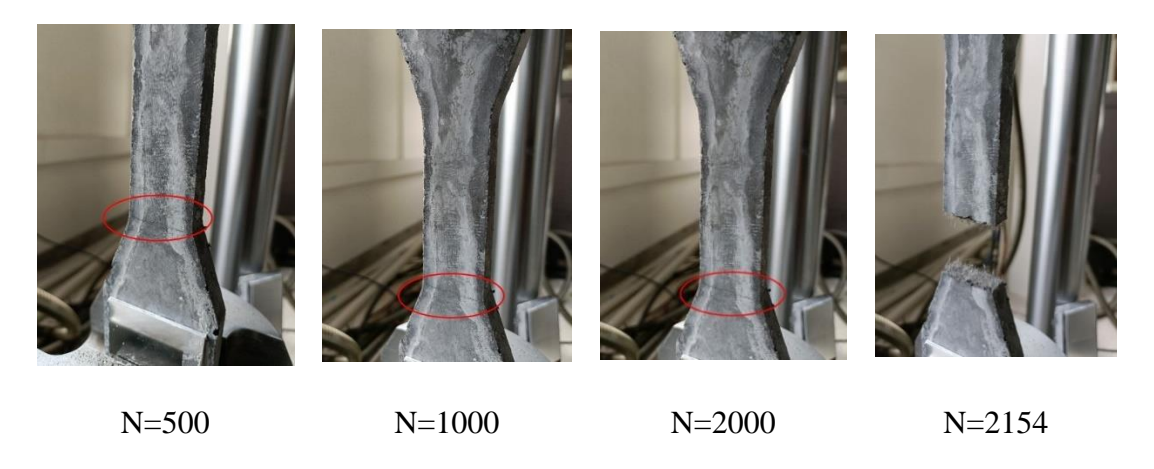


Fig. 3.3. Fatigue crack development at different stress levels for specimen F04-S09-5 in Table 3.4



Fig. 3.4. Typical crack patterns observed in specimens under static and fatigue loading conditions

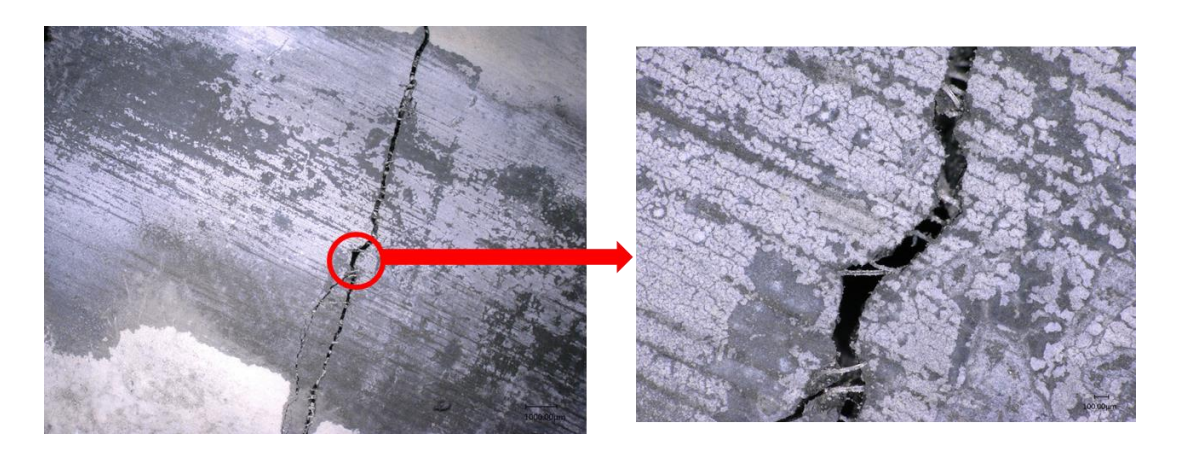


Fig. 3.5. Main crack at fatigue specimen

# 3.3.2 Fatigue life

Fatigue lives for each specimen under various loading conditions are detailed in Table 3.3 to Table 3.5. The test data indicates clear discrete characteristics in fatigue lives. In the realm of metal materials, the stress range is crucial in determining the fatigue life. Therefore, fatigue performance is commonly represented by the S-N curve, also known as the Wöhler curve. Some researchers have also extended the applicability of this S-N curve to concrete materials, and it can be expressed as follows (Oh 1991):

$$S = a - b \cdot lgN \tag{3-1}$$

where S represents the stress level, N denotes the fatigue life, and a and b are empirical constants. The S-N curves, derived from Eq. (3-1) and informed by the data contained in Table

3.3 to 3.5, are presented in Fig. 3.6. It is evident that the relationship for each loading frequency follows a log-linear function. The fitted equations are presented as follows:

$$f = 1 \text{ hz}, \qquad S = -0.061 \cdot lgN + 1.051, \qquad R^2 = 0.948$$
 (3-2)

$$f = 4 \text{ hz}, \qquad S = -0.063 \cdot lgN + 1.090, \qquad R^2 = 0.964$$
 (3-3)

$$f = 16 \text{ hz}, \qquad S = -0.063 \cdot lgN + 1.11, \qquad R^2 = 0.916$$
 (3-4)

Across diverse loading frequencies, the fatigue life decreases as stress increases. Specimens exposed to higher loading frequencies endure a larger number of repetitive cycles when exposed to tensile fatigue loads at an equivalent stress level. This suggests that the inclusion of fibers provides ECC with distinct advantages in high-frequency fatigue loads. This phenomenon can be ascribed to the influence of the loading rate, where the dynamic strength of concrete surpasses its static strength (Chen et al. 2017; Malvar and Ross 1998). Specimens under high loading frequencies possess a high dynamic strength, translating to a lower real stress level in comparison to the original stress level. This dynamic strength contributes significantly to the fatigue life N of ECC when subjected to high-frequency loading conditions.

Table 3.3 Results of fatigue tests under the loading frequency of 1 Hz

No.	Stress level (S)	Fatigue life (N)	lgN	p
F01-S09-1		236	2.373	0.167
F01-S09-2		299	2.476	0.333
F01-S09-3	0.9	328	2.516	0.500
F01-S09-4		622	2.794	0.667
F01-S09-5		1170	3.068	0.833
F01-S08-1	0.8	4332	3.637	0.167
F01-S08-2	0.8	4756	3.677	0.333

F01-S08-3		7692	3.886	0.500
F01-S08-4		15345	4.186	0.667
F01-S08-5		35441	4.550	0.833
F01-S07-1		246887	5.392	0.167
F01-S07-2		429317	5.633	0.333
F01-S07-3	0.7	743157	5.871	0.500
F01-S07-4		883859	5.946	0.667
F01-S07-5		1047560	6.020	0.833

Table 3.4 Results of fatigue tests under the loading frequency of 4 Hz

No.	Stress level (S)	Fatigue life (N)	lgN	P
F04-S09-1		469	2.671	0.167
F04-S09-2		1154	3.062	0.333
F04-S09-3	0.9	1587	3.201	0.500
F04-S09-4		1611	3.207	0.667
F04-S09-5		2154	3.333	0.833
F04-S08-1		13935	4.144	0.167
F04-S08-2		24290	4.385	0.333
F04-S08-3	0.8	41547	4.619	0.500
F04-S08-4		42123	4.625	0.667
F04-S08-5		115859	5.064	0.833
F04-S07-1		704951	5.848	0.167
F04-S07-2	0.7	1450447	6.162	0.333
F04-S07-3		1584601	6.200	0.500
		53		

F04-S07-4	1856231	6.269	0.667
F04-S07-5	2000000	6.312	0.833

Table 3.5 Results of fatigue tests under the loading frequency of 16 Hz

No.	Stress level (S)	Fatigue life (N)	lgN	P
F16-S09-1		445	2.648	0.167
F16-S09-2		2301	3.362	0.333
F16-S09-3	0.9	2351	3.371	0.500
F16-S09-4		4962	3.696	0.667
F16-S09-5		7280	3.862	0.833
F16-S08-1		26608	4.425	0.167
F16-S08-2		39588	4.598	0.333
F16-S08-3	0.8	64566	4.810	0.500
F16-S08-4		136707	5.136	0.667
F16-S08-5		256972	5.410	0.833
F16-S07-1		200000*	6.301	-
F16-S07-2	0.7	200000*	6.301	-
F16-S07-3		200000*	6.301	-

Note: \* indicates that fatigue failure did not occur even after the number of load cycles reached 2 million.

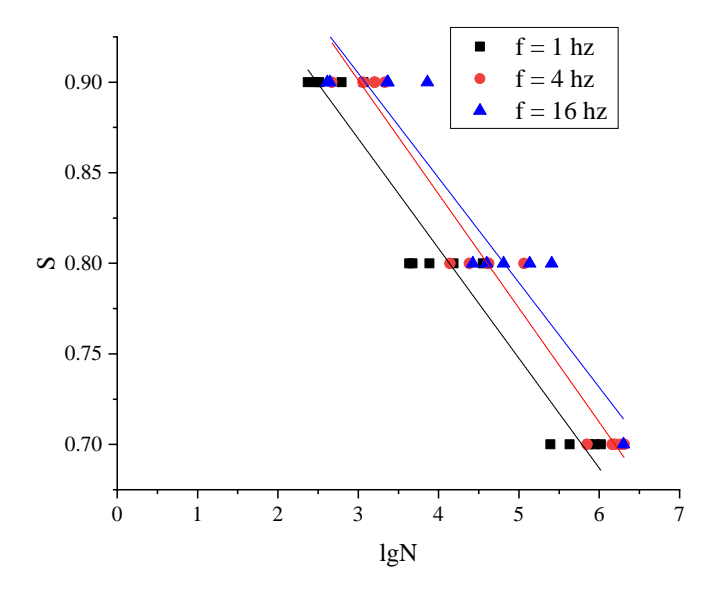


Fig. 3.6. The S-N relation under different loading frequencies

While, for concrete, factors such as stress level, stress ratio, and loading frequency all play a key role in fatigue performance (Oh 1991; Chen et al. 2017). To account for the influence of these factors, modifications to the log-linear S-N curve become imperative. Aas-Jakobsen (1970) proposed a classical equation incorporating the influence of stress ratio, as expressed in Eq. (3-5). Zhang et al. (1996) proposed an alternative model that takes into account the impact of loading frequency, as shown in Eq. (3-6).

$$S = 1 - \beta \cdot (1 - R) \cdot lgN \tag{3-5}$$

$$S = \left(ab^{-\lg(f)} + c\right) \left[1 - \beta \cdot (1 - R) \cdot \lg N\right] \tag{3-6}$$

where  $\beta$ , a, b, and c are adjusting parameters, R denotes the stress ratio, and f represents the loading frequency.

Typically, aforementioned models are validated for concrete fatigue in compression, bending, or splitting (Tepfers and Kutti 1979; Li et al. 2016). However, these models are rarely tested in

direct tensile fatigue scenarios. Moreover, despite the incorporation of fibers, the concrete's tensile strength remains notably inferior to its compressive strength. Even a slight variation in the absolute value of tensile static strength can result in a significant shift in the real stress level, particularly for specimens exposed to high stress levels. However, the dispersion of static strength is not accounted for in the aforementioned models.

In this study, the authors proposed a revised S-N relation aimed to characterize the fatigue behavior of ECC subjected to direct tensile loading. Starting from the classic Eq. (3-5), by substituting the dynamic strength  $f_{d,t}$  for the static strength in the stress level S, the following equation can be obtained:

$$S_d = \frac{\sigma_{max}}{f_{d,t}} = 1 - \beta \cdot (1 - R) \cdot lgN \tag{3-7}$$

The relationship between dynamic strength and static strength is established using the formula outlined by the FIB Code (Taerwe and Matthys 2013):

$$f_{d,t} = f_{s,t} \left(\frac{\dot{\sigma}_d}{\dot{\sigma}_s}\right)^{0.018} \ \dot{\sigma}_d < \frac{400 \ GPa}{s}$$
 (3-8)

where  $\dot{\sigma}_s$  represents the loading rate for the static test, while  $\dot{\sigma}_d$  denotes the loading rate for the fatigue test. Additionally,  $f_{s,t}$  represents the static tensile strength, whereas  $f_{d,t}$  indicates the dynamic tensile strength. The stress rate  $\dot{\sigma}_d$  for various fatigue loading conditions can be derived as follows:

$$\dot{\sigma}_d = 2f(1 - R)\sigma_{max} \tag{3-9}$$

The static tensile test in this research was conducted with a loading rate of 0.33 MPa/s. The stress rates for the fatigue test varied from 8.3 to 171.7 MPa/s, depending on different loading

frequencies and stress levels. By combining Eqs. (3-7), (3-8), and (3-9), the resultant equation is:

$$S_{d} = \frac{\sigma_{max}}{f_{t,s} \cdot \left(\frac{\dot{\sigma}_{d}}{\dot{\sigma}_{s}}\right)^{0.018}} = \frac{S}{\left(\frac{\dot{\sigma}_{d}}{\dot{\sigma}_{s}}\right)^{0.018}} = \frac{S}{\left(\frac{2f \cdot (1-R) \cdot \sigma_{max}}{\dot{\sigma}_{s}}\right)^{0.018}} = 1 - \beta \cdot (1-R) \cdot lgN \quad (3-10)$$

The modified S-N relation in Eq. (3-10) incorporates stress level and stress ratio. Through the introduction of dynamic strength, the equation accounts for the effects of loading frequency. Additionally, the static strength remains which can be used for probabilistic analysis in the later part of this research. Regression analysis, based on the data from Table 3.3 to Table 3.5, yields the parameter  $\beta$  of 0.0648, as shown in Fig. 3.7, with a correlation coefficient of 0.9994. The regression results demonstrate consistent performance across various loading frequencies, suggesting that the modified S-N relationship can effectively predict fatigue life at arbitrary loading frequencies within a certain range.

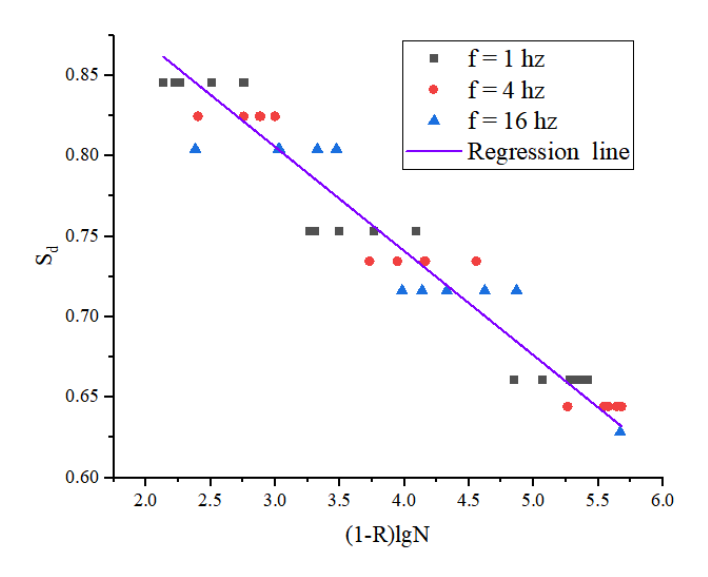


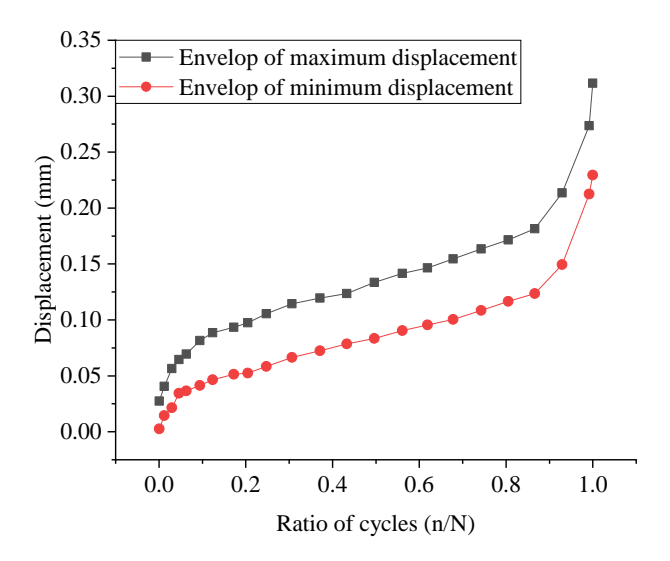
Fig. 3.7 Modified S-N relation of all tested specimens

#### 3.3.3 Fatigue deformation

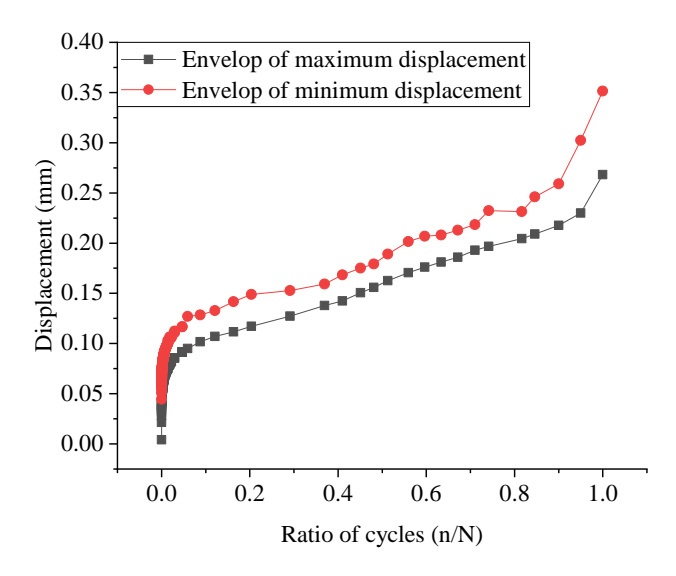
Throughout the fatigue test process, the deformation of the necked region of most specimens was measured. Numerous studies have demonstrated that the fatigue deformation of both plain concrete and fiber-reinforced concrete typically exhibits an S-shaped evolution (Cornelissen and Reinhardt 1984; Isojeh et al. 2017). The specimens evaluated in current research also follow this characteristic pattern. The overall evolution process can be categorized into three phases, namely, the initial phase of rapid growth, the subsequent phase of stable development, and the final phase of unstable growth. The initiation of crack development in the first phase is attributed to material flaws such as microcracks and pores, with several cracks becoming visible, as shown in Fig. 3.4. This phase, similar to that observed conventional normal concrete, progresses rapidly and typically constitutes less than 10% of the fatigue life. As the cyclic process continues, strain and deformation accumulate steadily, marking the stable development phase. During this phase, the strain and deformation increase at a relatively consistent rate, encompassing about 80% of the entire fatigue life. Microstructural changes during this phase are characterized by the deterioration of bonding between fibers and matrix, along with fiber rupture, playing key roles in the deterioration and growth of microcracks (Qiu et al. 2016; Qiu et al. 2017). The third phase is the failure phase, associated with the growth of the major crack. Due to the accumulated damage in the preceding two phases, one of the weakest cracks develops unsteadily until fatigue failure occurs. This phase progresses rapidly and constitutes less than 10% of the overall lifespan.

In the fatigue test, the location of the main crack occurs randomly, either within or beyond the measured length, or even directly at the LVDTs' contact points. Although this typically happens in the late stage of fatigue life, it can still introduce errors in the measured deformation. To

address this, several typical deformation evolution curves of fatigue specimens, in which the main crack is located within the measured necked region, are selected and presented in Fig. 3.8. Each figure includes the envelope of maximum deformation and minimum deformation corresponding to the maximum and minimum fatigue load, respectively.



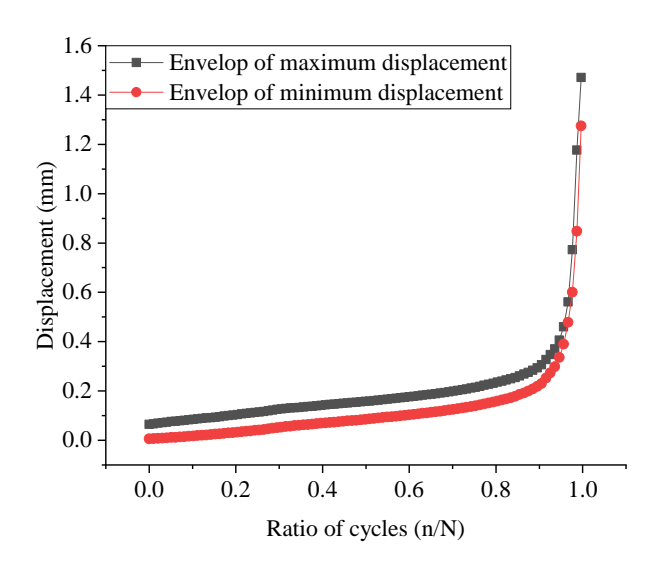
(a) 
$$S = 0.8$$
,  $R = 0.1$ ,  $f = 4$  Hz,  $N = 42123$ 



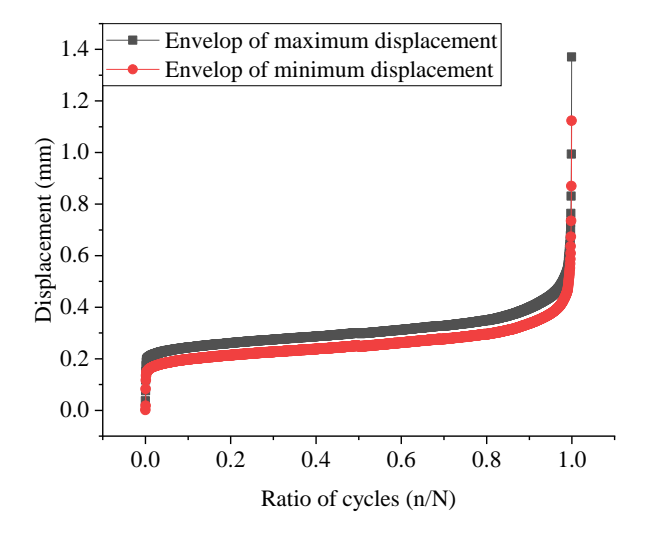
(b) S = 0.8, R = 0.1, f = 1 Hz, N = 24290

Fig. 3.8 Evolution curves of fatigue deformation of S-shape

The deformation evolution in Fig. 3.8 exhibits strain-hardening behavior after crack initiation. However, for specimens under high stress level fatigue loads, the maximum fatigue load in fatigue cycles may exceed the specimen's cracking strength, particularly considering the dispersion of tensile strength. Under these circumstances, the first stage and part of the second stage in the S-shaped evolution might disappear, leaving an exponential-shaped evolution curve, as illustrated in Fig. 3.9. This kind of specimen experienced significant damage in the first cycle, resulting in a much shorter fatigue life compared to a specimen with an S-shaped deformation evolution curve, even when both are exposed to same loading conditions. This discrepancy is attributed to the dispersion of tensile strength.



(a) S = 0.9, R = 0.1, f = 16 Hz, N = 445



(b) 
$$S = 0.9$$
,  $R = 0.1$ ,  $f = 16$  Hz,  $N = 2301$ 

Fig. 3.9. Evolution curve of fatigue deformation under high-stress level

### 3.3.4 Secondary strain rate

In the evolution curves of fatigue deformation, a nearly linear segment is evident, as illustrated in the previous section. This linear segment, also known as the secondary strain rate, has been reported in compressive or tensile fatigue tests on both plain and fiber-reinforced concrete (Cachim et al. 2002; Do et al. 1993). The deformation increment per cycle in this segment remains steady, as illustrated in Fig. 3.10. The secondary strain rate can be determined using the following equation (Huang et al. 2017):

$$\dot{\varepsilon} = \frac{\partial \varepsilon_{sec}}{\partial t} = \frac{\varepsilon_{sec,2} - \varepsilon_{sec,1}}{\frac{\left(n_2 - n_1\right)}{f}}$$
(3-11)

where  $n_2$  and  $n_1$  are two values of the cycles in the linear part of the S-shape evolution curve, and  $\varepsilon_{sec,2}$  and  $\varepsilon_{sec,1}$  are the two corresponding strains on the linear part.

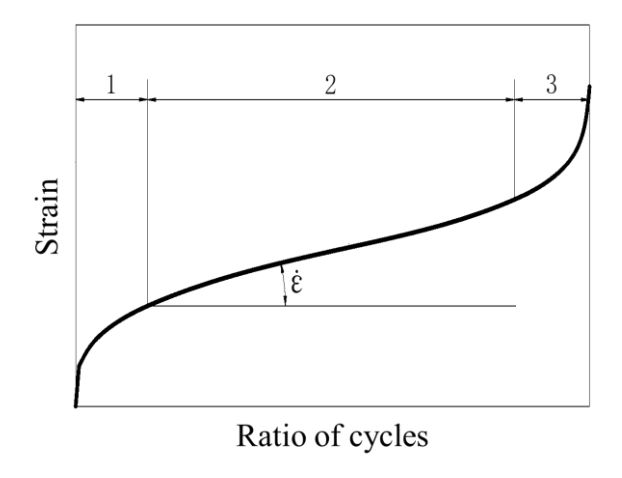


Fig. 3.10 Secondary strain rate

The secondary strain rate demonstrates a strong correlation with the fatigue life (Hordijk et al. 1995; Cornelissen 1984). As the secondary strain rate decreases, the fatigue life increases. Moreover, fatigue life can be estimated using the secondary strain rate, and this relationship can be described by the following formula. The relationship between the secondary strain rate and fatigue life can be described by the following formula (Taerwe and Matthys 2013):

$$\dot{\varepsilon} = e^b N^a \tag{3-12}$$

By dividing the recorded displacement by the measuring length, the secondary strain rate can be determined through Eq. (3-11). Fig. 3.11 demonstrates the correlation between the secondary strain rate and the fatigue life. Table 3.6 lists the regression parameters for various loading frequencies as given in Equation (3-10). Notably, the regression lines are almost parallel, and the intercept decreases with the decrease in loading frequency. From the preceding analysis, the secondary strain rate measurement of the specimen can be utilized to estimate its fatigue life.

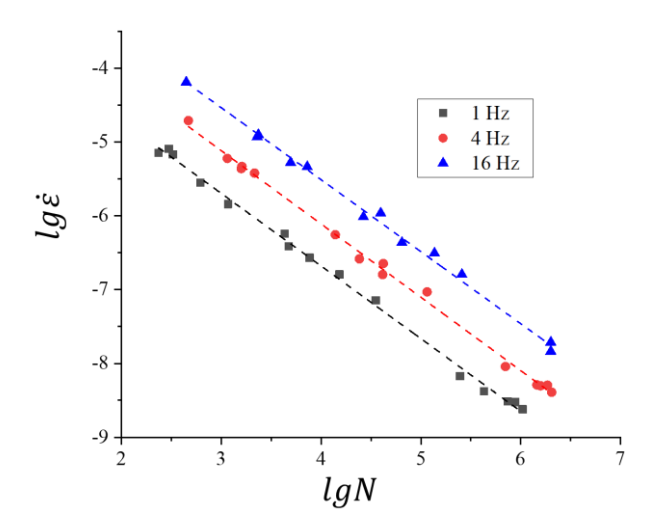


Fig. 3.11 Secondary strain rate plotted against the fatigue life

Table 3.6 Regression parameters of secondary strain rate

Frequency (Hz)	a	b
16	-0.9756	-1.6073
4	-0.9933	-2.1365
1	-0.9839	-2.7434

## 3.4 FATIGUE LIFE AND P-S-N MODELS

As mentioned before, the longevity of concrete under fatigue conditions is affected by multiple factors, including stress level, stress ratio, and loading frequency. In practice, the dispersion of the concrete's static strength also significantly affects fatigue life. The Weibull function is commonly employed to characterize concrete strength (Poveda et al. 2017; Medeiros et al. 2015) and has proven to be suitable for analyzing the fatigue life of cementitious materials (Zhou et al. 2015). Saucedo et al. (2013) proposed a probabilistic model to account for the initial static strength distribution for concrete compressive fatigue tests. Additionally, Huang et al. (2018) proposed a novel probabilistic model that accounts for the influence of static strength dispersion, stress levels, and stress ratios in tensile fatigue tests of fiber-reinforced

concrete. The fatigue lives presented in Table 3.3 to Table 3.5 exhibit considerable scatter. Therefore, our objective is to develop a tensile fatigue model for fiber-reinforced concrete, considering the initial static strength dispersion, as well as the influences of stress level, stress ratio, and loading frequency.

### 3.4.1 Distribution of static tensile strength and fatigue life

In the current work, the static strength is modeled using the Weibull distribution. The failure probability (PF) at various tensile stresses can be described using a two-parameter Weibull distribution, with the cumulative distribution function represented as follows:

$$PF(\sigma_{static}) = 1 - \exp\left(-\left(\frac{\sigma_{static}}{\lambda_0}\right)^{k_0}\right)$$
 (3-13)

where  $\lambda_0$  and  $k_0$  represent the scale and shape parameters respectively, and  $\sigma_{static}$  denotes the static tensile strength of fiber reinforced concrete. The probability of failure determined by Eq. (3-13) which ranges from 0 to 1 is the initial distribution of the material property. It is determined through multiple static experimental characterizations. The variations in measured static tensile strength and their corresponding failure probabilities are listed in Table 3.7. The Weibull distribution of tensile strength fitted by Eq. (3-13) is plotted in Fig. 3.12. The corresponding parameters  $\lambda_0$  and  $k_0$  are 6.8579 and 13.4953 respectively. The correlation coefficient r is 0.9901 suggesting that the tensile strength follows the Weibull distribution in general.

Table 3.7 Direct tensile test for static strength

Tensile strength (MPa)	PF
5.717	0.0769

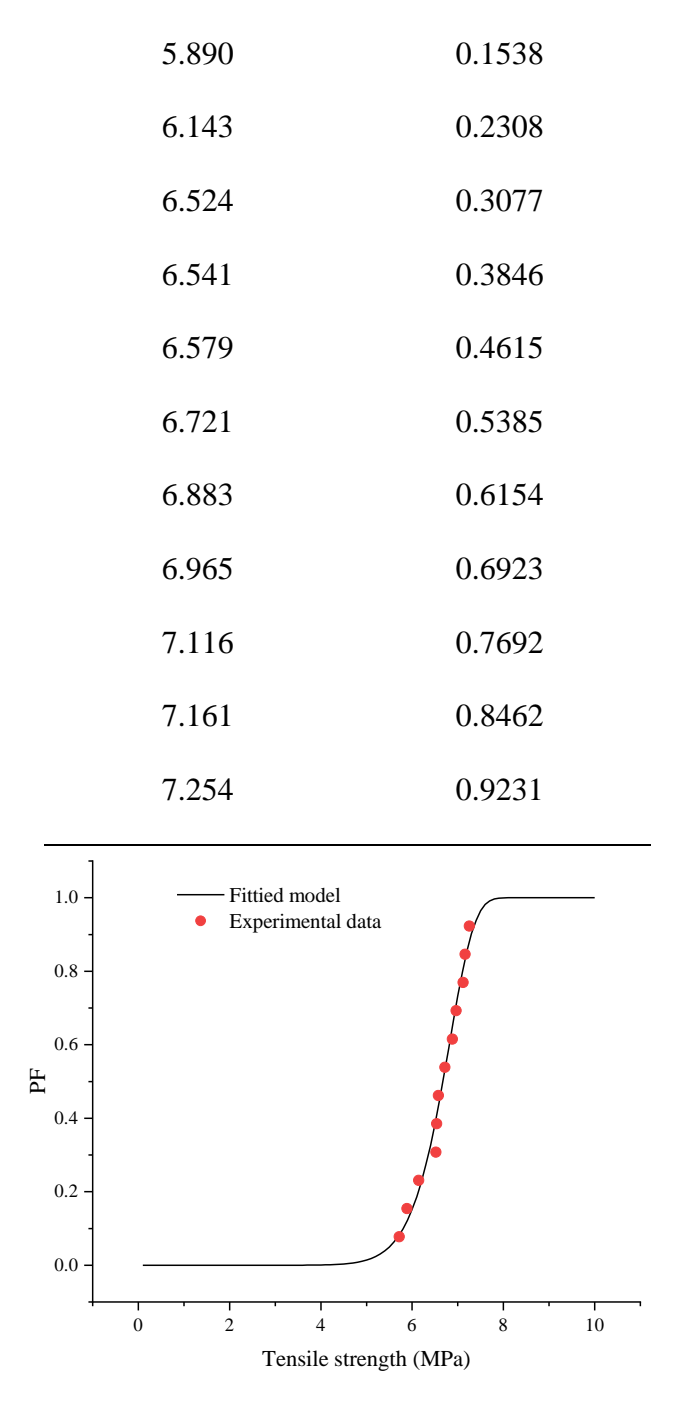


Fig. 3.12 Distribution of tensile strength fitted with the experimental measurements

For the fatigue life, the cumulative distribution function of a two-parameter Weibull function can be expressed as follows:

$$PF(N) = 1 - ex \, p\left(-\left(\frac{N}{\lambda_N}\right)^{k_N}\right) \tag{3-14}$$

where  $\lambda_N$  represents the scale parameter, and  $k_N$  denotes the shape parameter. N denotes the fatigue life under specific loading conditions. Based on the test results in Table 3.3 to Table 3.5, the  $\lambda_N$  and  $k_N$  for various stress levels and loading frequencies are presented in Table 3.7. The mean fatigue life can be defined as fatigue life with a failure probability of 0.5. By setting the PF = 0.5, the calculated mean fatigue lives are also presented in Table 3.8, including the corresponding Weibull distribution parameters. The coefficient of correlation r is also listed indicating that the fatigue life under different loading conditions generally conforms to the Weibull distribution. The scale parameters exhibit a correlation with fatigue life, increasing with frequency and decreasing with stress level. Conversely, the shape parameter is minimally influenced by loading conditions.

Table 3.8 Parameters for fitting the Weibull distribution

Loading	Stress level	1	1,		Fatigue life
frequency	Suess level	$\lambda_N$	$k_N$	r	at PF=0.5
1	0.9	603	1.476	0.921	470
1	0.8	14825	1.083	0.929	10570
1	0.7	801307	1.520	0.983	629643
4	0.9	1662	1.584	0.951	1319
4	0.8	54557	1.176	0.960	39946
4	0.7	1765598	2.242	0.940	1499285
16	0.9	4174	0.856	0.965	2721
16	0.8	119372	0.990	0.973	82446
16	0.7	-	-	-	-

#### 3.4.2 P-S-N models

In this section, we aim to obtain the curve of failure probability with respect to the fatigue life N. The fatigue loading conditions and static material properties serve as parameters in this expression. Each distinct curve within the plot represents a unique probability of failure corresponding to specific loading conditions.

As discussed in the preceding section, fatigue performance can be characterized by the modified S-N relation, expressed by Eq. (3-10). The dynamic-to-static strength ratio is represented by  $\alpha$ , and it is defined as follows:

$$\alpha = \frac{f_{d,t}}{f_{s,t}} = \left(\frac{\dot{\sigma}_d}{\dot{\sigma}_s}\right)^{0.018} \tag{3-15}$$

Eq. (3-10) can be expressed in the following manner:

$$\frac{S}{\alpha} = 1 - b(1 - R)lgN \tag{3-16}$$

To incorporate the impact of static strength on fatigue life, the following relation is assumed:

$$N(S, \sigma_{static}) = N(S) \left( \frac{\sigma_{static}}{\sigma_{static,ave}} \right)^{k}$$
 (3-17)

where  $\sigma_{static,ave}$  represents the average static strength, and k is the parameter. N(S) denotes the mean fatigue life under a specific failure probability, while  $N(S, \sigma_{static})$  signifies the fatigue life corresponding to a static strength of  $\sigma_{static}$ . This assumption is inspired by earlier works by Huang et al. (2018) and Saucedo et al. (2013), where they utilized the exponential function to establish a connection between stress and fatigue life which is similar to the S-N curve. By combining Eqs (3-16) and (3-17), the following expression can be derived:

$$\sigma_{static} = \sigma_{static,ave} \left( \frac{N(S, \sigma_{static})}{\frac{1 - \frac{S}{\alpha}}{10^{\overline{\beta} - \beta R}}} \right)^{1/k}$$
(3-18)

By substituting Eq. (3-18) into Equation (3-13), we obtain the general expression for the probability of failure at any stage in the fatigue test:

$$PF(N; S, R, f) = 1 - ex \, p \left( -\left( \frac{\sigma_{static, ave}^{k}}{\lambda^{k}} \frac{N}{10^{\frac{1-S/\alpha}{\beta(1-R)}}} \right)^{\frac{k_0}{k}} \right)$$
(3-19)

where N is treated as the primary variable, whereas the remaining factors are parameters set by a specific fatigue test or values characterized by static test. It's noteworthy that, due to the shifting of the cumulative probability distribution from static strength to fatigue life in Eqs (3-13) to (3-19), the shape parameter of static strength  $k_0$  is preserved in Eq. (3-19). However, the scale parameter is replaced by  $\lambda$  which is influenced by the stress level, stress ratio, and loading frequency. The expression maintains the form of a two-parameter Weibull function of  $\lambda$  and k, proving effective in fitting fatigue test data. The parameters determined in the fatigue test are incorporated into Eq. (3-19), with the loading frequency reflected by  $\alpha$  as follows:

$$\alpha = \left(\frac{2f \cdot (1-R) \cdot \sigma_{max}}{\dot{\sigma}_{s}}\right)^{0.018} \tag{3-20}$$

Using Eq. (3-19), the fatigue life N for a specified probability of failure and under specific loading conditions can be easily determined:

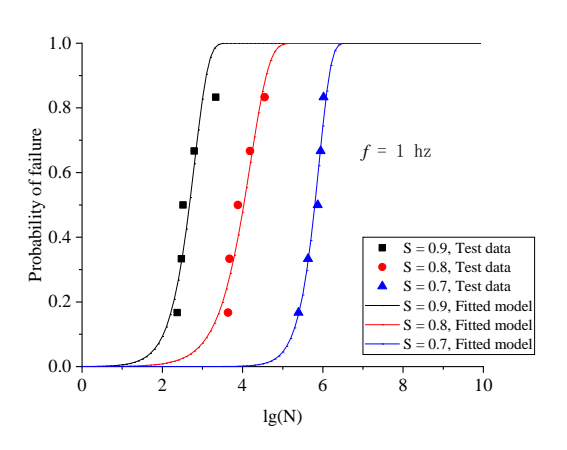
$$N = \left[-\ln(1 - PF)\right]^{\frac{k}{k_0}} \cdot 10^{\frac{1 - S/\alpha}{\beta(1 - R)}} \cdot \left(\frac{\lambda}{\sigma_{static,ave}}\right)^k \tag{3-21}$$

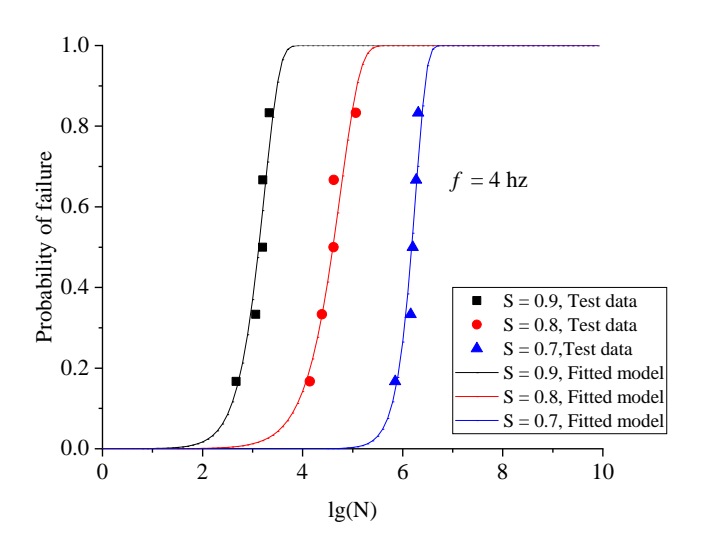
In addition, the stress level for a specific failure probability and design fatigue life can also be predicted as follows:

$$\frac{S}{\alpha} = 1 - \beta (1 - R) lg \frac{N}{\left[-\ln(1 - PF)\right]^{\frac{k}{k_0}} \cdot \left(\frac{\lambda}{\sigma_{static.ave}}\right)^k}$$
(3-22)

To validate the fatigue model presented in Eq. (3-19), Fig. 3.13 displays the distribution of fatigue life for different loading conditions, compared with the observed data. Table 3.9 provides the fitting parameters associated with this data. Notably, the model demonstrates excellent fitting results with the measured data. Fatigue life decreases as stress level increases, while it increases with higher loading frequency. The model can be used for probability assessment under specified loading conditions and loading history. Additionally, once the failure probability is determined, the model allows for estimating the fatigue life for a specific loading condition.

In summary, the proposed model proves effective in predicting fatigue life by incorporating the initial strength distribution and various loading conditions. To apply this P-S-N model, it is necessary to have the initial Weibull distribution of static strength, along with a set of fatigue lives under varying loading conditions, to obtain the necessary parameters. For future research, influence of stress ratio R especially for stress reverse is proposed to be taken into further investigation. It's worth noting that while this study focused on the tensile fatigue behavior of fiber-reinforced concrete, the same approach can be extended to other cementitious materials experiencing compression or tension.





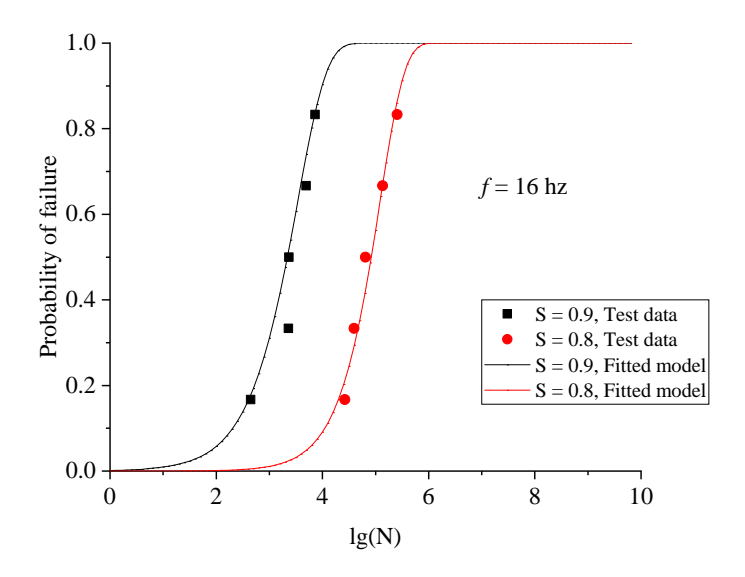


Fig. 3.13 Distribution of fatigue life under various loading conditions.

Table 3.9 Fitting parameters of Weibull distribution based on Equation (3-19)

Loading	Stress level	λ	k	r
frequency	Stress level	χ	λ	1
1	0.9	8.151	10.776	0.921
1	0.8	7.431	14.430	0.929
1	0.7	8.049	9.183	0.983
4	0.9	6.985	9.425	0.951
4	0.8	6.808	12.438	0.960
4	0.7	6.773	6.821	0.939
16	0.9	7.142	16.920	0.965
16	0.8	6.922	14.388	0.973
16	0.7	-	-	-

# 3.5 CONCLUSIONS

The tensile fatigue characteristics of fiber reinforced concrete across various loading conditions were investigated by performing various stress levels and loading frequencies in this chapter. The main conclusions are summarized below:

Like plain concrete and fiber-reinforced concrete, the fatigue life of UHPECC diminishes as the frequency decreases. This is due to the increase in the actual loading rate. An increase in stress level at the same loading frequency leads to a reduced fatigue life, resulting from a larger accumulation of damage per cycle under higher stress levels compared to lower stress levels. The relationship between stress level and fatigue life follows a log-linear pattern at the specified loading frequency.

The stress level affects the deformation behavior during fatigue. A higher stress level can transform the typical three-stage process into an exponential form.

By analyzing the correlation between the secondary strain rate and fatigue life, the fatigue life can be predicted for a specified loading condition once the secondary strain rate is measured.

It was observed that both the static strength and fatigue life adhere to a two-parameter Weibull distribution. A probabilistic fatigue model, taking into consideration static strength along with loading frequencies and stress levels, is proposed. This model could be applied in further structural applications.

# CHAPTER 4 TENSILE FATIGUE BEHAVIOR OF ULTRA-HIGH-PERFORMANCE ENGINEERED CEMENTITIOUS COMPOSITES CONSIDERING STRESS REVERSAL

# 4.1 INTRODUCTION

Fatigue failure involves the gradual cumulative of damage. When subjected to constant amplitude alternating stress, the S-N curve of a material or component can be served to quantify the number of cycles necessary to induce failure at varying stress levels, referred to as fatigue life. However, in practical engineering, structures are usually exposed to complex, random fatigue loads. In such scenarios, relying solely on the S-N curve is inadequate for estimating the fatigue life of the structure. Therefore, along with the S-N curve, employing cumulative fatigue damage theories is essential for predicting the lifespan of materials.

Given the context of this research, wave loads experienced by marine structures demonstrate randomness and continual variation over time. These loads fluctuate in intensity, frequency, and direction in real time. Consequently, the fatigue stress induced by wave loads also varies dynamically across different directions, intensities, and frequencies. In describing random fatigue stress, in addition to assuming the vibrational mode as a sine function, it is essential to know the loading frequency, stress level, and stress ratio. The preceding chapter explored how loading frequency and stress levels affect the tensile fatigue behavior of UHPECC. This chapter will expand these findings by introducing the influence of stress ratio, particularly considering stress reversals.

This chapter begins by supplementing a set of fatigue experiments on UHPECC, focusing on stress ratios of -0.1 and -1. In most previous test studies, the stress ratio is typically set at 0.1, representing tension-tension or compression-compression cycles. The introduction of the negative stress ratio in this chapter will lead to stress reversal during fatigue test, which constitutes an important addition to the study of fatigue performance. Subsequently, the chapter provides an overview of fatigue damage theories, selecting appropriate methods to develop the fatigue damage model that can be used for UHPECC. Finally, it explores the application method of the damage model under random loading conditions.

## **4.2 EXPERIMENTAL PROGRAM**

#### 4.2.1 Material

The proportion of UHPECC used for casting specimens, along with their dimensions, adhered to the specifications outlined in Chapter 3. Following the same casting process described in Chapter 3, specimens were removed from their molds after 24 hours and subsequently underwent curing for a duration of up to 28 days.

### **4.2.2** Testing method

The test procedures followed were consistent with those outlined in the previous chapter, except for the applied loading amplitude, which caused stress reversal. The test setup remained unchanged from Chapter 3. Each group consisted of ten specimens, totaling six groups. Three specimens were used to determine static tensile strength, while five underwent fatigue tests; two additional specimens served as backups. The average tensile strength for each group ranged from 5.51 to 6.88 MPa. Fatigue tests employed force-controlled loading, with the load amplitude determined by the static tensile strength of each group, along with the preset stress

levels and stress ratios. The fatigue load waveform for all specimens followed a sine wave. The loading frequency was fixed at 4 Hz, while the dynamic acquisition system recorded deformations in the central 80 mm measurement length of each specimen with a sampling rate of 32 Hz.

### 4.2.3 Experimental Phenomena

The failure mode of UHPECC specimens under tensile-compressive fatigue cyclic loading resembles that seen with tensile-tensile fatigue. This type of failure can be categorized as quasi-brittle. At the fracture section of the specimen, numerous PE fibers can be observed. The fibers aligned with the load direction mainly support the applied forces, while the transversely distributed fibers contribute to energy dissipation and maintain the matrix integrity.

Throughout the crack initiation and propagation, particularly when one crack becomes the main crack, the bridging effect of fibers and Saint Venant's principle has a notable impact on the surrounding area. Stress transmission facilitates the further extension of cracks, promoting the internal connection of cracks. In the central area of the specimen, clear evidence of fiber pull-out and fracture is visible. As the crack develops, the effective cross-sectional area of the specimen progressively reduces. Consequently, the specimen will quickly reach failure.

The specimen maintained its integrity despite losing the loading capacity, which can be attributed to the reinforcing fibers enhancing the crack resistance and deformability. The above performance aligns with the expectations set by the experiment's design.

Despite the inclusion of PE fibers, the tensile strength of ECC is notably less than its compressive strength. The most severe loading condition for all specimens occurred at the maximum tensile stress during fatigue loading in this study.

# 4.3 FATIGUE TEST RESULTS AND DISCUSSIONS

# 4.3.1 Fatigue life

Fatigue performance of materials is typically characterized by the relationship between the applied stress S and the number of cycles S until specimen failure. In fatigue loading, the maximum and minimum cyclic stress amplitude ( $S_{max}$  and  $S_{min}$ ) of a sinusoidal stress cycle are two fundamental variables describing the stress condition. In this chapter, the study focuses on tensile fatigue performance, with tensile stress considered positive and compressive stress considered negative.  $S_{max}$  denotes the maximum tensile stress induced in the specimen throughout the cyclic loading cycle, while  $S_{min}$  corresponds to the stress at the lower boundary of the applied load. The  $S_{min}$  could be a negative value for maximum compressive stress or a positive value for tensile stress. In the following discussion, the parameters used to describe the fatigue stress are as follows:

Stress ratio:

$$\frac{R = S_{min}}{S_{max}} \tag{4-1}$$

Stress level:

$$\frac{S = S_{max}}{f_t} \tag{4-2}$$

To investigate the impact of stress reversal, the test employs stress ratios of -0.1 and -1. Specifically, a stress ratio of -0.1 indicates that the specimen withstands tensile fatigue stress amplitude ten times greater than compressive fatigue stress amplitude. When the stress ratio is -1, it indicates that in symmetric cyclic loading, both tension and compression experience equal and opposite fatigue loads, referenced around zero. The stress levels are evaluated across three scenarios: 0.9, 0.8, and 0.7. A stress level of 0.9 means that the maximum tensile stress during the fatigue load cycle is 90% of the average tensile strength. Each loading condition contains five specimens. The loading frequency was not taken into consideration in this chapter, therefore, the loading frequency for all specimens is set at 4 Hz. The analysis will incorporate the specimens tested under the conditions of a loading frequency of 4 Hz and a stress ratio of 0.1, as detailed in Chapter 3.

Table 4.1 Results of fatigue test with a stress ratio of -0.1

No.	Stress level (S)	Fatigue life (N)	lgN	p
S09-RA-1		755	2.878	0.167
S09-RA-2		1050	3.021	0.333
S09-RA-3	0.9	1194	3.077	0.500
S09-RA-4		1356	3.132	0.667
S09-RA-5		1581	3.199	0.833
S08-RA-1		5394	3.732	0.167
S08-RA-2		7465	3.873	0.333
S08-RA-3	0.8	9515	3.978	0.500
S08-RA-4		19577	4.292	0.667
S08-RA-5		30699	4.487	0.833
S07-RA-1	0.7	86957	4.939	0.167

144816	5.161	0.333
234232	5.370	0.500
281413	5.449	0.667
367376	5.565	0.833
	234232 281413	234232 5.370 281413 5.449

Table 4.2 Results of fatigue test with a stress ratio of -1

No.	Stress level (S)	Fatigue life (N)	lgN	p
S09-B-1		422	2.625	0.167
S09-B-2		504	2.702	0.333
S09-B-3	0.9	832	2.920	0.500
S09-B-4		944	2.975	0.667
S09-B-5		1217	3.085	0.833
S08-B-1		2663	3.425	0.167
S08-B-2		3257	3.513	0.333
S08-B-3	0.8	3587	3.555	0.500
S08-B-4		4726	3.675	0.667
S08-B-5		5993	3.778	0.833
S07-C-1		23365	4.369	0.167
S07-C-2		39961	4.602	0.333
S07-C-3	0.7	64923	4.812	0.500
S07-C-4		75059	4.875	0.667
S07-C-5		103327	5.014	0.833

Table 4.1 and 4.2 present the fatigue life with stress ratios of -0.1 and -1, respectively. The fatigue life of the specimens exhibits significant variability. The Weibull distribution, as introduced in the previous chapter, is employed to analyze fatigue life under various loading conditions. For concrete materials, the Weibull distribution equation can be represented in a simplified form as shown below:

$$\ln\left[\ln\left(\frac{1}{p}\right)\right] = b\ln N - b\ln N_a \tag{4-3}$$

whereas p represents the survival rate; N denotes the fatigue life;  $N_a$  is the parameter defining the characteristic life; and b is the slope of the linear equation, which can be directly obtained from the fitted line.

From Eq. (4-3), it can be observed that  $\ln\left(\frac{1}{p}\right)$  is linearly related to  $\ln N$ . By defining  $Y = \ln\left[\ln\left(\frac{1}{p}\right)\right]$ ,  $X = \ln N$ ,  $c = b \ln N_a$ , the following equation can be derived:

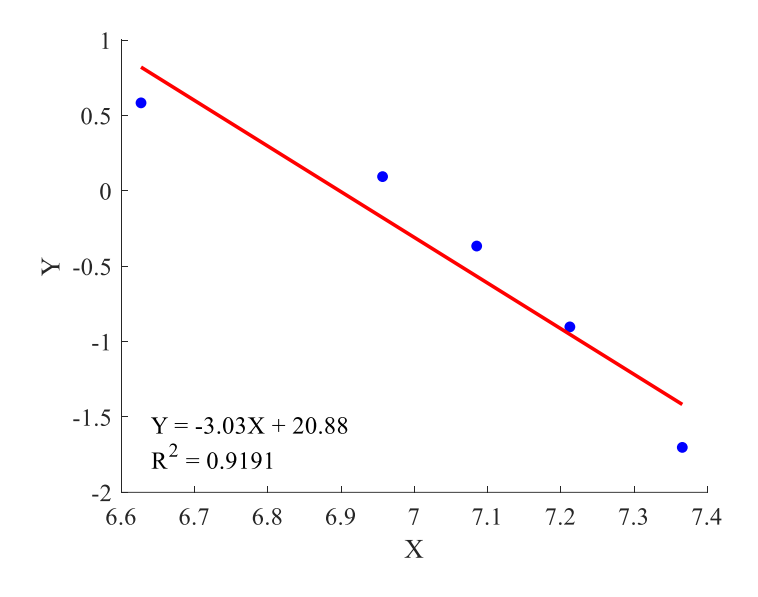
$$Y = bX - c \tag{4-4}$$

The survival rate p of the test specimen can be calculated based on its fatigue life, using the empirical formula:

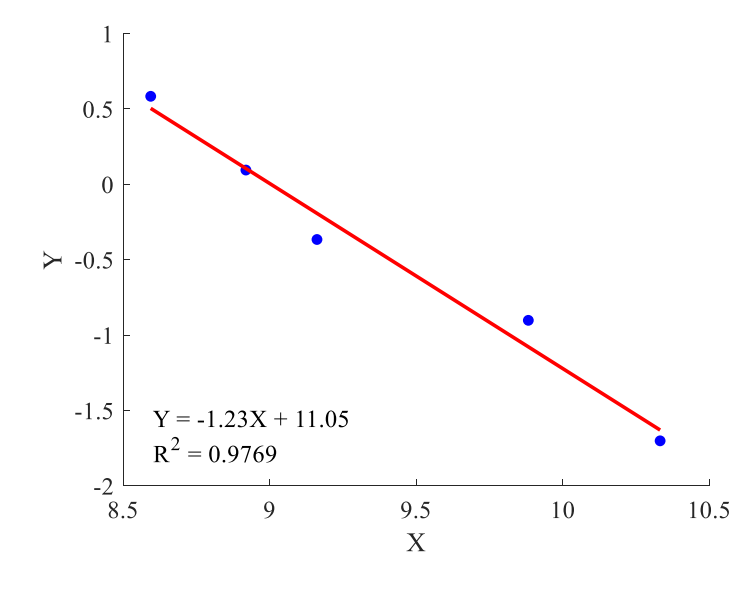
$$p = 1 - \frac{i}{m+1} \tag{4-5}$$

In this formula, i denotes the specimen's position within the group sorted by the number of failure cycles, ranging from 1 to m, where m represents the total number of specimens in the fatigue dataset under each loading condition. The calculated survival rater p for each specimen are provided in the finial columns of Table 4.1 and 4.2.

When using  $\ln\left(\frac{1}{p}\right)$  as the vertical axis and  $\ln N$  as the horizontal axis, the relationship curve  $\ln\left(\frac{1}{p}\right) - \ln N$  can be fitted, as shown in Fig. 4.1 and Fig. 4.2.



(a) S = 0.9, R = -0.1



(b) S = 0.8, R = -0.1

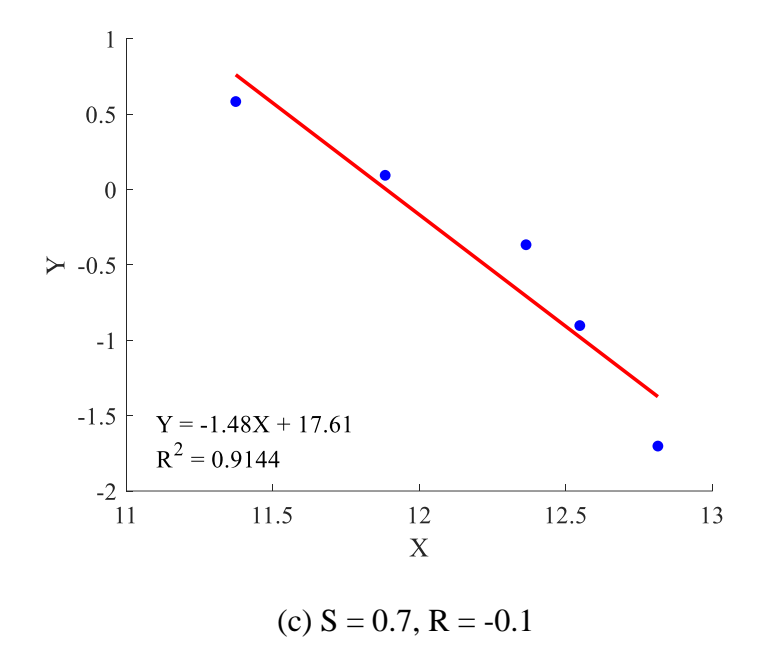
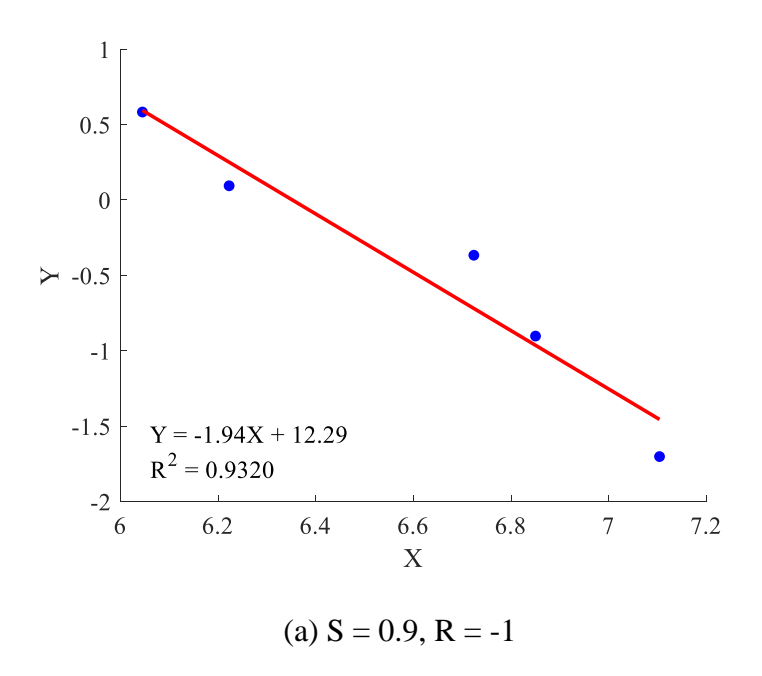
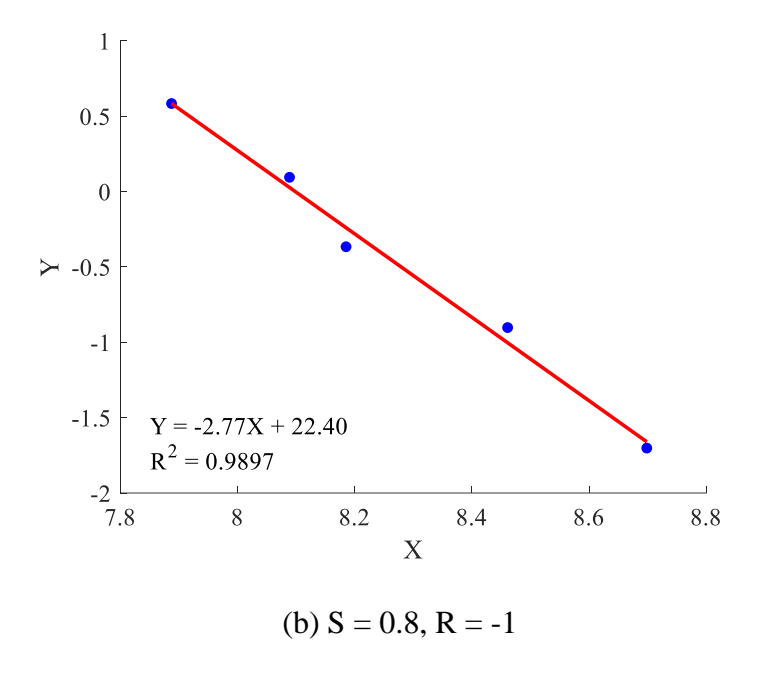


Fig. 4.1 Fatigue life fitted curves at each stress level under stress ratio of -0.1





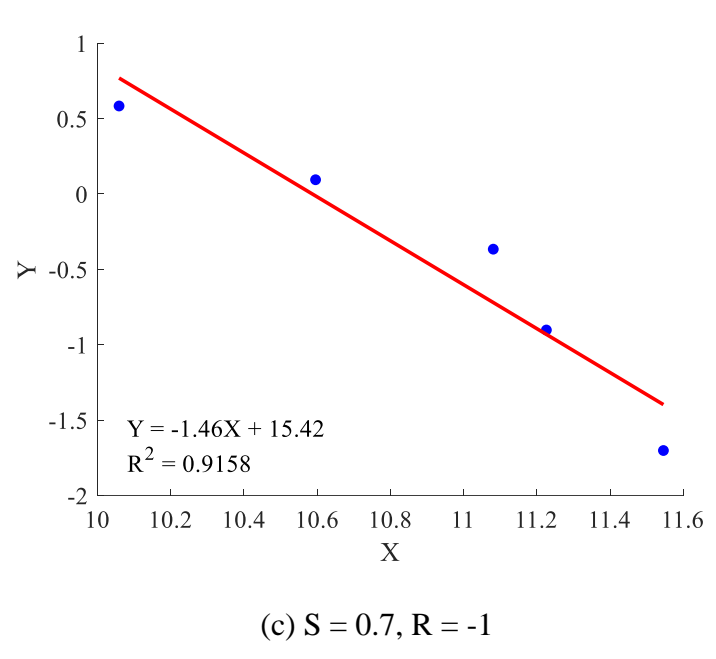


Fig. 4.2 Fatigue life fitted curves at each stress level under the stress ratio of -1

From Fig. 4.1, it can be seen that the relationship curve  $\ln\left[\ln\left(\frac{1}{p}\right)\right] - \ln N$  exhibits strong correlation, with  $R^2$  values exceeding 0.9 across all loading conditions. This high correlation indicates a robust fit, suggesting that the Weibull function effectively models the fatigue life of UHPECC under tension-compression reversal loading conditions. By setting the probability

of failure to 0.5, we can determine the characteristic fatigue life values corresponding to the respective fatigue loading conditions, as illustrated in Table 4.3.

Table 4.3 The fatigue life at a failure probability of 0.5 under different loading conditions

Stress ratio (R)	Stress level (S)	Fatigue life (N)
	0.9	693
-1	0.8	3754
	0.7	50907
	0.9	1117
0.1	0.8	10960
	0.7	186164
	0.9	1319
	0.8	39946
	0.7	1499285

By combining the data from Chapter 3, which includes fatigue specimens tested at a 4 Hz loading frequency and a stress ratio of 0.1 under tension-tension conditions, we can derive Fig. 4.3. This figure illustrates how fatigue life varies with changes in stress levels or stress ratios. From the figure and table, it is evident that under various stress ratio conditions, the characteristic value of fatigue life decreases as stress levels increase. Under a high tensile stress of 0.9, the fatigue life under various stress conditions is relatively low, with none exceeding 1500 cycles. As the stress level drops, the impact of the stress ratio on fatigue life becomes more obvious. At a tensile stress level of 0.7, the characteristic fatigue life for specimens with stress ratios of 0.1 are 8.1 times and 29.5 times higher than those with stress ratios of -0.1 and -1, respectively. The stress reversal of fatigue load has a significant negative influence on the

fatigue life of UHPECC. Specimens subjected to a stress ratio of -1 exhibit very limited fatigue life across all stress levels examined in this study.

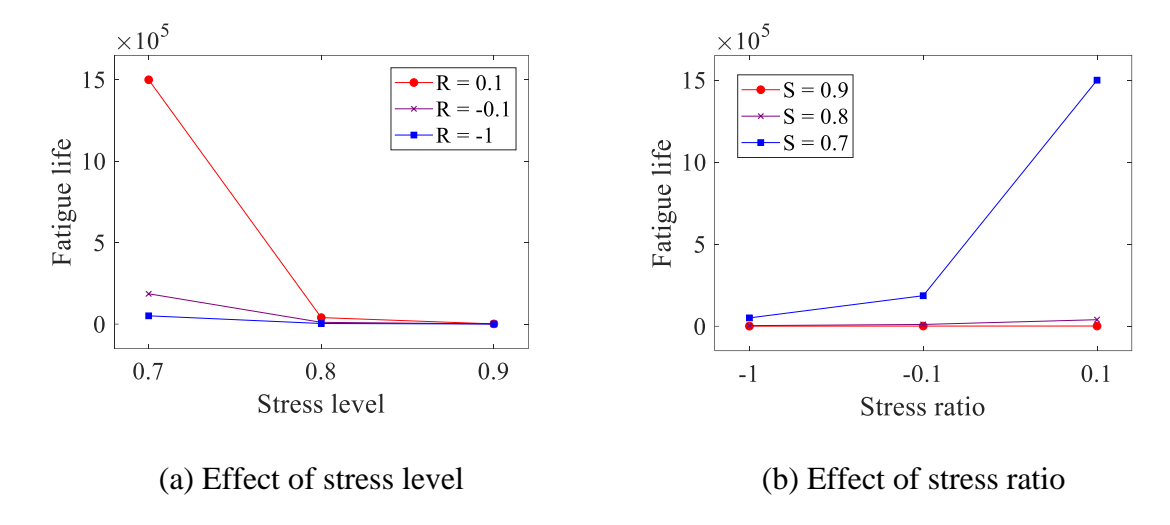


Fig. 4.3 Fatigue life versus experimental variables

### **4.3.2** S-N curves

In the past, the tensile fatigue performance of concrete was often regarded as insignificant or lacking in engineering practicality. However, experimental results with ECC incorporating PE fibers have demonstrated that they possess good tensile fatigue performance. In this context, the S-N curve is utilized to analyze the correlation between stress levels and fatigue life. Fig. 4.4 illustrates the comparison of S-N curves under different stress ratio conditions, while Table 4.4 details the corresponding expressions for each fitted line.

Table 4.4 S-N curve fitting expressions

Stress ratio (R)	Fitting expression	Coefficient of Determination
0.1	S = -0.0630lgN + 1.0902	$R^2 = 0.9643$
-0.1	S = -0.0845 lgN + 1.1503	$R^2 = 0.9449$
-1	S = -0.0997lgN + 1.1716	$R^2 = 0.9334$

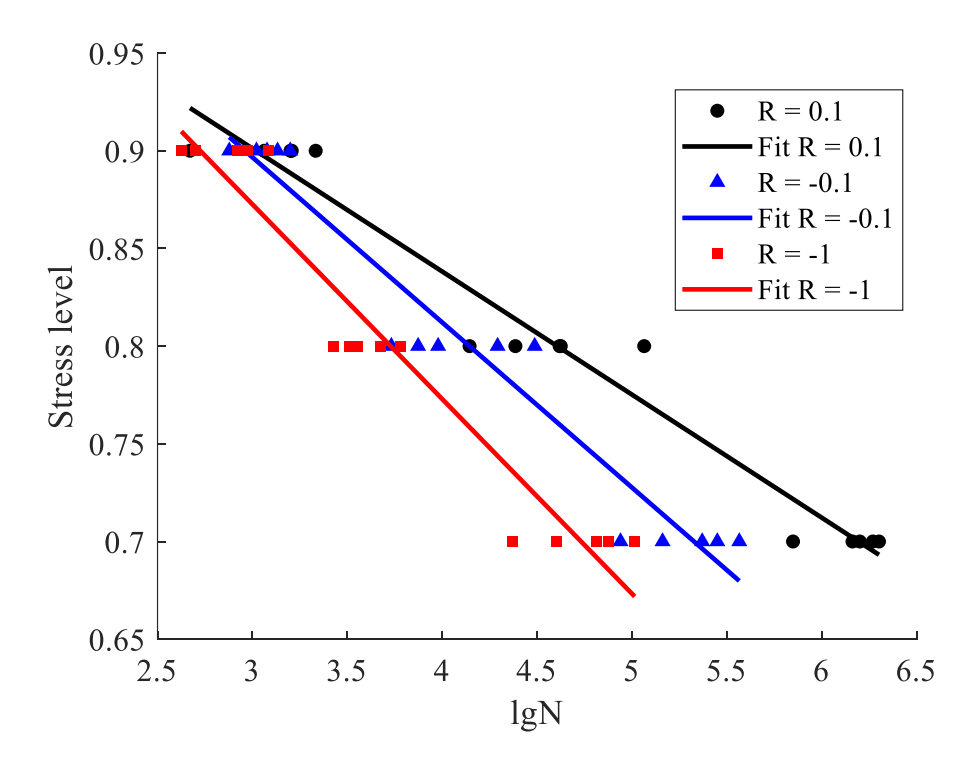


Fig. 4.4 The relationship between S and lgN

As shown in Fig. 4.4, there is a clear linear correlation between the fatigue stress level and the logarithm of the fatigue life for UHPECC. The provided fatigue S-N curve allows for predicting the fatigue life. In contrast to the previous chapter, where the slopes of fitted S-N curves remained similar with a fixed stress ratio despite varying loading frequencies, in this chapter, where the stress ratio varies while the loading frequency remains constant, the slopes of S-N curves for each condition are not similar. Across varying stress ratios, the correlation between fatigue life and stress level remains consistent: fatigue life increases as the stress level decreases. When subjected to the same stress level, specimens with lower stress ratios endure fewer cycles under fatigue loading. When comparing the test group with a stress ratio of -0.1 to the group with a stress ratio of 0.1, at higher stress levels, the fatigue life is similar. However, as the stress level decreases, the difference in fatigue life between tension-tension cycles and tension-compression cycles becomes more pronounced. Specifically, in tension-tension fatigue,

the fatigue life shows stronger performance increases at relatively lower stress levels. At a stress ratio of -1, specimens exhibit a significant decrease in fatigue life compared to those tested under the other two stress ratio conditions, across various stress levels.

The impact of the stress ratio on concrete's fatigue life is more pronounced than its impact on steel. However, research data on tension-compression reversal fatigue is limited. This is mainly due to normal concrete's limited tensile strength and brittleness, which leads to its perceived unreliability and consequent exclusion from fatigue calculations in practical engineering. The emergence of various fiber-reinforced concrete has enhanced the tensile strength of concrete, making it more valuable for practical applications. Consequently, accurately evaluating the effect of stress ratio on fatigue life is especially important. Engineering structures may face arbitrary fatigue loading conditions, leading to widely varying stress ratios. Specifically, these conditions can result in tension-tension fatigue, compression-compression fatigue, and tensioncompression fatigue. The latter category can be further subdivided into cases where the maximum absolute tension stress is greater and cases where the maximum absolute compression stress is greater. The present study begins with tension-tension fatigue and then extends to tension-compression fatigue. In all cases discussed, the magnitude of the compressive stress is smaller than that of the maximum tensile stress. The range of loading conditions that can be explored through experimental measurements is limited. Therefore, it is essential to utilize the available experimental parameters as effectively as possible to identify applicable patterns and laws within this scope.

Aas-Jakobsen (1970) proposed a classic formula introducing the influence of stress ratio and attempted to establish the correlation between fatigue life and stress level, as demonstrated below:

$$S = 1 - \beta \cdot (1 - R) \cdot lgN \tag{4-6}$$

where only  $\beta$  is the parameter that must be identified by fitting test data. Fitting the experimental data from this study using the Aas-Jakobsen equation yielded the results shown in Fig. 4.5.

Fig. 4.5 shows the fitting curves using data from three stress ratios, shown by the black line, and using only two stress ratios (0.1 and -0.1), depicted by the brown line. The coefficients  $\beta$ for the black and brown fitting lines are -0.0359 and -0.0475, respectively. The coefficient of determination  $R^2$  are 0.3913 and 0.9196, respectively. The coefficient of determination obtained by fitting the data for three different stress ratios is significantly lower than the coefficient obtained by considering only the two stress ratios, R = 0.1 and R = -0.1. This indicates that, on one hand, the equation has a specific range of applicability. When the formula was proposed, it was primarily based on the compressive fatigue of concrete (Tepfers and Kutti 1979). It also shows some applicability to fiber-reinforced concrete under tension-tension fatigue or tension-compression fatigue dominated by tensile stress. On the other hand, the failure mechanism for a stress ratio of -1 is significantly different from that under the other two stress ratio conditions. Therefore, for tension-compression fatigue with similar magnitudes of tensile and compressive stress, it is not appropriate to fit these conditions into the same formula as those dominated by tensile stress. The author believes that in fatigue cycles dominated by tensile stress, the microscopic failure mode is primarily characterized by the gradual pull-out and fracture of the fibers. In fatigue cycles where the magnitudes of tensile and compressive

stress amplitudes are similar, fibers gradually pull out under tensile stress and are then subjected to significant compression under compressive stress. This substantially increases the risk of fiber buckling and fracture. Under these loading conditions, fibers face increasing failure risks in both tensile and compressive directions. Consequently, the fatigue life of cycles with approximately equal amplitude in tension and compression at various stress levels is significantly lower compared to fatigue under pure tension or pure compression conditions.

Our current research is focused on a narrow range of stress ratios. For emerging materials such as ECC, conducting broader experiments to investigate the stress ratio effect on fatigue life is essential. This not only facilitates a more precise definition of the connection between fatigue life and stress level, considering the stress ratio but also provides valuable guidance and recommendations for engineering applications.

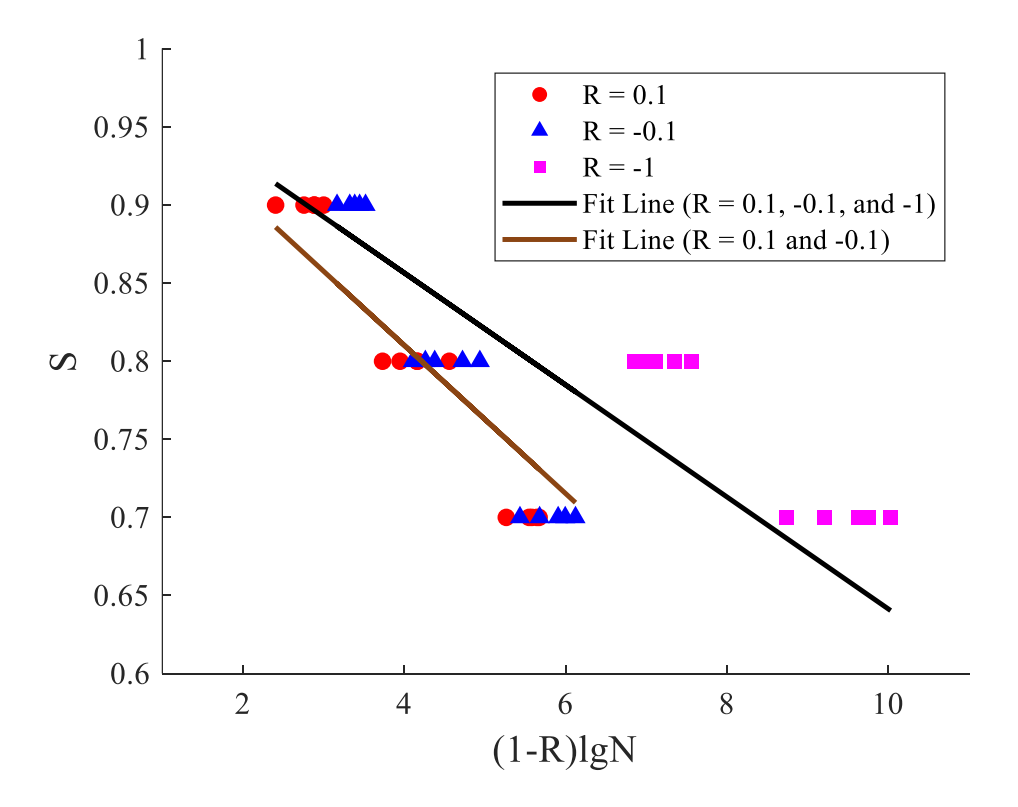
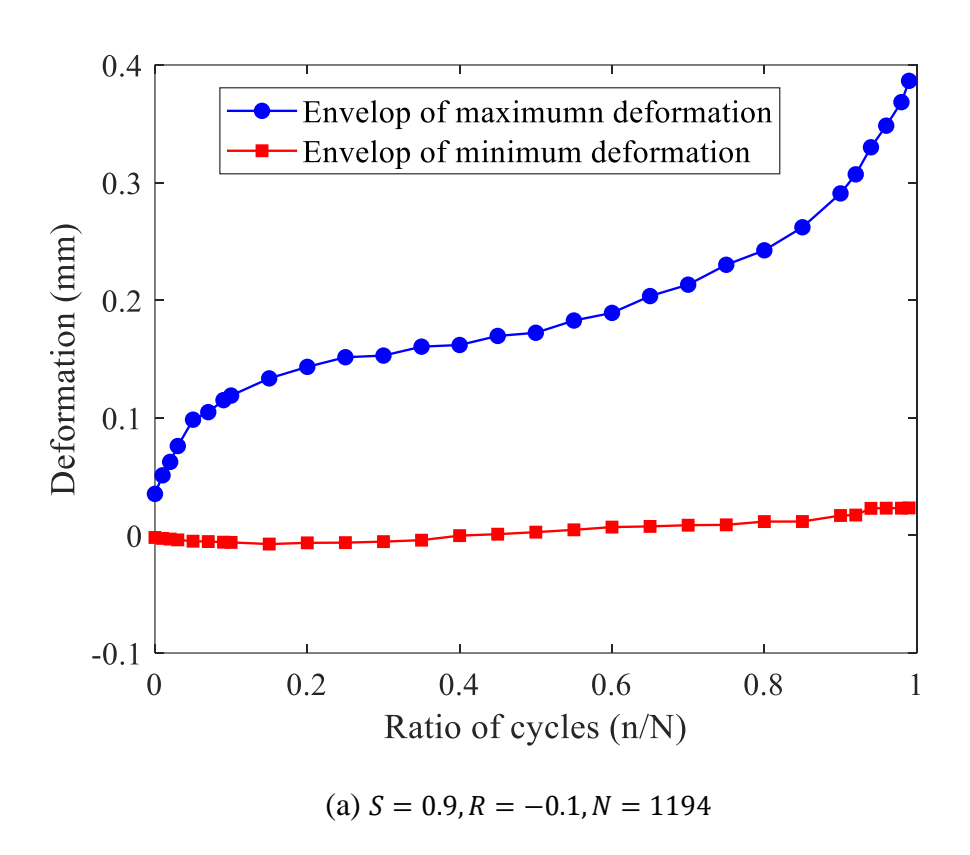
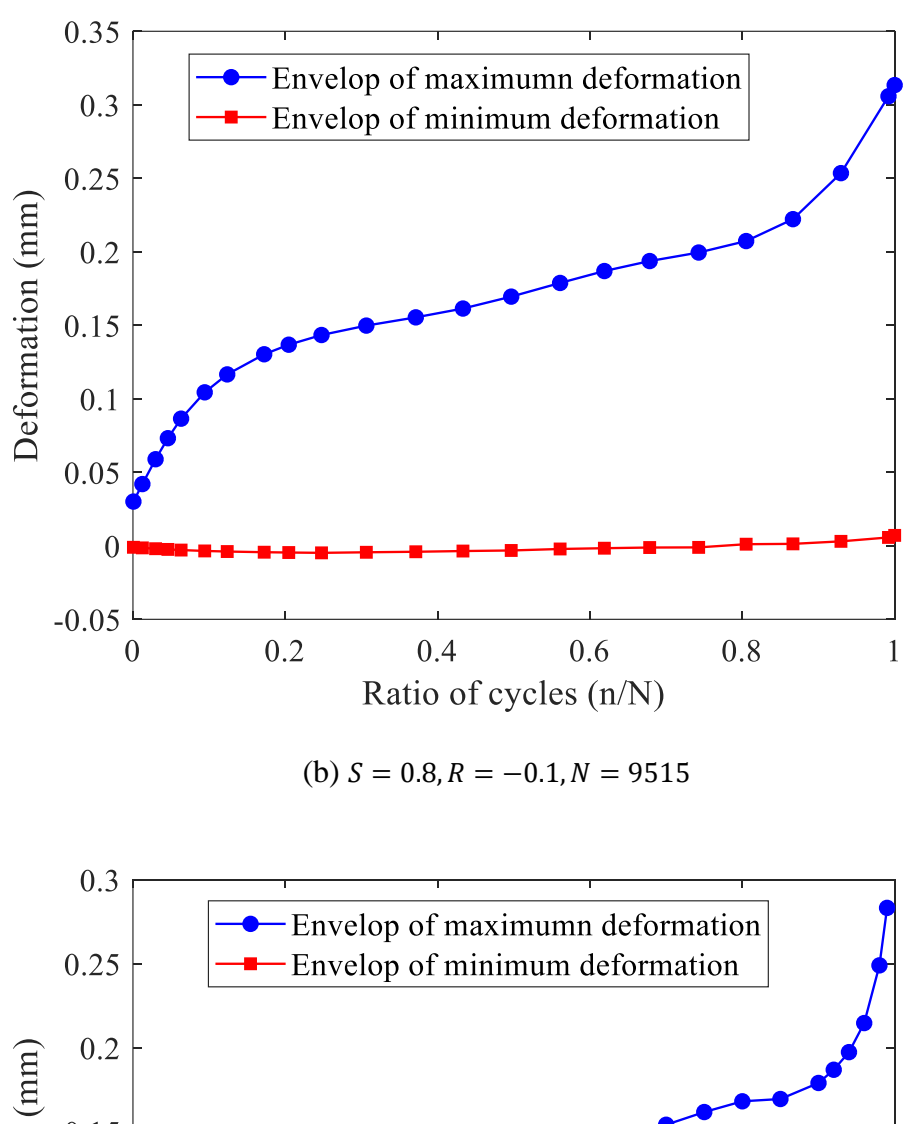


Fig. 4.5 The S-N relation based on Aas-Jakobsen's equation

# 4.3.3 Fatigue deformation

During the experiment, the real-time deformation of most specimens in the measurement section was recorded. However, not all specimens were fractured within this section. For each fatigue loading condition, the deformation evolution of the specimen that fractured within the measurement section and whose fatigue life is closest to the characteristic fatigue life with a 0.5 failure probability is selected and listed, as shown in Fig. 4.6 to Fig. 4.8.





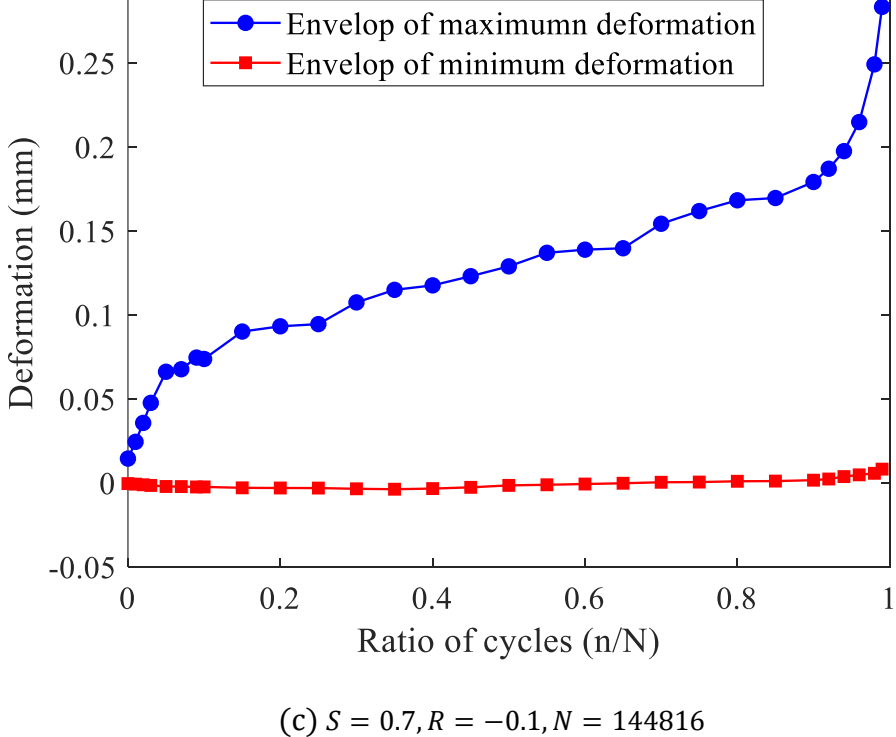
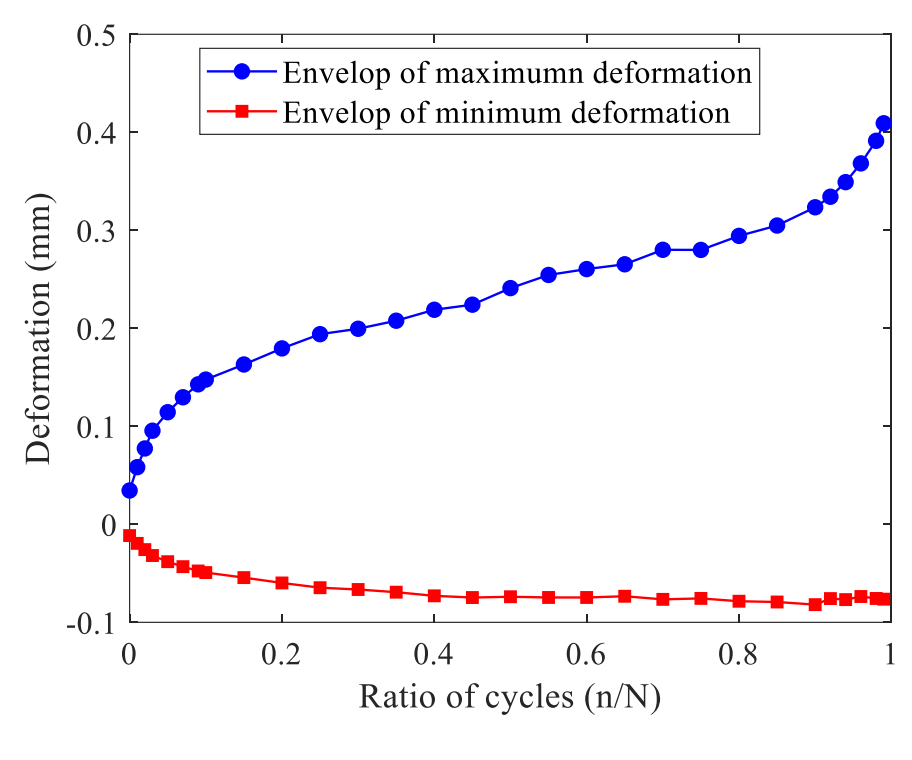
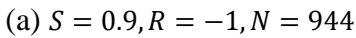
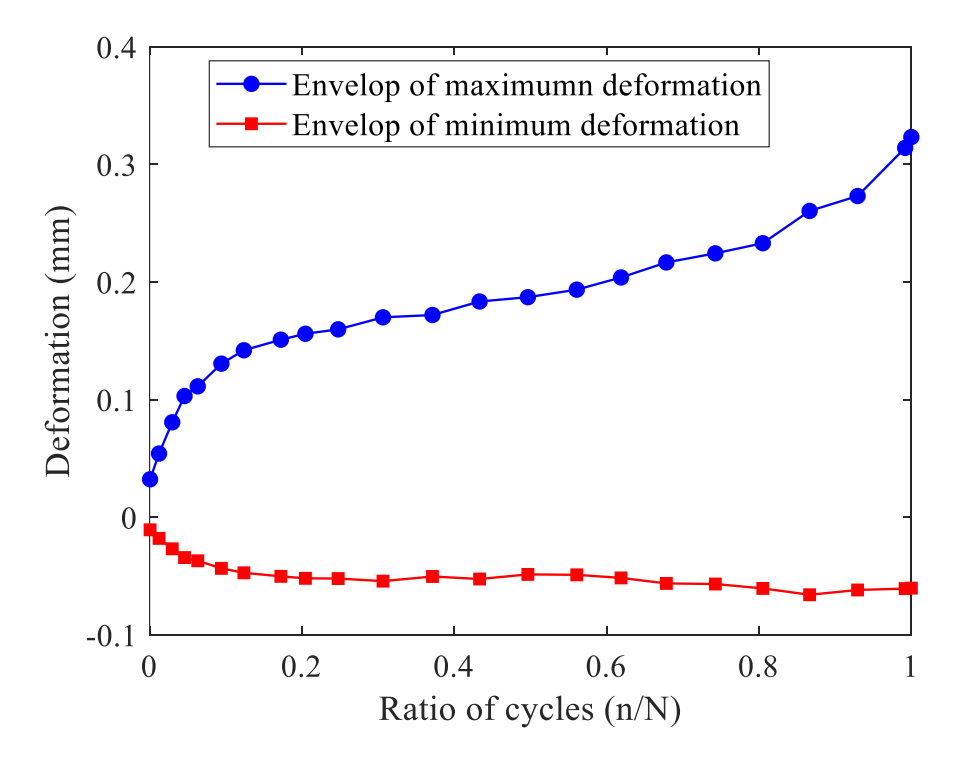


Fig. 4.6 Evolution curves of fatigue deformation with stress ratio of -0.1







(b) S = 0.8, R = -1, N = 3257

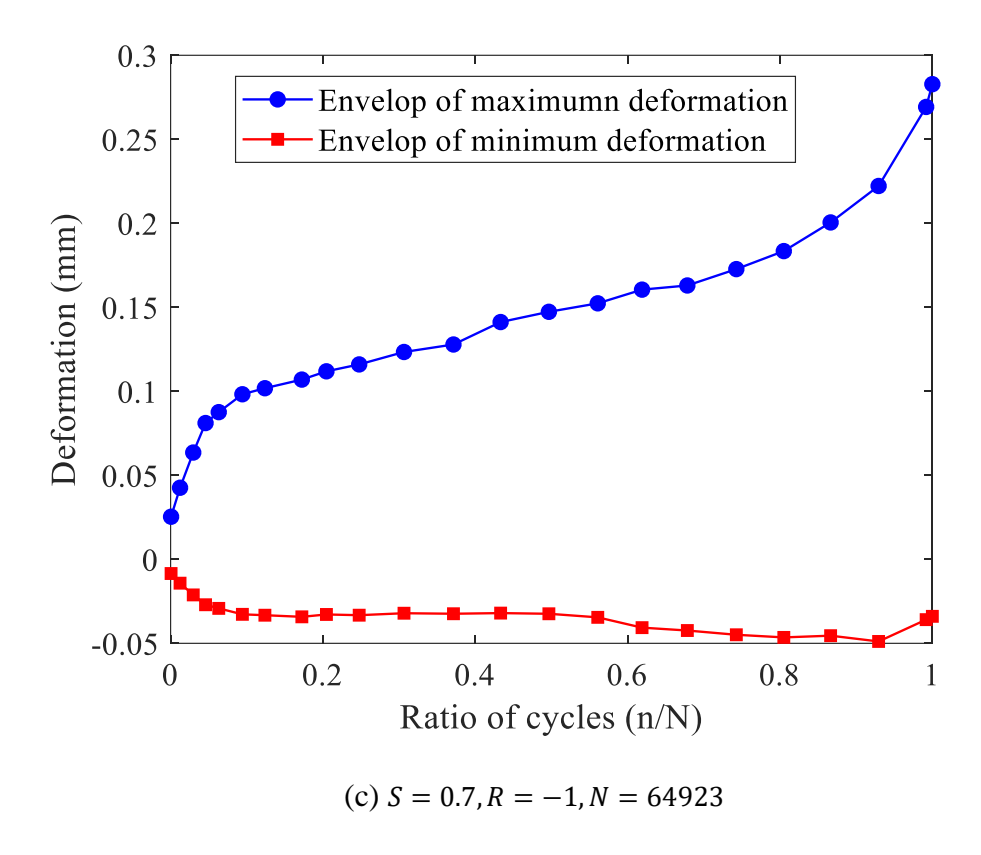
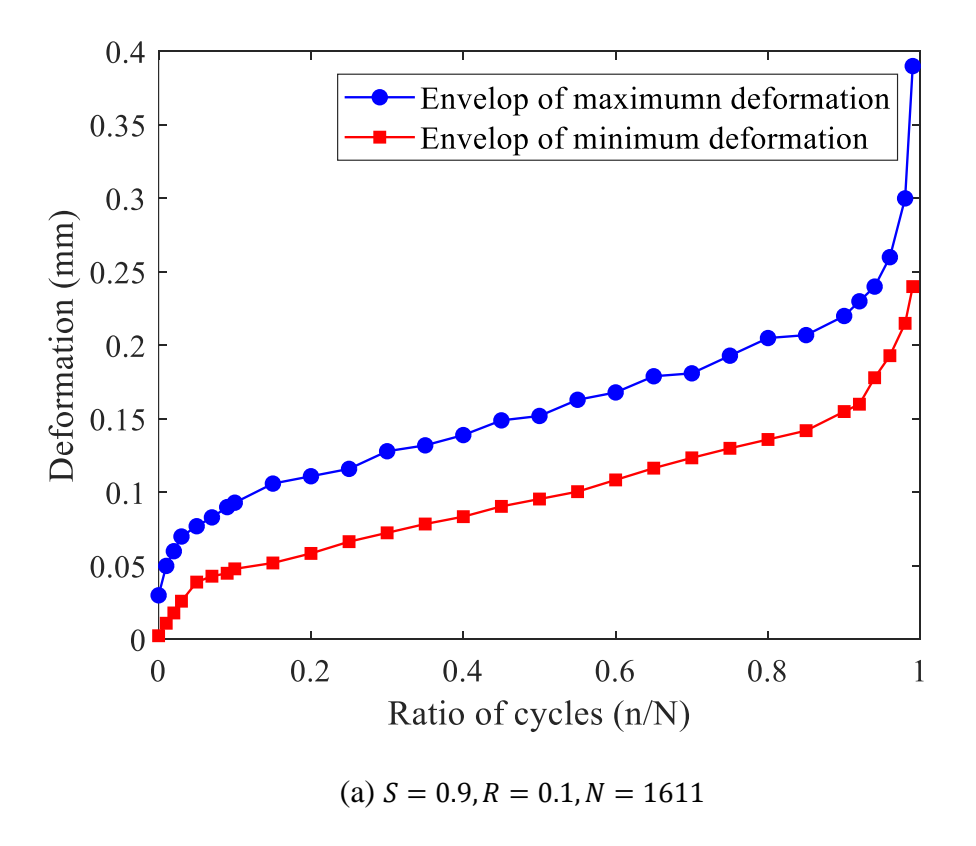


Fig. 4.7 Evolution curves of fatigue deformation with stress ratio of -1



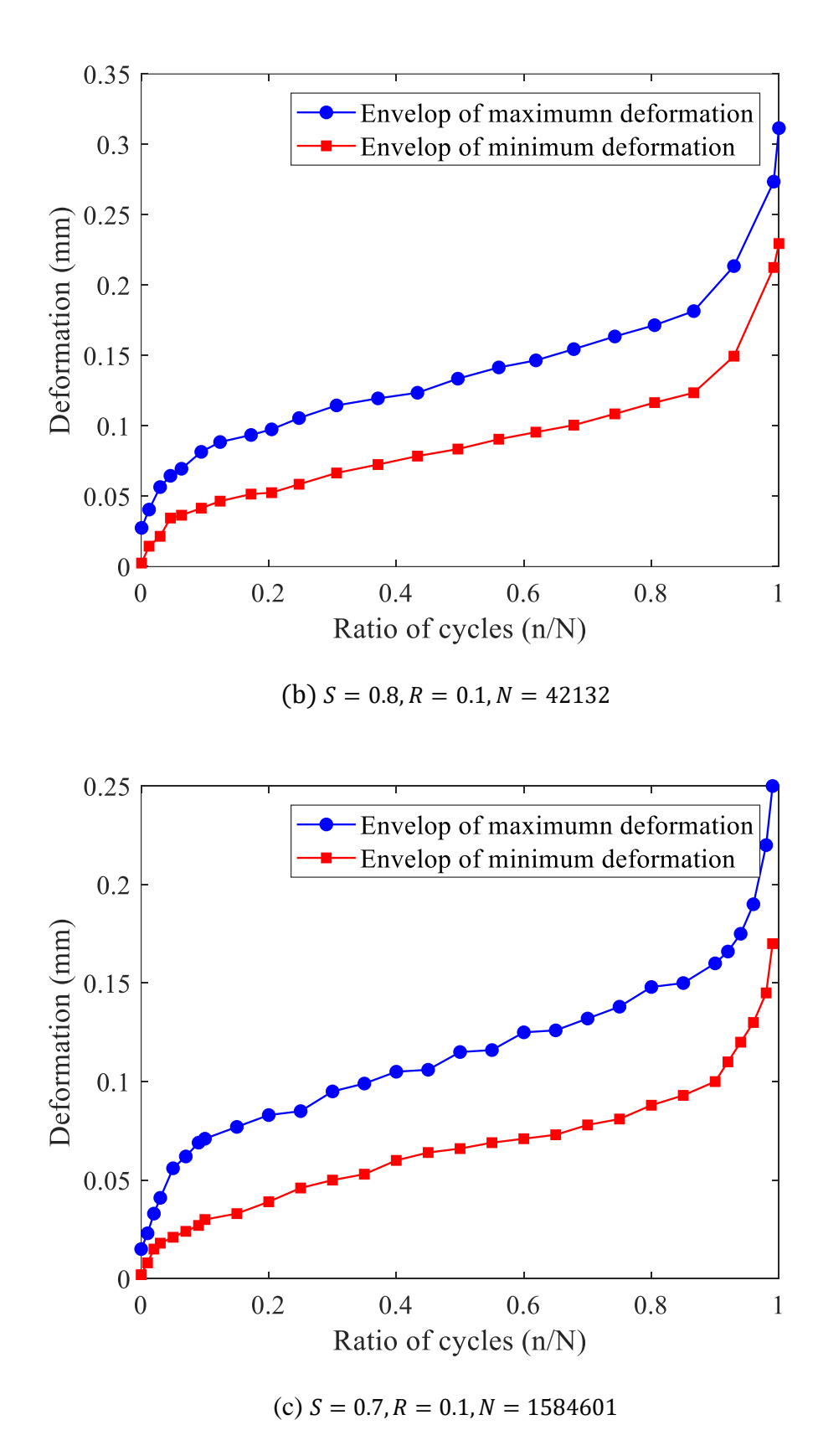


Fig. 4.8 Evolution curves of fatigue deformation with stress ratio of 0.1 (tested in chapter 3)

Fig. 4.6 to Fig. 4.8 shows the envelope representing the evolution of maximum and minimum deformations throughout fatigue cycles. Under various stress ratio conditions, the deformation evolution of UHPECC can be divided into three stages: the initial stage of rapid growth, a subsequent stage of steady development, and a final stage of unstable growth. However, the proportion of each stage changes depending on the stress levels. At a stress level of 0.9, the first and third stages are minimal, with the second stage being predominant. At stress levels of 0.8 or 0.7, the first and third stages each account for approximately 10% of the total lifespan, and the maximum strain demonstrates an inverted S-shaped evolution characteristic.

For specimens subjected to tension-compression fatigue stress reversal, the tensile deformation exceeds the compressive deformation because the elastic modulus is higher in compression than in tension. Additionally, as plastic deformation gradually increases on the tensile side, the overall deformation envelope progressively shifts towards the tensile side. Consequently, with a stress ratio of -0.1, even when the compressive stress reaches its maximum value in the later stages, the measured deformation remains greater than zero, indicating that the test section length exceeds the initial length.

#### 4.4 CUMULATIVE FATIGUE DAMAGE MODEL

# 4.4.1 Review of existing fatigue models

Similar to ordinary concrete, fiber-reinforced concrete contains numerous initial microcracks and micropores. As it undergoes repeated cycles of fatigue loading, these microcracks and micropores gradually expand, resulting in damage to the fiber-reinforced concrete. This damage manifests in its macroscopic mechanical properties, causing increased inelastic strain,

loss of stiffness, and diminished strength. Fully understanding the fatigue damage and mechanical response of fiber-reinforced concrete is highly significant.

An appropriate cumulative damage model that can describe the fatigue development process forms the basis for structural fatigue design. The Palmgren-Miner linear cumulative damage theory (Miner 1945), commonly referred to simply as Miner's rule, is the most classic and extensively used approach in this field. According to this theory, fatigue damage can be linearly accumulated under cyclic loads, with each stress level being independent and uncorrelated. Fatigue damage occurs in specimens or components when the cumulative damage value reaches 1. This is expressed as:

$$D = \sum \Delta D_i = \sum \frac{n_i}{N_i} = 1 \tag{4-7}$$

where  $\Delta D_i$  represents the damage coefficient at a stress level of  $S_i$ ,  $n_i$  denotes the count of cycles associated with this stress level, while  $N_i$  indicates the fatigue life for that stress level.

Miner's rule is founded on the following assumptions: (1) the energy dissipated per cycle at a given stress level remains constant; (2) cumulative damage is independent of the prior loading history; (3) the loading sequence does not impact the material's fatigue life. These assumptions indicate that Miner's rule simplifies the mechanism of cumulative fatigue damage.

The cumulative damage of materials under external load is an irreversible deterioration process. Numerous studies have demonstrated that this damage is influenced by the loading sequence, material properties, and stress levels. For many materials, the loading sequence plays a crucial role in influencing fatigue damage. Specimens that experience high-stress cycles first suffer more damage compared to those that undergo low-stress cycles first (Ou and Lin 1999).

Miner's linear cumulative fatigue damage theory has proven effective for metallic materials. Due to its simplicity, intuitiveness, and clarity, Miner's rule has found widespread application in engineering. However, its accuracy is limited when analyzing materials with significant defects, such as concrete or rock. This limitation becomes particularly apparent in two-stage or multi-stage loading scenarios, as the theory does not consider the effects of loading sequence or the interactions among different loading conditions.

To address this problem, numerous modified linear cumulative fatigue damage theories (Hilsdorf and Kesler 1966; Manson and Halford 1986) and nonlinear cumulative theories (Henry 1955; Marco and Starkey 1954) have been proposed. One notable example is the Corten-Dolan theory (Corten and Dolan 1956). The Corten-Dolan theory suggests that damage may occur at multiple locations on the specimen surface, with the number of damage sites influenced by the stress level the material endures. Under constant amplitude loading, the damage D resulting from n cycles can be represented as follow:

$$D = mrn^a (4-8)$$

where m is the number of locations where material damage occurs, which increases with higher stress levels; r is the crack growth coefficient, which is proportional to the stress level S; n represents the number of cycles at a specific stress level; and a is a constant.

For different loading histories, the total fatigue damage  $D_f$  at failure remains constant. Therefore, when the same component experiences stress  $S_1$  and  $S_2$  respectively, the overall damage can be represented as:

$$D_f = m_1 r_1 N_1^{a_1} = m_2 r_2 N_2^{a_2} (4-9)$$

where  $N_1$  and  $N_2$  represent the number of cycles at stress levels  $S_1$  and  $S_2$  respectively, at which the component fails.

If the fatigue loading process alternates between stress levels  $S_1$  and  $S_2$ , with  $S_1 > S_2$ , and assuming the number of damage locations m depends only on the higher stress level  $S_1$ , thus,  $m_2 = m_1$ . It can be assumed  $a_1 = a_2 = a$ . If the total number of cycles until failure under combined actions of  $S_1$  and  $S_2$  is  $N_f$ , and the percentage of cycles at stress level  $S_1$  is  $\lambda_1$ , then the percentage of cycles at the stress level  $S_2$  is  $(1 - \lambda_1)$ . Therefore,

$$\frac{N_f}{N_1} = \frac{1}{\lambda_1 + (r_2/r_1)^{\frac{1}{a}} (1 - \lambda_1)}$$
 (4-10)

here,  $(r_2/r_1)^{\frac{1}{a}}$  depends on the relative magnitudes of the two stress levels, expressed as:

$$\left(\frac{r_2}{r_1}\right)^{\frac{1}{a}} = \left(\frac{S_2}{S_1}\right)^d \tag{4-11}$$

where d is a material constant determined by experiments. Substituting Eq. (4-11) into Eq. (4-10) yields:

$$\frac{N_f}{N_1} = \frac{1}{\lambda_1 + (1 - \lambda_1) (S_2/S_1)^d}$$
 (4-12)

generalizing Eq. (4-12) from two stress levels to multi stress levels loading yields Eq. (4-13):

$$\frac{N_f}{N_1} = \frac{1}{\sum_{i=1}^k \lambda_i (S_i / S_1)^d}$$
 (4-13)

where  $N_f$  represents the total number of cycles to failure under multi-stress levels alternating stresses,  $S_1$  represents the highest stress level among several stress levels,  $N_1$  represents the

number of cycles to failure under the stress level of  $S_1$ ,  $\lambda_i$  is the percentage of cycles at the stress level  $S_i$ , and d is a material constant. By rearrangement:

$$\sum \frac{\lambda_i N_f}{N_1 \left(\frac{S_1}{S_i}\right)^d} = 1 \tag{4-14}$$

Eq. (4-14) resembles the Equation (4-7) from linear damage accumulation theory. In Eq. (4-14),  $\lambda_i N_f$  and  $N_1 \left(\frac{S_1}{S_i}\right)^d$  corresponds to  $n_i$  and  $N_i$  in Eq. (4-7), respectively. Rewriting this as  $\frac{N_i}{N_1} = \left(\frac{S_1}{S_i}\right)^d$ , and taking the logarithm of both sides, we get:

$$\log \frac{N_i}{N_1} = d \log \left(\frac{S_1}{S_i}\right) \tag{4-15}$$

From the above equation, it is evident that stress level  $S_i$  and fatigue life  $N_i$  exhibit a linear correlation in a double logarithmic coordinate system, with the slope of the line being related to the material constant d. This applies to a considerable portion of engineering materials. However, according to the Corten-Dolan theory, damage in materials initiates rapidly within a short period, followed by a phase of cumulative damage. In contrast, for concrete materials, it is widely recognized that the initial development of damage accounts for approximately 10% of its total lifespan. The fatigue damage evolution curve proposed by Corten-Dolan does not adequately capture or quantify this characteristic. Moreover, the accumulation of damage in each cycle does not consistently correlate with increasing stress levels. Observing fatigue damage evolution across various materials reveals a common pattern: damage develops rapidly in the initial cycles, then gradually decelerates to a stable rate, and finally accelerates sharply nearing failure, indicating a three-stage progression. Thus, the extent of damage cannot be

solely explained by the stress level. Other nonlinear models for cumulative fatigue damage have been proposed by scholars like Subramanyan (1976), Leve (1969), and Gatts (1961). While, these models typically exhibit greater complexity, posing challenges in parameter determination.

Many theories have been proven effective and widely used for metals or other materials that are not directly applicable to concrete materials. Conducting fatigue analysis of ECC materials requires addressing two key issues: defining damage appropriately and establishing a fatigue damage cumulative model specific to concrete.

### 4.4.2 Cumulative fatigue damage model

The dominant fatigue damage theory of concrete suggests that damage results from the extension of micropores or microcracks (Shah 1984; Hamdy 1997). These discontinuities at the micro level are regarded as continuous on a broader scale. Damage can induce various changes in material properties. As damage accumulates, the elastic modulus, strength, and hardness decrease. Conversely, strain, electrical resistance, and energy dissipation tend to increase gradually. Therefore, several methods have been developed to quantify damage based on these changes in material properties. Regardless of the parameters employed, the evolution of damage must align consistently with the development of microcracks. Thus, the definition of the damage variable must fulfill these essential criteria: it must have a precise physical interpretation, be easily measurable for practical engineering, and its changes should mirror the degradation process of the material.

In the tests conducted in this research, parameters like elastic modulus and deformation progression were identified as easily measurable. Given that fatigue loading in this chapter involves stress reversal, concrete demonstrates notable differences in tensile and compressive moduli. Hence, choosing deformation as the indicator of damage appears to be more appropriate. The deformation can be represented by maximum strain and residual strain. Maximum strain is defined as the strain when tensile stress reaches its peak, while residual strain is the strain measured when tensile stress hits its lowest point or when compressive stress is at its maximum during the fatigue cycle. While the experiment in this chapter involves stress reversal, the residual strain of specimens under a stress ratio of -1 is compressive, with corresponding measurements being negative. For specimens with a stress ratio of -0.1, the residual strain fluctuates between compressive and tensile, with measurements near zero. Since the failure mode of all specimens is a tensile fracture, using residual strain in this experiment does not reasonably reflect the evolution of fatigue damage. Therefore, the maximum strain is chosen as the parameter to characterize the progression of damage. The damage variable is represented as follows:

$$D = \frac{\varepsilon_{max}^{n} - \varepsilon_{max}^{0}}{\varepsilon_{max}^{f} - \varepsilon_{max}^{0}}$$
 (4-16)

in the equation,  $\varepsilon_{max}^0$ ,  $\varepsilon_{max}^n$ , and  $\varepsilon_{max}^f$  represent the initial maximum strain, instantaneous maximum strain after n fatigue cycles, and the ultimate maximum strain, respectively.

Eq. (4-16) indicates that accurately defining the evolution of strain is crucial for determining damage progression. As noted in the previous section, the maximum deformation of the specimens follows an inverted S-shaped pattern: it begins rapidly, then slows down, and finally accelerates. Various functional forms have been proposed by researchers to fit different

inverted S-shaped curves (Xiao et al. 2009; Liu and Zhou 2017). In this context, the author adopts an inverted S-shaped function proposed by Huang et al. (2019a), derived from the Weibull distribution equation. This function has been proven effective in fitting the fatigue deformation of concrete under different loading conditions. The expression is as follows:

$$\varepsilon = \varepsilon_0 + \lambda \left( -\ln\left(1 - \frac{n-1}{N_f}\right) \right)^{\frac{1}{k}} \tag{4-17}$$

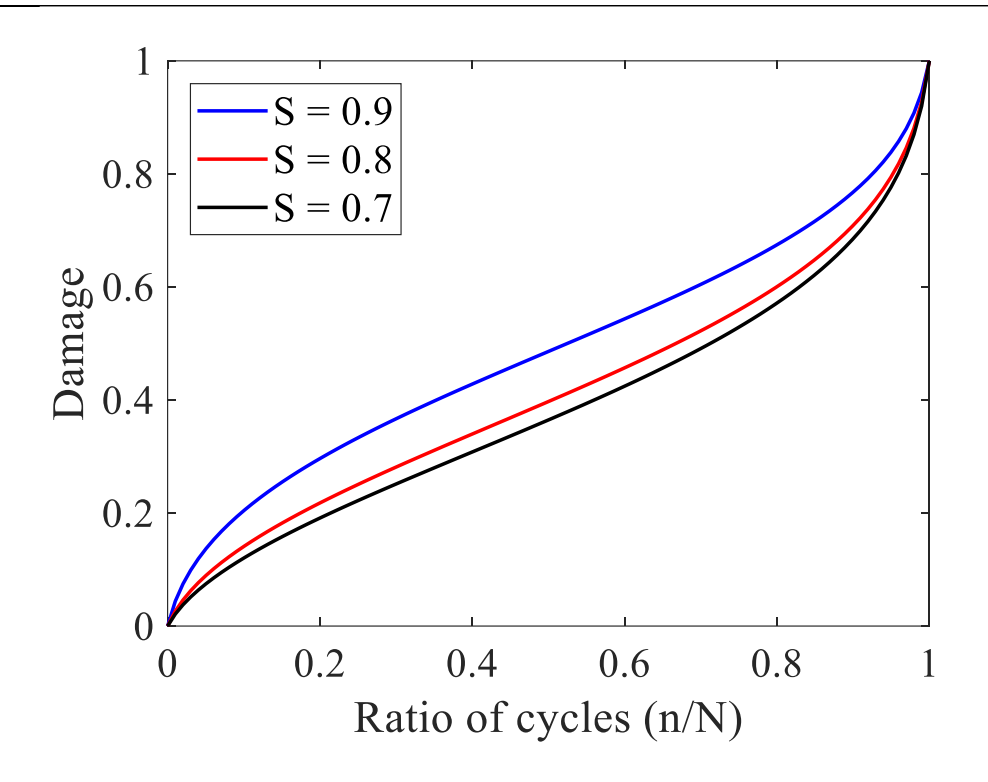
where  $\varepsilon_0$  represents the initial strain,  $\lambda$ , and k are scale parameters and shape parameters respectively. n denotes the fatigue cycle,  $N_f$  represents the fatigue of life at failure.

By dividing the deformation measured in the previous section by the length of the test section and fitting it using Eq. (4-17), we can obtain the fitting parameters  $\varepsilon_0$ ,  $\lambda$  and k under various loading conditions. Table 4.5 presents the results. Based on the strain evolution curve, further calculating the damage using Eq. (4-16) requires knowing both  $\varepsilon_{max}^0$  and  $\varepsilon_{max}^f$ . In this context, we set the fitted  $\varepsilon_0$  as the initial maximum strain  $\varepsilon_{max}^0$ . For the ultimate maximum strain  $\varepsilon_{max}^f$ , considering that the specimen's deformation becomes extremely unstable in the final stage before failure—with failure often occurring instantaneously and the slope of strain development increasing significantly—an excessively large  $\varepsilon_{max}^f$  would result in an underestimation of damage in the earlier stages. Therefore, we select the strain corresponding to a relative fatigue life of 0.99 (i.e., when  $n/N_f=0.99$ ) as  $\varepsilon_{max}^f$ . The resulting damage evolution is depicted in Fig. 4.9.

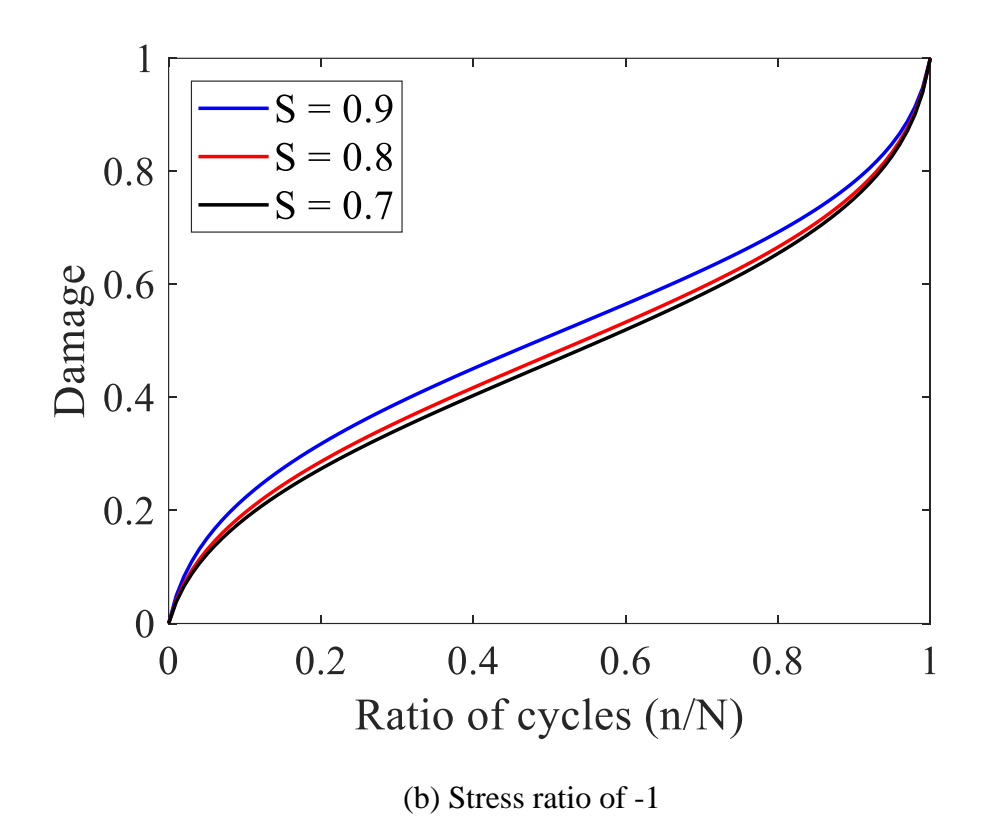
Table 4.5 Fitted value of maximum strain evolution curve

Stress ratio	Stress	Fatigue	۶۰	2	lz
(R)	level (S)	life (N)	20	λ	K

	0.9	1117	$6.2513 \times 10^{-4}$	$2.0086 \times 10^{-3}$	2.0474
-0.1	0.8	10960	$6.4737 \times 10^{-5}$	$2.3212 \times 10^{-3}$	3.3544
	0.7	186164	$2.8422 \times 10^{-4}$	$1.5197 \times 10^{-3}$	2.3026
	0.9	693	$2.6646 \times 10^{-4}$	$3.0121 \times 10^{-3}$	3.1848
-1	0.8	3754	$7.3261 \times 10^{-5}$	$2.5966 \times 10^{-3}$	3.7720
	0.7	50907	$2.6451 \times 10^{-4}$	$1.7940 \times 10^{-3}$	2.9874
	0.9	1319	$6.1392 \times 10^{-4}$	$1.5347 \times 10^{-3}$	1.8518
0.1	0.8	39946	$3.8120 \times 10^{-4}$	$1.5083 \times 10^{-3}$	2.3041
	0.7	1499285	$2.8279 \times 10^{-4}$	$1.3043 \times 10^{-3}$	2.2580



(a) Stress ratio of -0.1



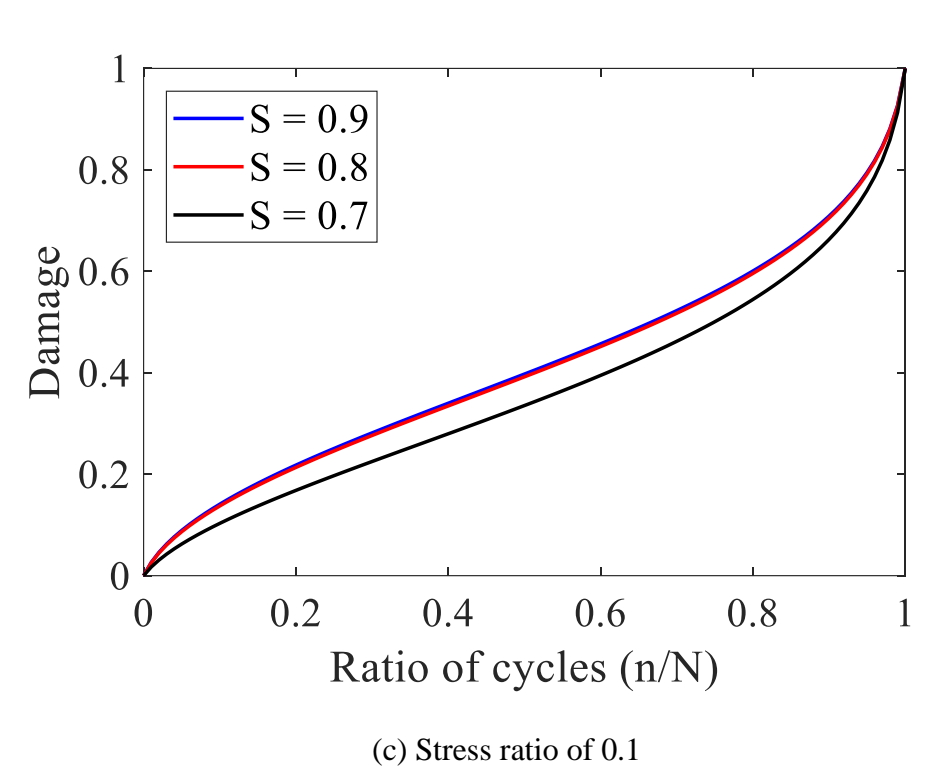


Fig. 4.9 Damage evolution under various loading conditions

#### 4.4.3 Method for estimating fatigue life under multilevel fatigue loading

The fatigue life of ECC under constant amplitude loading conditions can be estimated using the S-N curve derived from experimental data. However, for multilevel variable amplitude fatigue loads typical in engineering applications, a fatigue damage model is necessary to estimate fatigue life accurately. The procedure involves several specific steps: 1) identify the critical fatigue-prone areas of the structure; 2) obtain the local stress spectrum at these critical points; 3) Perform elastoplastic finite element analysis to calculate the local strain spectrum; 4) Analyze the range of the strain spectrum and corresponding loading conditions; 5) select representative loading conditions and verify the material strain evolution; 6) Based on the strain evolution, establish an S-shaped damage evolution curve; 7) Utilize fatigue damage accumulation theory to assess the fatigue life of the critical areas.

# 4.5 CONCLUSIONS

The effect of stress ratio on UHPECC, considering stress reversal, was investigated through a series of experiments in this chapter. Additionally, a tensile fatigue damage model was further developed. The findings lead to the following conclusions:

Under the stress ratios tested in this chapter, the fatigue failure mode of UHPECC is tensile fatigue fracture, with the specimens maintaining overall integrity upon failure. Additionally, under various stress ratios, the fatigue life decreases as the stress level increases.

Reducing the stress ratio to a negative value, resulting in tensile-compressive cyclic fatigue loading, has a significantly more adverse effect on fatigue life compared to tensile-tensile cycling. This effect is particularly pronounced when the magnitude of the compressive stress

is close to that of the tensile stress, as the compressive process can cause significant buckling of the fibers, thereby increasing the risk of fracture.

For fatigue loading involving stress reversal, the compressive strain is significantly less than the tensile strain, and the residual deformation caused by tensile strain accumulates continuously. The progression of the specimen's maximum deformation under various stress ratios follows an inverted S-shaped curve. A cumulative fatigue damage model was developed to estimate fatigue life under various loading conditions, based on the evolution curve of maximum strain.

# CHAPTER 5 CYCLIC FLEXURAL BEHAVIOR OF GFRP BAR-REINFORCED UHPECC BEAMS

#### 5.1 INTRODUCTION

In East Asia, megacities like Hong Kong, Osaka, and Singapore are facing growing constraints due to increasingly scarce land resources. Conventional approaches to expanding land supply, like land reclamation, face escalating costs as water depths increase. Additionally, they pose risks of environmental degradation, time consumption, and obstruction of shipping channels. One solution that achieves a balance between economic interests and environmental protection involves the development of ocean engineering, such as floating structures. So far, researchers in ocean engineering have proposed various concepts and designs, including floating oil storage facilities (Wan et al. 2018a), floating bridges (Chen et al. 2018), floating photovoltaic systems (Li et al. 2023), floating airport (Rognaas et al. 2001), etc. While structures mentioned above are typically designed as concrete or prestressed concrete structures, they encounter more severe corrosion environments and cyclic loads from winds and waves during long-term service periods compared to inland civil structures. Consequently, the corrosion and performance degradation of steel reinforcement within marine structures emerge as significant concerns.

FRP reinforcement has gained attention as a promising substitute for steel reinforcement, offering high strength, superior corrosion resistance, and effective electromagnetic transparency (Chen and Teng 2008). Although FRP materials offer promising durability and strength, their relatively lower elastic modules can lead to a significant decrease in stiffness. This reduction in stiffness may increase the risk of shear failure or premature concrete crushing.

To overcome these shortcomings, using high-performance concrete presents a potential solution. In recent years, ECC has been developed to show higher ductility in both compression and tension (Lepech and Li 2009). Due to the inclusion of fibers, the tensile load capacity can be sustained even after cracking. With the increasing load, multiple cracks will initialize and open to a certain width gradually. The formation of multiple cracks prevents ECC from brittle fracture and exhibits strain-hardening behavior. Taking advantage of fibers, ECC can typically achieve an ultimate strain of over 3% before one particular localized crack grows wide enough followed by softening behavior (Zhang et al. 2011). The compressive strength of high-strength ECC can reach 80-160 MPa (Huang et al. 2020). ECC exhibits enhanced performance over traditional concrete under different loading conditions, including monotonic, cyclic, fatigue, and impact loadings. The multiple cracking with fine cracks in the tensile zone makes ECC exhibits good ductility. The high spalling resistance with larger ultimate strain can prevent brittle failure due to crushing (Yuan et al. 2014).

A series of static behaviors of FRP-reinforced ECC members have been reported as mentioned before, but studies on the cyclic behavior of these components remains limited, particularly for FRP-reinforced high-strength ECC under cyclic loading. However, the cyclic behavior of FRP-reinforced high strength ECC beams has not been documented yet. Investigating this is crucial for extending the understanding of FRP-reinforced ECC from its monotonic behavior to cyclic performance.

In summary, the use of ECC in conjunction with FRP reinforcement can be a potential option for improving ductility performance and eliminating corrosion problems. This research focuses on examining the cyclic flexural behavior of UHPECC beams reinforced with FRP. An

extensive experimental program including eight beams was carried out to assess the influence of reinforcing ratio, fiber dosages, and loading types. Crack development, load-displacement response, failure modes, energy dissipation capacity, deformability, and strain evolution are measured and discussed. The results of this work will enhance the knowledge of the cyclic flexural behavior of FRP-reinforced UHPECC beams and broaden the scope of application for both FRP reinforcement and UHPECC.

#### 5.2 EXPERIMENTAL PROGRAM

#### **5.2.1** Materials

To utilize the strength of FRP as much as possible, ultra-high-performance ECC (UHPECC) was adopted in this study. Table 5.1 presents the mixture proportion for the UHPECC. Portland cement and silica fume served as the binders. Sea sand with a particle size under 1.18 mm was used as the fine aggregate. A superplasticizer equal to 1.35% of the weight of the binders was incorporated to enhance the workability of the ECC. Ultra-high molecular weight polyethylene (PE) fibers with two different fiber volumetric ratios, i.e., 1% and 2%, were investigated. Table 5.2 provides the details on the properties of the PE fibers. The powders were initially dry-mixed for 3 minutes, followed by the addition of water and superplasticizers, which were mixed for 5 minutes. Lastly, the PE fibers were gradually introduced and mixed for an additional 15 minutes. Following ASTM C1437-15 (2015), the mini-slump flow for ECC with a 2% PE fiber volumetric ratio was measured at approximately 180 mm. After casting, the specimens were immediately covered with plastic sheets and de-molded after 72 hours. They were then moisture-cured for 28 days. The compressive strength for each ECC batch was assessed by performing compression tests on 50 mm cubes (Fischer and Li 2003). The mean compressive strength was measured to be 132.6 MPa. Direct tensile tests on at least three dumbbell samples

for each batch of ECC were conducted according to JSCE's recommendation (2008). Fig. 5.1 presents two representative tensile stress-strain curves of ECC with different fiber volume ratios. The cracking strength is identified at the inflection point from the initial linear segment to the strengthening segment. The ECC demonstrated strain-hardening behavior, characterized by high post-cracking strength. The average cracking strengths for the ECC with 2% and 1% fiber volumetric ratios were 4.2 MPa and 2.2 MPa, respectively.

Table 5.1 Proportions of the ECC mixtures by weight ratio

Batch	Cement (kg/m³)	Silica fume (kg/m <sup>3</sup> )	Sea sand (kg/m³)	Water (kg/m <sup>3</sup> )	Superplasticizer (kg/m³)	PE (Vol.)
ECC-	1210	303	454	303	20.5	2%
Vf2.0	1210	303	13 1	303	20.3	270
ECC-	1210	303	454	202	20.5	10/
Vf1.0	1210	303	434	303	20.5	1%

Table 5.2 Properties of PE fibers

Length (mm)	Diameter (µm)	Tensile strength	Modulus (GPa)	Density
		(GPa)	Wodulus (Gra)	$(g/cm^3)$
12	24	3	116	0.97

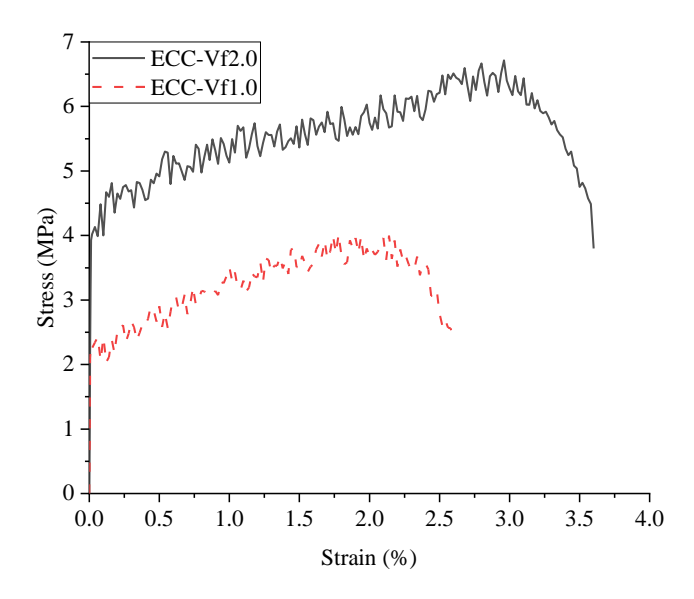


Fig. 5.1 Tensile stress-strain curves of ECC

GFRP rebars with two diameters (13.4 mm and 17.2 mm) were employed as the longitudinal reinforcement in the ECC beams. The tensile characteristics of the GFRP rebars were obtained through tensile testing methods in accordance with ASTM D7205/D7205M-06 (2016). The tensile strengths of the GFRP rebars of the two diameters were measured to be 971 and 946 MPa, respectively. The elastic moduli measured were 52 and 55 GPa, respectively. The ultimate strains of both types of rebars were larger than 1.83%. For ease of fabrication and given the chapter's emphasis on beam flexural properties, steel reinforcement is utilized as stirrups instead of FRP reinforcement. The stirrups with a diameter of 8 mm were spaced 12 cm apart.

#### 5.2.2 Specimen design and test setup

Eight rectangular UHPECC beams were fabricated and tested in the experimental program. The beams featured a clear length of 1800 mm and a cross-section measuring 200 mm by 160 mm. The shear span length is 610 mm. Fig. 5.2 illustrates the cross-sectional geometry and

reinforcement details. The steel stirrups were round steel rebars with a diameter of 8 mm. Steel stirrups, made from 8 mm diameter round rebars, were used with a longitudinal spacing of 120 mm. This arrangement was adopted to achieve a flexural failure mode for the beams according to theoretical analyses. Table 5.3 provides a detailed overview of the test matrix. The experimental parameters included the reinforcement ratio  $\rho$ , the fiber volumetric ratio  $V_f$ , and the loading types (monotonic, compression-compression cyclic or tension-compression cyclic). Each specimen was given the name S- $\rho$ x-Vy-z, where x represents the reinforcement ratio, y indicates the fiber volumetric ratio and z denotes the loading type. For example, S- $\rho$ 1.88-V2-M represents the specimen with a longitudinal reinforcement ratio of 1.88% and a fiber volumetric ratio of 2% under monotonic loading.

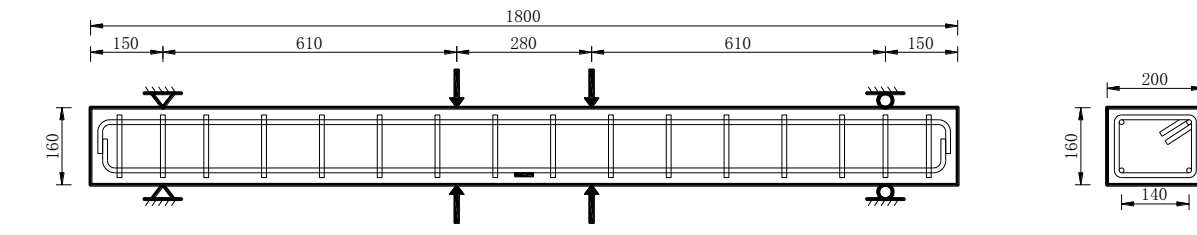


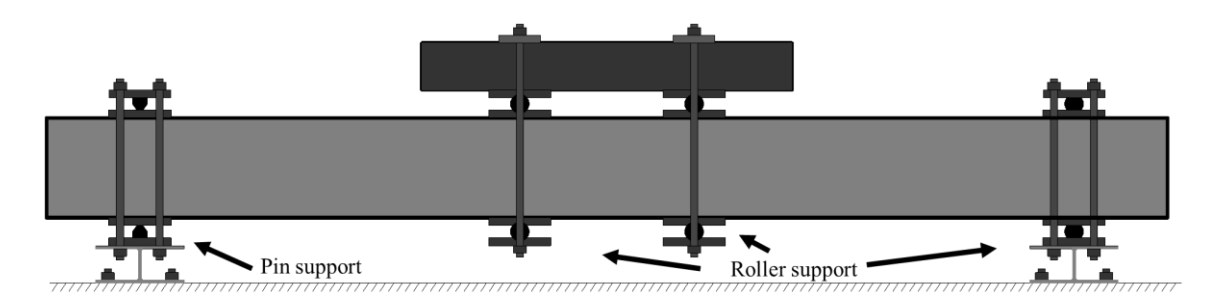
Fig. 5.2 Specimen details (unit: mm)



(a) Downward loading



(b) Upward loading



Details of cyclic loading device

Fig. 5.3 Test set up

Table 5.3 Test matrix

No.	Specimen	Reinforcement ratio	Fiber volumetric ratio (%)	Loading type
1	S-ρ1.88-V2- M			Monotonic
2	S-ρ1.88-V2- C1	1.88	2	Compression- compression cyclic
3	S-ρ1.88-V2- C2			Tension-compression cyclic
4	S-ρ1.13-V2- M	1.13	2	Monotonic
	<del>-</del>			

A customized loading device for applying the monotonic or cyclic loading on the beams was designed. As illustrated in Fig. 5.3, this loading device includes screws, supports, and a frame. At the loading point, two pairs of rotatable supports are arranged at the upper and lower sides of the test beam. These supports are fastened to the distribution beam using bolts and screws. Before the formal test loading, the height of the distribution beam is lowered until the monitored force sensor value reaches 1 kN, after which all bolts connecting the supports are tightened. Simply supported supports are arranged on both the upper and lower sides of the beam's ends. The upper supports are securely connected to the ground through screws, enabling them to provide reaction forces when upward loads are applied. The monotonic or cyclic loads were applied and recorded with a servo-controlled hydraulic actuator. The initial loading involved downward loads. All the tests were performed in a displacement control mode with a quasi-static loading rate set to 1 mm/min. According to FEMA 461 (2007), the cyclic loading scheme implemented in this present study is illustrated in Fig. 5.4. The tension-compression cyclic loading scheme contains two full loading cycles for each deformation amplitude. The deformation amplitude was 0.1% of the length of the shear span in the initial step and increased by 40% continuously afterward. The screws and supports for applying upward loading on the beams were removed when compression-compression cyclic or monotonic loading was conducted. The compression-compression cyclic loading scheme was similar to the tension-compression cyclic loading scheme but only applies downward cycles. During the unloading process, the actuator was not unloaded to the initial position but to a position with a load of about 1 kN to prevent the disengagement of supports under the distribution beams.

Three linear Variable Displacement Transducers (LVDTs) were positioned at the midspan and the supports to record the vertical deflections of each beam. Strain measurements were conducted using electrical resistance strain gauges attached to the bottom longitudinal FRP rebars. A data acquisition system recorded all the measurements, including strains, loads, and displacements. The development of cracks in the test ECC beams was monitored and the crack widths were measured with a handheld microscope.

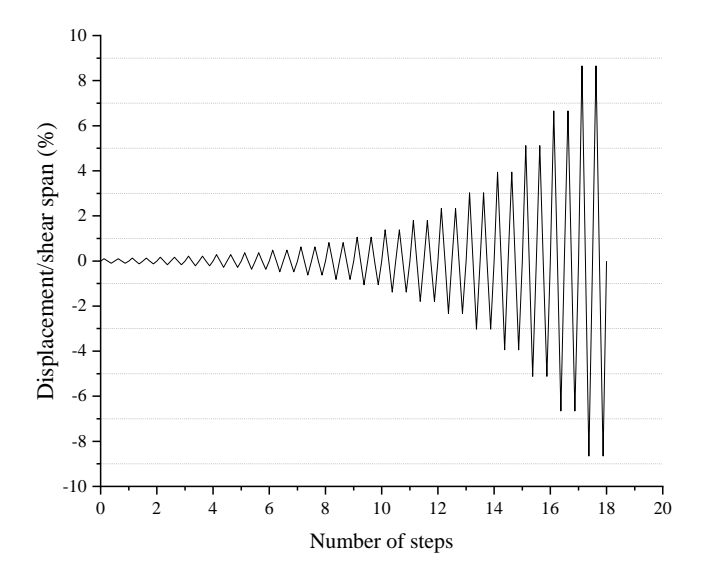


Fig. 5.4 Cyclic loading scheme

#### 5.3 EXPERIMENTAL RESULTS AND DISCUSSION

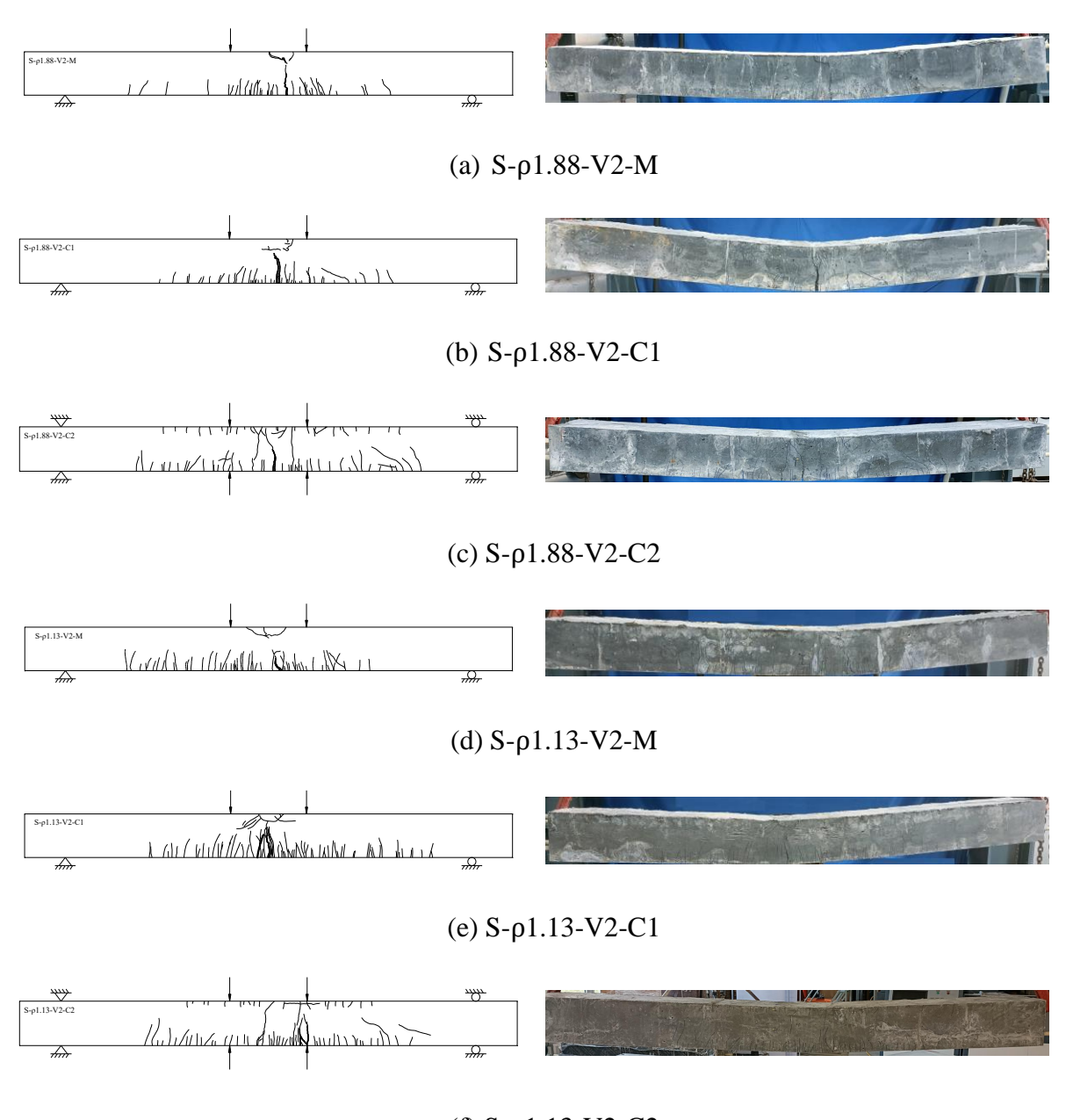
## 5.3.1 Crack patterns

Fig. 5.5 presents the crack patterns observed in all beams at the end of loading. Reinforced ECC beams exhibit a higher frequency of localized flexural cracks on the tensile side compared to traditional reinforced concrete beams, with the fibers demonstrating a positive effect by bridging these cracks. Upon the cracking moment, hairline flexural cracks first appeared near the bottom surface of the beam under either monotonic or cyclic loading conditions. When the cyclic amplitudes were relatively small, the cracks tended to be closed upon unloading indicating a good deformation recovery ability for the beam specimens. As the applied load increased, the flexural cracks extended deeper into the beam. A substantial number of cracks was noticeable on the beam surface in the pure bending zone. Most of the cracks were not further opened after they reached a certain width. The observation suggests that the tensile stress at the surface of each crack grows gradually to the hardening part of the stress-strain curve. For the specimens subject to compression-compression cyclic loading, to prevent loading supports under the distribution beam from being disengaged, the actuator did not return to its original position when the applied load was decreased to around zero, so cracks at the tension side could not be completely closed at the end of each cycle. For specimens under tension-compression cyclic loading, the cracks at the tension side could be closed upon the reversal of the load. However, as the loading amplitude increased, a larger reverse loading displacement was required to completely close the cracks on the tension side before the reversal of loading. This was primarily attributed to the occurrence of slips between FRP reinforcement and concrete. As the deflection increased, one or two major cracks developed with fibers being pullout. Thus, the deformation of longitudinal FRP reinforcement tended to be localized near the major cracks and rupture occurred once the local strains in the FRP reinforcement reached the ultimate tensile strain, accompanied by a sudden load drop.

The beams with larger reinforcement ratios exhibited greater load-carrying capacities, which in turn led to the emergence of larger tensile and shear stresses in ECC before failure. Consequently, this stress environment of concrete activated the generation of multiple cracks over a wider range of the specimen. Because of the multiple cracking patterns of ECC, the density of cracks tended to be unchanged with the same fiber volume ratio even when the reinforcement ratio differed. The specimens with a smaller fiber volume ratio exhibited more cracks compared to those with a larger fiber volume ratio, especially for the specimens exposed to cyclic loading. The discrepancy in crack numbers can be attributed to the distinct cracking strengths of concrete. An increased occurrence of cracks is notable at the tensile side of the specimens subjected to tension-compression cyclic loading. The reverse cyclic load caused the beam to elongate in the longitudinal direction, leading to the development of additional cracks on the tensile side. Crack localization occurred at the weakest plane with the stress concentration in the FRP reinforcement when the fiber-bridging capacity reached its ultimate state. One or few major localized cracks formed within the pure bending zone of the beams in this study.

Although all specimens failed by FRP reinforcement rupture, significant compressive damage of ECC occurred, despite the beneficial effect of fiber bridging in mitigating concrete spalling. For the specimens subjected to tension-compression cyclic loading, the compressive damage was relatively slight compared to that observed under monotonic or compression-compression cyclic loading. During the later cycles with substantial deflections, the longitudinal FRP

reinforcement sustained increased compressive forces, as indicated by the incomplete closure of flexural cracks under compression upon loading reversal. The slips between concrete and FRP reinforcement gradually accumulated as the reversal cyclic loading was processed. The unclosed cracks and accumulated slips allowed the beams to expand axially. This expansion was beneficial in delaying the concrete compressive damage under tension-compression cyclic loading.



(f) S-ρ1.13-V2-C2

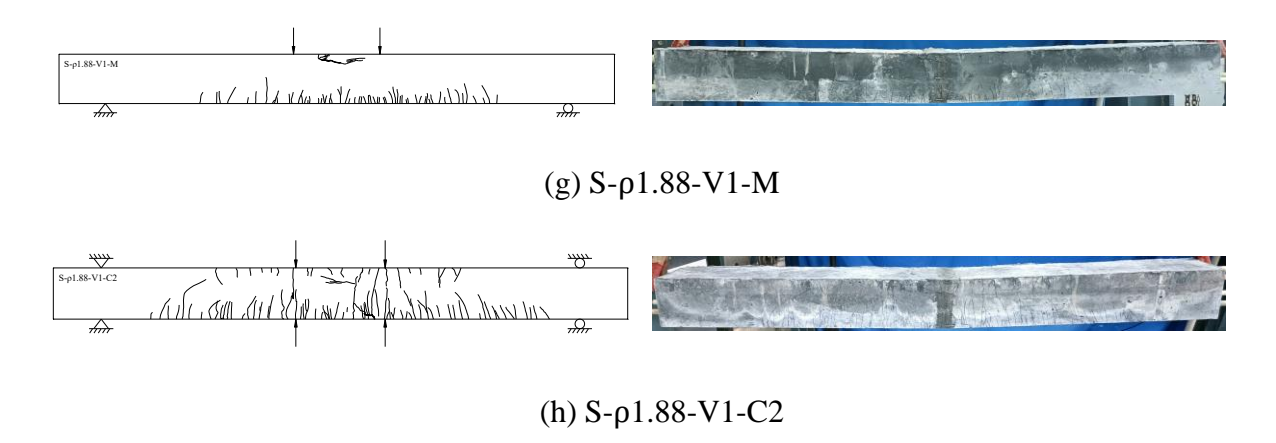


Fig. 5.5 Final crack patterns observed in various specimens

#### 5.3.2 Load-deflection curves

Fig. 5.6 compares the load-midspan deflection curves for specimens subjected to monotonic loading with different fiber volume ratios. It is evident that specimens without fibers exhibit significantly lower stiffness, loading capacity, and deformability compared to those with added fibers. It should be highlighted that beams without fibers fail mainly due to concrete crushing at the outer side of the loading support, whereas beams with fibers added all failed with FRP rupture. The addition of fibers effectively prevents concrete from splitting and helps maintain specimen integrity. Furthermore, it enhances the ultimate compressive strain of the concrete, allowing for the full utilization of FRP strength.

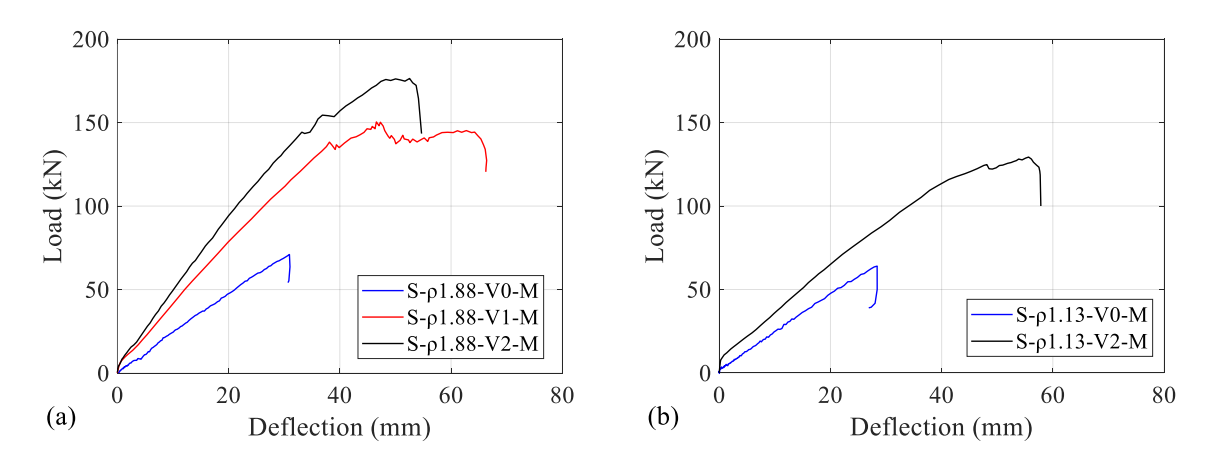
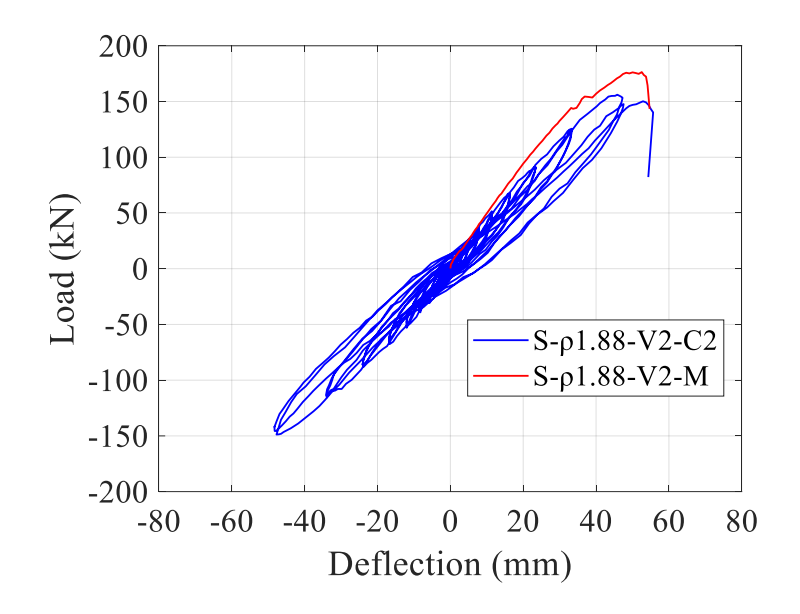


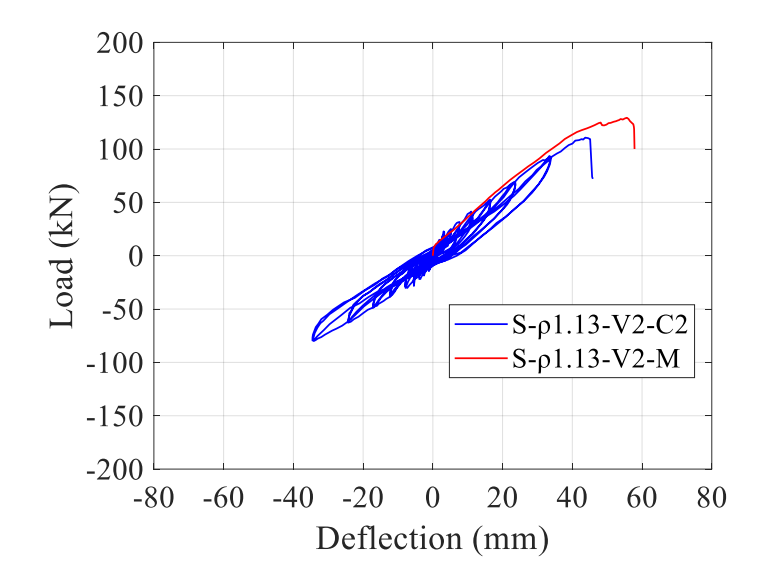
Fig. 5.6 Load-midspan deflection curves for specimens subjected to monotonic loading

Fig. 5.7 and Fig. 5.8 compare the load-midspan deflection curves for specimens subjected to cyclic loading with those subjected to monotonic loading. For all loading conditions, the loads and the deflections were defined to be positive when the beam was bent downwards (i.e., the actuator applied a compressive force).

The hysteretic curves of all specimens can be categorized into three stages: the elastic stage, the crack propagation stage, and the failure stage. Before concrete cracking, there was an approximately linear correlation between the applied load and the deflection. The hysteretic loop areas and residual deformation were relatively minor, and the beam's stiffness remained stable throughout the loading cycles. After concrete cracking, the beam's stiffness decreased and the hysteretic curves exhibited a nonlinear behavior with a decreased slope. The expansion of the hysteretic loops suggested a heightened capacity for energy dissipation. For each displacement amplitude, the cyclic loading was repeated twice. The load applied during the first cycle was typically greater than that applied in the second cycle for specimens subjected to both compression-compression and tension-compression cyclic loading, indicating a slight degradation in stiffness. For the failure stage, the stiffness degraded apparently and FRP rebars fractured with splitting sound until the peak load. For specimens subjected to compressioncompression cyclic loading, when the cyclic amplitude is relatively small, i.e. under 50% of the peak load, the cyclic effect is minimal, and the outer edge of the hysteresis curve closely follows the monotonic loading curve. However, as the loading amplitude increases, compression-compression cyclic loading results in a reduction of the specimen's loading capacity.

For conventional concrete beams, noticeable pinching was observed during the transition between compression and tension (Yuan et al. 2014). This can be attributed to two reasons: (1) poor integrity caused by concrete spalling and slip accumulation between reinforcement and concrete; (2) plastic strains after yielding of steel in tension which could not be recovered during compression, leading to the difference in the internal moment arms. The steel-reinforced concrete beams experienced significant stiffness decreases over a wide range both before and after loading reversal. In contrast, the decrease in stiffness for FRP-reinforced ECC beams is limited to a much smaller range, occurring only near the initial loading position. FRP rebars are linear elastic before rupture with an ultimate strain much larger than the steel yield strain. During the tension-compression transfer, tensile strains of FRP reinforcement returned to zero first, but the accumulated slips between FRP and concrete prevented the cracks that were about to be compressed from being fully closed. Then, until the loading displacement increases sufficiently to close the cracks on the compression side, the internal moment is solely sustained by the FRP reinforcement on both sides. The smaller arm length, i.e., the vertical spacing of the FRP bars, leads to decreased stiffness. After cracks in the compression zone were gradually closed, the cross-section stress was redistributed similar to that under monotonic loading, and the stiffness was restored. Furthermore, the inclusion of PE fibers ensured the integrity of the specimen and multiple cracks of ECC delayed the large localized slip of reinforcement.





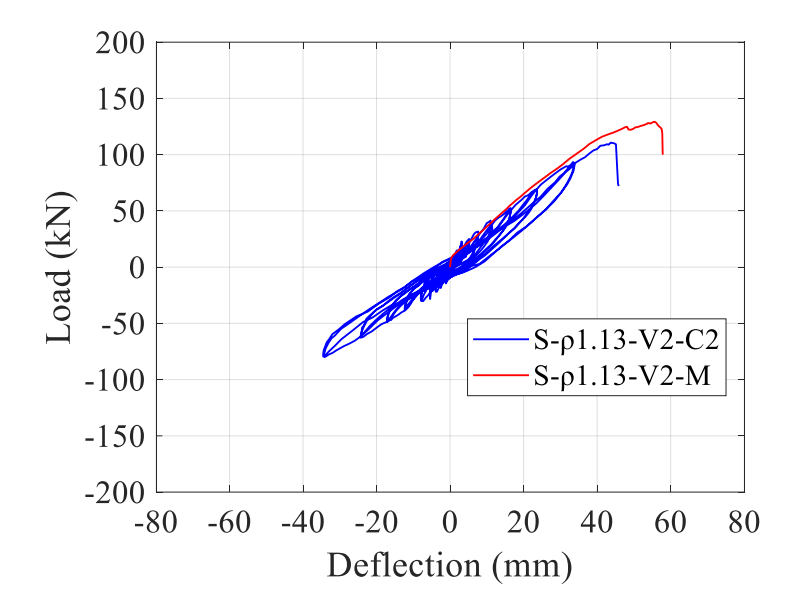


Fig. 5.7 Load versus midspan deflection curves for specimens subjected to tensioncompression cyclic loading

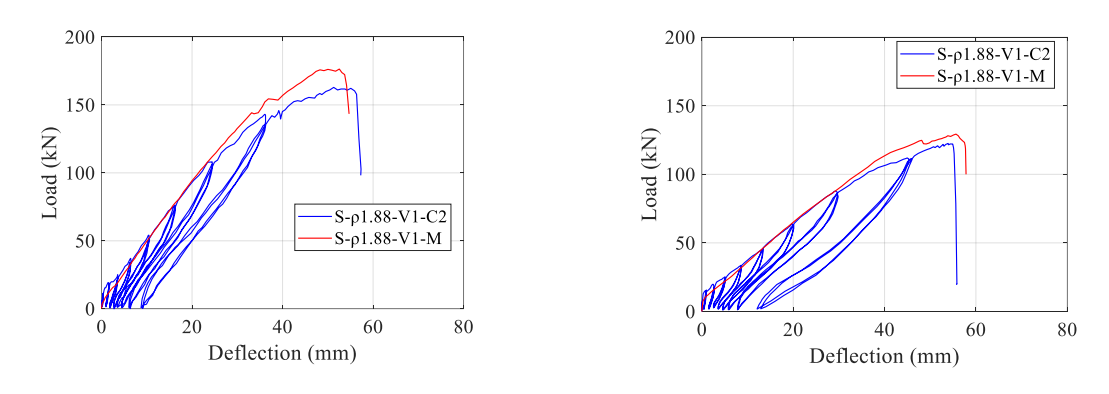


Fig. 5.8 Load versus midspan deflection curves for specimens subjected to compressioncompression cyclic loading

## 5.3.3 Skeleton curves and loading capacity

Fig. 5.9 compares the skeleton curves derived from the hysteretic curve envelopes of specimens under cyclic loading with those of specimens subjected to monotonic loading. Table 5.5. provides the values for the peak load and ultimate displacement at midspan.

For monotonically loaded specimens with the same FRP reinforcement ratio, a higher fiber volume ratio led to a larger loading capacity. The tensile strains of FRP rebars at failure were around 1.83%. The addition of PE fibers enhanced the tensile strain capacity of concrete, allowing it to sustain stress until the fracture of FRP. Concrete with different dosages possesses different tensile strain capacities as shown in Fig. 5.1. ECC with the fiber volume ratio of 2% had enough tensile strain capacity to maintain the fiber bridging capacity until the beam's failure. In contrast, concrete with a fiber volume ratio of 1% did not possess adequate tensile strain capacity to persist through to the beam's failure stage. Several main cracks went fully opened resulting in the fiber-birding capacity being exhausted. The estimated peak load without considering the tensile contribution of concrete is closer to the measured value of specimen S-ρ1.88-V1-M. However, for specimens with a fiber volume ratio of 2%, the estimated peak loads considering concrete tensile contribution closely match the experimental values.

As expected, the specimens with a lower reinforcement ratio possessed a lower peak load because of a smaller flexural sectional capacity. The drift capacities, which are the ratio of midspan deflection to shear span length, were comparable across specimens with varying reinforcement and fiber volume ratios. This similarity is attributed to the failure being controlled by the fracture of tensile FRP rebars, which shared similar ultimate strains. The addition of PE fibers made multiple localized cracks evenly distributed along the flexural tensile side leading to a complete utilization of the elongation of FRP rebar. Although the tensile strain capacity of ECC with 1% fiber volume ratio is limited compared to a 2% fiber volume ratio, it allows the cracks to develop sufficiently dispersed before the FRP fracture.

The strength envelops of specimens subjected to cyclic loading display differences compared to those subjected to monotonic loading. For example, in specimens with a fiber content of 2%, those subjected to cyclic loading demonstrated reduced strength compared to their counterparts subjected to monotonic loading. One contributing factor to this discrepancy is the damage inflicted on the fiber bridging effect by cyclic loading. Additionally, cyclic loading may lead to larger accumulated slips between concrete and FRP bars, resulting in more severe strength deterioration for the same loading displacement. The concrete offers less tensile force at the failure stage compared with monotonic loading. The strength envelope of specimens subjected to tension-compression cyclic loading exhibits a more significant reduction compared to those subjected to compression-compression cyclic loading. However, for specimens with a fiber volume ratio of 1%, the tensile strain capacity of concrete is close to the ultimate strain of FRP bars. The fiber bridging effect failed for both loading conditions at the final stage; thus, only the concrete in the compressive zone and FRP reinforcements were working and the peak loads of cyclic loading and monotonic loading were similar.

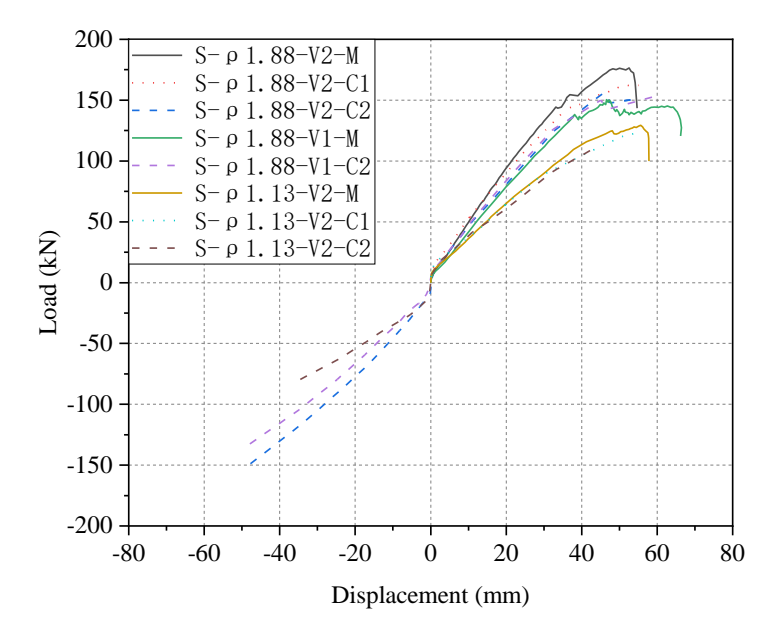


Fig. 5.9 Skeleton load-deflection curves of specimens

## **5.3.4 Energy dissipation**

The energy dissipation is determined by calculating the area enclosed within the load-deflection curve for each cycle, as shown in Fig. 5.10. Note that for each displacement amplitude, the average energy of two cycles was adopted. Fig. 5.11 illustrates the cumulative dissipated energy of the beam specimens under tension-compression cyclic loading. In the early stages of loading, a higher fiber volume ratio leads to greater energy dissipation, mainly attributed to fiber pull-out or fracture. However, the variation in energy dissipation among specimens of different fiber volume ratios is relatively small, suggesting that the dominant contributors to energy dissipation are the FRP reinforcement and compressed concrete. As expected, a higher FRP reinforcement ratio result in a greater capacity for final energy dissipation. Overall, FRP-reinforced concrete specimens exhibit lower energy dissipation capacities than steel-reinforced concrete specimens, due to the brittle characteristic of FRP reinforcement. The addition of fibers can enhance energy dissipation to a certain extent. However, further increases in the specimen's total energy dissipation capacity depend on increasing the diameter of the FRP reinforcement.

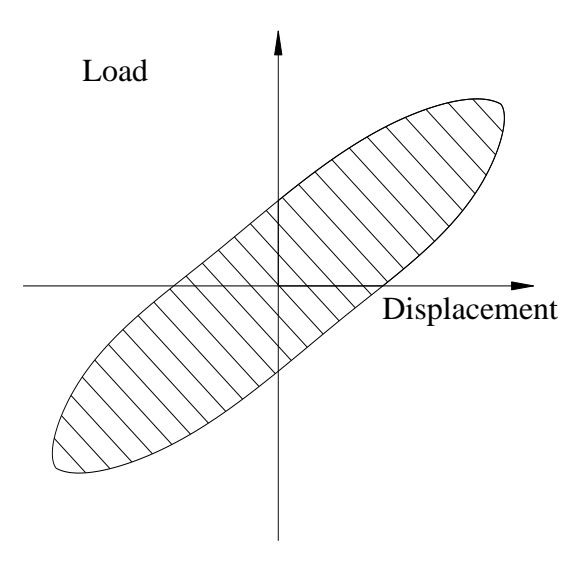


Fig. 5.10 Calculation of energy dissipation

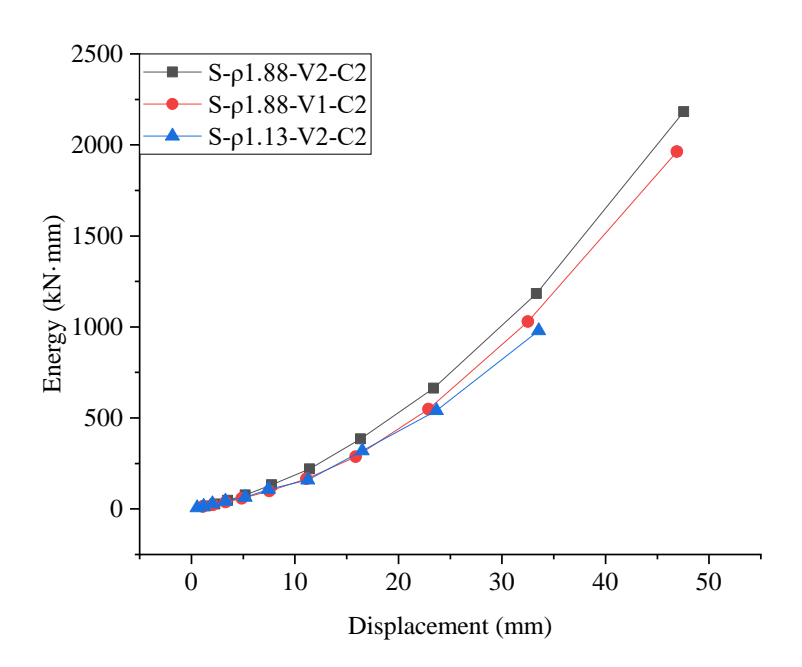


Fig. 5.11 Accumulated energy dissipations of specimens subjected to tension-compression cyclic loading

# 5.3.5 Deformation capacity

The ductility characterizes the deformation ability of a structure, which is a crucial criterion to assess the safety of the structure. A structure's ductility is influenced by the properties of the materials used. Unlike steel, FRP is a typical brittle material. FRP-reinforced structures generally exhibit lower ductility compared to those reinforced with steel. Thus, the commonly adopted ductility index for steel-reinforced concrete structures might not be suitable for FRP-reinforced concrete structures. Instead of using ductility, researchers often use the term deformability to describe the deformation capacity of structures reinforced with FRP. However, there remains a lack of consensus on the methods for quantifying and assessing the deformability of concrete structures reinforced with FRP. Various approaches for analyzing deformation capacity have been proposed in the open literature, including deflection-based

methods (Fischer and Li 2002a; Shao and Billington 2021), moment and deformation-based methods (Hung and Chueh 2016; Au and Du 2008), and energy-based methods (Abdelrahman et al. 1995; Rashid et al. 2005).

Considering the accuracy of various methods reported in the above literature, the authors believe that the energy-based method is preferable for examining the beam's deformation capacity in this study.

The energy-based approach for structural ductility was first introduced by Naaman and Jeong (1995), in which the ductility factor is calculated as follows:

$$\mu_N = \frac{E_t/E_{el} + 1}{2} \tag{5-1}$$

where  $\mu_N$  is the ductility factor; the total energy  $E_t$  consists of the elastic energy  $E_{el}$  and the plastic energy  $E_{pl}$ . The energy can be calculated as the area enclosed by a load-deflection curve as illustrated in Fig. 5.12. For the cyclically loaded specimens, the energies in Eq. (5-1) were calculated based on the loading envelope of the hysteretic curves.

Regarding the unloading stiffness, the slope S used to assess the elastic energy is defined as an equivalent unloading slope for all specimens. The calculation formula adopted from Naaman and Jeong (1995) is expressed in the following Eq.(5-2), in which  $S_1$  and  $S_2$  represent the slopes of the first two linear branches, respectively, as shown in Fig. 5.12;  $P_1$  and  $P_2$  are the corresponding loads at the inflection point.

$$s = \frac{P_1 S_1 + \left(P_1 - P_2\right) S_2}{P_2} \tag{5-2}$$

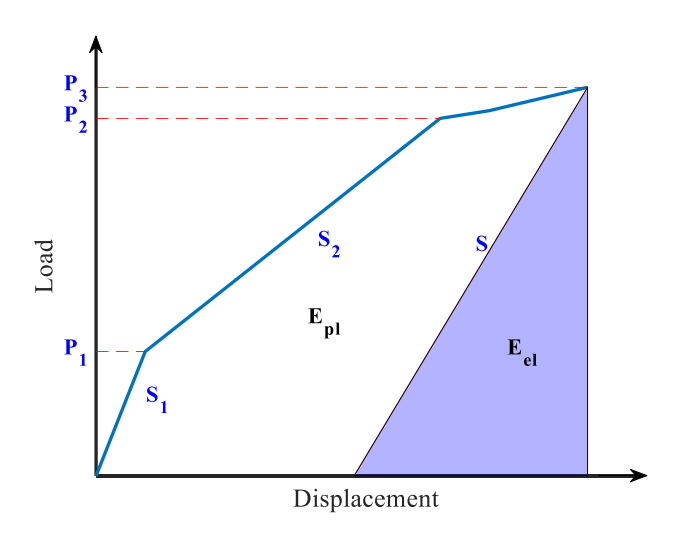


Fig. 5.12 Schematic diagram for energy calculation

Table 5.4 Deformation capacity of the test beams

No.	Specimen	$\mu_N$	
1	S-ρ1.88-V2-M	1.51	
2	S-p1.88-V2-C1	1.39	
3	S-p1.88-V2-C2	1.18	
4	S-ρ1.13-V2-M	1.91	
5	S-ρ1.13-V2-C1	1.16	
6	S-p1.13-V2-C2	1.13	
7	S-p1.88-V1-M	1.63	
8	S-p1.88-V1-C2	1.17	

The calculated deformation capacity indexes  $(\mu_N)$  for the test specimens are compared in Table 5.4. For specimens experienced cyclic loading, the deformation capacity is effectively captured by  $\mu_N$  because the elastic energy was obtained based on the unloading stiffness. For specimens subjected to monotonic loading, due to the uncertainty of the cracking load, there will be some variability in the equivalent unloading stiffness S and deformation capacity index  $\mu_N$ . In

general, the test beams demonstrate a certain level of deformation capacity, but it is still less than that of properly designed steel-reinforced concrete members which typically possess a deformation capacity index around 4 or 5. This suggests that while adding fibers increased the ductility of the concrete, it did not necessarily enhance the beams' flexural deformation capacity at the structural level. Table 4 also indicates that cyclic loading reduced the deformation capacity of the beams significantly. To enhance the beam's deformation capacity, approaches such as increasing the reinforcing ratio or reducing the thickness of the protective layer can be employed to shift the failure mode to compressive concrete crushing, which can make greater use of the compressive plastic strain of the ECC.

#### 5.3.6 Strain development in FRP reinforcement

The strain development in the bottom FRP reinforcement of tension-compression cyclic specimens with the increase of deflection is shown in Fig. 5.13. Tensile strains are considered positive, whereas compressive strains are regarded as negative. For specimens subjected to reversed cyclic loading, the bottom reinforcement also endures tensile stress during the load reversal when the loading amplitude is large enough, indicating a small height of the compression zone. The strains of FRP rebars developed approximately linearly with the deflection until failure for all loading conditions. The excellent deformation compatibility between ECC and FRP reinforcement ensured that the strain capacity of FRP reinforcement could be fully utilized. Observations indicate that, with a constant fiber volume ratio, a higher reinforcing ratio leads to a slower accumulation of strain in the FRP reinforcement. Similarly, when holding the reinforcing ratio constant, decreasing the fiber volume ratio from 2% to 1% results in a higher rate of increase in reinforcement strain.

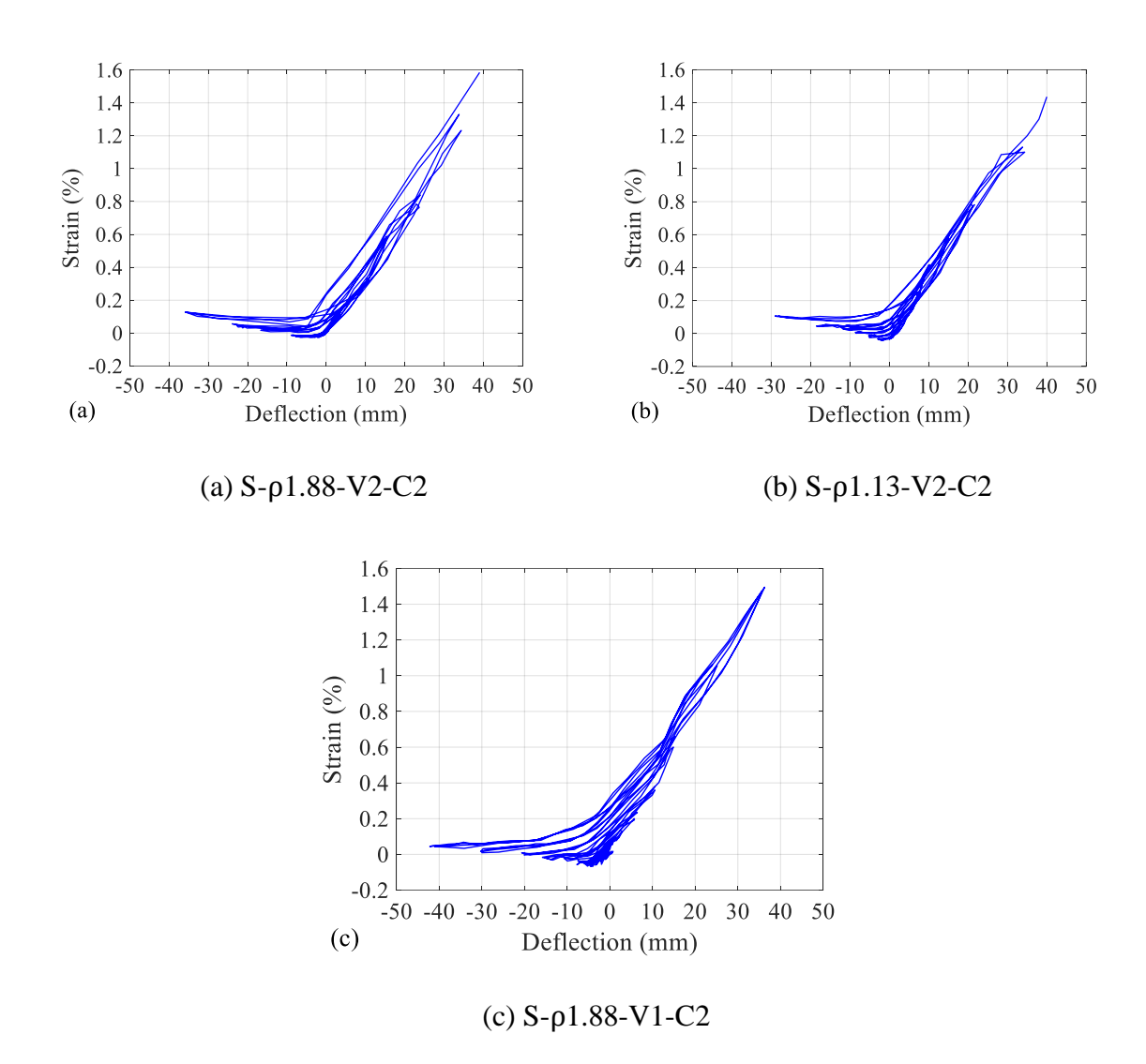


Fig. 5.13 Development of strains in FRP reinforcement with the deflection: a) S- $\rho$ 1.88-V2-

# **5.4 THEORETICAL ANALYSES**

# **5.4.1 Prediction of strength**

To better understand the strength provided by the fiber bridging effect in ECC, a theoretical analysis based on the section analysis was performed to estimate the beam's strength. The strength (i.e., peak load) of the beam may be controlled by the compressive strength of the concrete, the tensile strength of the concrete, and the strength of the FRP reinforcement. Cyclic

loading has been found to have minimal impact on the concrete compressive behavior before softening (Jaeger et al. 1997). Therefore, concrete compressive behavior was not expected to affect the peak load for either monotonic or cyclic loading in the current test. Since cyclic loading also has minimal impact on the FRP bars' strength. The reduction of peak loads resulted from lowered ECC tensile capacity induced by cyclic loading or low fiber volume ratio. For the specimens that failed with the fiber bridging effect maintained to the failure stage, i.e., specimens with the 2% fiber volume ratio under monotonic loading, the fiber bridging effect is included within the whole tension zone as shown in Fig. 5.14a. For cases of fiber bridging damage, the tension force was provided by FRP rebars only as Fig. 5.14b. By using ECC tensile strength derived from the material properties test in Table 5.1, the predicted value for monotonic loading and tension-compression cyclic loading specimens are also shown in Table 5.5. For monotonic loading specimens, as long as an appropriate stress distribution is selected, the peak load can be predicted with a mean absolute error of only 1.1%. For cyclic loading specimens, The theoretical value based on Fig. 5.14a suggests that the fiber bridging effect remains valid before failure, while those based on Fig. 5.14b indicate complete failure of the fiber bridging effect. However, the test value falls between these two extremes, indicating partial damage to the fiber bridging. Determining the extent of fiber damage is a challenging task that warrants further research.

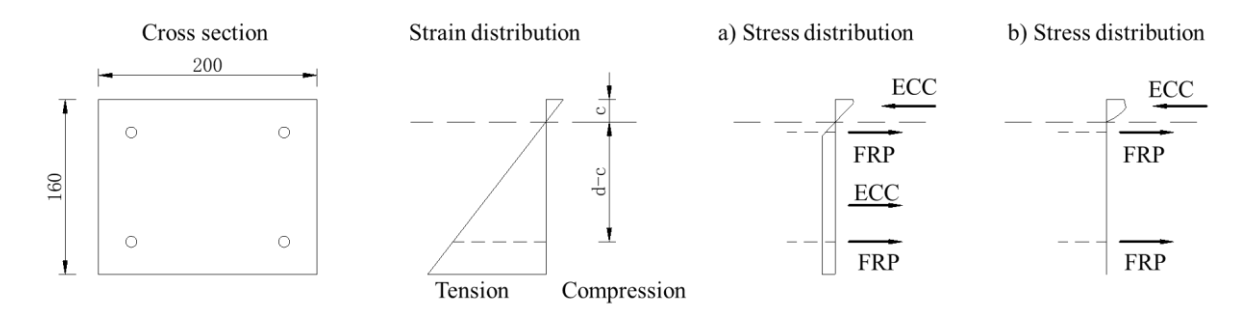


Fig. 5.14 Strength prediction method for a) specimens failed with fiber bridging maintained,
b) specimens failed after fiber bridging damaged

Table 5.5 Summary of test results and estimated load

	Peak load (kN)		Failure	Estimated	Assumed peak
Specimen	Positive	Negative	displacement at midspan (mm)	peak load (kN)	stress distribution
S-ρ1.88- V2-M	176.4	-	54.7	174.6	Fig. 5.14 a)
S-ρ1.88- V2-C1	162.9	-	57.3	-	
S-ρ1.88- V2-C2	156.1	-148.8	55.7	147.7	Fig. 5.14 b)
S-ρ1.13- V2-M	129.3	-	57.8	130.1	Fig. 5.14 a)
S-ρ1.13- V2-C1	122.5	-	55.9	-	
S-ρ1.13- V2-C2	110.7	-80.0	45.9	101.0	Fig. 5.14 b)
S-ρ1.88- V1-M	150.4	-	66.4	147.7	Fig. 5.14 b)
S-ρ1.88- V1-C2	152.1	-132.5	61.4	147.7	Fig. 5.14 b)

## 5.4.2 Strength difference under two loading directions

Beams under tension-compression cyclic were loaded in two directions. The strength envelops of positive loading, i.e., actuator applied compressive force, are larger than that of negative loading. This difference started after cracking and was maintained till to the end of the test. One potential reason for this variation could be the fiber orientation. Many researchers have reported that the casting process plays a crucial role in determining the fiber orientation in ECC (Zhou and Uchida 2017; Oesch et al. 2018). The fiber direction is more likely distributed along

the direction of concrete casting flow, resulting in more fibers distributed parallel to the longitudinal reinforcement at the bottom of the beam. And the fibers at the top of the beam were more randomly dispersed. Therefore, the ECC at the bottom of the beam may exhibit greater tensile strength in the longitudinal direction compared to the top. When a compressive positive load is applied, tensile cracks on the underside of the beam are effectively bridged by the parallel fibers, while this effect is relatively weak at the top side. For the same loading amplitude after cracking, the loading capacity difference between positive and negative is comparable, as illustrated in Fig. 5.15. Since the FRP reinforcements at both the top and bottom are identical, the peak load difference in positive and negative directions was mainly attributed to the ECC tensile strength difference. The reversal cyclic-induced damage was more severe than that of compression-compression cyclic. Similar results were observed for beams with steel fibers added under reversal cyclic loading (Shao and Billington 2020). Concrete with PE fiber added also exhibited a significant reduction in tensile strength. When cracks are open, PE fibers and steel fibers are pulled and slip is inevitable. While cracks are closed in compression, steel fibers, and PE fibers exhibit different damage mechanisms. Steel fibers cannot retract and some of the fibers suffer localized buckling. Additionally, it is believed that low-cycle fatigue contributes to the damage of the steel fibers (Kesner et al. 2003). In contrast, PE fibers are flexible which eliminates the buckling problem, and possess high fatigue resistance (Huang et al. 2019b). The reduction of tensile strength comes from accumulative slip between PE fibers and concrete, especially for the later stage with a larger crack width.

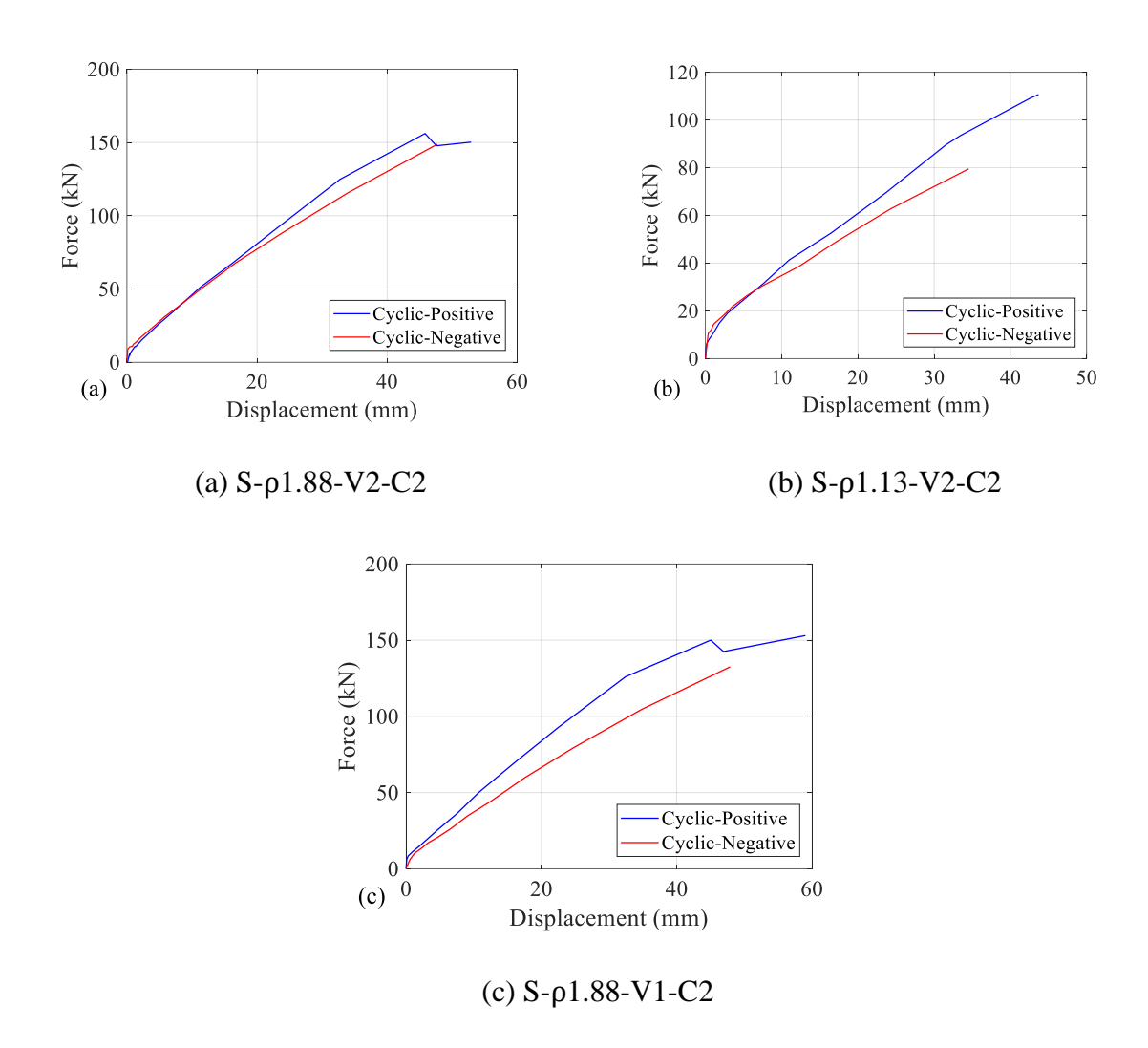


Fig. 5.15 Strength envelop compare of (a) S- $\rho$ 1.88-V2-C2, (b) S- $\rho$ 1.13-V2-C2, (c) S- $\rho$ 1.88-V1-C2

# **5.5 CONCLUSIONS**

This study investigates the flexural performance of FRP-reinforced UHPECC beams, focusing on varying reinforcement ratios and fiber volumes under different loading types. Beams were cyclically and monotonically tested. The test results showed that beams with PE fiber added under monotonic and cyclic loading both exhibited ample deformation capacity before failure. The failure mode observed in the FRP-reinforced UHPECC beams was dominated by the fracture of longitudinal FRP rebar. The conclusions drawn from this study are as follows:

- 1) The material properties of UHPECC were translated into multiple cracking and evenly distributed slip between FRP and concrete. A higher reinforcing ratio and/or a lower fiber volume ratio results in more localized cracks and a larger elongation of the whole FRP rebar, ensuring appropriate moment and force redistribution among the flexural members. Therefore, the development of concentrating strain at localized concrete main cracks and FRP fracture can be delayed, and the drift capacity increases.
- 2) For beams under the same loading conditions, more localized cracks were observed as the increasing of reinforcing ratio and the decreasing of fiber volume ratio. Since the slip between FRP rebars and concrete is restrained within the area surrounding each localized crack, a higher number of localized cracks suggests a greater extent of slip.
- 3) Repeated opening and closing of cracks under both compression-compression and tension-compression cyclic loading impair the fiber bridging capability and reduce the tensile strength of UHPECC, resulting in a lower failure strength compared to beams subjected to monotonic loading.
- 4) The test investigates the flexural behavior of the beam under different loading directions.

  The same beam exhibits lower strength under negative loading compared to positive loading. This difference arises from the casting process of concrete flow which leads to different fiber direction distribution at the beam's top and bottom.
- 5) Slip between concrete and FRP accumulates under cyclic loading. Not all flexural cracks can be completely closed in the compression zone, and the FRP reinforcement endures more compression force relative to the monotonic loading specimen at failure, thus reducing the actual effective height of the beam and lowering the failure load.

In summary, the flexural members of ECC reinforced with FRP rebars effectively improve its performance by enhancing loading strength, ductility, self-centering capacity, and energy dissipation capacity. This study thus illustrates the practicality of employing FRP-reinforced UHPECC beams when subjected to cyclic loading. Given that the tensile strength of ECC and its structural performance are influenced by the flow of the casting and the distribution of fiber direction, more studies are advised to explore casting methods that can be useable for targeted applications and its impact on structural performance.

# CHAPTER 6 EXPERIMENTAL INVESTIGATION ON GFRP-REINFORCED UHPECC BEAMS SUBJECTED TO VARIOUS CYCLIC DEFORMATION HISTORIES

## 6.1 INTRODUCTION

The deterioration of infrastructure caused by steel corrosion has emerged as a significant global challenge (Peng and Xue 2018). To address this challenge, the incorporation of FRP in civil and marine structures has shown to be an effective approach thanks to its outstanding resistance to corrosion, superior strength, and lightweight. These advantages have sparked growing research interest among civil engineering researchers worldwide (Guo et al. 2018; Zeng et al. 2021). Replacing steel reinforcement with GFRP in concrete structures has emerged as a significant area of development (Lau and Pam 2010; Aiello and Ombres 2000). Although GFRP bars can effectively eliminate corrosion issues and provide excellent durability (Guo et al. 2018), their elastic modulus is considerably lower compared to that of steel bars. This disparity in modulus results in reduced structural serviceability performance, and their linear stress-strain behavior results in a brittle failure (Chaallal and Benmokrane 1996).

In recent decades, various methods have been suggested by researchers to improve the performance of concrete beams reinforced with FRP. These involve using FRP jackets to wrap plastic hinge areas, combining FRP reinforcements with steel reinforcements in concrete beams, developing steel-fiber composite bars, employing ductile mechanisms, and adding fibers into concrete (Xiao et al. 2021; Wang and Belarbi 2011; Walker and Karbhari 2007; Chellapandian et al. 2020; Qu et al. 2009). While each aforementioned methods has its advantages and is suited to specific application scenarios, the authors consider adding fibers into concrete

particularly advantageous for both construction convenience and corrosion resistance. ECC offers exceptional toughness and ductility due to the incorporation of polymeric fibers, typically at a volume fraction of 2% (Maalej and Li 1995). When subjected to tension, ECC demonstrates multiple crack patterns and strain-hardening behavior. Its ultimate tensile strain can vary between 0.25% and 5%, depending on factors like the material's size, shape, and mix design (Lepech and Li 2009; Huang et al. 2020; Kanda and Li 1999). Taking these advantages, ECC has been introduced into FRP-reinforced components to improve their structural behavior. Due to its superior deformation ability, ECC effectively minimizes relative slip and bond stress between itself and FRP reinforcement (Fischer and Li 2003). Additionally, the inclusion of fibers helps prevent concrete surface spalling and improves the ultimate compressive strain, thereby better utilizing the reinforcement's tensile strength (Wang and Belarbi 2011; Maalej and Leong 2005). Through appropriate design, structural members composed of ECC reinforced with FRP bars can achieve notable enhancements in loading capacity, ductility, and durability.

Several studies have previously studied the static behavior of FRP-reinforced concrete members. However, there was comparatively less study on their cyclic behavior. Fischer and Li (2003) examined the cyclic performance of FRP-reinforced normal strength ECC columns. Peng et al. (2023) carried out tests on normal-strength concrete beams reinforced with polypropylene fibers, prestressed CFRP tendons, and nonprestressed steel bars to evaluate their cyclic behavior. In the previous studies on cyclic behavior, the applied deformation typically follows recommendations outlined in codes. This involves starting with a small amplitude, repeating for one to three cycles, and then gradually increasing the amplitude step by step until either specimen failure occurs or the test value reaches the target value. However, to the

author's knowledge, the influence of deformation history on FRP-reinforced UHPECC structural members remains unclear owing to the scarcity of accessible test data. Although the study on the impact of loading history on steel-reinforced beams is also very limited, those available results suggest that this influence cannot be ignored. Lignos et al. (2014) discovered that the cracking pattern of high-performance fiber-reinforced cement-based composite, under recorded ground motion records, differs notably from that under a gradually increasing deformation history. Frank et al. (2018) tested steel-reinforced ECC beams under different deformation histories, revealing that the deformation history has a wide range of effects on the ductility, cracking pattern, strain accumulation in steel reinforcement, and damage of the fibers.

This study aims to explore how the response of UHPECC beams reinforced with FRP varies with different reinforcement ratios when exposed to various deformation histories. The reinforcement ratio is chosen as a variable because it greatly influences the tensile strain experienced by the beam. As the reinforcement ratio decreases, the tensile strain increases at a given curvature. This increase in tensile strain is expected to cause fiber pull out or rupture within the ECC, which will contribute to the growth of cracks. The accumulation of tensile strain and crack localization in ECC subsequently induces strain localization in the reinforcement. Previous studies have suggested that a decrease in the reinforcement ratio leads to fewer flexural cracks, regardless of whether FRP or steel reinforcement is used. The absence of distributed cracks in reinforced ECC beams with relatively low reinforcement ratios suggests that tensile stress in the fibers will be concentrated in the reinforcement. The effectiveness of fibers will significantly influence the cyclic performance of the beams. The deformation history can be another key factor influencing crack development and fiber effectiveness. Beams experiencing large deformations at earlier stages present challenges in determining the state of

fibers. They may either fail completely due to pull-out or rupture, or they may remain in the strengthen section of the ECC stress-strain curve, influenced by the combined effects of reinforcement ratio and applied deformation amplitude. Conversely, beams with small deformations at an earlier stage are expected to maintain their fibers, gradually experiencing pulling as the applied deformation amplitude increases.

To address this, this study details an experimental investigation into the cyclic behavior of FRP-reinforced UHPECC beams, examining different reinforcement ratios and deformation histories. Beams with different parameters were designed and tested, examining crack development, load-displacement behavior, strain evolution, deformability, and energy absorption capacity. This research will enhance the understanding of the impact of loading history on the cyclic performance of FRP-reinforced UHPECC beams, thereby expanding the potential applications of both FRP reinforcement and UHPECC.

# **6.2 EXPERIMENTAL PROGRAM**

## **6.2.1 Specimen geometry**

Eight UHPECC beams reinforced with GFRP reinforcements were tested. The naming convention for each specimen shown in Table 6.1 includes information about the specimen number, the reinforcement ratio, and the applied history. For example, S1-ρ1.88-F represents the first specimen with a reinforcement ratio of 1.88%, following the loading protocol outlined in FEMA 461 (2007). The mechanisms of various loading protocols will be detailed in a subsequent section. The specimen's geometry is illustrated in Fig. 6.1. The flexural cross-sectional dimensions are 200×160 mm, and the total length of the beam is 1800 mm. The beams were tested under four-point bending cyclic loading, with a shear span of 610 mm. Symmetrical

reinforcement was implemented by placing two longitudinal GFRP bars on each side of the cross-section. GFRP reinforcements with diameters of 13.4 mm and 17.2 mm were adopted, representing two different reinforcement ratios. The upper and lower longitudinal reinforcement is arranged symmetrically in the same manner to withstand cyclic loads. Steel stirrups with an 8 mm diameter were spaced at 120 mm intervals along the entire length of the beam.

Table 6.1 Tested specimens

Specimen name	Reinforcement ratio	Bar diameter	Deformation history	
Specimen name	(%)	Dar diameter	Deformation instory	
S1-ρ1.88-F	1.88	16	FEMA 461	
S2-ρ1.88-SP	1.88	16	Small pulse	
S3-p1.88-LP	1.88	16	Large pulse	
S4-ρ1.88-LP	1.88	16	Large pulse	
S5-ρ1.13-F	1.13	13	FEMA 461	
S6-ρ1.13-SP	1.13	13	Small pulse	
S7-ρ1.13-LP	1.13	13	Large pulse	
S8-ρ1.13-LP	1.13	13	Large pulse	

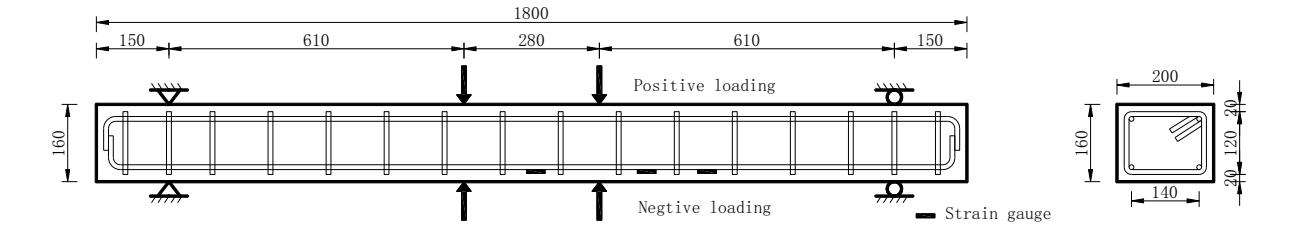


Fig. 6.1 Details of the specimens (unit: mm)

#### **6.2.2** Materials

The mixture proportions for the UHPECC are consistent with those used in previous chapters.

To accommodate the high-strength matrix, the PE fiber was added to the concrete with a fiber

volume content of 2%. All PE fibers had a diameter of 24 µm and a length of 12 mm. The ECC was mixed in a mortar mixer. After mixing the dry powders and water into a mortar with sufficient fluidity, gradually incorporate PE fibers while continuing to mix. The ECC poured into wooden forms possesses a mini-slump flow of 180 mm based on ASTM C1437-15 (2015). The specimens were cured under plastic sheets with moisture for up to 28 days prior to testing.

The UPHECC achieved a mean compressive strength of 132.6 MPa based on tests conducted on 50-mm cubes (ASTM C109/C109M-16a 2016). The tensile strength of UHPECC was determined through a direct tensile test following the recommendation provided by JSCE (2008). The cracking strength, identified as the point at which the curve shifts from the initial linear region to the segment where strengthening occurs, averages 4.2 MPa. The UHPECC demonstrates strong post-cracking strength, with an ultimate strain of up to 3%.

The properties of longitudinal GFRP reinforced were tested according to ASTM D7205/D7205M-06 (2016). The yield strengths of GFRP bars were 971 MPa for a diameter of 13.4 mm and 946 MPa for a diameter of 17.2 mm, respectively. The elastic modulus is larger than 52 GPa, while the ultimate strain exceeds 1.83%.

## **6.2.3** Test setup and instrumentation

Four-point bending tests were performed on each specimen, with the test setup illustrated in Fig. 6.2. During testing, two sides of the beam were tightly secured to a steel wide-flange section, which was firmly attached to the reaction frame floor with bolts. Rotatable supports were positioned on both the top and bottom ends of each side of the beam. A similar arrangement was employed in the loading points for the pure bending area, with all supports

fixed onto the red distribution beam. The distribution beam was bolted to the actuator and then fixed on the reaction frame. Additionally, the actuator was equipped with a load sensor, and electrical resistance strain gauges were affixed on the reinforcements in the pure bending area. Displacements at midspan and two side supports were recorded using Linear Variable Displacement Transducers (LVDTs). An automatic data acquisition system was used to capture and monitor all these signals simultaneously. The actuator's orientation changed slightly throughout the test due to the beam's up-and-down movement with each cycle. A spherical joint was used to maintain the load's perpendicular alignment with the distribution beam. This system can effectively perform cyclic loading on beams. Initially, vertical downward loads were applied, and all specimens were loaded to failure. All tests were performed under displacement-controlled conditions at a rate of 1 mm/min. Periodically, the tests were intermittently halted to inspect cracks, take photographs, and gather data.

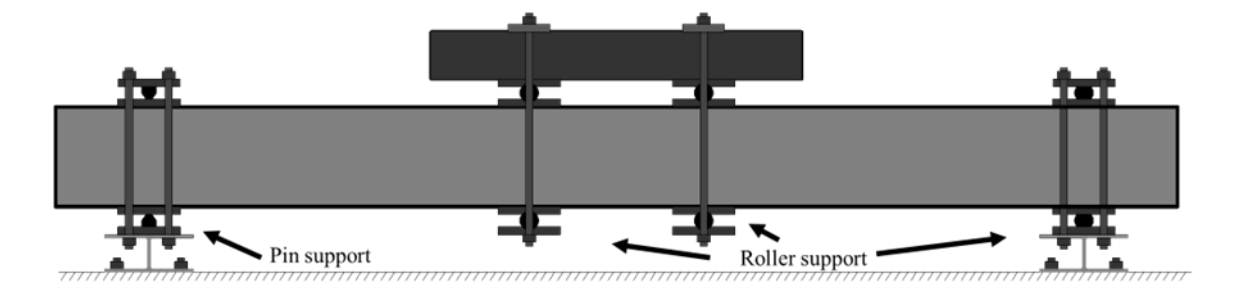


Fig. 6.2 Test set up

## **6.2.4** Applied deformation histories

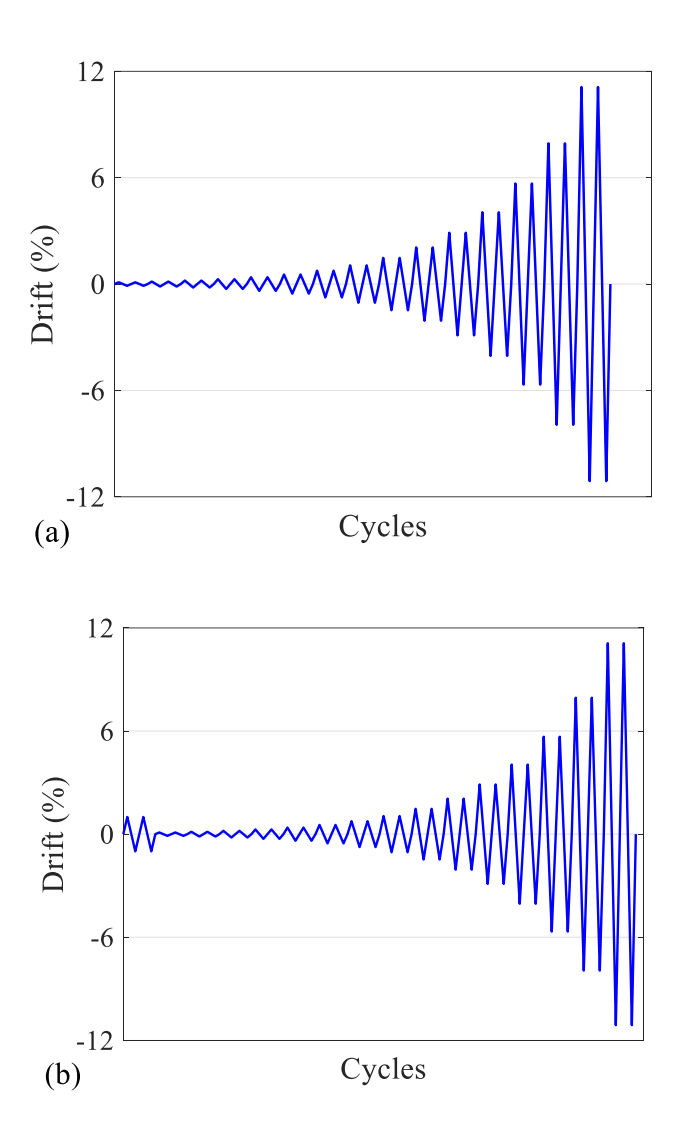
The main goal of this study is to explore the effects of loading history. Therefore, the determination of the loading protocol is crucial. As for basic reference specimens, loading protocol as per FEMA 461 recommendations (2007) was adopted, which will be referred to as the FEMA deformation history from this point forward. The FEMA deformation history consists of two complete repeat cycles in each step, with each cycle's amplitude being 40%

greater than that of the preceding one. The amplitude of the first cycle was set to 0.1% of the shear span length. One specimen with each reinforcement ratio was tested according to the FEMA deformation history.

Two distinct types of cyclic deformation histories were introduced, derived from the FEMA deformation history. The modification involved adding two initial pulse cycles before applying the FEMA deformation inspired by the research of Frank et al. (2018). For specimens reinforced with steel, the initial pulse amplitude could range from 2% to 7% drift which is defined as the ratio of midspan displacement to the length of the shear span (2018). While the deformability of the FRP-reinforced components is much lower. In this study, the amplitude of the initial pulse is set to 1% and 2.5% of the shear span length, defined as the small pulse (SP) and large pulse (LP) deformation histories, respectively. For each reinforcement ratio, one beam experienced the SP deformation history, while two beams underwent the LP deformation history, as listed in Table 6.1. The detailed loading protocol of the various loading histories mentioned above is shown in Fig. 6.3. Downward loading is defined as positive loading. All cyclic loading and initial pulses start from the positive loading direction, meaning that the measured midspan displacement starts with a positive value.

Based on monotonic loading tests, concrete on the tensile side reached the cracking strength for various reinforcement ratios under both SP and LP deformation histories. Each test proceeded until one side of the reinforcement fractured.

Initial pulses were incorporated to replicate the impact of early damage, such as that induced by earthquakes or extreme wave loads, on the cyclic behavior of structural members. It was anticipated that the deformation pulses would trigger the onset of crack formation. The occurrence of crack localization and the softening of ECC are influenced by both the amplitude of the initial pulse and the reinforcement ratio. Small initial pulses may not transfer microcracks into visible main cracks, so the behavior of the beam with small initial pulses is anticipated to resemble that of a beam without any initial pulses. However, large initial pulses are likely to cause one or several crack localizations randomly appearing in the pure bending region. Therefore, an additional repeated specimen with large initial pulses was arranged for each reinforcement ratio.



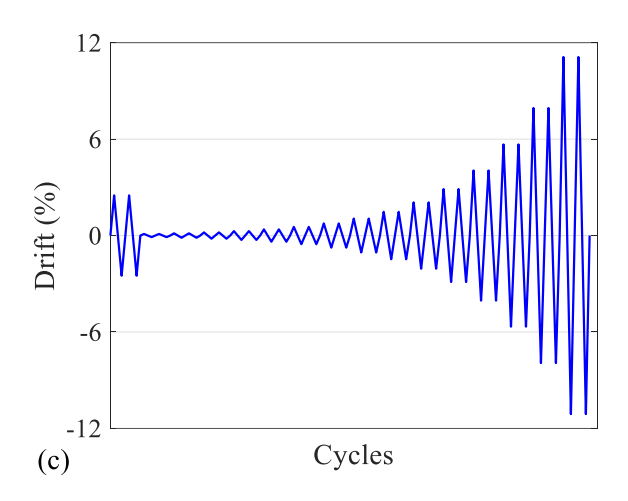


Fig. 6.3 Cyclic loading protocol: (a) FEMA, (b) Small-pulse, and (c) Large-pulse deformation histories

## 6.3 EXPERIMENTAL RESULTS AND DISCUSSION

## 6.3.1 Failure mode

The crack pattern of the specimens at their failure are illustrated in Fig. 6.4. The failure mode of all specimens was FRP reinforcement fracture. Concrete spalling is effectively mitigated, indicating that the PE fiber provides beneficial confinement to the concrete. This enhancement greatly improves the compressive ductility and residual strength of UHPECC. It is evident that the fiber bridging effect leads to the formation of multiple cracks in the pure bending region. This indicates that the characteristic of multiple cracking observed in ECC materials can also be applied at the structural scale. Test specimens with a greater reinforcement ratio tend to develop more cracks, influenced by their ultimate bearing capacity and final deformation capacity. Regarding the influence of loading history, specimens that have undergone initial loading pulses show a degree of cracking and softening in the concrete on the tension side during subsequent cycles. After the initial pulses, during subsequent cycling processes, the specimen tends to widen existing cracks at previously cracked locations rather than initiate new

cracks. The final crack patterns indicate that, despite the similarity in crack patterns and the average number of cracks in FRP-reinforced UHPECC members across various deformation histories, the reinforcement ratio and deformation history affect the behavior of crack-bridging fibers in distinct ways. The fiber integrity in ECC structural components with an initial impulse deformation history is inferior to that in components subjected to a monotonically increasing cyclic deformation history. It is important to mention that there was no evidence of early bond failure between the FRP and concrete prior to the failure of the specimen. Typically, this type of failure manifests as the rapid formation of main cracks on the tension side of the concrete. The results suggest that the deformation capability of ECC is sufficient to coordinate with the deformation of FRP, allowing both materials to work together effectively.



(a)  $S1-\rho 1.88-F$ 



(b)  $S2-\rho 1.88-SP$ 



(c) S3-p1.88-LP



(d) S4- $\rho$ 1.88-LP



(e) S5-ρ1.13-F



(f) S6-ρ1.13-SP



(g) S7-p1.13-LP



(h) S8-p1.13-LP

Fig. 6.4 Final crack patterns of different specimens

## 6.3.2 Crack width evolution

To closely monitor crack evolution and the cyclic effect, a digital image correlation (DIC) system was installed to monitor four specimens. These included two specimens with small initial pulses and two with large initial pulses. The monitored region is the constant moment region on one side of the beam. Throughout the loading process, strain in the monitored region and crack width can be measured using virtual extensometers within the DIC system. The crack width, measured by a virtual extensometer approximately 10 mm in length within the DIC

system, spanned the bottom localized crack. Fig. 6.5 illustrates the configuration of the DIC system.

Fig. 6.6 illustrates the evolution of the main crack propagation width throughout the entire process. The vertical axis in Fig. 6.6 represents the relative displacement between two points on the virtual extensometer positioned near the bottom edge of the monitored section. A measured value greater than zero indicates tension or cracking, while a measured value less than zero suggests compression after cracking closure in the concrete. This measurement enables monitoring of the cracking behavior during cyclic loading.

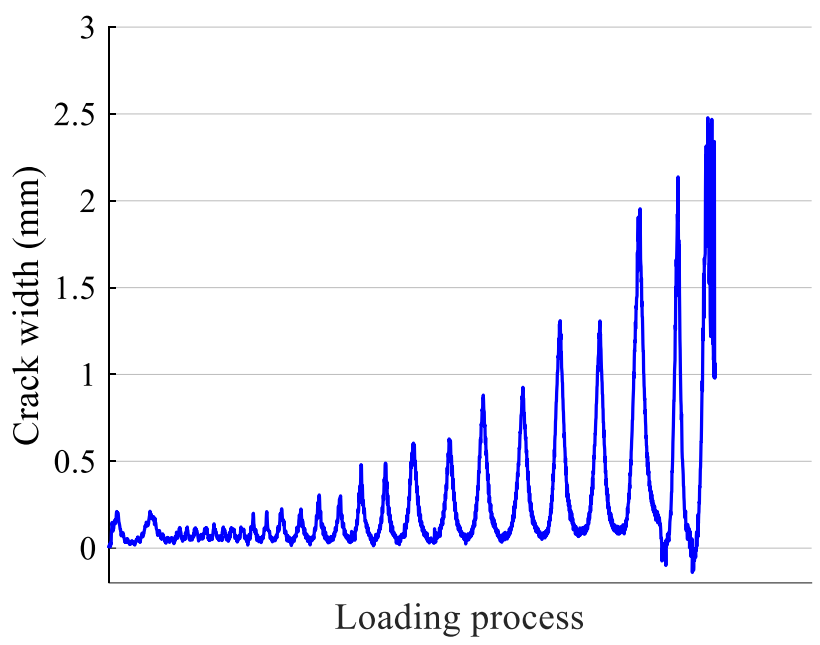
The initial pulses of both amplitudes exceed the cracking load of the specimen. For two different reinforcement ratios, the crack widths at the peak of the large pulses are 0.386 and 0.212 mm, and the crack widths observed at the peak of the small pulse measure 0.287 mm and 0.146 mm, respectively. Specimens with a larger reinforcement ratio showed wider cracks for the same initial pulse amplitude. After the initial pulses, the entire specimen exhibited deformation offset towards positive loading. Even when the applied loading displacement returned to the initial zero position, the cracks generated by the initial pulses could not fully close. This offset is greater for large initial pulses.

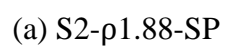
After the initial pulses, the crack width periodically increases or decreases with the applied cyclic deformation. The maximum crack width at each peak of positive loading deformation increases gradually with the increase of cyclic amplitude. For the negative loading, the crack at the bottom side could not be completely closed when the cyclic deformation amplitude is small. This also suggests that an irreversible slip occurred between the ECC and the FRP

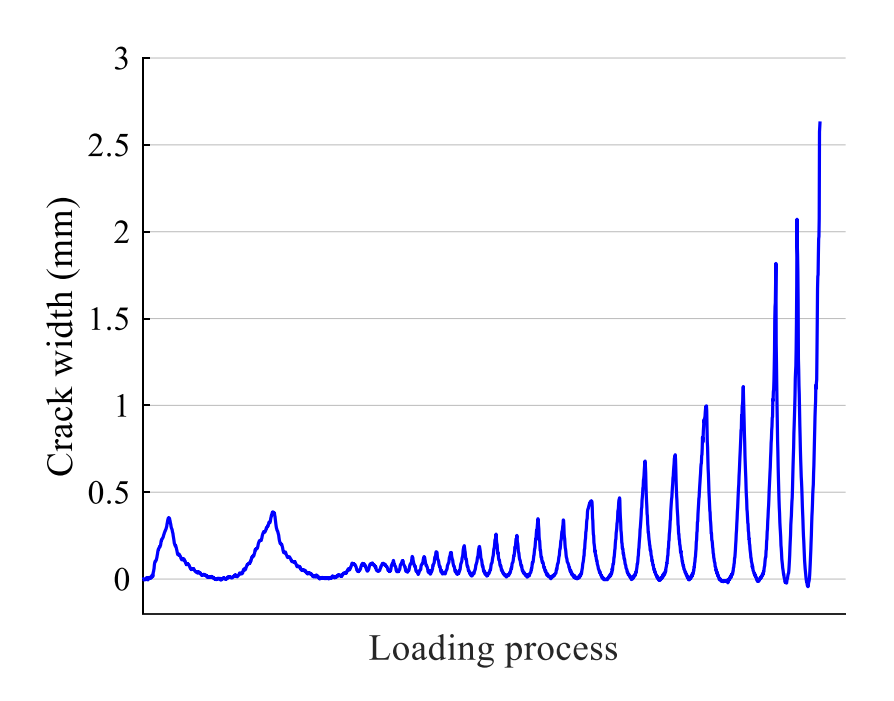
reinforcement. Even if the amplitude of the deformation cycle is further increased, the measured value of the virtual extensometer will only slightly turn negative. For specimen S8-  $\rho$  1.13-LP, the measured value from the virtual extensometer remains greater than zero throughout the entire testing process. The authors attribute this to the low reinforcing ratio of the specimen and large initial pulses. During these pulses, the FRP reinforcement experiences high stress, while there is insufficient bond strength between the reinforcement and ECC. This results in a significant relative slip at the measurement position. The above observations are consistent with the strain evolution of the cross-section during the cyclic process. When the virtual extensometer experiences tension, the neutral axis moves further away from the virtual extensometer, resulting in larger tensile strains at the bottom side of the section under the same loading amplitude. Conversely, in compression, the neutral axis moves closer to the virtual extensometer, leading to a slower development rate of compressive strains.



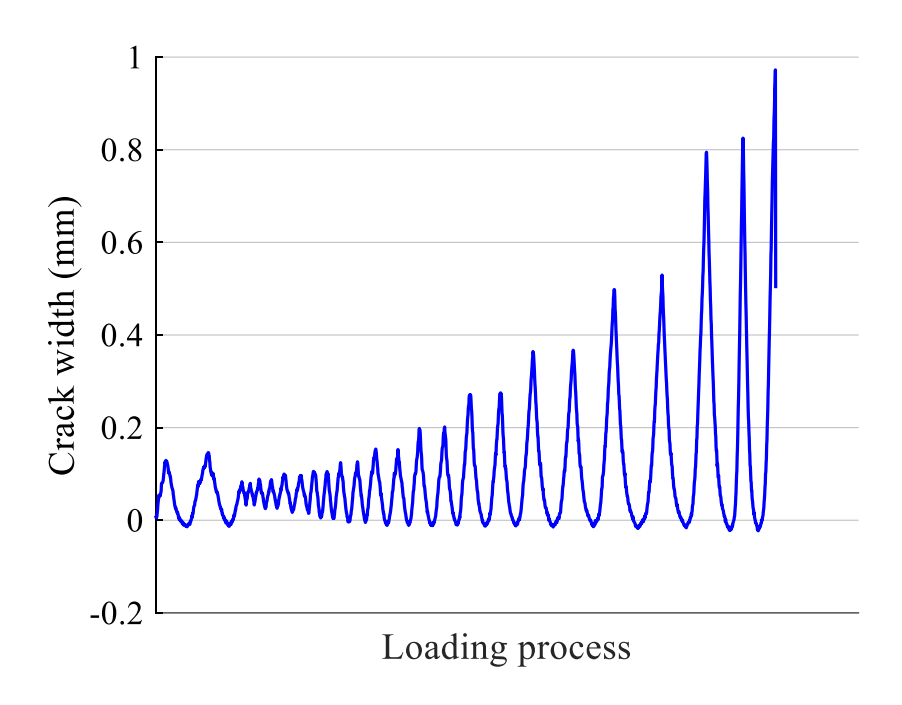
Fig. 6.5 Setup of DIC system



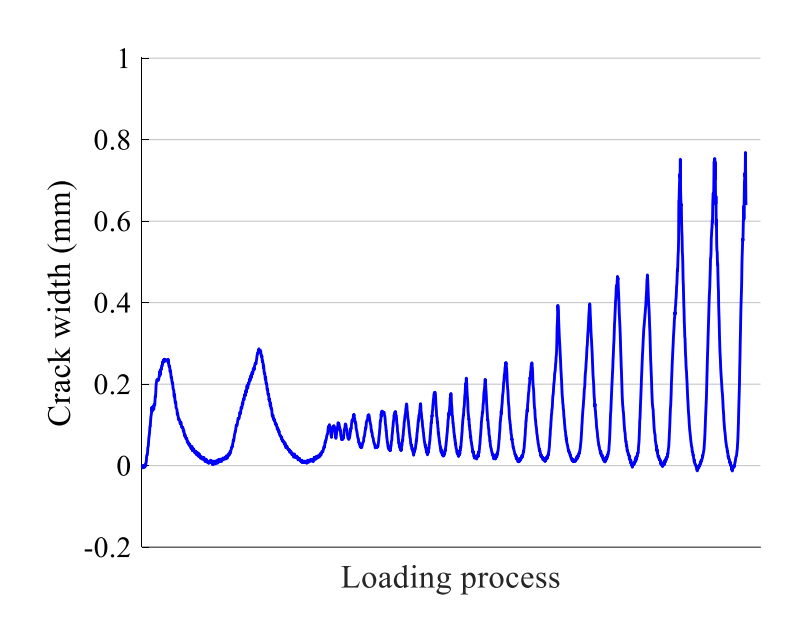




(b) S4-ρ1.88-LP



(c) S6-p1.13-SP



(d) S8-ρ1.13-LP

Fig. 6.6 Evolution of crack width

#### 6.3.3 Hysteretic response

Fig. 6.7 and Fig. 6.8 illustrate the hysteretic response of the test specimens with varying reinforcement ratios, where the entire loading process is indicated by black lines. When the specimens were loaded with initial pulses, the parts of the curve caused by these pulses are highlighted in red. Consistent with expectations, the peak strength of the beam increased as the ratio of FRP reinforcement increased. This enhancement in strength was attributed to the extra tensile strength provided by the higher longitudinal FRP reinforcement across various deformation histories. All specimens failed due to the fracture of the FRP reinforcement. The strain in FRP reinforcement with a smaller diameter grows quicker than that with a larger diameter, resulting in a decrease in failure midspan displacement. This pattern of lower deformability ability in FRP-reinforced UHPECC specimens with a lower reinforcement ratio is consistent with observations in steel-reinforced ECC studies (Frank et al. 2018; Bandelt 2015; Bandelt and Billington 2016).

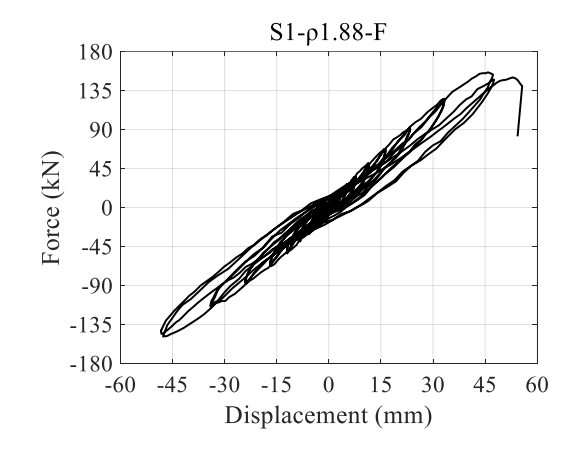
In general, there are some similarities in the hysteretic response observed in beams subjected to the FEMA deformation history and those undergoing the SP deformation history. This suggests that despite the ECC near the tensile side surface experiencing some large tensile strain or even material softening within the initial two cycles, the damage to the ECC is limited, and the overall hysteretic response is not significantly affected. The peak strength of specimens under SP and FEMA deformation histories is smaller than that of specimens loaded monotonically which were tested in the authors' previous research. This phenomenon can be attributed to crack development and failure mechanisms in the specimens. In beams under cyclic loading with either no initial pulse or small initial pulses, several cracks developed at the initial stage with small cyclic amplitudes. Due to the slip between ECC and the FRP

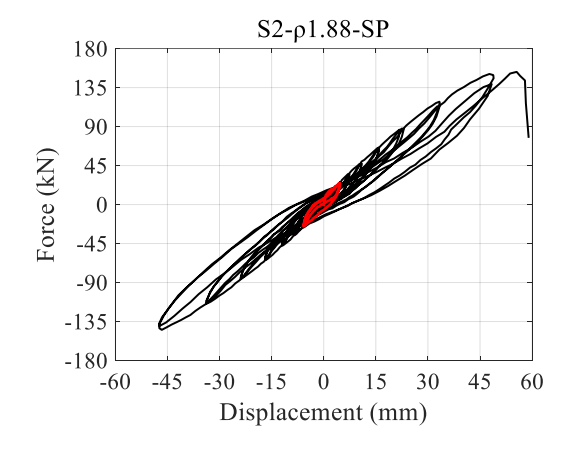
reinforcement, the cracks on the tensile side cannot completely close when the load reverses. This characteristic accelerated crack localization on the tensile side of specimens compared to monotonic loading specimens. As the cyclic amplitude increases, instead of developing new cracks, cyclic specimens tend to widen previously localized cracks. In the final stage, fewer localized cracks developed in the pure bending area, leading to strain concentration on the FRP reinforcement and resulting in lower strength. Furthermore, the ultimate deformation of the beams was reduced.

The hysteretic response of specimens under the LP deformation history varies depending on the reinforcement ratio. For a small reinforcement ratio (i.e., bars diameter of 13mm), the hysteretic curves under the LP deformation histories are quite similar to those observed under SP and FEMA deformation histories, and the peak strengths are slightly lowered for the LP deformation history situation. However, for a larger reinforcement ratio (i.e., bars diameter of 16 mm), the peak strength is enhanced compared to specimens experiencing smaller or no initial pulses. For all specimens under the LP deformation history, no crushing was observed in the first large pulse on the compression side, and the spalling was resisted by the fibers. Thus, the difference comes from the tensile side. Visible cracks were observed during the larger initial pulses, for smaller reinforcement ratio specimens, the crack development and localized pattern are similar to that of specimens with no initial pulse or smaller initial pulses as described in the aforementioned paragraph. In cases with a large reinforcement ratio, large initial pulses can generate more cracks in the pure bending area compared to specimens with small initial pulses or no initial pulses. This is because the stress and strain of both reinforcement and concrete increase with the increase of deformation amplitude. This increase in the number of cracks cannot occur in specimens with the small reinforcement ratio due to the limited per unit length bond strength between small diameter reinforcement and concrete, aligning with the behavior observed under monotonic loading conditions. Since more cracks formed under the large initial pulses, these cracks have the potential to widen further, facilitating a more even distribution of relative slip between the reinforcement and concrete during subsequent increases in deformation amplitude. Consequently, in the final stage, more FRP reinforcements are involved in a high-stress state in the pure bending area, which delays the strain concentration on the reinforcement and results in a slightly higher strength of the beam compared to the SP deformation history and FEMA deformation history specimens. However, the strength of specimens under the LP deformation history is still lower than that observed in cases of monotonic loading, highlighting the tendency of cyclic loading to widen existing cracks rather than develop new ones.

Fig. 6.9 shows the impact of initial pulse amplitude on the deformability of the specimen. The ultimate displacement and initial pulse amplitude are described by drift in this figure. The nearly horizontal trendline for the specimen with a 1.88% reinforcement ratio suggests that the initial pulse amplitude has minimal impact on deformability for nominally identical specimens. This indifference was first reported by Frank et al. (2018) on steel-reinforced ECC specimens. They attributed this behavior to the compression damage tolerance of ECC. Since the relative slip and unclosed cracks on FRP-reinforced members are smaller than those on steel-reinforced members, this explanation can be also extended to FRP-reinforced structures. For specimens with a reduced reinforcement ratio of 1.13%, increasing the initial pulse amplitude significantly impairs the deformability of the specimen. This negative effect caused by the reduction of the reinforcement ratio occurs earlier in FRP reinforcement components compared to steel-reinforced specimens. In steel-reinforced concrete members, this phenomenon is only observed

when the reinforcement ratio is reduced to 0.73%. For specimens with reinforcement ratios between 0.95% and 1.5%, the trend lines depicting ultimate drift versus initial pulse amplitude remain nearly horizontal (Frank et al. 2018). These findings suggest that the deformability of specimens with low reinforcement ratios, whether steel-reinforced or FRP-reinforced, can be influenced by their deformation history. The bond strength of FRP with ECC is less than that of steel bars with ECC, and FRP also has a lower elastic modulus compared to steel bars. Therefore, FRP specimens are more susceptible to this weakening effect even with a slightly higher reinforcement ratio and a smaller initial pulse amplitude. Generally, it has been observed that with a sufficient reinforcement ratio in FRP-reinforced components, deformability can be preserved despite the influence of deformation history. This finding is quite useful for the design of FRP-reinforced structures under random cyclic loads. However, further testing is necessary to determine the critical reinforcement ratio that ensures deformability remains unaffected.





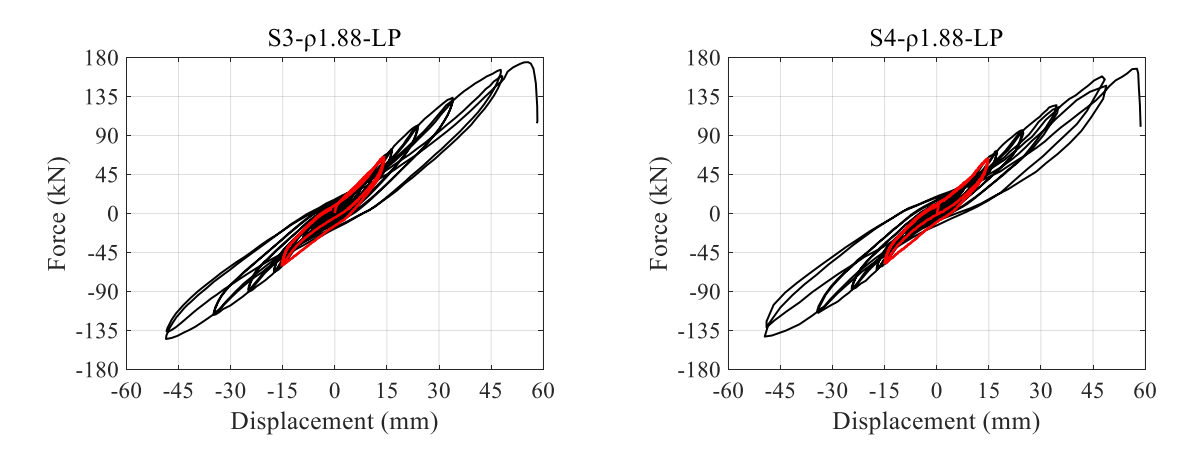


Fig. 6.7 Hysteresis curves of specimens with 1.88% reinforcement ratio

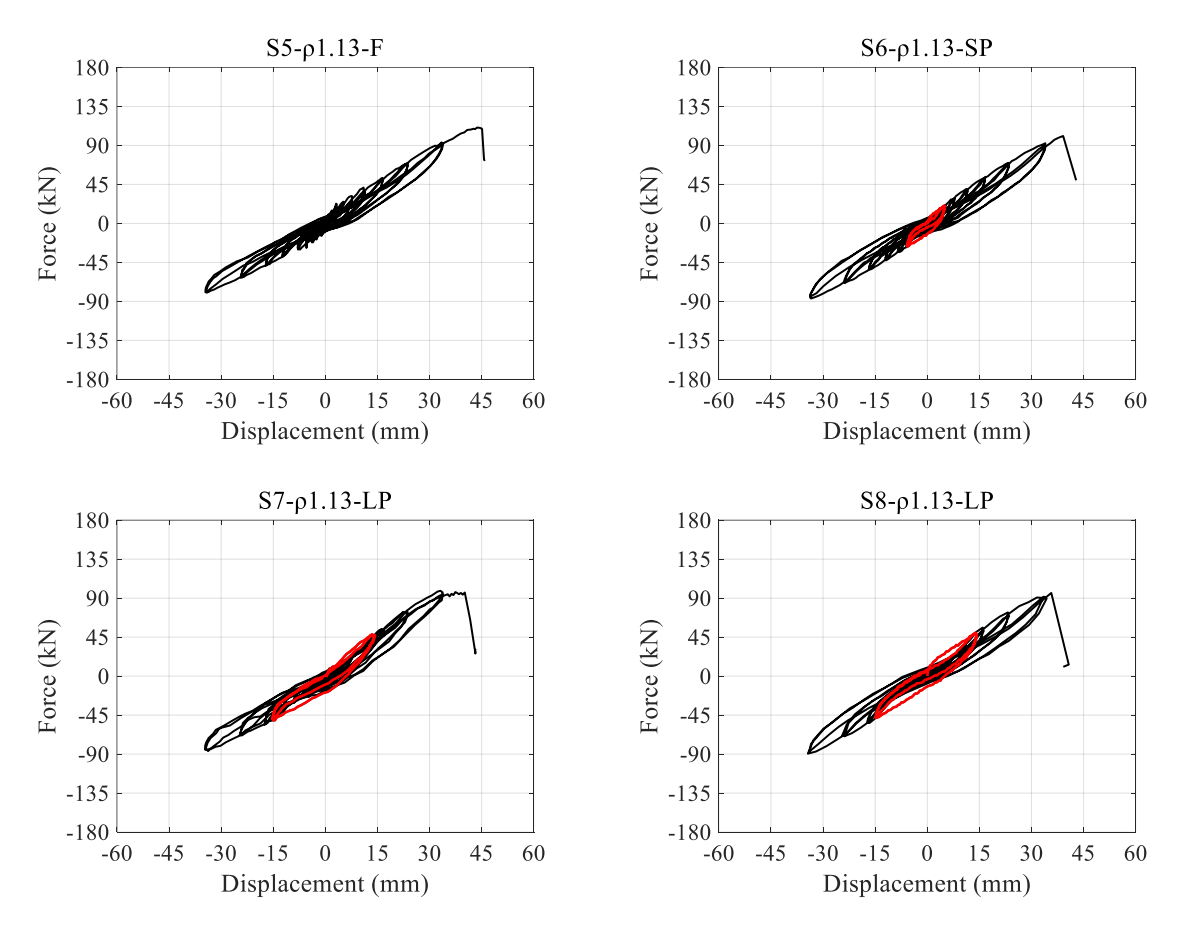


Fig. 6.8 Hysteresis curves of specimens with 1.13% reinforcement ratio

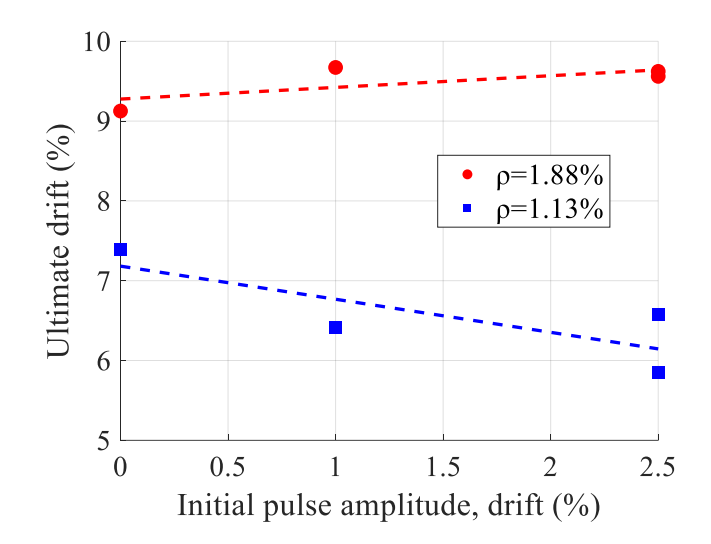


Fig. 6.9 Impact of the initial pulse amplitude on ultimate drift, categorized by reinforcement ratio

#### **6.3.4 Reinforcement strain evolution**

Three strain gauges were mounted on the FRP reinforcement that is under tension during positive loading of each specimen to observe the strain evolution in the reinforcement. The locations of the strain gauges are positioned at the midspan pure bending area, 25 cm from the midspan, and 40 cm from the midspan, respectively, as illustrated in Fig. 6.1.

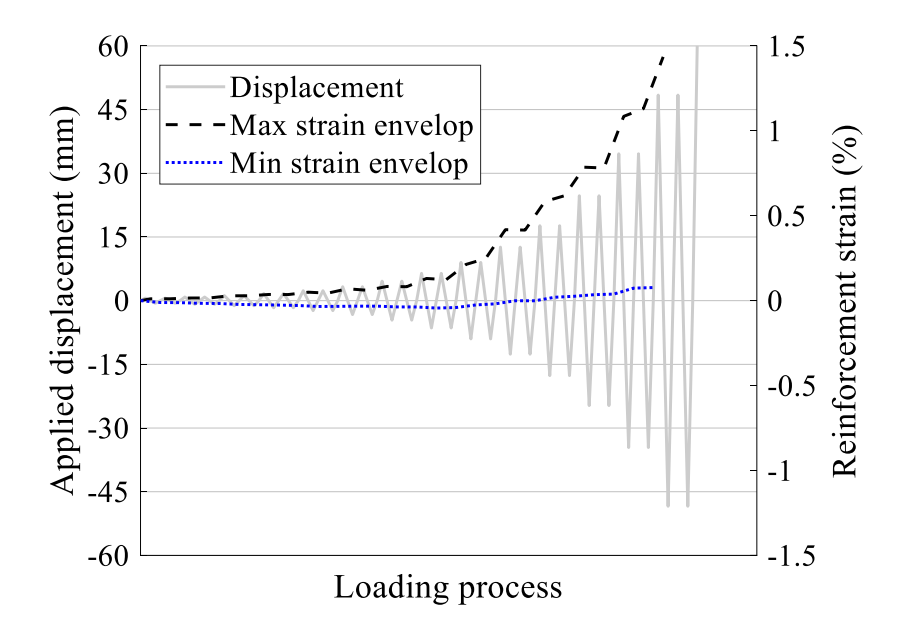
Fig. 6.10 presents the envelope of strain measured at peaks and valleys of all cycles. As the specimen experiences cyclic loading, the periodic variation of strain is expected. The strain envelopes are plotted against the completed portion of the applied deformation history up to the point of specimen failure.; therefore, the fluctuations in strain are not illustrated.

In all cyclically loaded specimens, the FRP reinforcement remained in a linear elastic state until fracturing occurred. However, the stain evolution of FRP reinforcement is not uniform and does not progress linearly with increasing loading deformation. During the initial pulses

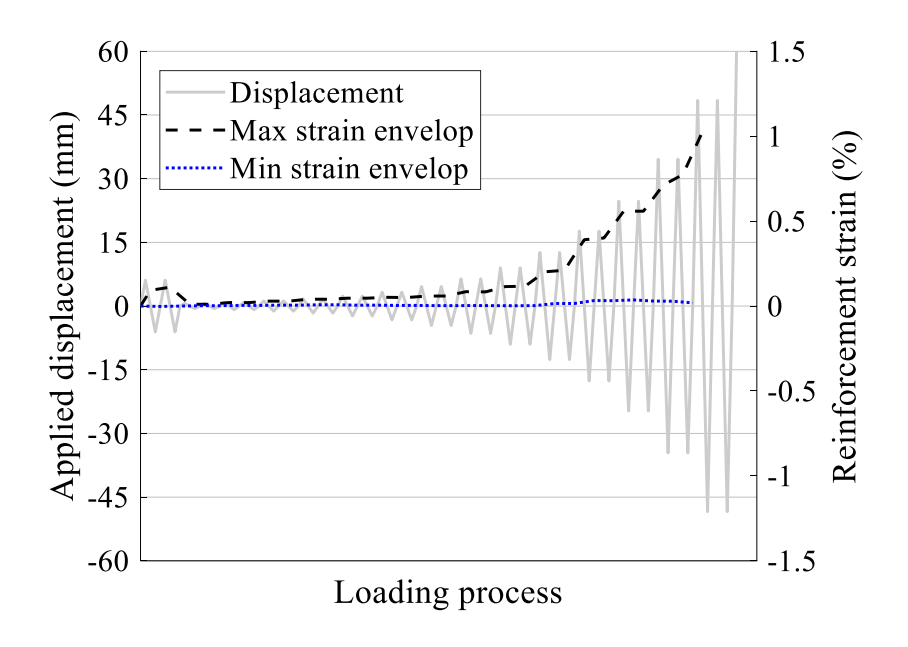
or first several cycles, the variation of strain in the pure bending area approximately corresponds consistently to the variation in displacement. When examining the strain in FRP reinforcement among specimens that experienced the same drift level, it was evident that the strain in FRP reinforcement within beams that have a lower reinforcement ratio increased more rapidly. For example, when subject to the small initial pulse at the first peak of positive loading, the reinforcement strain in the pure bending area of specimen S2- $\rho$ 1.88-SP and S6- $\rho$ 1.13-SP was 0.11% and 0.17%, respectively.

The strain development along the longitudinal direction of the FRP reinforcement is quite uneven, as shown in Fig. 6.11. At 40 cm from the mid-span, the strain gauges exhibit minimal fluctuations over an extended period, contrasting with the higher strains at the mid-span. This difference arises from two factors: firstly, the reduced section bending moment nearer to the support, and secondly, the fewer cracks in this region, resulting in the ECC bearing a significant portion of the tensile stress. The reinforcement strain variation observed 25 cm from the midspan was found to be similar to that at the mid-span. Throughout the entire loading process, the strain in the reinforcement generally increased with each tensile excursion and decreased with each compressive excursion. Notably, under identical loading deformation amplitudes, the peak strain in FRP reinforcement during tensile excursions exceeded that during compressive excursions. This discrepancy comes from the stress distribution within the cracked concrete section. The peak strain mentioned here refers specifically to the maximum strain during tensile excursions, which gradually increases with initial and intermediated loading stages. However, with further increments in loading amplitude, the peak strain of some specimens decreased. While it was anticipated that reducing the peak strain in the FRP reinforcement would delay specimen failure due to the direct relationship between increasing strain and bar fracture, no clear correlation was observed between the reduction of peak strain and the occurrence of specimen failure. The authors attribute this to stress concentration caused by crack localization. Crack localization is random, and the specific locations of occurrence are uncertain, leading to uncertainty in strain evolution on the reinforcement. Considering that the strain gauge, positioned 25 cm from the mid-span, is situated near the region of pure bending and only 6 cm from the outer edge of the loading support, it may also experience stress concentration due to the crack localization.

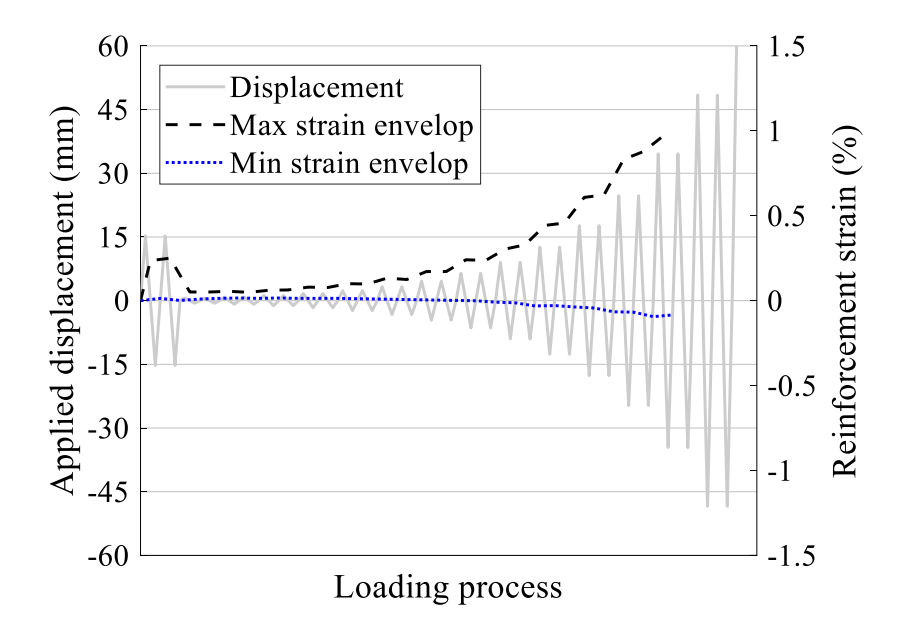
Given that some strain gauges were damaged before the specimen failed, and considering the random occurrence of cracks, it is challenging to draw reliable conclusions about the effect of deformation history on the strain of reinforcement. While, the overall trend indicates that, under identical loading deformations, the reinforcement strain for specimens with either small initial pulses or no initial pulses developed faster compared to those in specimens with large initial pulses. Thus, when fracture of the FRP reinforcement is the intended failure mode for FRP-reinforced UHPECC components, employing a gradually increasing cyclic load is a conservative approach for design when the deformation history in the field is unknown.



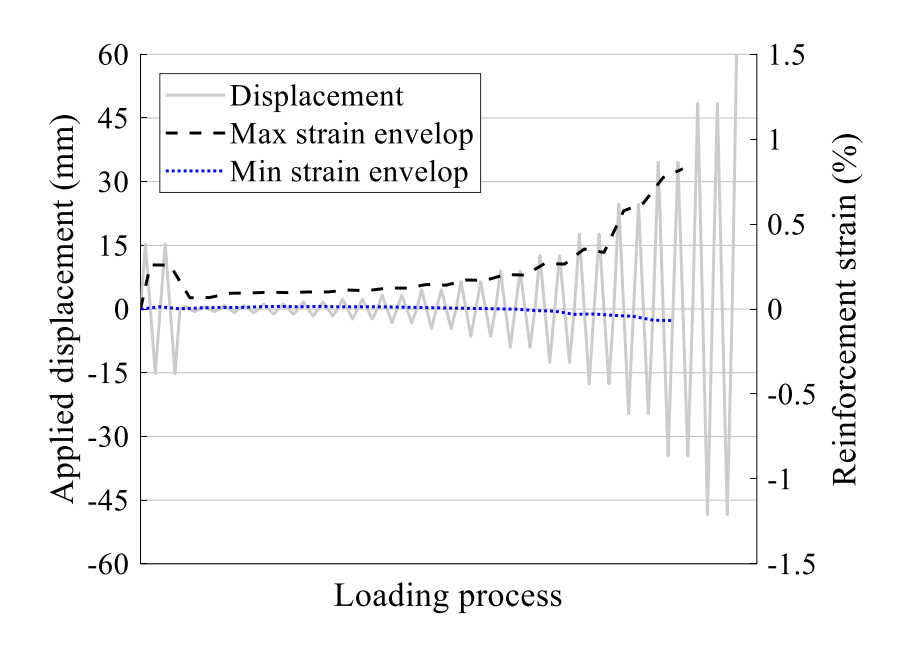
(a) S1-ρ1.88-F



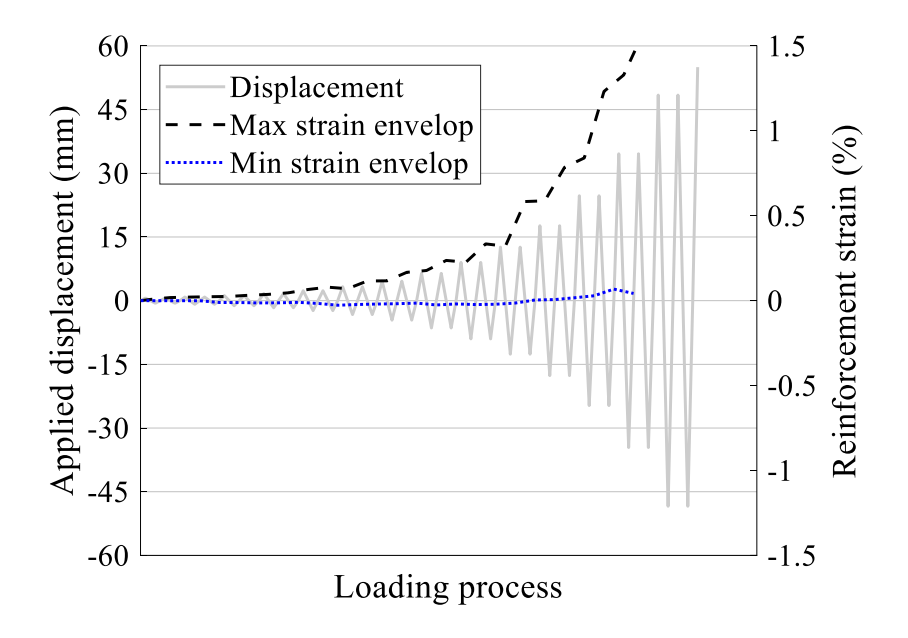
(b) S2-ρ1.88-SP



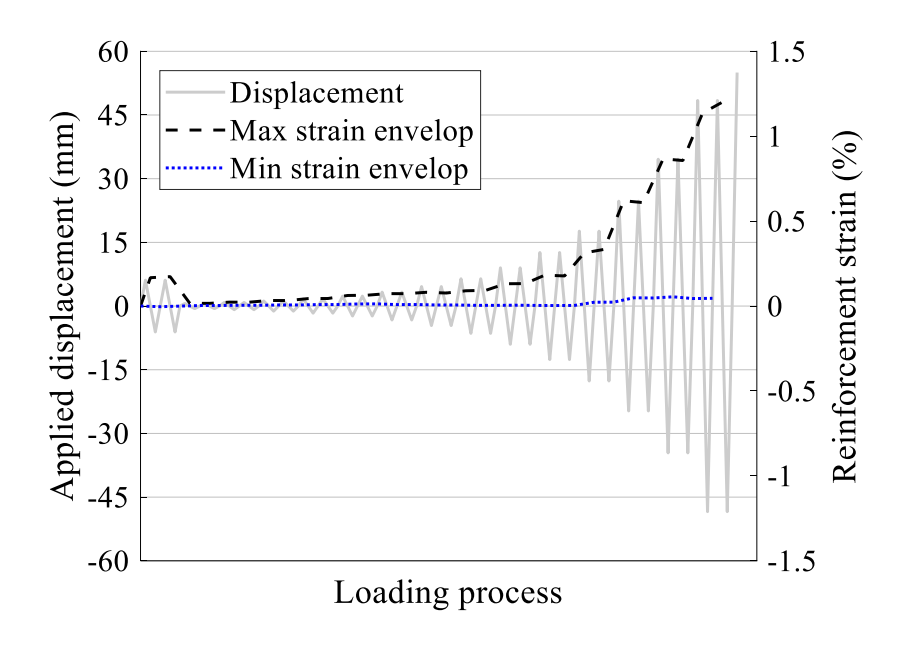
(c) S3-p1.88-LP



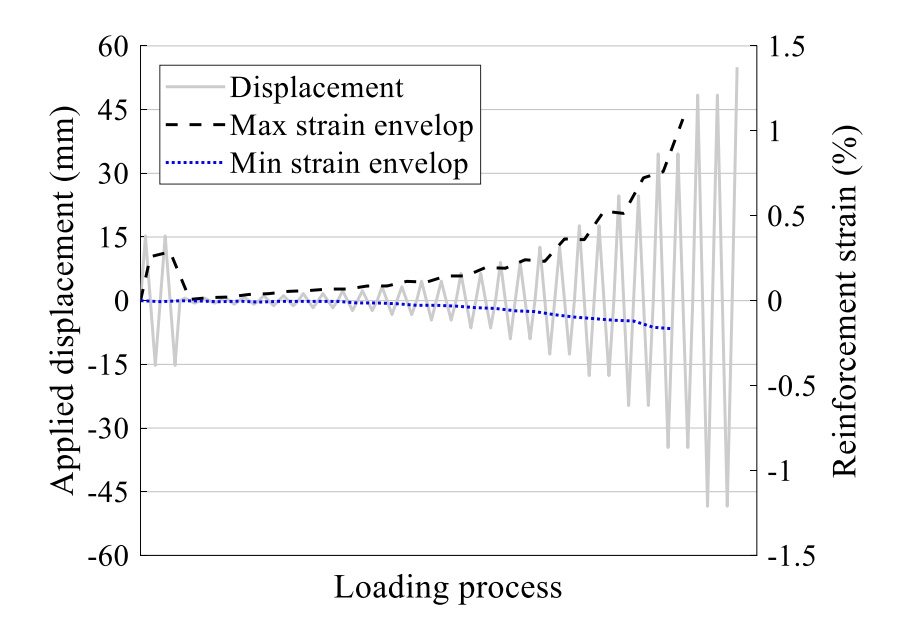
(d) S4-ρ1.88-LP



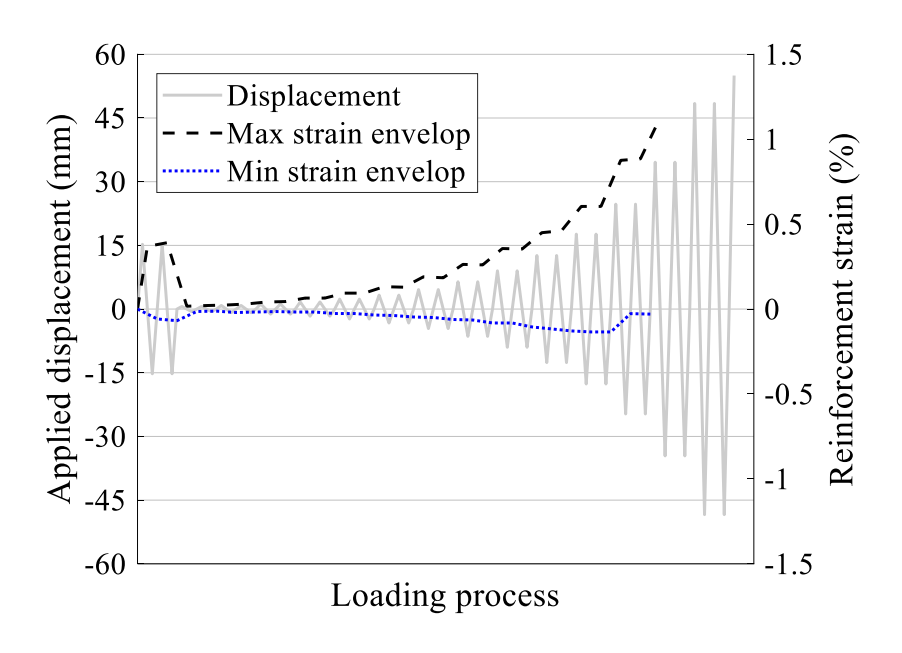
(e) S5-ρ1.13-F



(f) S6-p1.13-SP

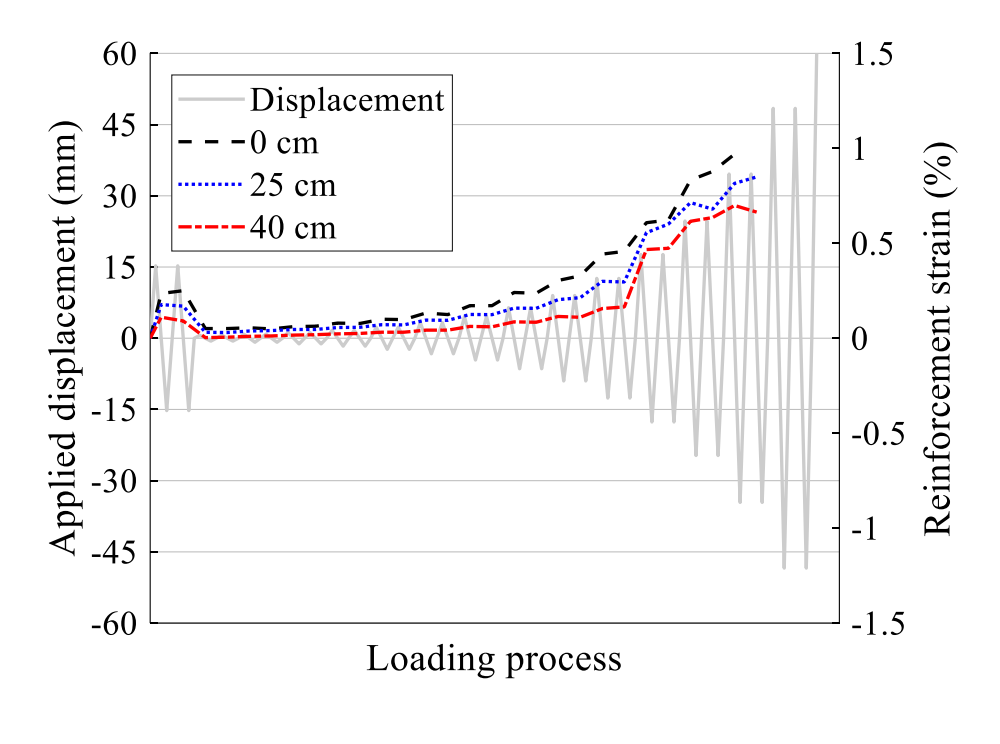


(g) S7-ρ1.13-LP

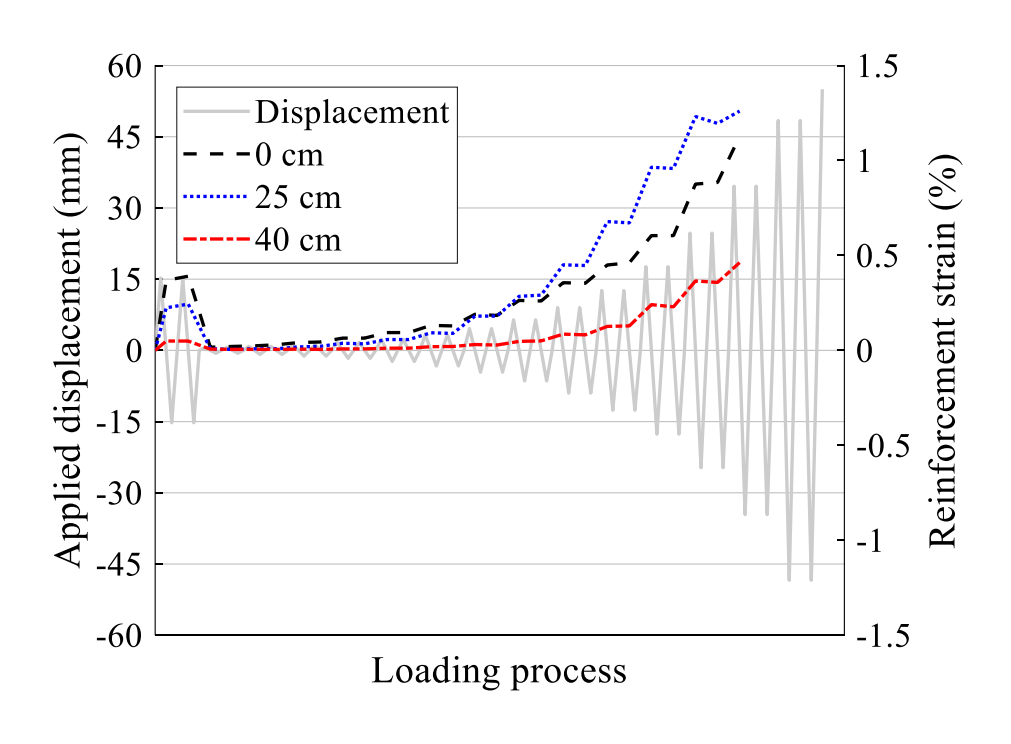


(h) S8-ρ1.13-LP

Fig. 6.10 Strain envelops in the middle span of FRP reinforcement



(a) S3-p1.88-LP



(b) S8-ρ1.13-LP

Fig. 6.11 Strain variation along longitudinal direction in the FRP reinforcement

# **6.4 CONCLUSIONS**

To investigate the influence of deformation history on the flexural behavior of FRP-reinforced UHPECC components, eight beams were designed and tested with various cyclic deformation histories. Previous studies have typically focused on monotonic or gradually increasing amplitude cyclic deformation histories. However, engineering structures are subject to unknown and random loads. Therefore, understanding the impact of loading history on structural behavior is crucial and requires further investigation. In this study, four specimens with each reinforcement ratio were tested under three different deformation histories. These histories were based on recommendations from FEMA, with additional modifications involving the inclusion of two initial pulse cycles of varying amplitudes at the start. The results of this study offer new insights and supplement our understanding of the response of FRP-reinforced UHPECC components under deformation histories including initial pulses or damage.

The initial deformation pulses were observed to have diverse impacts on the cyclic behavior of FRP-reinforced UHPECC beams. Specimens experienced small initial pulse amplitudes showed minimal initial damage, with the evolution of the hysteretic curve closely resembling that of specimens without initial pulses. This similarity extended to the peak strength and ultimate drift as well. However, the situation differed significantly for specimens that experienced large initial pulses. Specimens with a lower reinforcement ratio experienced large pulses displayed behaviors similar to those exposed to either small pulses or no pulses at all. On the other hand, high reinforcement ratio specimens subjected to large initial pulses can develop more evenly distributed cracks along the pure bending area on the tension side of the beam. This phenomenon helps to delay stress concentration on the FRP reinforcement,

resulting in enhanced peak strength and ultimate drift of the beam. More tests are necessary to determine the minimum reinforcement ratio for FRP-reinforced UHPECC structures. Once the reinforcement ratio exceeds this minimum threshold, employing gradually increasing cyclic loads consistently proves to be the most conservative condition, providing significant assistance in structural design.

The strain in the FRP reinforcement was observed to accumulate at a slower rate in specimens experienced large initial pulses compared to those exposed to gradually increasing cycles or small initial pulses. The development of peak strain on the FRP reinforcement along the longitudinal direction is non-uniform. The peak strain occurs at locations of crack localization, where stress concentrations on the reinforcement are highest. Otherwise, the peak strain may remain constant or even decrease with increasing applied deformation. Maximizing the length of FRP reinforcement is conducive to fully utilizing its material properties and enhancing the peak strength and deformability of the structure.

# CHAPTER 7 OFFSHORE STORAGE TANK: STRUCTURAL CONCEPT AND FEASIBILITY

# 7.1 INTRODUCTION

The petroleum and petrochemical sectors are vital to sustaining China's economy and ensuring its energy security. With an annual oil consumption surpassing 700 million tons, China produces only 200 million tons domestically, relying heavily on imports for the remaining balance. The supply chain of crude oil is of primary importance to national security. This challenge is not exclusive to China. East Asian countries like Singapore, Japan, and South Korea also confront similar circumstances. Importing and storing substantial quantities of crude oil has become an issue to be addressed for these nations.

Due to economic and logistical considerations, refineries and petrochemical facilities are typically situated in coastal areas. Driven by both residential and industrial needs, the demand for developable land in coastal cities like Hong Kong, Singapore, and Tokyo have surged in recent years. Additionally, these cities are at risk of losing land in the coming decades due to rising sea levels driven by climate change. Land reclamation can be a possible solution, but it is both expensive and time-consuming. Moreover, it may have irreversible effects on the ecosystem and is constrained by territorial boundaries. In this context, offshore facilities utilizing sea space have emerged as a viable, eco-friendly, flexible, and cost-effective alternative. A variety of offshore structures have been built or proposed globally for numerous applications.

Storage tanks are commonly used for the large-scale storage of hazardous substances, encompassing various fuels and chemicals at industrial locations such as petrochemical plants, oil refineries, and gas facilities. Above-ground tanks are integral to the functioning of oil refineries, petrochemical facilities, and other industrial establishments by serving as storage units for both raw and refined materials. Typically built from welded thin steel plates forming vertical cylinders, these tanks can accommodate more than a million liters of chemicals and are the most widely utilized equipment in the industry. To conserve land, there has been a trend toward expanding storage space through marine structures. Japanese were pioneers in this field with two successful applications of two floating storage facilities located at Kamigoto Island and Shirashima Island (Ueda 2014). They repurposed retired oil barges into floating storage tanks. Positioned in moderate sea states through mooring systems, these floating storage tanks serve as long-term and large-scale strategic reserves. However, maintaining the structural integrity of these steel barges in the marine environment is crucial to prevent oil leakage and pollution. Another innovative solution for oil storage comes from Singapore researchers, who have proposed floating hydrocarbon storage tanks made of concrete. Singaporean researchers proposed another solution for oil storage named the floating hydrocarbon storage tank (Zhang et al. 2019, 2020a, 2020b). Tanks have capacities ranging from 5,000 m<sup>3</sup> and 35,000 m<sup>3</sup>. The storage capacity of these floating tanks is considerably smaller compared to typical aboveground tanks, such as those with a volume of 100,000 m<sup>3</sup>. This is because a large part of the buoyancy created by the tank is needed to offset the considerable weight of the concrete structure. Meanwhile, to prevent overturning and collision among multiple tanks, it is essential to install and maintain numerous fenders and mooring systems to effectively control the dynamic behavior of tanks subjected to wave loads.

To address the limitations of the aforementioned schemes, the authors proposed a cylindrical bottom-supported tank, referred to as the offshore fixed storage tank, which can be positioned in offshore coastal areas. Through proper design and calculation, the tank can withstand wave, current, and wind loads. Furthermore, taking advantage of its structural form and material properties, the tank exhibited improved performance in terms of leakage prevention and corrosion resistance.

Since the type of tank is newly proposed, there is currently a deficiency in relevant research and design basis. Thus, for the feasibility study, the research on the above-ground tanks subjected to hurricane-induced surges or floods is adopted for reference. Despite the usual construction of above-ground tanks with steel shells, which differs from the proposed tank, the similarities in structural form (thin-walled vertical cylindrical shell) and the types of loads (wave, current, buoyancy) allow for relevant comparison. Various failure modes observed in above-ground tanks, including floatation, sliding, buckling, and roof failure, can serve as testing criteria to assess the feasibility of the proposed tank types.

Failure of above-ground tanks can result in severe environmental damage, harming wildlife and fragile ecosystems through the leakage of hazardous substances. Additionally, these failures may incur substantial economic impacts, including clean-up costs, legal actions, disruptions in port activities, and production losses (Kingston 2002). Given the significant consequences of above-ground tank failures and the vital role of the oil industry, ensuring the safety of offshore storage tanks requires increased attention and careful design. Failures of offshore storage tanks in ocean space can have more serious consequences than those occurring on land. The anticipated rapid growth of oil consumption and import in China in the future

years emphasizes the necessity for additional storage facilities. The offshore storage tank provides an effective solution without occupying land resources. Therefore, a comprehensive study is imperative, including the determination of environmental loads, tank geometry, and structural design, as well as the behavior of shell members.

# 7.2 CONCEPT DEVELOPMENT

## 7.2.1 Types of offshore storage tanks

Generally, three types of oil tanks are proposed: semi-submerged tank, submerged tank, and f Offshore fixed storage tank. Each type of tank can be slightly adjusted in roof type, anchorage, etc., which will be explained in detail below.

# Semi submerged tank

This type of tank is adapted from the above-ground tank. The layout and geometry are quite similar. Two main differences include: 1) the steel tank shell is replaced by the sandwich composite shell and 2) the lower part of the tank is inundated at working conditions which leads to extra buoyancy and external pressure compared to the above-ground tank.

The floating roof is widely used in large-scale tanks for its good mechanical performance and volatilization loss control. But when the oil surface level is lower than the outer water surface as shown in Fig. 7.1, the inoperative roof drain may lead to roof failure during heavy rain events. Thus, a fixed conical roof is preferred to prevent the rainfall effect as shown in Fig. 7.2.

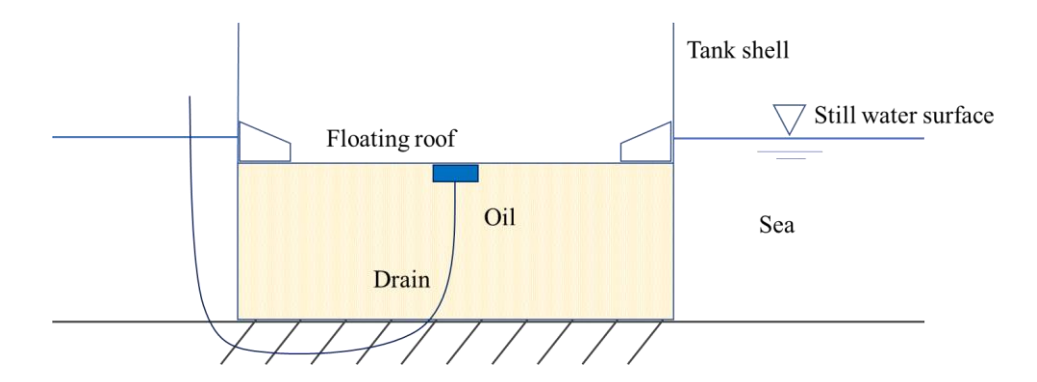


Fig. 7.1 Semi submerged tank with a floating roof

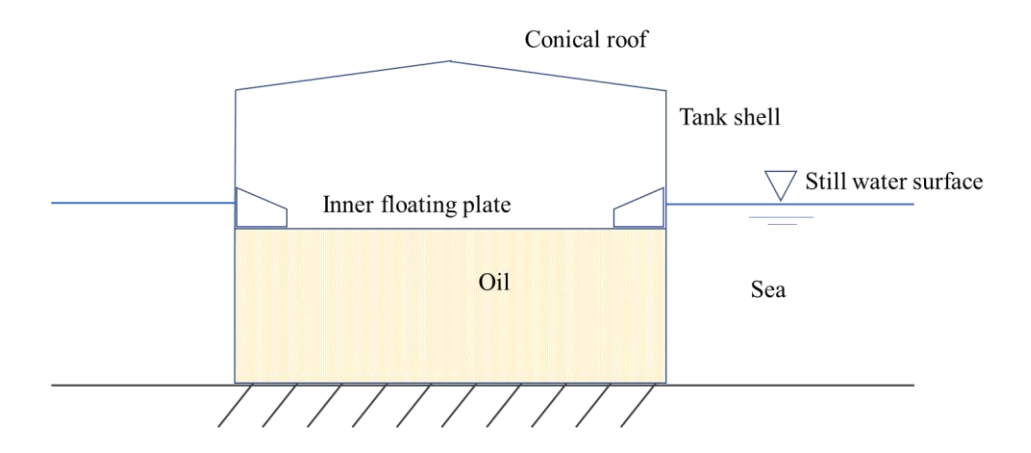


Fig. 7.2 Semi submerged tank with a conical roof

The offshore storage tank suffers extra buoyancy from the seawater because the inner liquid is lighter than seawater. The relative density of different contents, including crude oil, gasoline, and diesel, compared to water  $(1,000 \ kg/m^3)$  ranges from 0.72 to 1. Kameshwar and Padgett (2018) established the relative density of stored contents ranging from 0.5 to 1, based on data from 4,000 storage tanks at the Houston Ship Channel. To keep the tank fixed and stable, the extra buoyancy needs to be balanced by tank gravity. When the volume of the tank grows, some extra efforts are needed as shown in Fig. 7.3 and Fig. 7.4 to lower the buoyancy or increase the resistance force.

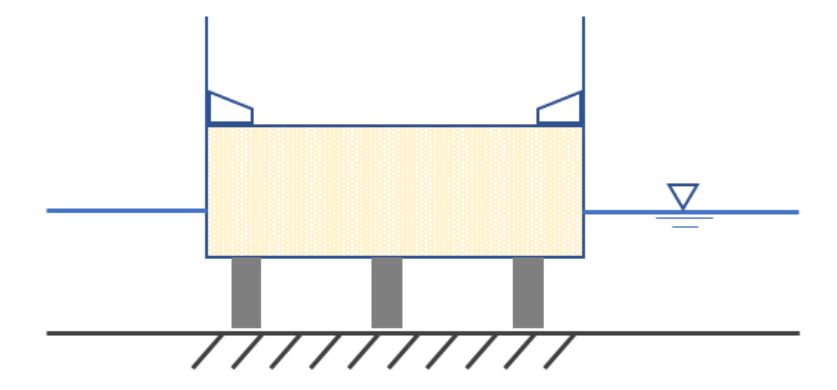


Fig. 7.3 Semi submerged tank supported by piers

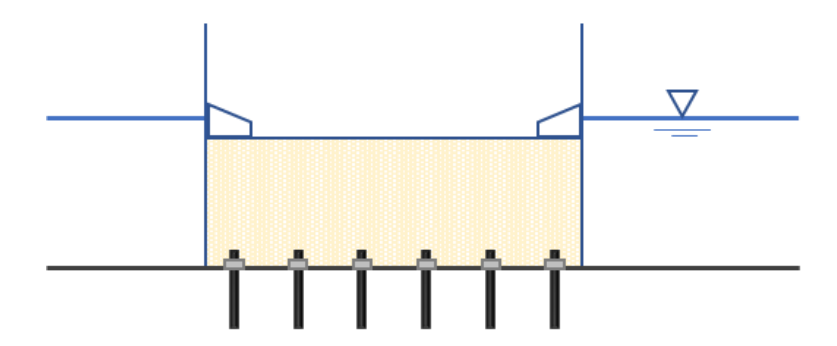


Fig. 7.4 Semi submerged tank with anchorage

# Submerged tank

The submerged tank is shown in Fig. 7.5 and Fig. 7.6. The difference between these two schemes is the relative position of the oil. Tank A places the oil from the base of the tank, and Tank B reverses. The oil is separated from seawater by a moveable plate. Some anchorage or mooring systems can be added at the base or tank shell. For tank A in Fig. 7.5, there is no roof. The upper part of the tank can connect to the sea environment directly. For tank B in Fig. 7.6, the roof of the tank should be flat as the conical roof will form a convex zone which makes the discharge of oil at this region impossible. The water inside the tank is connected to the outer water by a pipe placed at the seabed.

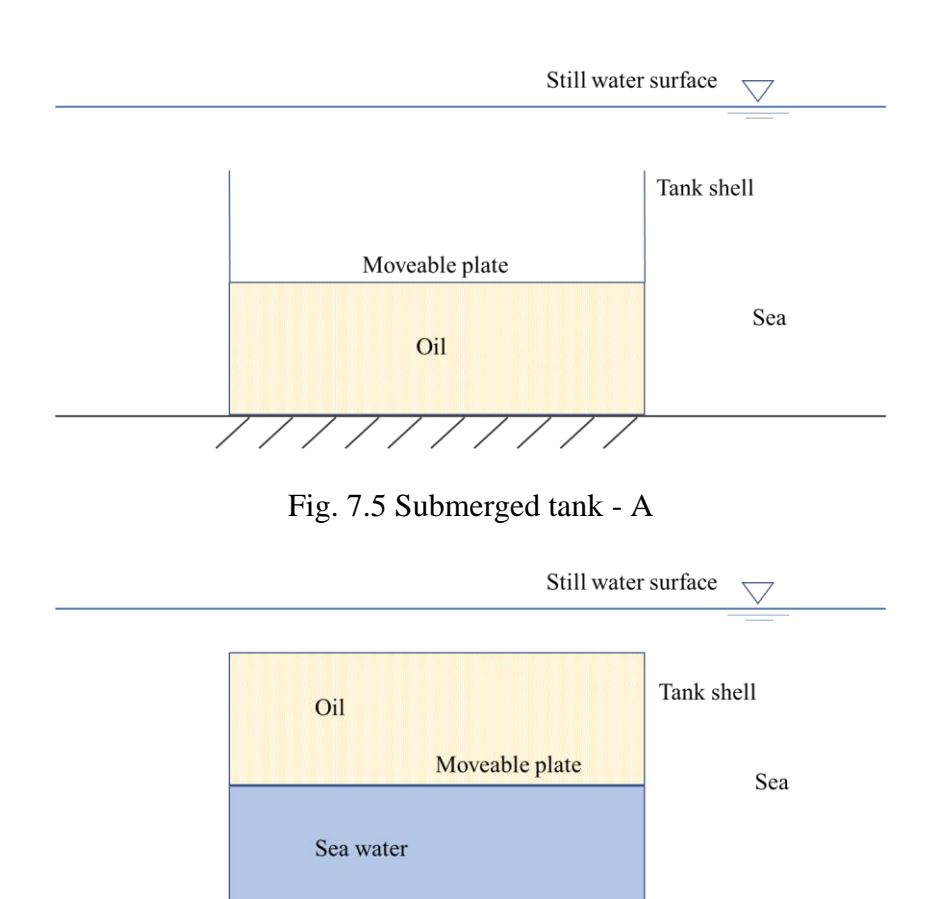


Fig. 7.6 Submerged tank - B

# 7.2.2 Offshore fixed storage tank

The aforementioned proposed schemes for storing oil in the sea have several limitations, with the most critical being the density difference between seawater and hydrocarbons. Since seawater is denser than hydrocarbons, the storage structure must counteract the significant buoyancy caused by this density disparity. Hence, there is a need for a stable and sizable facility that possesses the full functionality of an above-ground tank. To address this issue, the authors proposed a novel design named the offshore fixed storage tank, depicted in Fig. 7.7. This concept features a cylindrical tank securely fixed and supported at the seabed. The tank's wall can be constructed from materials like concrete, steel, or composite materials. The concrete

foundation is anchored to the seabed to enhance stability, with pipe connectors at the base's edge strategically placed to balance hydrostatic pressure on both sides of the shell. The oil is constrained by a floating roof and a moveable plate positioned between the oil and the bottom seawater. These components allow for automatic adjustments to achieve balance under varying tide levels and oil volumes, facilitated by the hydrostatic pressure. If necessary, anchors can be added to the foundation of the tank to further enhance stability.

The proposed offshore storage tank is designed to be situated in coastal shallow water areas with a depth of less than 50 meters. The tank's diameter can vary from 20 to 100 meters with a capacity of 5000 to 100, 000 m<sup>3</sup>. This flexibility allows for adjusting the tank's capacity to meet the specific requirements of national strategic reserves or the oil refining industry. The thickness and material of the tank shell and base can be adjusted as needed, providing adaptability to various specifications and ensuring compatibility with different operational scenarios.

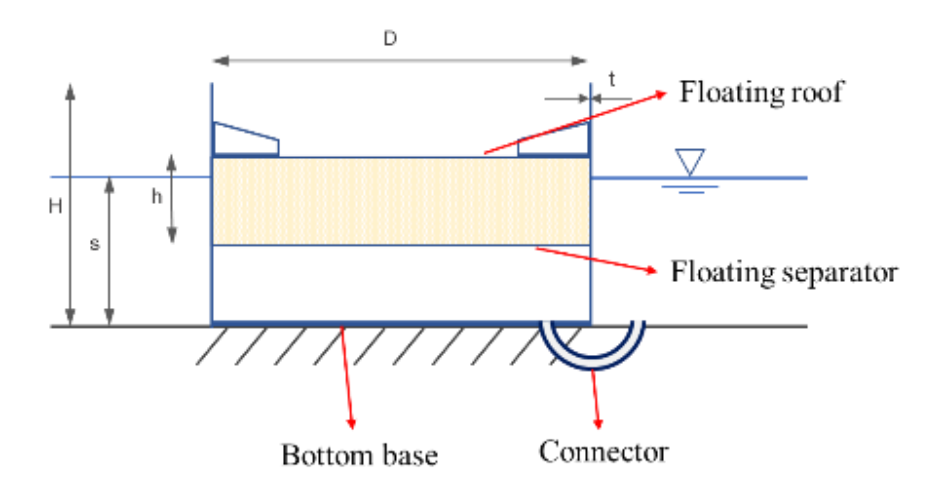


Fig. 7.7 The layout of the offshore storage tank

The proposed offshore storage tanks combine the advantages of both above-ground tanks and floating storage tanks with a lifespan of 60 years. The single-hull structure offers a notable

advantage by enabling a substantial balance between internal and external hydrostatic pressures, thereby reducing the requirement for wall thickness. In comparison to above-ground tanks, offshore storage tanks enhance ocean space utilization and enhance safety by being situated at a considerable distance from urban areas. The seawater can provide better thermal properties to the whole system. Unlike floating structures that require complex mooring systems and motion control, the proposed tanks can maintain stability in the sea independently. This stability is attributed to the buoyancy released by connectors, effectively balancing pressure on both sides of the tank. The inherent gravity of the tank ensures stability in most sea states, while for severe sea conditions, anchors at the base can offer additional resistance force.

# 7.3 ASSESSMENT OF FAILURE MODES IN OFFSHORE STORAGE TANKS

#### 7.3.1 Possible failure modes

For offshore storage tanks to gain widespread practice use, extensive research is required to gain a deeper insight into their performance in the ocean environment and to develop appropriate design methods. Despite being a newly proposed concept, insights from several failure modes in above-ground tanks can be applied, given the similarity in loading conditions. In coastal regions where above-ground tanks are extensively built, the storm surge generated by hurricanes toward the coastline can lead to significant waves, floods, and inundation events. Additionally, hurricanes are typically accompanied by heavy rainfall, which may cause the sinking of floating roofs. Table 7.1 provides a summary of failure modes in above-ground tanks identified in prior studies, which are related to diverse natural hazards associated with hurricanes.

Table 7.1Failure modes of above-ground tanks

Loads	Failure modes	References	
Wind	Buckling	Godoy 2007; Mayorga et al. 2019; Lin 2014	
Wave and current	Floatation Sliding Buckling Impact	Khakzad and Van Gelde 2018; Landucci et al. 2012; Mayorga et al. 2019; Bernier and Padgett 2020; Bernier and Padgett 2019;	
Rainfall	Roof sinking Excessive stress	Sun et al. 2008; Bernier and Padgett 2018	

Offshore storage tanks may suffer hazards and loads similar to those faced by coastal above-ground tanks. But differences arise from two aspects. Firstly, offshore storage tanks experience significant buoyancy, making them more vulnerable to floatation and sliding during hurricane events. Secondly, the proposed tank's shell is considerably thicker than a steel shell, making wind-induced buckling less critical. However, strength requirements become crucial to prevent cracks or ruptures.

The roof should be carefully considered in the offshore storage tanks as rainfall is much heavier in offshore areas than in inland areas. In large-volume tanks with floating roofs, it is crucial that the drainage system efficiently drains rainwater in a timely manner. The design of the roof system can adhere to the standards outlined in the American Petroleum Institute (API) 650 Standard (2013). Tanks with small capacity and conical roofs avoid the risk of rainfall-induced floating roof failure. This research primarily focuses on tank stability and the behavior of the cylindrical shell; therefore, rainfall-induced floating roof failure is not discussed in the subsequent sections. Similarly, further elaboration on impact failure is omitted due to the

preventive measures implemented by the barge system. Table 7.2 outlines the possible failure modes for offshore storage tanks, categorized into preliminary design and structural design. Failure modes under preliminary design will be quickly assessed in this section, while the structural design aspects will be conducted thoroughly in later sections.

Table 7.2 Possible failure modes for offshore storage tanks.

Loads	Failure mode	Design stage	
Static load	Floatation		
	Overturning	D 11 1 1 1 1	
	Sliding	Preliminary design	
Static load + Wave load + current load	Buckling		
53275710 TOUG	Shell bending, tension, and fatigue	Structural design	

#### 7.3.2 Environmental conditions

In designing offshore structures, self-weight and buoyancy constitute the fundamental and simplest loads. Ensuring stability in the working environment requires that buoyancy remains smaller than the foundation reaction force at all times. Additionally, environmental loads, including waves, currents, and wind, can exert significant forces, potentially reaching undesirable levels. Consequently, determining an appropriate scale for these loads becomes crucial.

#### Wind

The drag force of wind load can be evaluated and calculated from

$$F_{wind} = \frac{1}{2} \rho_{\alpha} C_D A V^2 \tag{7-1}$$

where  $\rho_{\alpha}$  represents the density of air  $(1.2 \ kg/m^3)$ . The variable A denotes the projected area of the structure that is perpendicular to the wind flow. The drag coefficient,  $C_D$ , is suggested to be 0.5 for cylindrical sections according to API (2013). Meanwhile, V(t) indicates the average wind velocity at the structure's location.

The average wind velocity at a height z above the ground, denoted as V(z), can be expressed using the power law profile (Haritos 2007):

$$V(z) = V_{ref} \left(\frac{z}{z_{ref}}\right)^{\alpha} \tag{7-2}$$

where  $\alpha$  represents the power law exponent and "ref" indicates a reference point, typically set at a height of 10 meters. In coastal areas classified as rough sea conditions, the descriptive parameter  $\alpha$  can be determined as 0.12.

#### Current

The current drag force per meter can be evaluated from the following expression:

$$F_{current} = \frac{1}{2} C_D \rho_w A V_c^2 \tag{7-3}$$

 $\rho_w$ , A, and  $V_c$  represent water density, projected area perpendicular to the flow direction, and current velocity, respectively.  $C_D$  denotes the drag coefficient, dependent on the characteristics of the current and the shape of the structure. In this study, a value of 1.8 is considered for  $C_D$  (Landucci et al. 2012).

#### Wave

The wave loads applied on offshore structures depend on factors such as their geometry scale, size relative to the wavelength, sea state conditions, and structural stiffness. Structures that are sufficiently large to deflect incident waves (with a diameter-to-wavelength ratio, D/L > 0.2) experienced loading in the diffraction regime. For offshore storage tanks, where the large-scale geometry falls into this category, the analysis can be conducted based on diffraction theory. The detailed solution process will be presented in subsequent sections, while parameters describing waves are discussed here.

According to the Chinese code of hydrology for sea harbors (JTS145-2-2013), when checking the strength and stability of the pier or column-shaped structures, the return period of the design wave should be 50 years with the cumulative frequency of the design wave height being less than 1%. In this study, the sea conditions near Shenzhen are selected as the design basis.

According to the environmental impact report of Shenzhen harbor by CCCC's second navigation engineering survey and Design Institute Co., Ltd, the design wave factors are presented in

Table 7.3. In this study, random waves are generated using the Jonswap spectrum, with the standard peakedness parameter set at  $\gamma = 3.3$ . At a height of 10 m, the average wind speed at the specified location is 4.7 m/s, with a maximum wind speed reaching 23 m/s.

The maximum current speed is 1.8 m/s. The water depth in the selected area mainly ranges from 5 m to 50 m.

Table 7.3 Design wave factors for 50 years return period

Item	$H_{1\%}(m)$	$H_{4\%}(m)$	$H_{13\%}(m)$	$\overline{H}(m)$	$T_p(s)$
Value	3.34	2.84	2.31	1.47	6.3

#### 7.3.3 Floatation

The displacement of above-ground tanks due to floatation has been widely reported after Hurricane Katrina (Godoy 2007; Santella et al. 2010). This displacement can reach up to 30 m due to the storm surge generated by the hurricane, resulting in severe structural damage and environmental pollution.

Offshore storage tanks demand heightened stability as the consequences of floatation failure in a sea environment are much more severe and difficult to handle. As illustrated in Fig. 7.8, to prevent tank floatation, the resisting forces, including the tank's weight  $W_T$  and the weight of the contained liquid  $W_L$ , must surpass the buoyant force  $F_B$ . However, most liquids in the oil industry have lower densities compared to seawater. In large-scale storage, it becomes impractical to balance the additional buoyancy induced by the stored liquid with the tank's weight. Thus, the authors incorporated connections at the seabed to release pressure and eliminate the extra buoyance. This design ensures that hydrostatic pressure inside and outside the tank remains balanced automatically across all loading conditions, mitigating the risk of floatation failure for the proposed offshore storage tank.

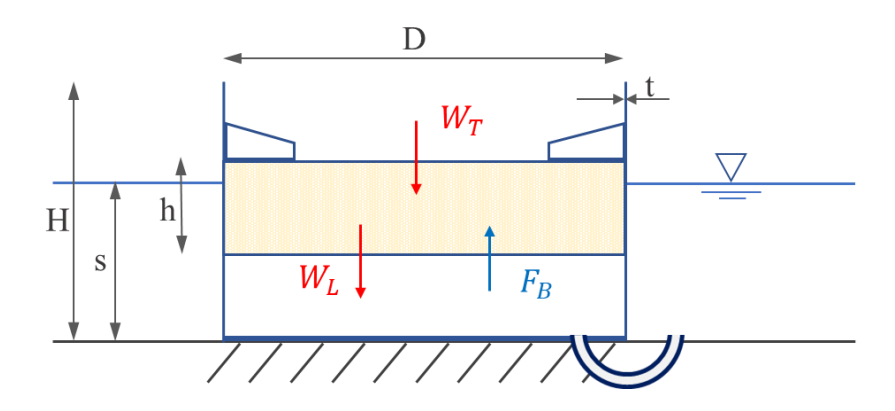


Fig. 7.8 Schematic of the load-resistance forces considered for offshore storage tank floatation.

# **7.3.4 Sliding**

For both unanchored storage tanks and anchored storage tanks on the ground, sliding caused by hydrodynamic pressure has been recognized as a potential failure mode, affecting both large-scale and small-scale tanks (Cozzani et al. 2010; Mebarki et al. 2014). Offshore storage tanks, in particular, are more susceptible to larger hydrodynamic pressure. To assess the sliding failure mode, it is necessary to formulate the limit state equation. As illustrated in Fig. 7.9, sliding occurs when the hydrodynamic force from the storm surge ( $F_d$ ) surpasses the friction force ( $F_{fr}$ ) between the tank's base and the ground. The limit state equation can be expressed as:

$$F_D > F_{fr} \tag{7-4}$$

$$F_{fr} = C_{fr} F_N \tag{7-5}$$

$$F_N = W_S + W_B + W_R - F_{str} \tag{7-6}$$

$$F_D = F_{current} + F_{wind} (7-7)$$

where  $C_{fr}$  is the friction coefficient (~0.4 according to the API-Standard 650 2013),  $F_N$  represents the normal force applied to the storage tank by the ground.  $W_S$  and  $W_B$  are the

gravity of the tank shell and base, respectively.  $W_R$  is the anchor resistance force.  $F_{str}$  is the buoyancy of structure.  $F_D$  is the drag force which can be determined from Eqs (7-1) and (7-3).

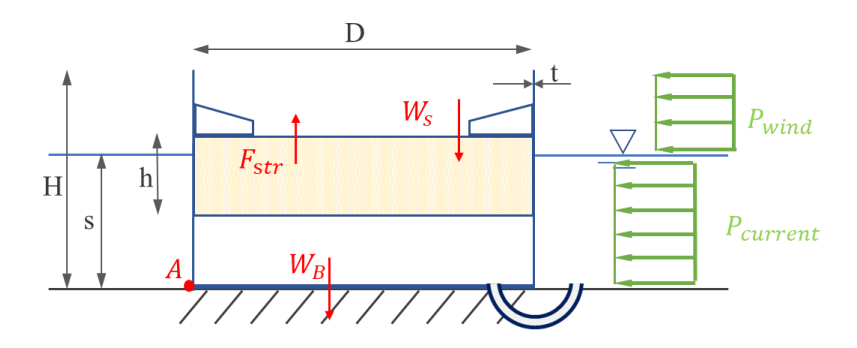


Fig. 7.9 Schematic of the load-resistance forces considered for offshore storage tank sliding.

Anchorage is not taken into consideration in this case. Thus,

$$F_{N} = W_{T} + W_{B} + W_{R} = \pi D t_{shell} (H \rho_{shell} - s \rho_{seawater}) + \frac{\pi D^{2}}{4} t_{base} (\rho_{base} - \rho_{seawater})$$

$$(7-8)$$

D represents the tank's diameter, while H denotes its height.  $t_{shell}$ ,  $t_{base}$ ,  $\rho_{shell}$  and  $\rho_{base}$  denote the thickness and density of the tank's shell and base. For a specific instance, a tank with a diameter of 60 m and a height of 30 m is placed at a water depth of 20 m. The thickness of the shell and base is set to 1/250 of the tank's diameter, with both components having a density of  $2,200 \ kg/m^3$ . The friction force  $F_{fr}$  for this tank is calculated as  $11,194 \ kN$ . The drag force in the given environment is  $3,682 \ kN$ , indicating a low risk of sliding failure. Fig.  $7.10 \ illustrates$  the relationship between the friction force and the tank's geometry. The ordinate indicates the ratio of friction force to drag force, while the abscissa represents the aspect ratio (diameter/tank height). The diameter-to-shell thickness ratio for all tanks is set to 250, and the tank stands  $10 \ meters$  above the still-water surface. For tanks of varying scales at different coastal water depths, sliding failure can be avoided when the aspect ratio is greater than 1.

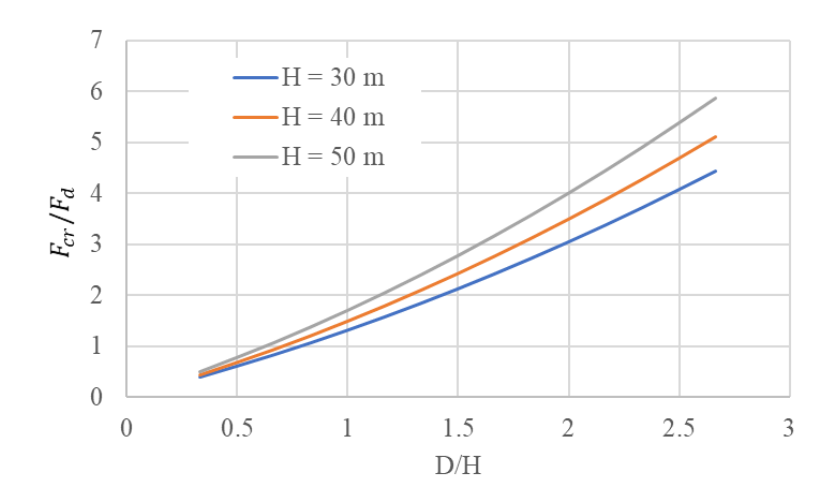


Fig. 7.10 Impact of aspect ratio on sliding failure

# 7.3.5 Overturning

Overturning is another type of dislocation failure. While this failure mode is not as common as the previous ones due to the typically smaller aspect ratio of storage tanks. Once overturning failure occurs, the consequences are the most serious (Necci et al. 2018). Overturning failure may occur when the moment with respect to point A in Fig. 7.9 generated by the environment exceeds the resistance moment. To prevent overturning failure, the following equation should be satisfied:

$$M_R = F_N \cdot \frac{D}{2} > M_L = F_{current} \cdot \frac{s}{2} + F_{wind} \cdot \frac{H+s}{2}$$
 (7-9)

Similar to the sliding ratio, overturning failure will not occur when  $M_R/M_L > 1$ . As shown in Fig. 7.11, overturning can be prevented easily for different scales of tanks.

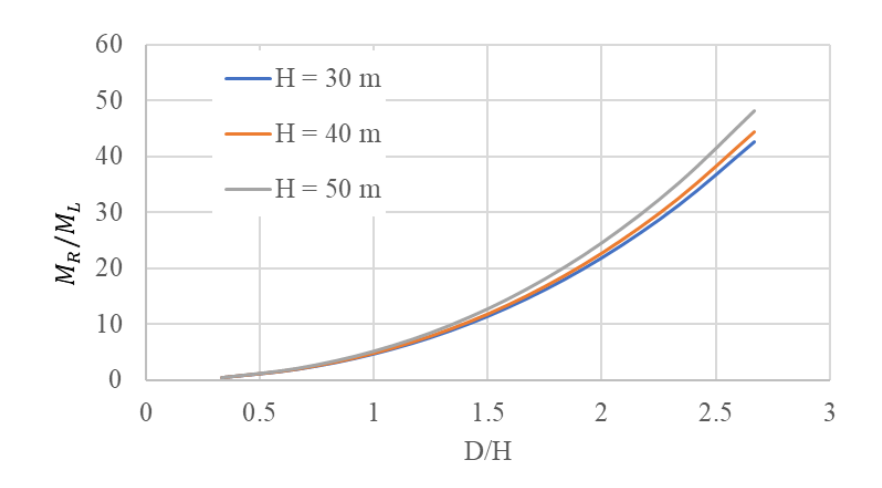
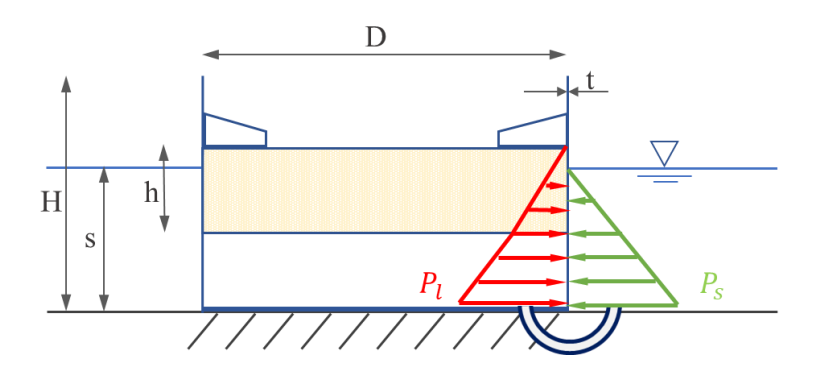


Fig. 7.11 Impact of aspect ratio on overturning failure

# 7.3.6 Buckling

The buckling of oil tanks caused by hurricanes has been widely reported as steel above-ground tanks usually have a diameter-to-thickness ratio larger than 1000 (Khakzad and Van Gelde 2018; Landucci et al. 2014). The hydrostatic pressure from flood or storm surge inundation contributes to a substantial external pressure. Shell buckling occurs once when this external pressure surpasses the combined value of the internal pressure and the critical buckling pressure. For offshore tanks constructed from concrete materials, the relatively large diameter-to-thickness ratio results in a high buckling critical pressure. Additionally, as shown in Fig. 7.12(a), the internal and external pressures are equal at the bottom of the sea due to the presence of pipe connectors. Given that hydrocarbon products are lighter than seawater, the liquid surface inside can always be higher than the surrounding seawater level. The net pressure is always outward, thereby protecting the tank from the risk of shell buckling as shown in Fig. 7.12(b).



(a) External (loading) and internal (resisting) pressure distribution

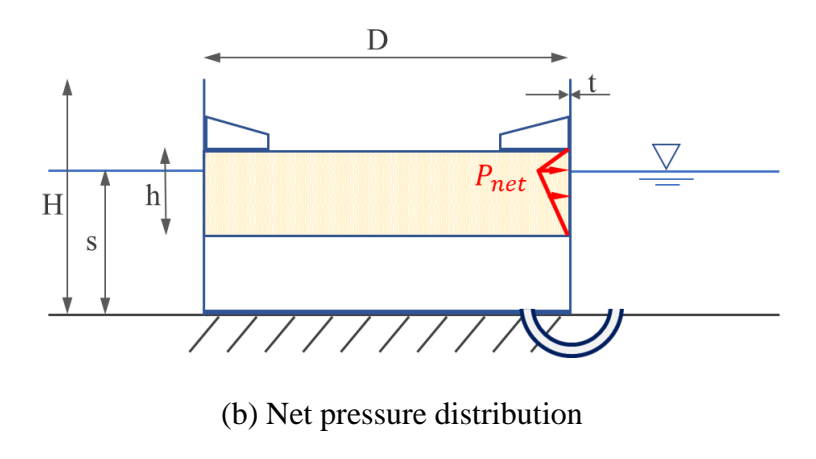


Fig. 7.12 Schematic of the hydrostatic pressure considered for offshore storage tank buckling.

# 7.3.7 Recommended geometry range based on the above failure modes

Based on the preceding analysis, the proposed offshore storage tank demonstrates good feasibility in the coastal environment. This is primarily attributed to the connector, which balances the internal and external pressures, ensuring the tank maintains stability at sea and avoids various dislocations and shell buckling. Tanks with an aspect ratio larger than 1 are preferred.

### 7.4 RESPONSE OF CYLINDRICAL TANKS UNDER WAVE LOAD

# 7.4.1 Regular wave-induced pressure distribution on a cylindrical shell

The fixed offshore storage tank can be treated as a large-scale vertical cylinder. To perform a structural analysis of the cylindrical shell, the first step is to determine the pressure distribution on the shell surface induced by regular waves.

In the context of wave forces acting on offshore structures, three phenomena influence the total force: drag, inertia, and diffraction. Drag is dominant when considering small and slender structures, while inertia and diffraction become dominant when dealing with larger structures.

When a wave interacts with a large-scale vertical cylinder, it will generate significant diffraction. The calculation of wave excitation forces on large vertical cylinders can be carried out using either potential flow theory or the boundary element method. For cylindrical structures with simple sections such as a circle or ellipse, analytical solutions are possible. The MacCany and Fuchs method can be employed to determine the wave force acting on a large fixed vertical cylinder (MacCamy and Fuchs 1954). Fig. 7.13 presents a schematic diagram of the wave force.

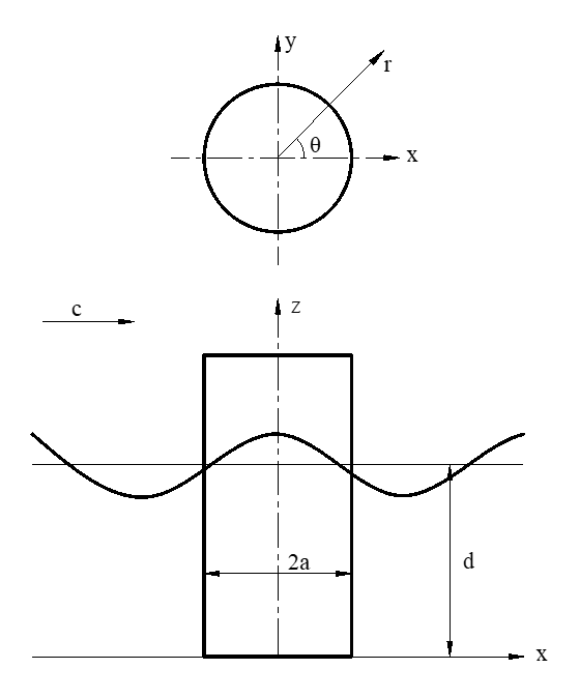


Fig. 7.13 Schematic of wave diffraction around a bottom fixed cylinder

The method is considered valid when the Keulegan-Carpenter number  $K_c$  is less than 2. For a cylinder in wave condition,  $K_c$  can be defined by the equation  $K_c = \pi H_{max}/D$ , where  $H_{max}$  represents the maximum wave height, and D represents the diameter of the cylinder. The Keulegan-Carpenter number reflects the proportion of the drag force to the gravitational force (DNV-RP-C205 2010). For cylinders with large diameters, a small  $K_c$  suggests that the drag force is not the predominant factor.

The velocity potential can be separated into two components: the potential of the incident wave and the potential due to diffraction.

$$\phi(r,\theta,z,t) = [\phi_I(r,\theta,z) + \phi_D(r,\theta,z,)]e^{-i\omega t}$$
(7-10)

where  $\phi(r, \theta, z, t)$  is the total velocity potential.  $\phi_I(r, \theta, z)$  represents the potential of the incident wave.  $\phi_D(r, \theta, z)$  denotes the diffraction potential.

Incident wave potential can be expressed by:

$$\phi_{I}(r,\theta,z) = -\frac{igA}{\omega} \frac{\cosh k(z+d)}{\cosh kd} \sum_{m=-\infty}^{\infty} J_{m}(ka) e^{\frac{im\pi}{2}} e^{im\theta}$$
 (7-11)

The meaning of each parameter is shown below.

g - Acceleration of gravity

A – Wave amplitude

 $\omega$  – Wave frequency

k – Wavenumber

d – Water depth

 $J_m(\cdot)$  – Bessel function of the first kind

The diffraction potential  $\phi_D(r, \theta, z)$  should follow the flowing conditions:

Laplace's equation

$$\nabla^2 \phi_D = 0 \tag{7-12}$$

Free surface equation (z = d)

$$\frac{\partial \phi_D}{\partial z} - \frac{\omega^2}{a} \phi_D = 0 \tag{7-13}$$

Seabed boundary condition (z = 0)

$$\frac{\partial \phi_D}{\partial z} = 0 \tag{7-14}$$

Structure surface boundary condition (r = a, 0 < z < d)

$$\frac{\partial \phi_D}{\partial r} + \frac{\partial \phi_I}{\partial r} = 0 \tag{7-15}$$

Far-field condition

$$\lim_{r \to \infty} \sqrt{r} \left( \frac{\partial \phi_D}{\partial r} - ik\phi_D \right) = 0 \tag{7-16}$$

Based on the above theory, the hydrodynamic pressure exerted on the cylindric shell surface can be described by the following expression.

$$p(r,\theta,t) = \rho g \frac{H \cosh kz}{2 \cosh kd} \left\{ \sum_{m=0}^{\infty} \beta_m \left[ J_m(kr) - \frac{J_m'(ka)}{H_m'(ka)} H_m(kr) \right] \cos(m\theta) \right\} e^{-i\omega t} \quad (7-17)$$

where z represents the distance above the seabed, H is the height of the incident wave, k is the wave number, d is the depth of the water and a signify the radius of the cylinder.

$$A(ka) = \frac{1}{\sqrt{[J_1'(ka)]^2 + [Y_1'(ka)]^2}}$$
(7-18)

and

$$\tan \alpha = \frac{J_1'(ka)}{Y_1'(ka)} \tag{7-19}$$

in which J and Y are Bessel functions of the first kind and second kind.

The overall force exerted on the cylinder is calculated by integrating  $f_{Hx}(z)$  from bottom to top:

$$F_{H} = \int_{0}^{d} f_{H} dz = \int_{0}^{d} \frac{2\rho gH}{k} \frac{\cosh kz}{\cosh kd} A(ka) \sin(\omega t - \alpha) dz$$
$$= \frac{2\rho gH}{k^{2}} \tanh kd \cdot A(ka) \sin(\omega t - \alpha)$$
(7-20)

The corresponding turning moment about the bottom is:

$$M_H = \int_0^d f_H z dz = \frac{2\rho g H}{k^2} \frac{A(ka)}{\cosh kd} [kd \sinh kd - \cosh kd + 1] \sin(\omega t - \alpha)$$
 (7-21)

The moment arm *e* is:

$$e = \frac{M_H}{F_H} = \frac{1}{k} \left( \frac{kd \sinh kd - \cosh kd + 1}{\sinh kd} \right)$$
 (7-22)

In relation to the aforementioned solution, a depiction of the hydrodynamic pressure distribution under regular waves can be illustrated for a given cylindrical tank. Fig. 7.14 presents multiple snapshots capturing the pressure distribution within the specified tank. The tank has a diameter of 80 meters and is positioned at a water depth of 20 meters. The wave height is fixed at 1 m, accompanied by a wavelength of 100 meters. Consequently, the wave period is calculated to be 8.68 s. For ease of observation, the cylindrical shell is expanded into a plane. The two axes on this plane represent the angle and height, respectively. At t=0, it is denoted that the wave crest traverses through the center of the cylindrical shell for clarity in visualization.

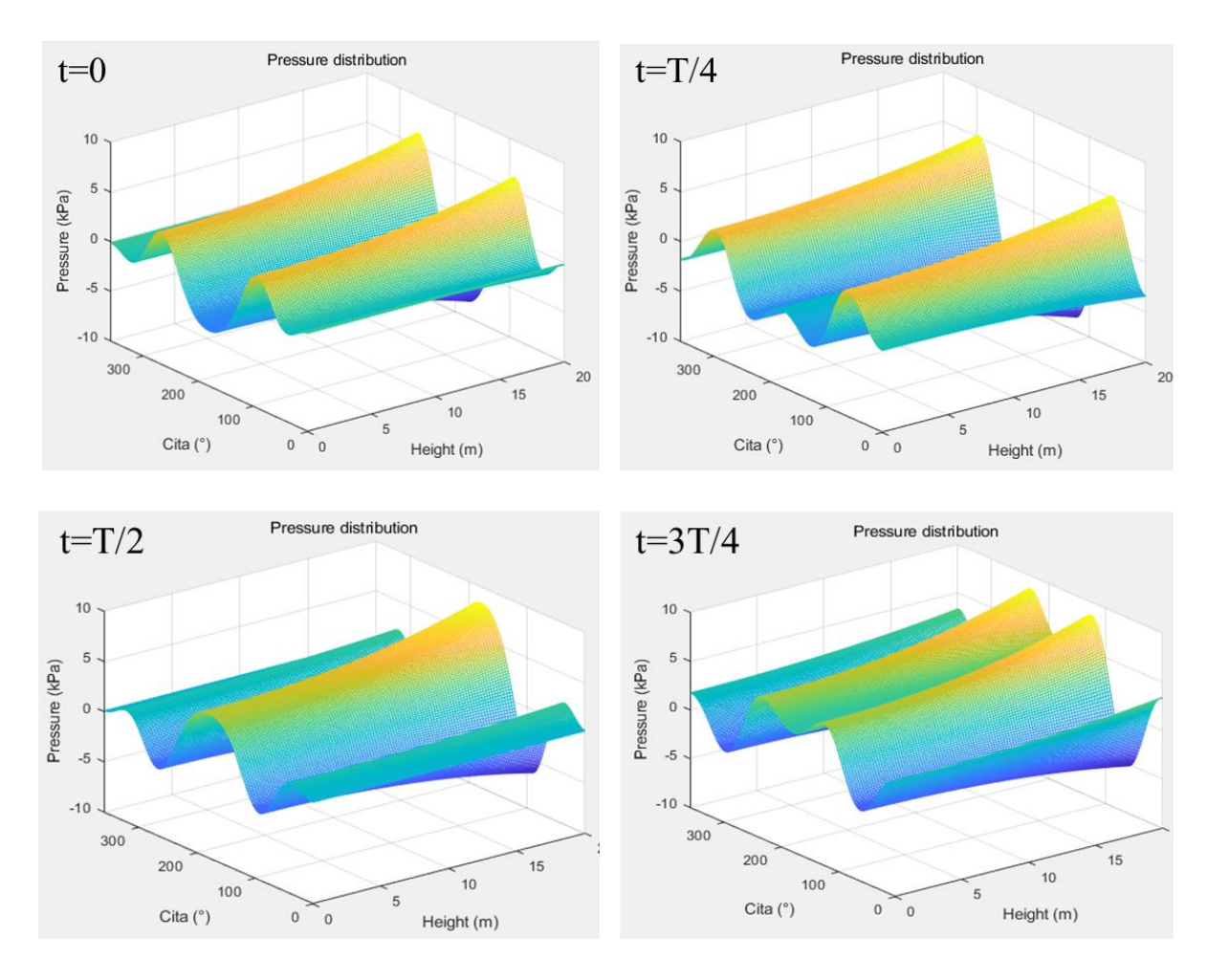


Fig. 7.14 Snapshots of hydrodynamic pressure distribution on a cylindrical tank with Diameter = 80 m, water depth = 20 m, wave height = 1 m, and wavelength = 100 m

#### 7.4.2 Methodology for calculating stress response spectra

Utilizing the above methods to derive the regular wave-induced hydrodynamic pressure on the cylindrical shell, the wave load can be incorporated into the numerical models of offshore storage tanks. The pressure can be defined within an analytical field and subsequently mapped onto the cylindrical surface. In cases where tanks exhibit varying geometry and service environments, a spectral-based analysis process can be employed to extract the response spectra. The procedure is demonstrated in Fig. 7.15.

Initially, the wave spectrum at a specific location can be obtained using hydrology data and the Jonswap spectrum. This spectrum is then subdivided into multiple regular waves. Within the spectrum range, various regular waves, each with a unit wave height, are applied to distinct offshore storage tanks. Each model is developed independently. From the results of each tank, each variable at different locations exhibits a response amplitude operator (RAOs). For instance, each element on the cylindrical shell possesses its RAO for hoop stress. Aggregating the RAOs around the entire surface, the maximum RAO is extracted to form a maximum envelope of RAOs for the cylindrical surface. This implies that the maximum hoop stress RAO on the cylindrical shell may appear at different elements for varying wave frequencies. Finally, the maximum response spectra can be derived using the following equation:

$$S_R(\omega) = RAO^2 \cdot S(\omega) \tag{7-23}$$

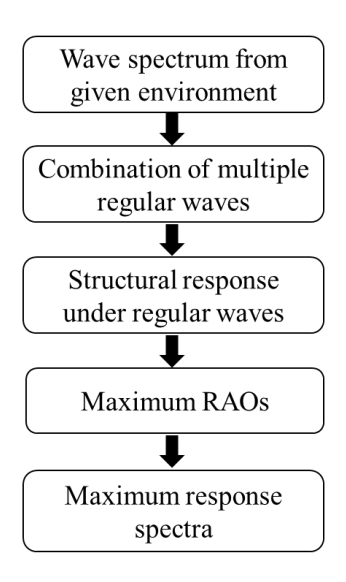


Fig. 7.15 Methodology to derive stress response spectra

Applying the above methodology, the finite element models with various scales are developed under different wavelengths. Table 7.4 provides the details for the parameters of the offshore storage tanks.

Table 7.4 Tanks with different geometry parameters

Item	Diameter (m)	Height (m)	Water depth (m)	Shell thickness (mm)
1				160
2	40	30	20	240
3				400
4				240
5	60	30	20	360
6				600
7				320
8	80	30	20	480
9				800
10				320
11	80	40	30	480
12				800

#### 7.4.3 Regular wave-induced stress on a cylindrical shell

Due to the high diameter-thickness ratio, the cylindrical shell can be treated as a thin-walled structure. Finite element models for the offshore tank are developed using Abaqus. The tank shell is fixed to the seabed, and the cylindrical shell is modeled with S4R shell elements. The elastic modulus for the concrete is specified as 36 GPa. The structure experiences regular wave loading, and a time history analysis is conducted over a duration that is equal or greater than the wave period. Response, such as hoop stress and axial stress, are expressed as  $\sigma = A \cdot \sin(\omega t + \varphi)$ , where  $\omega$  represents the angular frequency of the regular wave, and A denotes the response amplitude. The amplitude for each response can be derived from the finite element results.

Fig. 7.16 illustrates the stress amplitude distribution for an offshore storage tank situated at a depth of 20 m, featuring a diameter (D) of 60 m and a height (H) of 30 m. The ratio of diameter to thickness is 250. The depicted hoop stress amplitude represents the cylindrical shell's response to a regular wave with a height of 1 m, a wavelength of 100 m, and a period of 8.68s.  $\theta$ =0° is on the up-wave side.

In Fig. 7.16, the maximum amplitude of hoop stress occurs at a height (H=16.5 m) close to the water surface. This is because the influence area of the circumferentially distributed load on this shell is about 4 m. As the water depth increases, the pressure induced by wave loads diminishes. In the circumferential direction, the peak amplitude manifests on the up-wave side due to the relation between wavelength and the tank's diameter. The extended wavelength of long waves prompts the cylindrical shell to generate substantial membrane force on the up-wave side. Analyzing amplitude and phase, the stress on the outer and inner surfaces can be

decomposed into membrane stress and bending stress. Fig. 7.17 shows the amplitude of membrane stress and bending stress for the elements in Fig. 7.16(a). Membrane stress is dominant under long waves, as demonstrated. Examining a regular wave with a 180 m wavelength in Fig. 7.18, membrane stress becomes more pronounced with increasing wavelength. Conversely, for short waves, the scenario flips. When the perimeter significantly exceeds the wavelength, the wave load pressure reverses several times along the cylindrical shell's surface, augmenting the contribution of bending stress. Fig. 7.19 presents the results under a 30 m regular wave load.

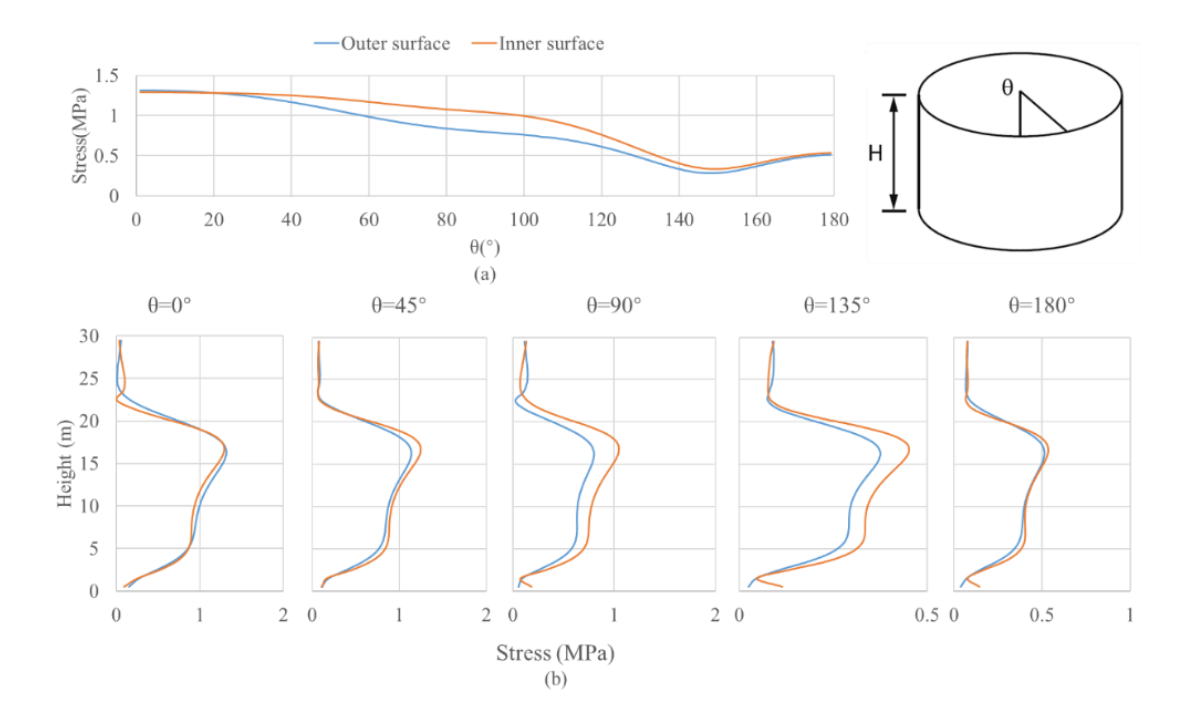


Fig. 7.16 Hoop stress amplitude distribution at regular wave load for a cylindrical shell with D=60 m, H=30 m, water depth = 20 m, wavelength = 100 m, and wave height = 1 m. (a) Stress amplitude along the cylindrical shell circumference at the height of 16.5 m; (b) Stress amplitude along with the cylindrical shell height at different locations

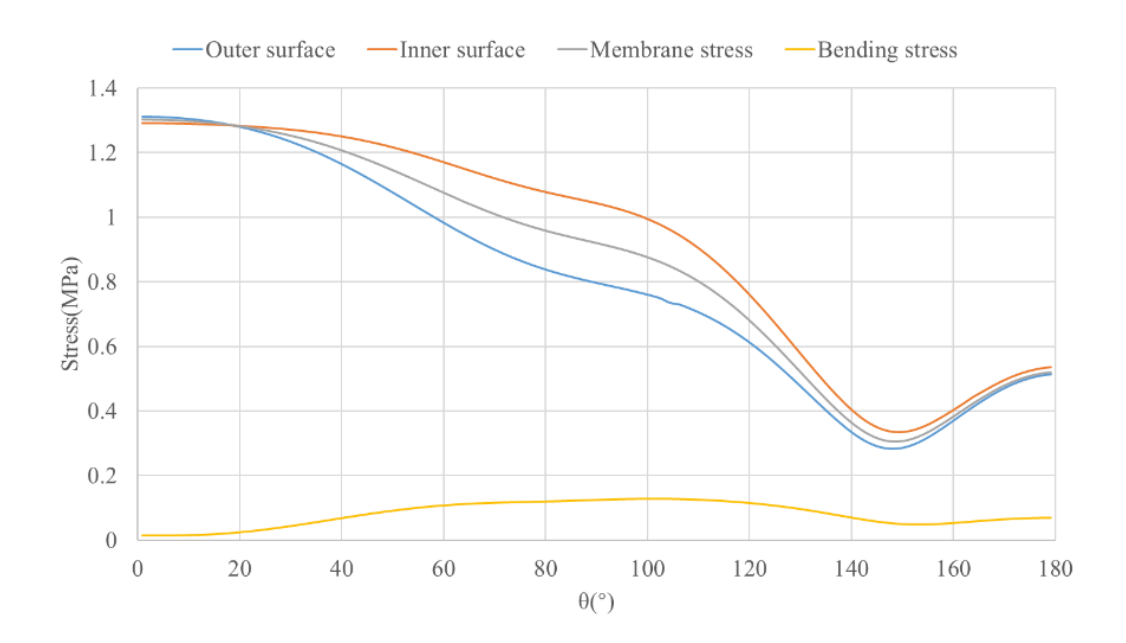


Fig. 7.17 Hoop stress amplitude along the cylindrical shell circumference at the height of 16.5 m (D = 60 m, H = 30 m, water depth = 20 m, wavelength = 100 m, and wave height = 1 m)

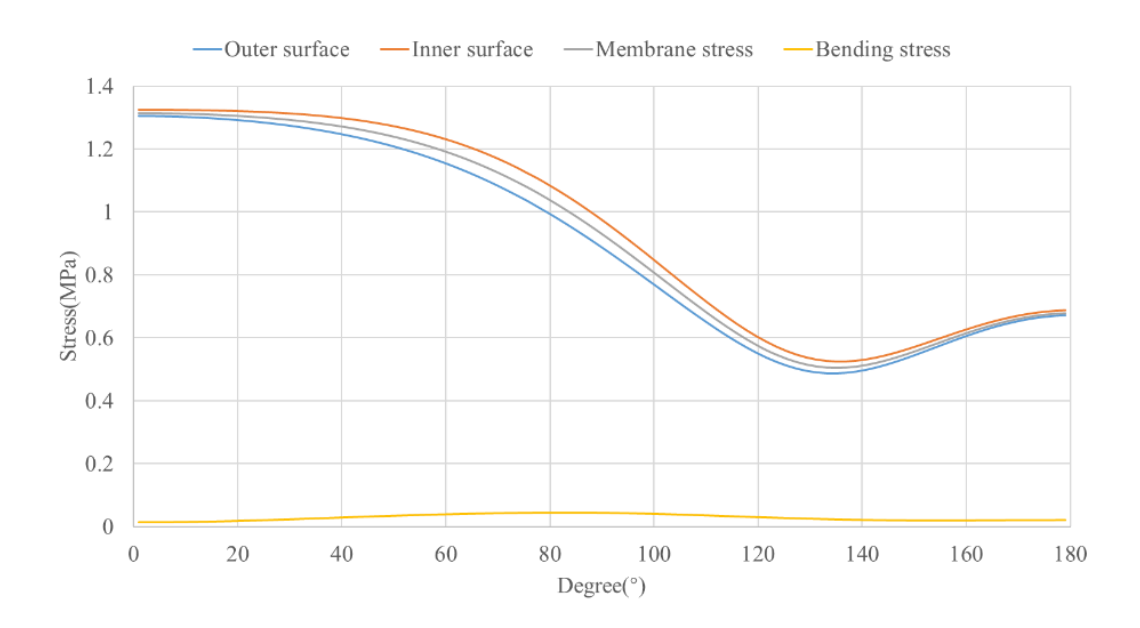


Fig. 7.18 Hoop stress amplitude along the cylindrical shell circumference at the height of 16.5 m (D = 60 m, H = 30 m, water depth = 20 m, wavelength = 180 m, and wave height = 180 m

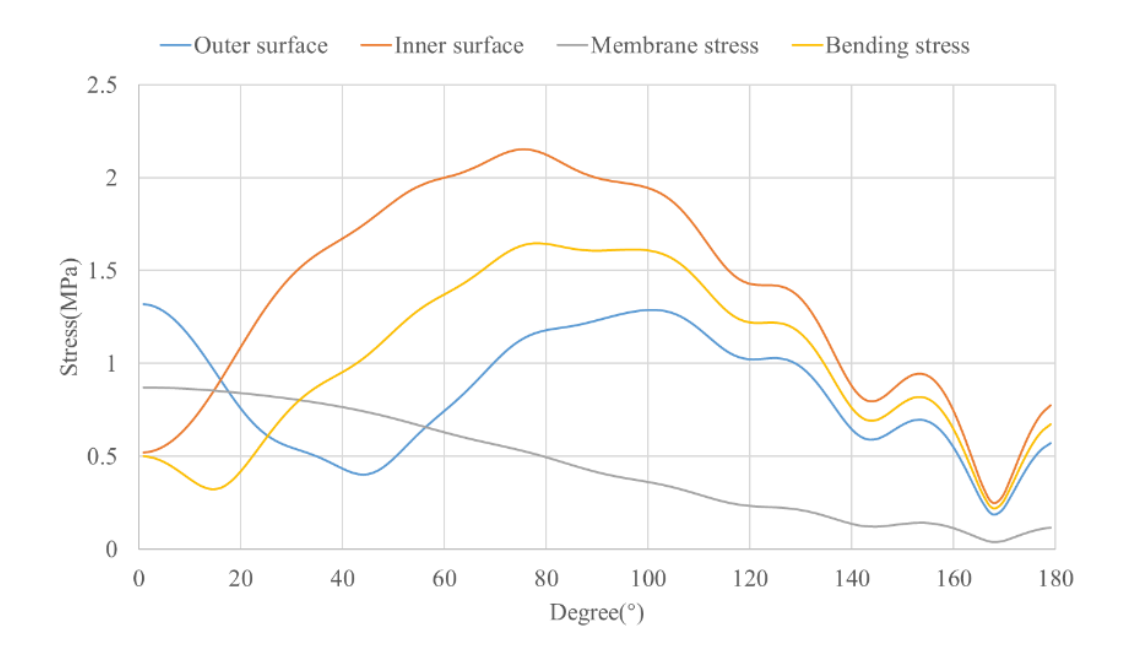
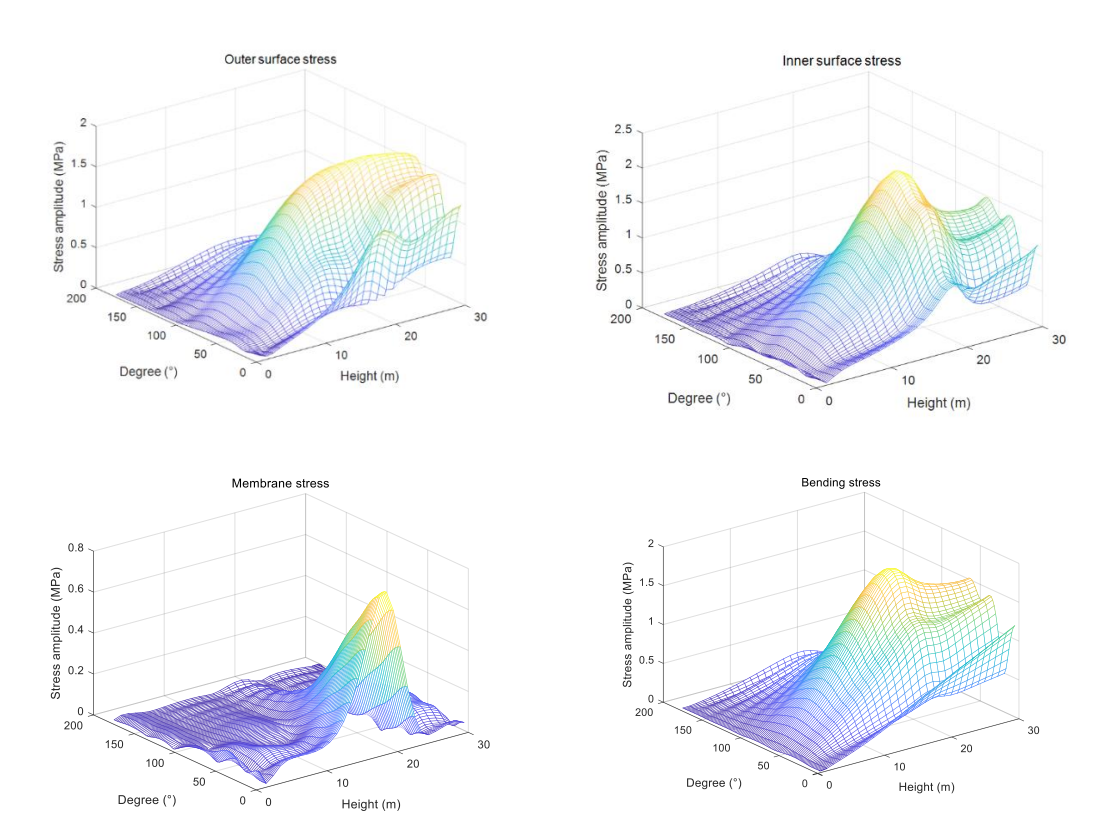
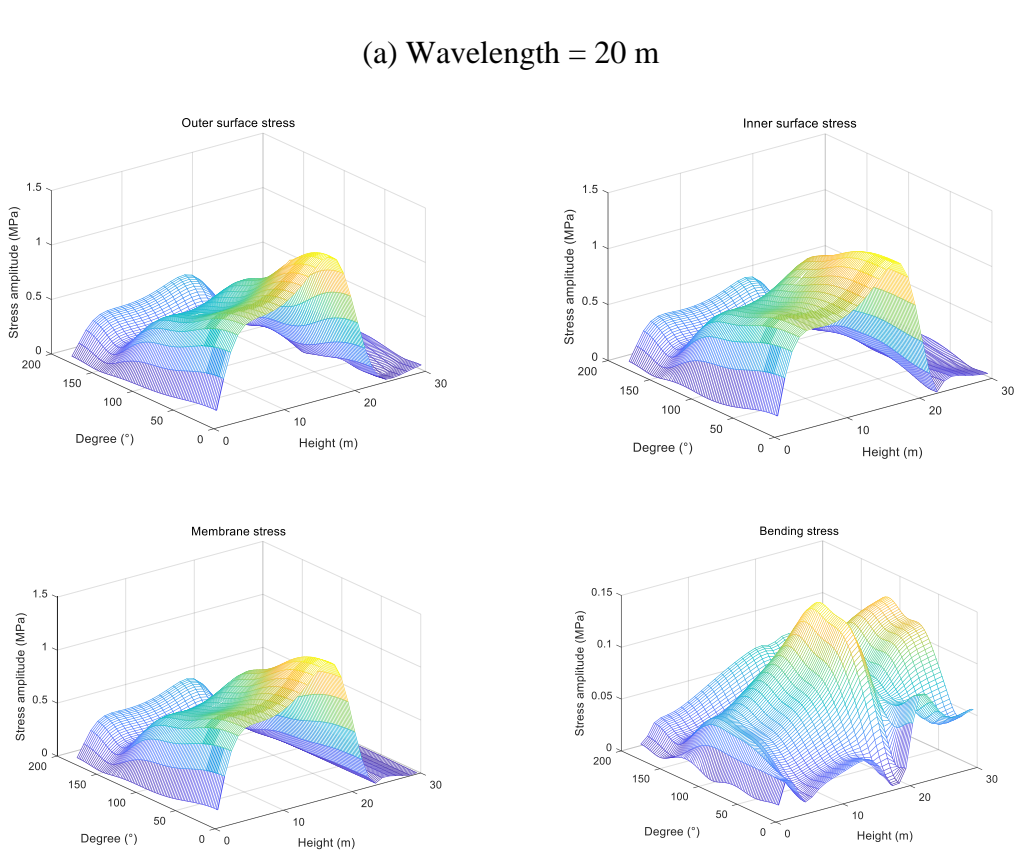


Fig. 7.19 Hoop stress amplitude along the cylindrical shell circumference at the height of 16.5 m (D = 60 m, H = 30 m, water depth = 20 m, wavelength = 30 m, and wave height = 1 m)

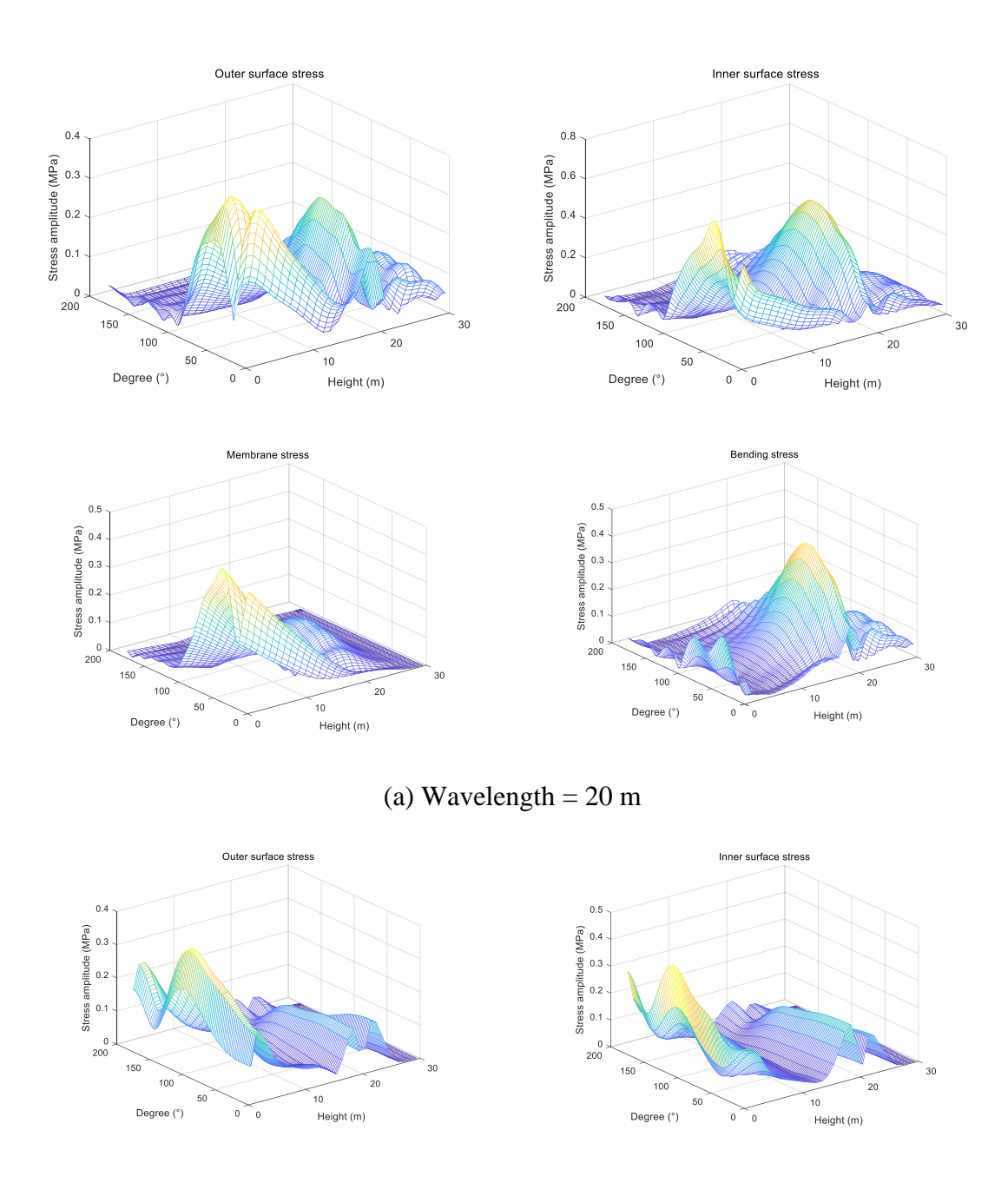
Fig. 7.16 to Fig. 7.19 show the amplitude distribution along several lines on the cylindrical shell. Extending this method to all elements on the shell allows the derivation of stress amplitudes. Fig. 7.20 and Fig. 7.21 depict the hoop stress and axial stress amplitude of the shell under short wave conditions (20 m) and long wave conditions (100 m), respectively. The cylindrical surface is flattened into a plane, with the two coordinates denoting the angle and height of the cylindrical shell. The vertical axis represents the stress amplitude. Notably, whether it's hoop stress or axial stress, long waves primarily contribute to membrane stress, while short waves induce bending stress.

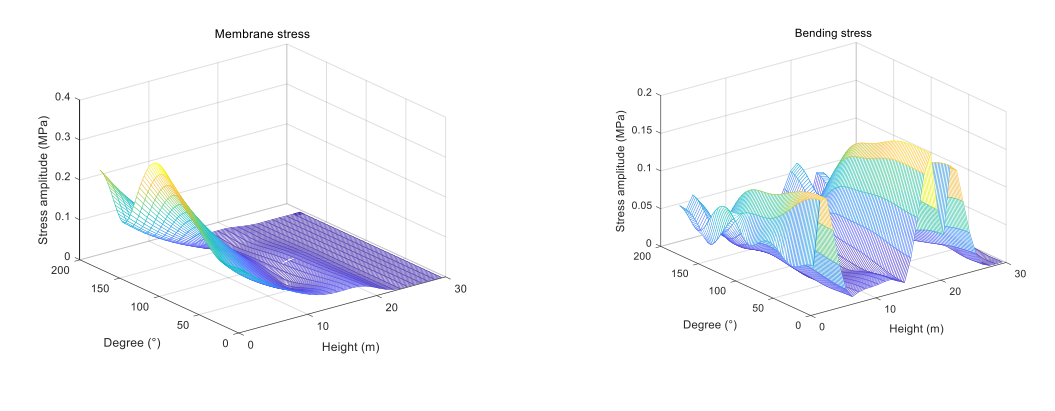




(b) Wavelength = 100 m

Fig. 7.20 Hoop stress amplitude of the cylindrical shell (D = 60 m, H = 30 m, water depth = 20 m, shell thickness = 240 mm, and wave height = 1 m)



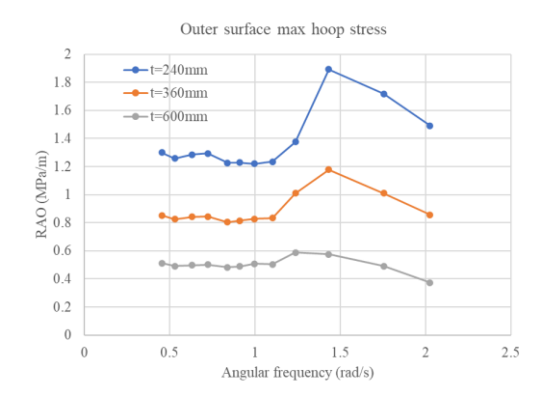


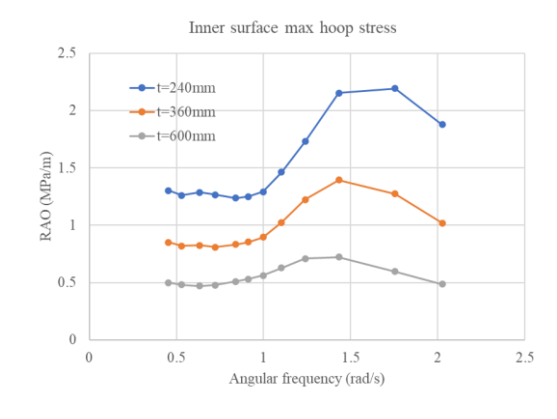
(b) Wavelength = 100 m

Fig. 7.21 Axial stress amplitude of the cylindrical shell (D = 60 m, H = 30 m, water depth = 20 m, shell thickness = 240 mm, and wave height = 1 m)

## 7.4.4 Stress response spectra of a cylindrical shell under the given wave spectrum

For regular waves of varying wavelengths, the cylindrical shell exhibits different stress responses. The regular waves discussed in the previous section all have unit wave heights. Thus, the stress amplitudes presented in Fig. 7.20 and Fig. 7.21 can also be interpreted as the RAOs of stress. The maximum RAOs values across the entire surface under different wavelengths are extracted, and by combining these maximum values, an envelope of RAO can be established. For the specific tank parameters (D = 60 m, H = 30 m, water depth = 20 m), three distinct shell thicknesses of 240 mm, 360 mm, and 600 mm are considered. The comparison of maximum stress RAOs is shown in Fig. 7.22 and Fig. 7.23.





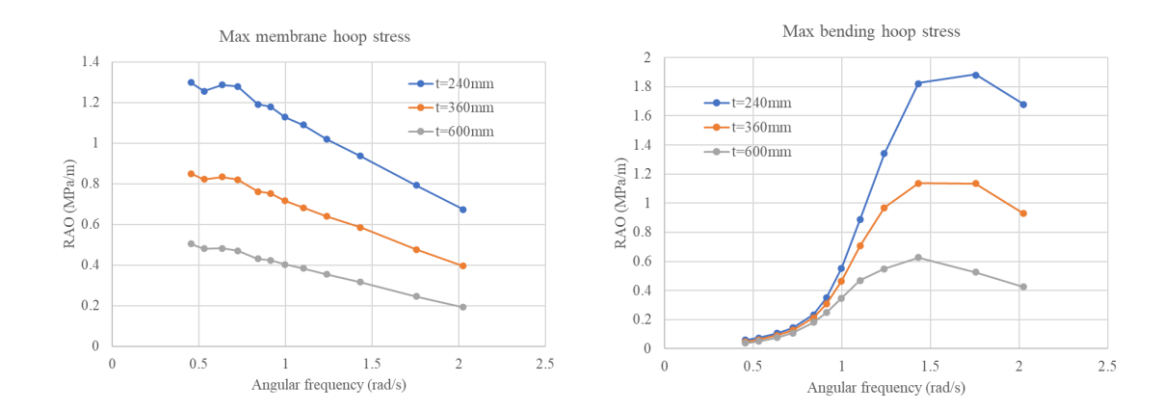


Fig. 7.22 Max hoop stress RAOs of the cylindrical shell (D = 60 m, H = 30 m, water depth = 20 m)

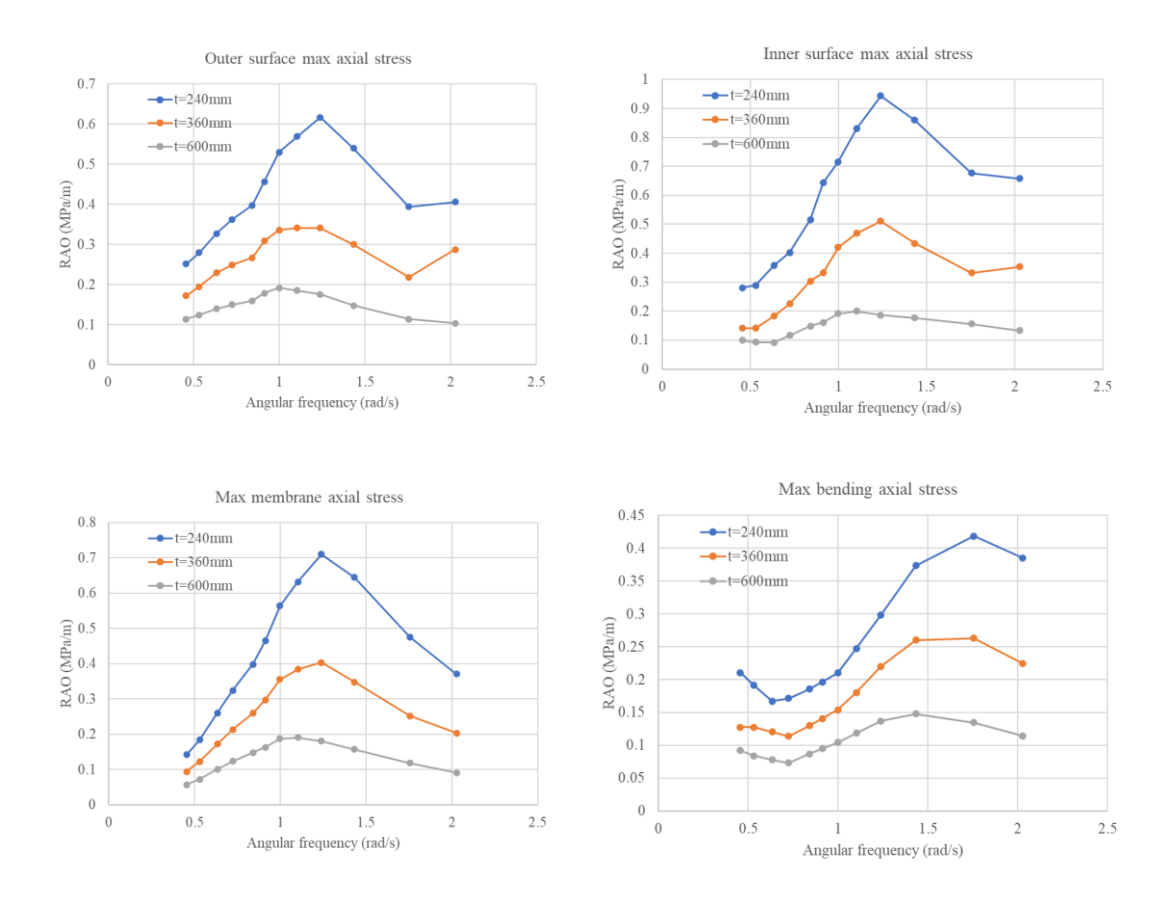


Fig. 7.23 Max axial stress RAOs of the cylindrical shell (D = 60 m, H = 30 m, water depth = 20 m)

The wave spectrum at the selected service place is depicted in Fig. 7.24. Despite the peak frequency of the wave spectrum not overlapping with the maximum RAOs, it is essential to carefully examine the membrane stress RAOs at the peak frequency. Based on Eq. (7-24), the stress response spectra are presented in Fig. 7.25, considering responses as Rayleigh distributions. The probability density distribution of the response can be derived from the following equation:

$$p(R) = \frac{R}{4m_0} \exp\left[-\frac{R^2}{8m_0}\right]$$
 (7-24)

 $m_0$  is the 0-order spectral moment. Through integration, the cumulative distribution functions of the response can be obtained. The largest value of the first one percent is extracted from the cumulative distribution functions as the maximum stress experienced by the tank. Fig. 7.26 shows the cumulative distribution functions for hoop stress in one case.

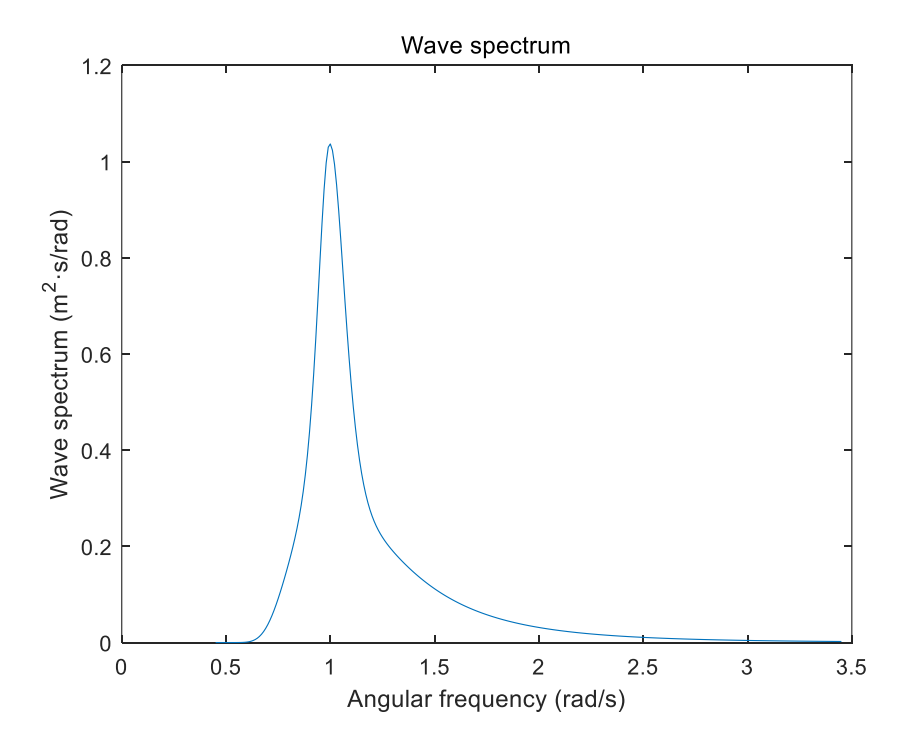


Fig. 7.24 Wave spectrum at the selected place

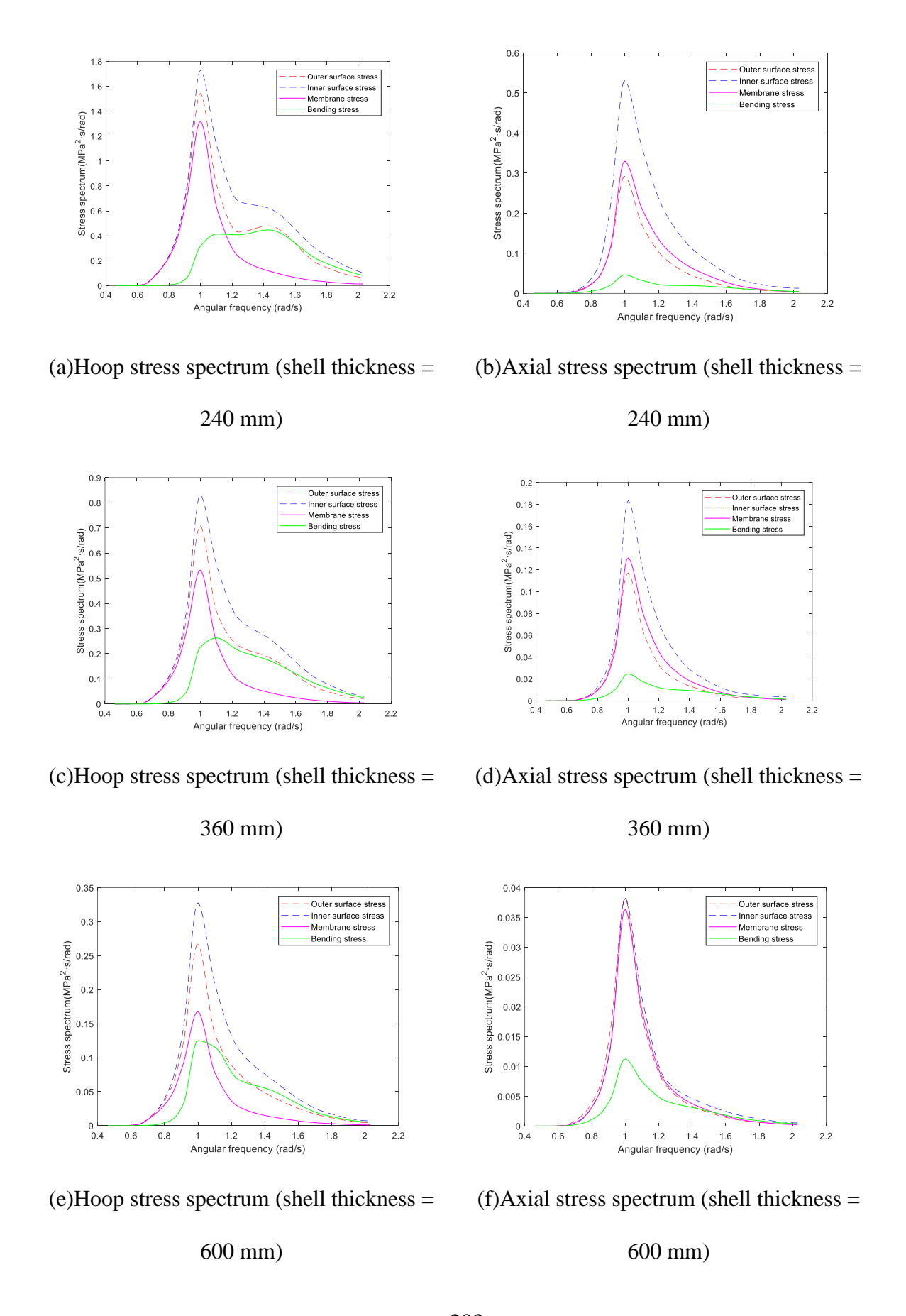


Fig. 7.25 Response spectrum of the cylindrical shell (D = 60 m, H = 30 m, water depth = 20

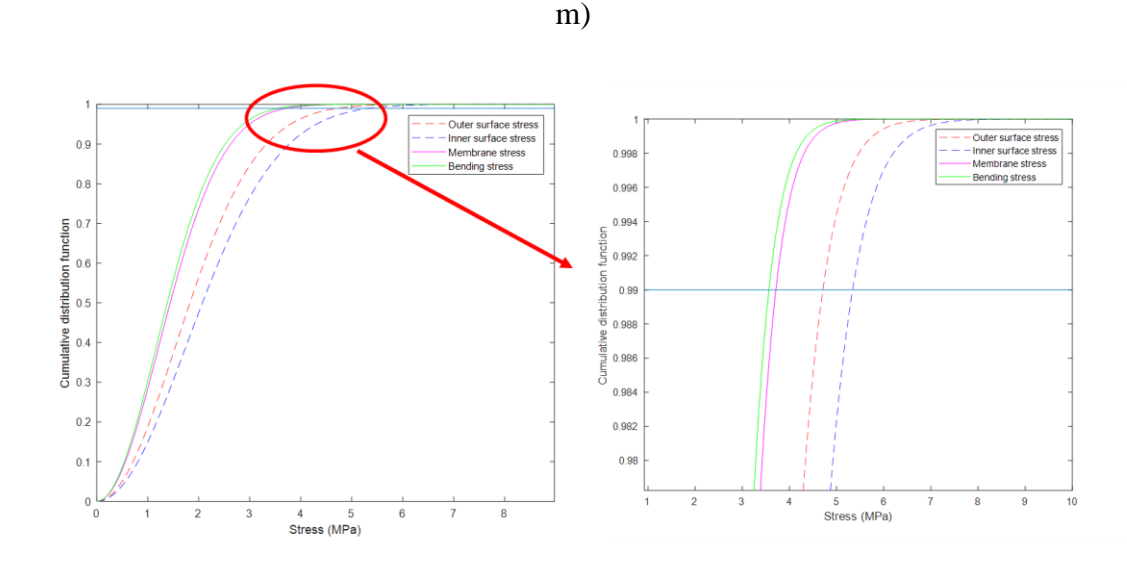


Fig. 7.26 The cumulative distribution function for the hoop stress in the cylindrical shell (D = 60 m, H = 30 m, water depth = 20 m, shell thickness = 240 mm)

## 7.4.5 Parametric analysis

To further study the effects of different parameters on the stress distribution in cylindrical shells, tanks listed in Table 7.4 were analyzed with the aforementioned methods. The effects of diameter-to-shell thickness ratio, water depth, tank diameter, and the reduction of concrete modulus are compared in this section.

## 7.4.5.1 Effects of diameter and diameter to shell thickness ratio

To compare tanks of varying diameters and shell thicknesses, the water depth remains fixed at 20 meters, while the height of the tank is maintained at 30 meters. The diameters of the tanks vary between 40 m and 80 m, with diameter-to-shell thickness ratios of 100,166.7, and 240.

Fig. 7.27 illustrates the peak stresses for various parameters. The diameter has little effect on the maximum bending stress. This is due to the fact that bending stress, primarily generated by short waves, is relatively small. Short waves have wavelengths significantly smaller than the tank perimeter. Consequently, the bending stress induced by short waves is predominantly influenced by the bending stiffness of the cylindrical shell and shows minimal dependence on the tank diameter. In contrast, for membrane stress, smaller diameter tanks experience higher maximum membrane stress. In the axial direction, the peak value occurs at the shell's root area, positioned 90 degrees from the wave direction. The smaller tank, with greater overall stiffness, is more prone to the drag force of the wave, leading to increased bending along the axial direction and consequently higher stress. As for the pressure in the hoop direction, reference Fig. 7.28. This snapshot illustrates the pressure induced by the wave along the circumferential surface of the tank at the still water level, corresponding to the point of maximum membrane stress. The maximum value appears at 0 degrees, aligning with the direction from which the wave originates. With a wavelength of 70 m, near the wave spectrum's peak, the red arrow indicates the direction of pressure action. Maximum stress occurs under specific pressure combinations, notably when the pressure is reversed twice between 0 and 180 degrees, as depicted in Fig. 7.28. The maximum stress occurs under certain pressure combinations. The maximum membrane stress is most likely to be observed when the pressure is reversed twice between 0 and 180° as shown in Fig. 7.28. For the selected tank diameters, larger tanks facilitate the formation of this pressure combination around the circumference, especially with wavelengths near the peak of the wave spectrum.

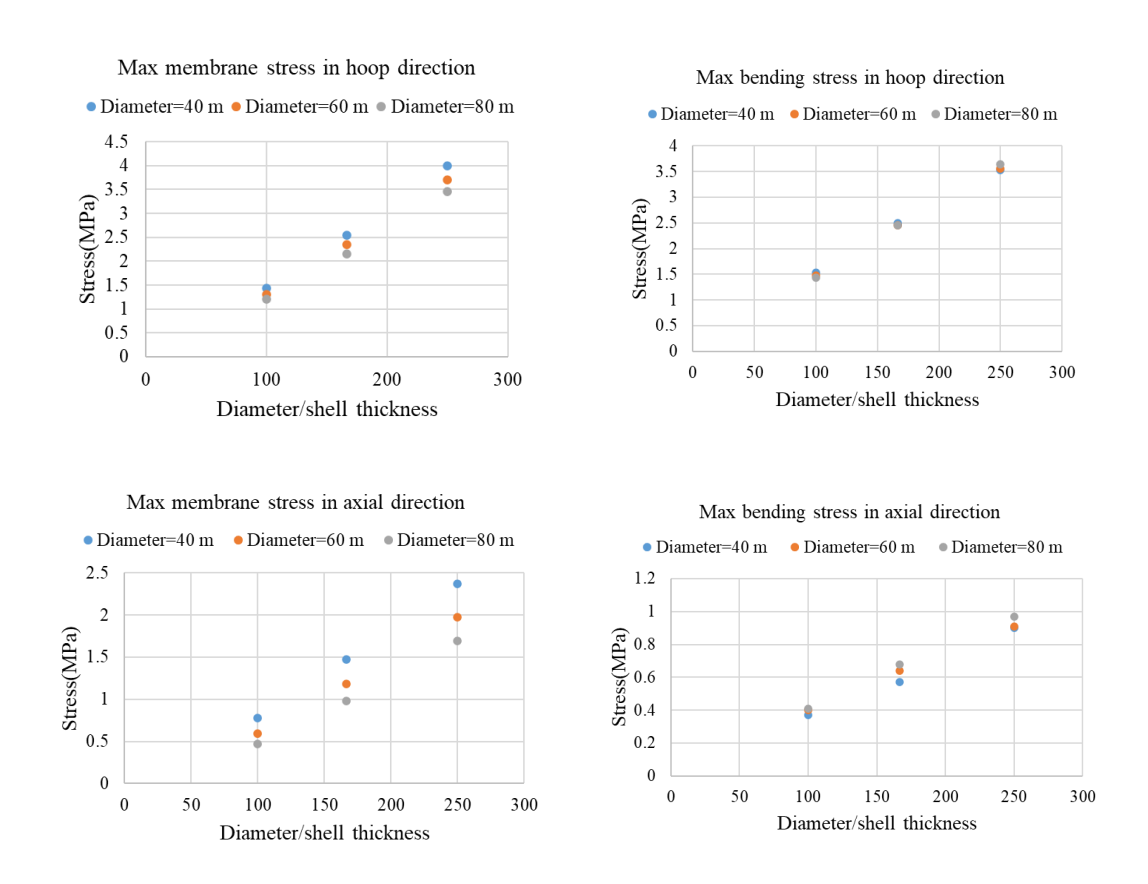


Fig. 7.27 Effect of diameter/shell thickness ratio (H = 30 m, water depth = 20 m)

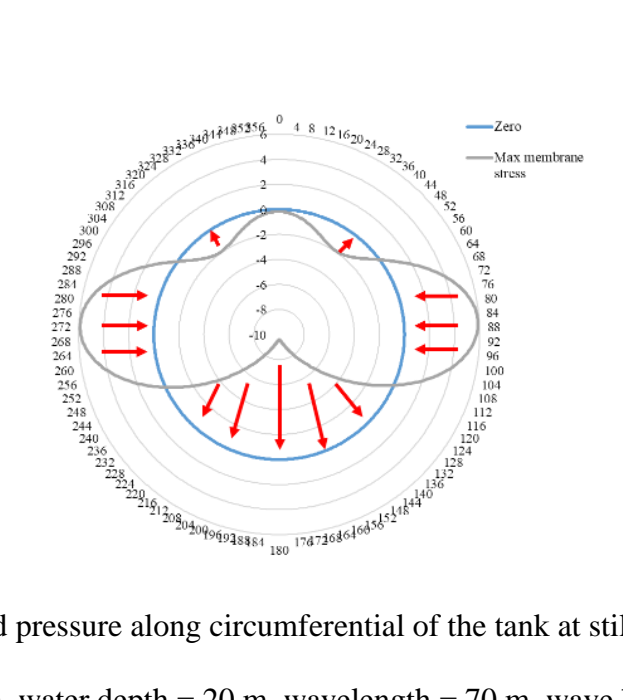


Fig. 7.28 Wave-induced pressure along circumferential of the tank at still water surface (Unit:

MPa, D = 60 m, water depth = 20 m, wavelength = 70 m, wave height = 1 m)

The impact of the diameter-to-shell thickness ratio is evident. For a tank with a specific geometry, reducing the shell thickness results in an increase in the maximum stress. The internal force on any section of the cylindrical shell is determined once the tank's geometry and loading conditions are known. Subsequently, the maximum stresses are influenced by the section properties.

## 7.4.5.2 Effects of water depth

To compare stress responses at different water depths, the tank's diameter is fixed at 80 m, considering water depths of 20 m and 30 m. Fig. 7.29 illustrates that when the diameter and shell thickness are consistent, the maximum membrane stress remains nearly the same under varying water depths. This can be attributed to the characteristics of waves in coastal shallow water.

In the case of long waves governing membrane stress, the variation in water depth is minimal when compared to the wavelength. Consequently, the potential flow field generated by waves remains similar, leading to comparable wave-induced pressure and cylindrical shell stress. In contrast, the difference is notable for short waves generated pressure, given that the range of water depth that waves can affect is about half of the wavelength. Tanks in deeper environments experience larger bending stress.

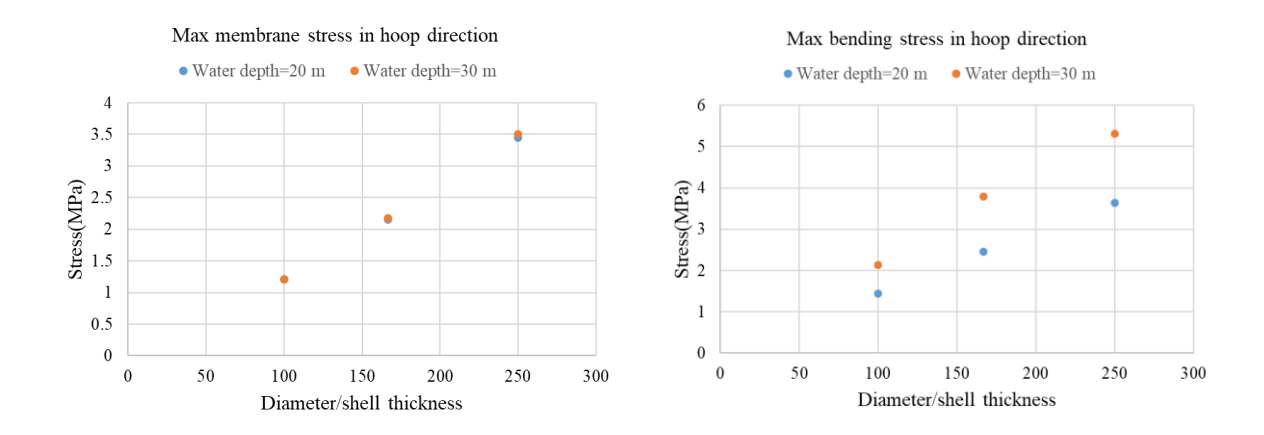


Fig. 7.29 Effect of water depth (D = 80 m)

#### 7.4.6 Discussions

The analysis reveals that membrane stress is affected by the ratio of tank perimeter to wavelength, while the maximum bending stress is dependent on the shell's local bending stiffness. The thickness of the shell and the stress exhibit a roughly inverse correlation. In coastal shallow water areas, water depth has little influence on the maximum membrane stress but significantly impacts the maximum bending stress. Across all cases, hoop stress consistently surpasses axial stress, emphasizing the importance of hoop direction in cylindrical shell design.

Based on the calculations presented in this section, the maximum tensile stress in the front 1% of the cylindrical shell subjected to wave loads can be controlled to approximately 5 MPa. This peak value is below the tensile strength of UHPECC mentioned earlier and only slightly above the cracking strength, suggesting that the application of this material in the proposed offshore engineering structure is viable. In practice, parameters such as structural thickness, cross-sectional area, and reinforcement ratio can be adjusted based on actual wave conditions and long-term service requirements to maintain stress within a reasonable range for stable, long-

term operation. Moreover, more studies are required to confirm the feasibility of these applications.

# 7.5 CONCLUSIONS

In this chapter, a novel offshore storage tank is proposed. This innovative structural system utilizes pipe connectors to release excess buoyancy, ensuring stability in the sea. This novel structural system offers substantial storage capacity without the need for land space, making it an ideal solution for strategic reserves.

This paper presents a feasibility study on various failure modes. Dislocations, such as floatation, sliding, and overturning, can be prevented by ensuring the tank's aspect ratio is greater than 1. The impact of diameter, thickness, and water depth on the maximum stress of cylindrical shells subjected to wave loads in coastal areas was investigated. The cylindrical shell requires a specific thickness to withstand tensile stress, particularly in the hoop direction.

For large-scale cylindrical shell structures, wave loads can induce both membrane and bending stresses. Long waves generate membrane stresses, while short waves cause bending stresses. When constructing such structures with concrete materials, it is advisable to position them in calm sea conditions or install artificial breakwaters. This helps to avoid significant tensile membrane stresses caused by long waves.

For future studies, it would be beneficial to conduct further investigations into the fatigue performance, particularly considering the long-term fatigue load imposed by wave actions.

Furthermore, exploring the optimization of shell sections using composite materials can offer opportunities to enhance both structural strength and cost-effectiveness.

# CHAPTER 8 CONCLUSIONS AND FUTURE WORK

## 8.1 CONCLUSIONS

In this thesis, the focus was on evaluating high-performance materials, specifically UHPECC and FRP, to enhance the long-term safety of structures in marine environments. Given that wave loads can generate long-term cyclic loads, the tensile fatigue performance of ECC is initially examined, considering various stress levels and loading frequencies. Subsequently, stress ratios, specifically the impact of stress reversal, were incorporated. S-N curves were established from experimental data, and a P-S-N model was developed to assess fatigue life, taking into account variations in initial static strength. Finally, a cumulative damage fatigue model considering different load conditions was also developed. At the structural level, this thesis conducted monotonic loading and cyclic loading tests on FRP-reinforced ECC beams. The study compared the impact of varying reinforcement ratios, fiber volume ratios, and loading conditions on the loading capacity, deformation capacity, and energy dissipation of flexural members. Additionally, to assess the impact of different load histories, the study included testing the cyclic loading protocol with initial pulse conditions and compared the performance of flexural members with those subjected to conventional cyclic loading histories. The thesis finally proposed a new type of offshore storage tank designed to be placed in coastal marine environments, capable of achieving substantial storage capacity. The feasibility of the proposed tank was initially assessed. A method to determine the hydrodynamic pressure generated by wave loads on the cylindrical shell was developed. Numerical models were built to evaluate the wave-induced stress on the cylindrical shell. The major conclusions of this thesis were summarized:

- 1) The study investigated the tensile fatigue properties of UHPECC under various loading conditions by testing different stress levels and loading frequencies. It was found that the fatigue life of ultra-high-performance engineered cementitious composites decreases with lower frequencies due to the increased actual loading rate. Additionally, the fatigue life shortens as stress levels increase at the same loading frequency, as higher stress levels cause more damage per cycle. The relationship between stress level and fatigue life follows a log-linear pattern for a given loading frequency.
- 2) The deformation pattern of UHPECC under fatigue is affected by the stress level, with higher stress levels potentially altering the usual three-stage process into an exponential form. By examining the secondary strain rate, the fatigue life for a specific loading condition can be predicted. Both static strength and fatigue life adhere to a two-parameter Weibull distribution. A probabilistic fatigue model considering static strength, loading frequencies, and stress levels is proposed for application in structural engineering.
- 3) The effect of stress reversal on tensile fatigue behavior of UHPECC was also investigated through a series of experiments. The experiments reveal that under the stress ratios tested, the fatigue failure mode of UHPECC is tensile fatigue fracture. Despite this, the specimens maintain overall structural integrity upon failure. It is observed that as the stress level increases, the fatigue life of the material decreases across various stress ratios.
- 4) When the stress ratio becomes negative, leading to tensile-compressive cyclic fatigue loading, the adverse impact on fatigue life is significantly greater compared to tensile-

tensile cycling. This is especially true when the compressive stress magnitude is similar to that of the tensile stress, as this can cause significant fiber buckling and increase the risk of fracture. For fatigue loading involving stress reversal, the compressive strain is considerably less than the tensile strain, with the residual deformation from the tensile strain accumulating continuously. The evolution of the maximum deformation under various stress ratios follows an inverted S-shaped curve. This curve was used to develop a fatigue cumulative damage model to estimate fatigue life under different loading conditions.

- 5) The material characteristics of ECC result in multiple cracks and a uniformly distributed slip between the FRP and concrete. When the reinforcing ratio is increased and/or the fiber volume ratio is decreased, cracks tend to become more localized, leading to greater elongation of the FRP rebar. This promotes better moment and force redistribution among flexural members, helping to delay the concentration of strain at main cracks and preventing FRP fracture, ultimately enhancing drift capacity. For beams under identical loading conditions, an increased reinforcing ratio and decreased fiber volume ratio lead to more localized cracks, indicating a broader distribution of slip around each localized crack.
- 6) Cyclic loading causes cracks to open and close, impairing the fiber bridging effect and reducing the tensile strength of ECC, which in turn lowers the failure strength compared to beams subjected to monotonic loading. Flexural performance tests reveal that beams exhibit lower strength under negative loading due to the concrete casting process, which affects fiber distribution differently at the beam's top and bottom. Additionally, cyclic loading causes slip accumulation between the concrete and FRP, preventing the complete closure of all flexural cracks in the compression zone. Consequently, the reinforcing FRP

sustains more compression force than in monotonically loaded specimens, reducing the effective height of the beam and decreasing the failure load.

- The initial deformation pulses impacted the cyclic performance of FRP-reinforced UHPECC beams in varying ways. Beams subjected to small initial pulses exhibited minimal initial damage, displaying hysteretic curves similar to those without initial pulses and maintaining comparable peak strength and ultimate drift. Conversely, beams subjected to large initial pulses demonstrated different behaviors based on their reinforcement ratios. Beams with a low reinforcement ratio behaved similarly to those with small or no pulses. However, beams with a high reinforcement ratio developed evenly distributed cracks in the bending area, which delayed stress concentration on the FRP reinforcement and resulted in increased peak strength and ultimate drift.
- 8) In specimens experienced large initial pulses, the strain in the FRP reinforcement accumulated more slowly compared to those exposed to gradually increasing cycles or small initial pulses. Peak strain development along the longitudinal direction of the FRP reinforcement was uneven, occurring mainly at crack localization points with high stress concentration. Maximizing the length of FRP reinforcement helps fully utilize its material properties, enhancing the peak strength and deformability of the structure.
- 9) Storing crude oil and various chemical products in ocean space presents considerable opportunities. The key challenge in deploying storage facilities in marine environments is overcoming the huge buoyancy generated by the density difference between stored products and seawater. This study proposes an innovative offshore storage tank design

aimed at ensuring stability by effectively releasing excess buoyancy. The feasibility of this design is substantiated through a thorough examination of potential failure modes, including floating, sliding, and overturning scenarios.

10) For large-scale cylindrical shells, the distribution of external hydrodynamic pressure on the surface under wave loads of varying frequencies is analyzed. The stress response of the cylindrical shell under these wave loads is obtained through finite element simulation. Long waves induce membrane stress in the shell, whereas short waves primarily generate bending stress. When constructing such structures with concrete materials, it is recommended to place them in calm sea conditions or to install artificial breakwaters. In combination with wave spectrum analysis, significant tensile membrane stress caused by long waves should be avoided.

# 8.2 FUTURE WORK

Due to constraints within current research strategies and processes, several aspects require further exploration to provide additional contributions to the relevant field. Below are suggested directions for future research.

1) Enhance the experimental data on ECC under cyclic fatigue loads, particularly focusing on tensile and tensile-compressive stress conditions. Include considerations for different stress ratios. Investigate the influence of load sequencing in fatigue testing, including stress amplitude loading with sequences of initially high and subsequently low stress levels, or vice versa. Develop fatigue damage accumulation models based on comprehensive experimental data suitable for various loading conditions and histories. Additionally,

explores factors influencing fatigue life such as load waveforms, fiber volume ratios, fiber types, and a wide range of loading frequencies. Conduct a probabilistic study to determine realistic and conservative stress or deformation histories for experimental testing in areas where ECCs have potential applications. Expand investigations to include fatigue tests under random loading conditions, establish damage accumulation models, and validate them.

- 2) To enhance the comprehension of the failure mechanisms of FRP-reinforced UHPECC members, further research should explore the loading capacity, deformation capability, and other performance aspects under different shapes (e.g. I girder, larger-scale specimens), types of FRP, and shear-span ratios. In order to enhance the economic and practical feasibility of these components, investigations should also explore cost-effective solutions such as reducing fiber content, optimizing reinforcement detailing, and structural design methods. Additionally, research is warranted on the shear resistance, impact resistance, fatigue resistance, and durability in marine environments of such structures. Furthermore, suitable finite element methods should be explored to accurately depict the nonlinear evolution behavior of FRP-reinforced ECC members under cyclic or fatigue loading.
- 3) To extend the application of FRP and ECC in marine structures, more comprehensive hydrodynamic and structure coupling calculation models should be established. These models must account for the design and analysis of various irregular and complex structures, enabling motion response and stress response. Based on effective calculation models, marine engineering structures should be designed and optimized to reduce costs, enhance loading capacity, and improve durability. Additionally, for marine engineering structures

developed with new materials, construction techniques should be considered, and the potential risks, failure modes, and reliability throughout the entire lifecycle from construction to service should be evaluated.

# References

- Aas-Jakobsen, K. (1970). Fatigue of concrete beams and columns: Bulletin no 70-1. *Trondheim, Norway: Institute for beton konstruksjoner*.
- Abdelrahman, A. A., Tadros, G., & Rizkalla, S. H. (1995). Test model for first canadian smart highway bridge. *ACI Structural Journal*, 92(4), 451-458.
- ACI Committee 440. (2015). Guide for the Design and Construction of Structural Concrete Reinforced with Fiber-reinforced Polymer FRP Bars. American Concrete Institute.
- Ahlström, J., & Karlsson, B. (2005). Fatigue behaviour of rail steel—a comparison between strain and stress controlled loading. *Wear*, 258(7-8), 1187-1193.
- Aiello, M. A., & Ombres, L. (2000). Load-deflection analysis of FRP reinforced concrete flexural members. *Journal of Composites for Construction*, 4(4), 164-171.
- Amaechi, C. V., Reda, A., Butler, H. O., Ja'e, I. A., & An, C. (2022). Review on fixed and floating offshore structures. Part I: Types of platforms with some applications. *Journal of Marine Science and Engineering*, 10(8), 1074.
- ASTM C109/C109M-16a (2016) Standard test method for compressive strength of hydraulic cement mortars
- ASTM C1437-15 (2015) Standard Test Method for Flow of Hydraulic Cement Mortar.
- ASTM D7205/D7205M-06 (2016) Standard Test Method for Tensile Properties of Fiber Reinforced Polymer Matrix Composite Bars
- Au, F. T., & Du, J. S. (2008). Deformability of concrete beams with unbonded FRP tendons. *Engineering structures*, 30(12), 3764-3770.
- Bandelt, M. J. (2015). Behavior, modeling, and impact of bond in steel reinforced highperformance fiber-reinforced cement-based composites. Stanford University.

- Bandelt, M. J., & Billington, S. L. (2016a). Bond behavior of steel reinforcement in high-performance fiber-reinforced cementitious composite flexural members. *Materials and structures*, 49, 71-86.
- Bandelt, M. J., & Billington, S. L. (2016b). Impact of reinforcement ratio and loading type on the deformation capacity of high-performance fiber-reinforced cementitious composites reinforced with mild steel. *Journal of Structural Engineering*, *142*(10), 04016084.
- Barton, D. C., & Parker, J. V. (1987). Finite element analysis of the seismic response of anchored and unanchored liquid storage tanks. *Earthquake engineering & structural dynamics*, 15(3), 299-322.
- Batson, G., Ball, C., Bailey, L., Landers, E., & Hooks, J. (1972, November). Flexural fatigue strength of steel fiber reinforced concrete beams. In *Journal Proceedings* (Vol. 69, No. 11, pp. 673-677).
- Bazant, Z. P., & Hubler, M. H. (2014). Theory of cyclic creep of concrete based on Paris law for fatigue growth of subcritical microcracks. *Journal of the Mechanics and Physics of Solids*, 63, 187-200.
- Behloul, M., Chanvillard, G., Pimienta, P., Pineaud, A., & Rivillon, P. (2005). Fatigue flexural behavior of pre-cracked specimens of special UHPFRC. *Special Publication*, 228, 1253-1268.
- Bernier, C., & Padgett, J. E. (2018, November). Forensic investigation of aboveground storage tank failures during Hurricane Harvey using fragility models. In *Eighth Congress on Forensic Engineering* (pp. 975-985). Reston, VA: American Society of Civil Engineers.
- Bernier, C., & Padgett, J. E. (2019). Fragility and risk assessment of aboveground storage tanks subjected to concurrent surge, wave, and wind loads. *Reliability engineering & system safety*, 191, 106571.

- Bernier, C., & Padgett, J. E. (2020). Probabilistic assessment of storage tanks subjected to waterborne debris impacts during storm events. *Journal of Waterway, Port, Coastal, and Ocean Engineering*, 146(3), 04020003.
- Bhattacharya, B., Fujikubo, M., Hudson, D. A., Riggs, H. R., Seto, H., Shin, H., ... & Zong, Z. (2006, August). Very large floating structures. In *Proceedings of the16th international ship and offshore structures congress, Southampton* (pp. 391-442).
- Billington, S. L., & Yoon, J. K. (2004). Cyclic response of unbonded posttensioned precast columns with ductile fiber-reinforced concrete. *Journal of Bridge Engineering*, 9(4), 353-363.
- Cachim, P. B., Figueiras, J. A., & Pereira, P. A. (2002). Fatigue behavior of fiber-reinforced concrete in compression. *Cement and concrete composites*, 24(2), 211-217.
- Canbolat, B. A., Parra-Montesinos, G. J., & Wight, J. K. (2005). Experimental study on seismic behavior of high-performance fiber-reinforced cement composite coupling beams. *ACI Structural Journal*, 102(1), 159.
- Cazenave, A., & Cozannet, G. L. (2014). Sea level rise and its coastal impacts. *Earth's Future*, 2(2), 15-34.
- Cazenave, A., Meyssignac, B., Ablain, M., Balmaseda, M., Bamber, J., Barletta, V., ... & Wouters, B. (2018). Global sea-level budget 1993-present.
- Chaallal, O., & Benmokrane, B. (1996). Fiber-reinforced plastic rebars for concrete applications. *Composites Part B: Engineering*, 27(3-4), 245-252.
- Chellapandian, M., Mani, A., & Prakash, S. S. (2020). Effect of macro-synthetic structural fibers on the flexural behavior of concrete beams reinforced with different ratios of GFRP bars. *Composite Structures*, 254, 112790.

- Chen, D., Feng, X., Hou, C., & Chen, J. F. (2022). A coupled frequency and time domain approach for hydroelastic analysis of very large floating structures under focused wave groups. *Ocean Engineering*, 255, 111393.
- Cheng, Z., Gao, Z., & Moan, T. (2018). Hydrodynamic load modeling and analysis of a floating bridge in homogeneous wave conditions. *Marine Structures*, *59*, 122-141.
- Chen, J. F., & Teng, J. G. (2008). Shear strengthening of reinforced concrete (RC) beams with fibre-reinforced polymer (FRP) composites. In *Strengthening and Rehabilitation of Civil Infrastructures Using Fibre-Reinforced Polymer (FRP) Composites* (pp. 141-157). Woodhead Publishing.
- Chen, L., & Rotter, J. M. (2012). Buckling of anchored cylindrical shells of uniform thickness under wind load. *Engineering Structures*, 41, 199-208.
- Chen, W. F. (2007). Plasticity in reinforced concrete. J. Ross Publishing.
- Chen, X., Bu, J., Fan, X., Lu, J., & Xu, L. (2017a). Effect of loading frequency and stress level on low cycle fatigue behavior of plain concrete in direct tension. *Construction and Building Materials*, 133, 367-375.
- Chen, X., Ge, L., Zhou, J., & Wu, S. (2017b). Dynamic Brazilian test of concrete using split Hopkinson pressure bar. *Materials and Structures*, 50, 1-15.
- CHI, Z. (2020). HYDRODYNAMICS OF COMPLIANT MODULAR LARGE FLOATING STRUCTURES: A COMPLEX MULTI-BODY SYSTEM.
- Collet, P., Vaucquelin, N., & Bury, A. (2014, June). Floating concrete barge assessment and inspection plan: N'KOSSA case study, a large pre-stressed concrete floating production unit in operation in Congo. In *International Conference on Offshore Mechanics and Arctic Engineering* (Vol. 45431, p. V04BT02A017). American Society of Mechanical Engineers.

- Cornelissen, H. A. W. (1984). Fatigue failure of concrete in tension. HERON, 29 (4), 1984.
- Cornelissen, H. A. W., & Reinhardt, H. W. (1984). Uniaxial tensile fatigue failure of concrete under constant-amplitude and programme loading. *Magazine of concrete Research*, 36(129), 216-226.
- Corten, H. T., & Dolan, T. J. (1956, September). Cumulative fatigue damage. In *Proceedings* of the international conference on fatigue of metals (Vol. 1, pp. 235-242). London, UK: Institution of Mechanical Engineering and American Society of Mechanical Engineers.
- Cozzani, V., Campedel, M., Renni, E., & Krausmann, E. (2010). Industrial accidents triggered by flood events: Analysis of past accidents. *Journal of hazardous materials*, 175(1-3), 501-509.
- Curtis, L. B., & Shepler, J. C. (1970, April). Dubai Khazzan-pioneer of large undersea storage system. In *Offshore Technology Conference* (pp. OTC-1193). OTC.
- Dai, J., Ang, K. K., Jin, J., Wang, C. M., Hellan, Ø., & Watn, A. (2019). Large floating structure with free-floating, self-stabilizing tanks for hydrocarbon storage. *Energies*, *12*(18), 3487.
- Davis, D. W. (2006). The aftermath of Hurricanes Katrina and Rita on south Louisiana. *LAOSR* a. D. Program, Ed., ed. Baton Rouge, LA: United States Environmental Protection Agency.
- Dieng, H. B., Cazenave, A., Meyssignac, B., & Ablain, M. (2017). New estimate of the current rate of sea level rise from a sea level budget approach. *Geophysical Research Letters*, 44(8), 3744-3751.
- Dnv, G. L. (2010). DNV-RP-C205: Environmental conditions and environmental loads. *Norw* ay: DetNorskeVeritas, 896.
- Do, M. T., Chaallal, O., & Aïtcin, P. C. (1993). Fatigue behavior of high-performance concrete. *Journal of Materials in civil Engineering*, 5(1), 96-111.

- Eidem, M. E. (2017, June). Overview of floating bridge projects in Norway. In *International Conference on Offshore Mechanics and Arctic Engineering* (Vol. 57779, p. V009T12A018). American Society of Mechanical Engineers.
- El-Kashif, K. F., & Maekawa, K. (2004). Time-dependent nonlinearity of compression softening in concrete. *Journal of Advanced Concrete Technology*, 2(2), 233-247.
- Fabbrocino, G., Iervolino, I., Orlando, F., & Salzano, E. (2005). Quantitative risk analysis of oil storage facilities in seismic areas. *Journal of hazardous materials*, *123*(1-3), 61-69.
- Fang, Y., Fang, Z., Jiang, R., Jiang, Z., & Zhu, D. (2020). Effect of temperature on the transverse impact performance of preloaded CFRP wire. *Composite Structures*, 231, 111464.
- FEMA, A. (2007). 461/Interim Testing Protocols for Determining the Seismic Performance Characteristics of Structural and Nonstructural Components. *Applied Technology Council, Redwood City, CA*, 113.
- Feng, X., & Song, Y. (2006). Fatigue crack resistance analysis of the positive section of prestressed concrete members. *Journal of Harbin Institute of Technology*, 38(3), 414-416. (in Chinese)
- Fischer, G., & Li, V. C. (2002a). Effect of matrix ductility on deformation behavior of steel-reinforced ECC flexural members under reversed cyclic loading conditions. *Structural Journal*, 99(6), 781-790.
- Fischer, G., & Li, V. C. (2002b). Influence of matrix ductility on tension-stiffening behavior of steel reinforced engineered cementitious composites (ECC). *Structural Journal*, 99(1), 104-111.

- Fischer, G., & Li, V. C. (2003). Deformation behavior of fiber-reinforced polymer reinforced engineered cementitious composite (ECC) flexural members under reversed cyclic loading conditions. *Structural Journal*, 100(1), 25-35.
- Fitik, B. (2022). Fatigue behaviour of ultra high performance concrete under cyclic stress reversal loading. In *Proceedings of International Conference on Istanbul and Earthquake* 2022; *Istanbul Aydin University publications* (pp. 91-103). Istanbul Aydin University.
- Flores, F. G., & Godoy, L. A. (1998). Buckling of short tanks due to hurricanes. *Engineering Structures*, 20(8), 752-760.
- Frank, T. E., Lepech, M. D., & Billington, S. L. (2018). Experimental testing of reinforced ECC beams subjected to various cyclic deformation histories. *Journal of Structural Engineering*, 144(6), 04018052.
- Galbraith, D. N., Hodgson, T., & Darby, K. (1993, September). Beryl Alpha–Condeep GBS Analysis. In SPE Offshore Europe Conference and Exhibition (pp. SPE-26689). SPE.
- Gatts, R. R. (1961). Application of a cumulative damage concept to fatigue.
- Godoy, L. A. (2007). Performance of storage tanks in oil facilities damaged by Hurricanes Katrina and Rita. *Journal of performance of constructed facilities*, 21(6), 441-449.
- Godoy, L. A., Portela, G., Sosa, E., Suarez, L. E., Virella, J. C., & Zapata, R. (2002). Damage due to buckling in aboveground storage tanks. In *Proceedings of the International Conference on the Behavior of Structures with Damage, University of Puerto Rico, Mayaguez, Puerto Rico.*
- Grace, N., Jensen, E., Matsagar, V., & Penjendra, P. (2013). Performance of an AASHTO beam bridge prestressed with CFRP tendons. *Journal of Bridge Engineering*, 18(2), 110-121.
- Greiner, R., & Derler, P. (1995). Effect of imperfections on wind-loaded cylindrical shells. *Thin-Walled Structures*, 23(1-4), 271-281.

- Grzybowski, M., & Meyer, C. (1993). Damage accumulation in concrete with and without fiber reinforcement. *Materials Journal*, *90*(6), 594-604.
- Guo, F., Al-Saadi, S., Raman, R. S., & Zhao, X. L. (2018). Durability of fiber reinforced polymer (FRP) in simulated seawater sea sand concrete (SWSSC) environment. *Corrosion Science*, *141*, 1-13.
- Guo, M., Zhong, Q., Zhou, Y., Hu, B., Huang, Z., & Yue, Y. (2020). Influence of flexural loading and chloride exposure on the fatigue behavior of high-performance lightweight engineered cementitious composites. *Construction and Building Materials*, 249, 118512.
- Hamdy, U. M. A. (1997). A damage-based life prediction model of concrete under variable amplitude fatigue loading. The University of Iowa.
- Hanson, J. M., Ballinger, C. A., & Linger, D. (1974). Considerations for design of concrete structures subjected to fatigue loading. *ACI J*, 71(3), 97-120.
- Haritos, N. (2007). Introduction to the analysis and design of offshore structures—an overview. *Electronic Journal of Structural Engineering*, (1), 55-65.
- Haroun, M. A., & Housner, G. W. (1981). Earthquake response of deformable liquid storage tanks.
- Henry, D. L. (1955). A theory of fatigue-damage accumulation in steel. *Transactions of the American Society of Mechanical Engineers*, 77(6), 913-918.
- Hilsdorf, H. K. (1966, October). Fatigue strength of concrete under varying flexural stresses.

  In *Journal Proceedings* (Vol. 63, No. 10, pp. 1059-1076).
- Hirata, H. (1973). U.S. Patent No. 3,779,193. Washington, DC: U.S. Patent and Trademark Office.
- Hollaway, L. C., & Teng, J. G. (Eds.). (2008). Strengthening and rehabilitation of civil infrastructures using fibre-reinforced polymer (FRP) composites. Elsevier.

- Holmen, J. O. (1982). Fatigue of concrete by constant and variable amplitude loading. *Special Publication*, 75, 71-110.
- Hordijk, D. A., Wolsink, G. M., & De Vries, J. (1995). Fracture and fatigue behaviour of a high strength limestone concrete as compared to gravel concrete. *HERON-ENGLISH EDITION-*, 40, 125-146.
- Hornung, U., & Saal, H. (2002). Buckling loads of tank shells with imperfections. *International Journal of Non-Linear Mechanics*, *37*(4-5), 605-621.
- Hsu, T. T. (1981, July). Fatigue of plain concrete. In *Journal Proceedings* (Vol. 78, No. 4, pp. 292-305).
- Huang, T., Zhang, Y. X., Lo, S. R., & Lee, C. K. (2017). Experimental study on crack bridging in engineered cementitious composites under fatigue tensile loading. *Construction and Building Materials*, 154, 167-175.
- Huang, B. T., Li, Q. H., Xu, S. L., & Zhou, B. M. (2017). Frequency effect on the compressive fatigue behavior of ultrahigh toughness cementitious composites: experimental study and probabilistic analysis. *Journal of Structural Engineering*, *143*(8), 04017073.
- Huang, Z. M. (2018a) *Investigation on mechanical performance of RPC Beams Prestressed* with External CFRP Tendons (Master's thesis, Hunan University). (in Chinese)
- Huang, B. T. (2018b). Fatigue performance of strain-hardening fiber-reinforced cementitious composite and its functionally-graded structures (Doctoral dissertation, Zhejiang University).
- Huang, B. T., Li, Q. H., Xu, S. L., & Zhou, B. M. (2018). Tensile fatigue behavior of fiber-reinforced cementitious material with high ductility: Experimental study and novel PSN model. *Construction and Building Materials*, 178, 349-359.

- Huang, B. T., Li, Q. H., & Xu, S. L. (2019a). Fatigue deformation model of plain and fiber-reinforced concrete based on Weibull function. *Journal of Structural Engineering*, 145(1), 04018234.
- Huang, B. T., Li, Q. H., Xu, S. L., & Zhang, L. (2019b). Static and fatigue performance of reinforced concrete beam strengthened with strain-hardening fiber-reinforced cementitious composite. *Engineering Structures*, 199, 109576.
- Huang, B. T., Wu, J. Q., Yu, J., Dai, J. G., & Leung, C. K. (2020). High-strength seawater seasand Engineered Cementitious Composites (SS-ECC): Mechanical performance and probabilistic modeling. *Cement and Concrete Composites*, 114, 103740.
- Hung, C. C., & Chueh, C. Y. (2016). Cyclic behavior of UHPFRC flexural members reinforced with high-strength steel rebar. *Engineering Structures*, 122, 108-120.
- Hutchinson, T. C., & Wood, R. L. (2013). Cyclic load protocol for anchored nonstructural components and systems. *Earthquake Spectra*, 29(3), 817-842.
- Hwang, T. H., & Scribner, C. F. (1984). R/C member cyclic response during various loadings. *Journal of Structural Engineering*, 110(3), 477-489.
- International Organization for Standardization, & Technical Committee ISO/TC 165, Timber structure. (2003). *Timber structures: Joints made with mechanical fasteners: Quasi-static reversed-cyclic test method*. ISO.
- Isojeh, B., El-Zeghayar, M., & Vecchio, F. J. (2017). Fatigue behavior of steel fiber concrete in direct tension. *Journal of Materials in Civil Engineering*, 29(9), 04017130.
- Jaejer, L. G., Mufti, A. A., & Tadros, G. (1997, October). The concept of the overall performance factor in rectangular-section reinforced concrete beams. In *Proceedings of the 3rd international symposium on non-metallic (FRP) reinforcement for concrete structures* (Vol. 2, pp. 551-558).

- Japan Society of Civil Engineers. (2008). Recommendations for Design and Construction of High Performance Fiber Reinforced Cement Composites with Multiple Fine Cracks (HPFRCC). In *High performance fiber reinforced cement composites* (Vol. 2). Springer Tokyo, Japan.
- Jiang, D., Tan, K. H., Wang, C. M., Ong, K. C. G., Bra, H., Jin, J., & Kim, M. O. (2018).

  Analysis and design of floating prestressed concrete structures in shallow waters. *Marine Structures*, *59*, 301-320.
- JTS (Ministry of Communications of the People's Republic of China). (2013) Code of Hydrology for Sea Harbour, JTS145-2-2013, *China Communication Press, Beijing*. (in Chinese)
- Kameshwar, S., & Padgett, J. E. (2015). Fragility assessment of above ground petroleum storage tanks under storm surge.
- Kameshwar, S., & Padgett, J. E. (2018). Fragility and resilience indicators for portfolio of oil storage tanks subjected to hurricanes. *Journal of Infrastructure Systems*, 24(2), 04018003.
- Kanda, T., & Li, V. C. (1999). New micromechanics design theory for pseudostrain hardening cementitious composite. *Journal of engineering mechanics*, *125*(4), 373-381.
- Kawashima, K., & Koyama, T. (1988). Effect of number of loading cycles on dynamic characteristics of reinforced concrete bridge pier columns. *Doboku Gakkai Ronbunshu*, 1988(392), 205-213.
- Kesner, K., & Billington, S. L. (2005). Investigation of infill panels made from engineered cementitious composites for seismic strengthening and retrofit. *Journal of Structural Engineering*, 131(11), 1712-1720.
- Kesner, K. E., Billington, S. L., & Douglas, K. S. (2003). Cyclic response of highly ductile fiber-reinforced cement-based composites. *Materials Journal*, 100(5), 381-390.

- Khakzad, N., & Van Gelder, P. (2017). Fragility assessment of chemical storage tanks subject to floods. *Process Safety and Environmental Protection*, 111, 75-84.
- Khakzad, N., & Van Gelder, P. (2018). Vulnerability of industrial plants to flood-induced natechs: A Bayesian network approach. *Reliability Engineering & System Safety*, 169, 403-411.
- Kindrachuk, V. M., Thiele, M., & Unger, J. F. (2015). Constitutive modeling of creep-fatigue interaction for normal strength concrete under compression. *International Journal of Fatigue*, 78, 81-94.
- Kingston, P. F. (2002). Long-term environmental impact of oil spills. *Spill Science & Technology Bulletin*, 7(1-2), 53-61.
- Kou, J., Zhao, K., Zhang, H., (2018). Experimental study on tension and compression fatigue properties of high ductile fiber concrete. *CHINA CIVIL ENGINEERING JOURNAL*, 51(9), 17-25. (in Chinese)
- Krawinkler, H. (2009, October). Loading histories for cyclic tests in support of performance assessment of structural components. In 3rd International conference on advances in experimental structural engineering (p. 10).
- Krawinkler, H., Parisi, F., Ibarra, L., Ayoub, A., & Medina, R. (2001). *Development of a testing* protocol for woodframe structures (Vol. 102). Richmond, CA: CUREe.
- Landucci, G., Antonioni, G., Tugnoli, A., & Cozzani, V. (2012). Release of hazardous substances in flood events: Damage model for atmospheric storage tanks. *Reliability Engineering & System Safety*, 106, 200-216.
- Landucci, G., Necci, A., Antonioni, G., Tugnoli, A., & Cozzani, V. (2014). Release of hazardous substances in flood events: Damage model for horizontal cylindrical vessels. *Reliability Engineering & System Safety*, 132, 125-145.

- Lappa, E. S., Rene, C., & Walraven, C. (2006). Flexural fatigue of high and ultra-high strength fiber reinforced concrete. In *Proceedings of International RILEM Workshop on High Performance Fiber Reinforced Cementitious Composites in Structural Applications, Ann, Arbor, MI* (pp. 509-518).
- Lau, D., & Pam, H. J. (2010). Experimental study of hybrid FRP reinforced concrete beams. *Engineering Structures*, *32*(12), 3857-3865.
- Lee, M. K., & Barr, B. I. G. (2004). An overview of the fatigue behaviour of plain and fibre reinforced concrete. *Cement and Concrete Composites*, 26(4), 299-305.
- Lepech, M. D., & Li, V. C. (2009). Application of ECC for bridge deck link slabs. *Materials* and *Structures*, 42, 1185-1195.
- Leung, C. K., Cheung, Y. N., & Zhang, J. (2007). Fatigue enhancement of concrete beam with ECC layer. *Cement and Concrete Research*, *37*(5), 743-750.
- Leve, H. L. (1969). Cumulative damage theories.
- Lignos, D. G., Moreno, D. M., & Billington, S. L. (2014). Seismic retrofit of steel moment-resisting frames with high-performance fiber-reinforced concrete infill panels: Large-scale hybrid simulation experiments. *Journal of Structural Engineering*, 140(3), 04013072.
- Li, H., Xu, S., & Leung, C. K. (2009). Tensile and flexural properties of ultra high toughness cemontious composite. *Journal of Wuhan University of Technology-Mater. Sci. Ed.*, 24(4), 677-683.
- Lin, Y. (2014). Wind load and wind-induced buckling of large steel tanks. *Hangzhou: Zhejiang University*, 92-110.

- Li, Q., Huang, B., Xu, S., Zhou, B., & Rena, C. Y. (2016). Compressive fatigue damage and failure mechanism of fiber reinforced cementitious material with high ductility. *Cement and Concrete Research*, 90, 174-183.
- Liu, F., & Zhou, J. (2017). Research on fatigue strain and fatigue modulus of concrete. *Advances in Civil Engineering*, 2017(1), 6272906.
- Liu, Y., Zwingmann, B., & Schlaich, M. (2015). Carbon fiber reinforced polymer for cable structures—A review. *Polymers*, 7(10), 2078-2099.
- Li, V. C., & Leung, C. K. (1992). Steady-state and multiple cracking of short random fiber composites. *Journal of engineering mechanics*, 118(11), 2246-2264.
- Li, V. C., & Matsumoto, T. (1998). Fatigue crack growth analysis of fiber reinforced concrete with effect of interfacial bond degradation. *Cement and concrete composites*, 20(5), 339-351.
- Li, V. C., & Wang, S. (2002). Flexural behaviors of glass fiber-reinforced polymer (GFRP) reinforced engineered cementitious composite beams. *Materials Journal*, 99(1), 11-21.
- Li, Z., Chen, D., & Feng, X. (2023). Hydroelastic and expansibility analysis of a modular floating photovoltaic system with multi-directional hinge connections. *Ocean Engineering*, 289, 116218.
- Lukkunaprasit, P., & Thepmangkorn, J. (2004). Load history effect on cyclic behavior of reinforced concrete tied columns. *Journal of Structural Engineering*, 130(10), 1629-1633.
- Lyu, P. (2002). Experimental study on uniaxial and biaxial dynamic strength and deformation of concrete (Doctoral dissertation, Dalian: Dalian University of Technology). (in Chinese)
- Maalej, M., & Leong, K. S. (2005). Engineered cementitious composites for effective FRP-strengthening of RC beams. *Composites Science and Technology*, 65(7-8), 1120-1128.

- Maalej, M., & Li, V. C. (1995). Introduction of strain-hardening engineered cementitious composites in design of reinforced concrete flexural members for improved durability. *Structural Journal*, 92(2), 167-176.
- MacCamy, R. C., & Fuchs, R. A. (1954). Wave forces on piles: a diffraction theory (No. 69).

  US Beach Erosion Board.
- Maekawa, K., Okamura, H., & Pimanmas, A. (2003). *Non-linear mechanics of reinforced concrete*. CRC Press.
- Maekawa, K., Gebreyouhannes, E., Mishima, T., & An, X. (2006a). Three-dimensional fatigue simulation of RC slabs under traveling wheel-type loads. *Journal of Advanced Concrete Technology*, 4(3), 445-457.
- Maekawa, K., Toongoenthong, K., Gebreyouhannes, E., & Kishi, T. (2006b). Direct path-integral scheme for fatigue simulation of reinforced concrete in shear. *Journal of Advanced Concrete Technology*, 4(1), 159-177.
- Maki, A. W. (1991). The Exxon Valdez oil spill: Initial environmental impact assessment. Part 2. *Environmental Science & Technology*, 25(1), 24-29.
- Makita, T., & Brühwiler, E. (2014). Tensile fatigue behaviour of ultra-high performance fibre reinforced concrete (UHPFRC). *Materials and structures*, 47, 475-491.
- Makita, T., & Brühwiler, E. (2015). Damage models for UHPFRC and R-UHPFRC tensile fatigue behaviour. *Engineering Structures*, *90*, 61-70.
- Malvar, L. J., & Ross, C. A. (1998). Review of strain rate effects for concrete in tension. *Materials Journal*, 95(6), 735-739.
- Manson, S. S., & Halford, G. R. (1986). Re-examination of cumulative fatigue damage analysis—an engineering perspective. *Engineering Fracture Mechanics*, 25(5-6), 539-571.

- Marco, S. M., & Starkey, W. L. (1954). A concept of fatigue damage. *Transactions of the American Society of Mechanical Engineers*, 76(4), 627-632.
- Matsumoto, T., Chun, P., & Suthiwarapirak, P. (2004). Effect of fiber fatigue rupture on bridging stress degradation in fiber reinforced cementitious composites. *Proceedings of Fracture Mechanics of Concrete Structures*, 653-660.
- Matsumoto, T., Suthiwarapirak, P., & Kanda, T. (2003). Mechanisms of multiple cracking and fracture of DFRCC under fatigue flexure. *Journal of advanced concrete technology*, *1*(3), 299-306.
- Matsumoto, T., Wangsiripaisal, K., Hayashikawa, T., & He, X. (2010). Uniaxial tension—compression fatigue behavior and fiber bridging degradation of strain hardening fiber reinforced cementitious composites. *International journal of fatigue*, 32(11), 1812-1822.
- Mayorga, S. Z., Sánchez-Silva, M., Olivar, O. J. R., & Giraldo, F. M. (2019). Development of parametric fragility curves for storage tanks: A Natech approach. *Reliability Engineering* & System Safety, 189, 1-10.
- Mebarki, A., Willot, A., Jerez, S., Reimeringer, M., & Prod'Homme, G. (2014). Vulnerability and resilience under effects of tsunamis: case of industrial plants. *Procedia Engineering*, 84, 116-121.
- Medeiros, A., Zhang, X., Ruiz, G., Rena, C. Y., & Velasco, M. D. S. L. (2015). Effect of the loading frequency on the compressive fatigue behavior of plain and fiber reinforced concrete. *International Journal of Fatigue*, 70, 342-350.
- Miner, M. A. (1945). Cumulative damage in fatigue.
- Moreno, D. M., Trono, W., Jen, G., Ostertag, C., & Billington, S. L. (2014). Tension stiffening in reinforced high performance fiber reinforced cement-based composites. *Cement and Concrete Composites*, 50, 36-46.

- Müller, S., & Mechtcherine, V. (2017). Fatigue behaviour of strain-hardening cement-based composites (SHCC). *Cement and Concrete Research*, 92, 75-83.
- Naaman, A., & Jeong, M. (1995, August). 45 Structural ductility of concrete beams prestressed with FRP tendons. In *Non-Metallic (FRP) Reinforcement for concrete structures:* proceedings of the second international RILEM symposium (Vol. 29, p. 379). Boca Raton, FL, USA: CRC Press.
- NECCI, A., GIRGIN, S., & KRAUSMANN, E. (2018). Understanding Natech Risk Due to Storms-Analysis, Lessons Learned and Recommendations.
- Niwa, A., & Clough, R. W. (1982). Buckling of cylindrical liquid-storage tanks under earthquake loading. *Earthquake Engineering & Structural Dynamics*, 10(1), 107-122.
- Nordby, G. M. (1958, August). Fatigue of concrete-a review of research. In *Journal Proceedings* (Vol. 55, No. 8, pp. 191-219).
- Oesch, T., Landis, E., & Kuchma, D. (2018). A methodology for quantifying the impact of casting procedure on anisotropy in fiber-reinforced concrete using X-ray CT. *Materials and Structures*, *51*, 1-13.
- Oh, B. H. (1991). Fatigue life distributions of concrete for various stress levels. *Materials Journal*, 88(2), 122-128.
- Oil&Gas Journal (2019). Guide to World Crudes: Total Updates Assay for Congolese N'Kossa.

  Available online: https://www.ogj.com/drilling-production/drilling-operations/article/17232666/guide-to-world-crudestotal-updates-assay-for-congolese-nkossa
- Otter, D. E., & Naaman, A. E. (1988). Properties of steel fiber reinforced concrete under cyclic load. *Materials Journal*, 85(4), 254-261.

- Ou, J. P., & Lin, Y. Q. (1999). Experimental study on performance degradation of plain concrete due to high-cycle fatigue damage. *China Civ. Eng. J*, 5, 15-22.
- Palinkas, L. A., Downs, M. A., Petterson, J. S., & Russell, J. (1993). Social, cultural, and psychological impacts of the Exxon Valdez oil spill. *Human organization*, *52*(1), 1-13.
- Parant, E., Rossi, P., & Boulay, C. (2007). Fatigue behavior of a multi-scale cement composite. *Cement and Concrete Research*, *37*(2), 264-269.
- Paris, P., & Erdogan, F. (1963). A critical analysis of crack propagation laws.
- Parra-Montesinos, G. J., & Chompreda, P. (2007). Deformation capacity and shear strength of fiber-reinforced cement composite flexural members subjected to displacement reversals. *Journal of Structural Engineering*, 133(3), 421-431.
- Paskova, T., & Meyer, C. (1997). Low-cycle fatigue of plain and fiber-reinforced concrete. *Materials Journal*, 94(4), 273-286.
- Peng, F., & Xue, W. (2018a). Analytical approach for flexural capacity of FRP prestressed concrete T-beams with non-prestressed steel bars. *Journal of Composites for Construction*, 22(6), 04018063.
- Peng, F., & Xue, W. (2018b). Design approach for flexural capacity of concrete T-beams with bonded prestressed and nonprestressed FRP reinforcements. *Composite Structures*, 204, 333-341.
- Peng, F., Xue, W., & Yu, T. (2023). Cyclic behavior of polypropylene fiber reinforced concrete beams with prestressed CFRP tendons and nonprestressed steel bars. *Engineering Structures*, 275, 115201.
- Pine, J. C. (2006). Hurricane Katrina and oil spills: Impact on coastal and ocean environments. *Oceanography*, 19(2), 37-39.

- Portela, G., & Godoy, L. A. (2005a). Wind pressures and buckling of cylindrical steel tanks with a conical roof. *Journal of Constructional Steel Research*, 61(6), 786-807.
- Portela, G., & Godoy, L. A. (2005b). Wind pressures and buckling of cylindrical steel tanks with a dome roof. *Journal of Constructional Steel Research*, 61(6), 808-824.
- Poveda, E., Ruiz, G., Cifuentes, H., Rena, C. Y., & Zhang, X. (2017). Influence of the fiber content on the compressive low-cycle fatigue behavior of self-compacting SFRC. *International Journal of Fatigue*, 101, 9-17.
- Qiu, J., Lim, X. N., & Yang, E. H. (2016). Fatigue-induced deterioration of the interface between micro-polyvinyl alcohol (PVA) fiber and cement matrix. *Cement and Concrete Research*, 90, 127-136.
- Qiu, J., Lim, X. N., & Yang, E. H. (2017). Fatigue-induced in-situ strength deterioration of micro-polyvinyl alcohol (PVA) fiber in cement matrix. *Cement and Concrete Composites*, 82, 128-136.
- Qiu, J., & Yang, E. H. (2016). A micromechanics-based fatigue dependent fiber-bridging constitutive model. *Cement and Concrete Research*, 90, 117-126.
- Qin, R., Zhu, J., & Khakzad, N. (2020). Multi-hazard failure assessment of atmospheric storage tanks during hurricanes. *Journal of Loss Prevention in the Process Industries*, 68, 104325.
- Qu, W., Zhang, X., & Huang, H. (2009). Flexural behavior of concrete beams reinforced with hybrid (GFRP and steel) bars. *Journal of Composites for construction*, *13*(5), 350-359.
- Rashid, M. A., Mansur, M. A., & Paramasivam, P. (2005). Behavior of aramid fiber-reinforced polymer reinforced high strength concrete beams under bending. *Journal of composites for construction*, 9(2), 117-127.

- Rodrigues, R., Gaboreau, S., Gance, J., Ignatiadis, I., & Betelu, S. (2021). Reinforced concrete structures: A review of corrosion mechanisms and advances in electrical methods for corrosion monitoring. *Construction and Building Materials*, 269, 121240.
- Rognaas, G., Xu, J., Lindseth, S., & Rosendahl, F. (2001). Mobile offshore base concepts.

  Concrete hull and steel topsides. *Marine Structures*, *14*(1-2), 5-23.
- Sahmaran, M., Lachemi, M., & Li, V. C. (2010). Assessing the durability of engineered cementitious composites under freezing and thawing cycles. *Concrete*, 6, 85-91.
- Saito, M. (1983, September). Direct tensile fatigue of concrete by the use of friction grips. In *Journal Proceedings* (Vol. 80, No. 5, pp. 431-438).
- Sakai, F., Nishimura, M., & Ogawa, H. (1984). Sloshing behavior of floating-roof oil storage tanks. *Computers & Structures*, 19(1-2), 183-192.
- Salzano, E., Iervolino, I., & Fabbrocino, G. (2003). Seismic risk of atmospheric storage tanks in the framework of quantitative risk analysis. *Journal of Loss Prevention in the Process Industries*, 16(5), 403-409.
- Santella, N., Steinberg, L. J., & Sengul, H. (2010). Petroleum and hazardous material releases from industrial facilities associated with Hurricane Katrina. *Risk Analysis: An International Journal*, 30(4), 635-649.
- Saucedo, L., Rena, C. Y., Medeiros, A., Zhang, X., & Ruiz, G. (2013). A probabilistic fatigue model based on the initial distribution to consider frequency effect in plain and fiber reinforced concrete. *International journal of fatigue*, 48, 308-318.
- Sengul, H., Santella, N., Steinberg, L. J., & Cruz, A. M. (2012). Analysis of hazardous material releases due to natural hazards in the United States. *Disasters*, *36*(4), 723-743.
- Shaheen, E., & Shrive, N. G. (2007). Cyclic loading and fracture mechanics of Ductal® concrete. *International journal of fracture*, *148*, 251-260.

- Shah, S. P. (1984). Predictions of comulative damage for concrete and reinforced concrete. *Matériaux et Construction*, 17, 65-68.
- Shao, Y., & Billington, S. L. (2020). Flexural performance of steel-reinforced engineered cementitious composites with different reinforcing ratios and steel types. *Construction and Building Materials*, 231, 117159.
- Shao, Y., & Billington, S. L. (2021). Impact of cyclic loading on longitudinally-reinforced UHPC flexural members with different fiber volumes and reinforcing ratios. *Engineering Structures*, 241, 112454.
- Sinha, B. P., Gerstle, K. H., & Tulin, L. G. (1964, February). Stress-strain relations for concrete under cyclic loading. In *Journal Proceedings* (Vol. 61, No. 2, pp. 195-212).
- Sonobe, Y., Fukuyama, H., Okamoto, T., Kani, N., Kimura, K., Kobayashi, K., ... & Teshigawara, M. (1997). Design guidelines of FRP reinforced concrete building structures. *Journal of composites for Construction*, 1(3), 90-115.
- Sparks, P. R. (1982). The influence of rate of loading and material variability on the fatigue characteristics of concrete. *Special Publication*, 75, 331-342.
- Sparks, P. R., & Menzies, J. B. (1973). The effect of rate of loading upon the static and fatigue strengths of plain concrete in compression. *Magazine of concrete research*, 25(83), 73-80.
- Standard, A. P. I. (2013). Welded tanks for oil storage. American Petroleum Institute, 1220.
- Subramanyan, S. (1976). A cumulative damage rule based on the knee point of the SN curve.
- Sulaiman, O. O., Magee, A., Bahrain, Z., Kader, A. S. A., Maimun, A., Pauzi, A. G., ... & Othman, K. (2013). Mooring analysis for very large offshore aquaculture ocean plantation floating structure. *Ocean & coastal management*, 80, 80-88.

- Sun, X., Liu, Y., Wang, J., & Cen, Z. (2008). Stress and deflection analyses of floating roofs based on a load-modifying method. *International journal of pressure vessels and piping*, 85(10), 728-738.
- Taerwe, L., & Matthys, S. (2013). Fib model code for concrete structures 2010.
- Takewaka, K., Yamaguchi, T., & Maeda, S. (2003). Simulation model for deterioration of concrete structures due to chloride attack. *Journal of Advanced concrete technology*, *1*(2), 139-146.
- Task Committee on Seismic Evaluation and Design of Petrochemical Facilities of ASCE. (2011, January). Guidelines for seismic evaluation and design of petrochemical facilities.

  American Society of Civil Engineers.
- Teng, J. G., Lin, X., Rotter, J. M., & Ding, X. L. (2005). Analysis of geometric imperfections in full-scale welded steel silos. *Engineering Structures*, 27(6), 938-950.
- Tepfers, R. (1979, August). Tensile fatigue strength of plain concrete. In *Journal Proceedings* (Vol. 76, No. 8, pp. 919-934).
- Tepfers, R., & Kutti, T. (1979, May). Fatigue strength of plain, ordinary, and lightweight concrete. In *Journal Proceedings* (Vol. 76, No. 5, pp. 635-652).
- Theriault, M., & Benmokrane, B. (1998). Effects of FRP reinforcement ratio and concrete strength on flexural behavior of concrete beams. *Journal of composites for construction*, 2(1), 7-16.
- Ueda, S. (2014). Floating oil storage base. In *Large Floating Structures: Technological Advances* (pp. 91-105). Singapore: Springer Singapore.
- Walker, R. A., & Karbhari, V. M. (2007). Durability based design of FRP jackets for seismic retrofit. *Composite structures*, 80(4), 553-568.

- Wang, H., & Belarbi, A. (2011). Ductility characteristics of fiber-reinforced-concrete beams reinforced with FRP rebars. *Construction and Building Materials*, 25(5), 2391-2401.
- Wang, K., Jansen, D. C., Shah, S. P., & Karr, A. F. (1997). Permeability study of cracked concrete. *Cement and concrete research*, 27(3), 381-393.
- Wan, L., Magee, A. R., Hellan, Ø., Arnstein, W., Ang, K. K., & Wang, C. M. (2017, June). Initial design of a double curved floating bridge and global hydrodynamic responses under environmental conditions. In *International Conference on Offshore Mechanics and Arctic Engineering* (Vol. 57779, p. V009T12A045). American Society of Mechanical Engineers.
- Wan, L., Han, M., Jin, J., Zhang, C., Magee, A. R., Hellan, Ø., & Wang, C. M. (2018a). Global dynamic response analysis of oil storage tank in finite water depth: Focusing on fender mooring system parameter design. *Ocean Engineering*, 148, 247-262.
- Wan, L., Zhang, C., Magee, A. R., Jin, J., Han, M., Ang, K. K., & Hellan, Ø. (2018b). An innovative mooring system for floating storage tanks and stochastic dynamic response analysis. *Ocean Engineering*, 170, 361-373.
- Wan, L., Zhang, C., Magee, A. R., Jin, J., Han, M., Ang, K. K., & Hellan, Ø. (2018c, June).

  Dynamic response analysis of floating storage tank system considering hydrodynamic and mechanical interactions. In *International Conference on Offshore Mechanics and Arctic Engineering* (Vol. 51258, p. V006T05A032). American Society of Mechanical Engineers.
- Watanabe, E., Utsunomiya, T., & Wang, C. M. (2004). Hydroelastic analysis of pontoon-type VLFS: a literature survey. *Engineering structures*, 26(2), 245-256.
- Whaley, C. P., & Neville, A. M. (1973). Non-elastic deformation of concrete under cyclic compression. *Magazine of Concrete Research*, 25(84), 145-154.

- Xiao, J. Q., Ding, D. X., Xu, G., & Jiang, F. L. (2009). Inverted S-shaped model for nonlinear fatigue damage of rock. *International journal of rock mechanics and mining sciences*, 46(3), 643-648.
- Xiao, S. H., Lin, J. X., Li, L. J., Guo, Y. C., Zeng, J. J., Xie, Z. H., ... & Li, M. (2021). Experimental study on flexural behavior of concrete beam reinforced with GFRP and steel-fiber composite bars. *Journal of Building Engineering*, 43, 103087.
- Xiong, W., Cai, C. S., Zhang, Y., & Xiao, R. (2011). Study of super long span cable-stayed bridges with CFRP components. *Engineering Structures*, *33*(2), 330-343.
- Xue, W., Li, L., Cheng, B., & Li, J. (2008). The reversed cyclic load tests of normal and prestressed concrete beams. *Engineering structures*, *30*(4), 1014-1023.
- Xue, W., Peng, F., & Zheng, Q. (2016). Design equations for flexural capacity of concrete beams reinforced with glass fiber–reinforced polymer bars. *Journal of Composites for Construction*, 20(3), 04015069.
- Yan, F., Lin, Z., & Yang, M. (2016). Bond mechanism and bond strength of GFRP bars to concrete: A review. *Composites Part B: Engineering*, 98, 56-69.
- Yang, Y., Fahmy, M. F., Guan, S., Pan, Z., Zhan, Y., & Zhao, T. (2020). Properties and applications of FRP cable on long-span cable-supported bridges: A review. *Composites Part B: Engineering*, 190, 107934.
- Yuan, F., Pan, J., Dong, L., & Leung, C. K. Y. (2014). Mechanical behaviors of steel reinforced ECC or ECC/concrete composite beams under reversed cyclic loading. *Journal of Materials in Civil Engineering*, 26(8), 04014047.
- Yuan, F., Pan, J., Xu, Z., & Leung, C. K. Y. (2013). A comparison of engineered cementitious composites versus normal concrete in beam-column joints under reversed cyclic loading. *Materials and structures*, 46, 145-159.

- Zanuy, C., Albajar, L., & De la Fuente, P. (2009). Sectional Analysis of Concrete Structures under Fatique Loading. *ACI Structural Journal*, *106*(5).
- Zeng, J. J., Zheng, Y. W., Liu, F., Guo, Y. C., & Hou, C. (2021). Behavior of FRP Ring-Confined CFST columns under axial compression. *Composite Structures*, 257, 113166.
- Zhang, B., Phillips, D. V., & Wu, K. (1996). Effects of loading frequency and stress reversal on fatigue life of plain concrete. *Magazine of concrete research*, 48(177), 361-375.
- Zhang, C., Fonseca, N., Ren, N., Magee, A. R., & Ang, K. K. (2020a). Experimental and numerical investigation of wave-induced hydrodynamic interactions of a sub-floating hydrocarbon storage tank system in shallow waters. *Ocean Engineering*, 216, 108104.
- Zhang, C., Magee, A. R., Fonseca, N., Hellan, Ø., & Ang, K. K. (2020b). Hydrodynamic responses and loads of a model floating hydrocarbon storage tank system for concept validation and numerical verification. In *WCFS2019: Proceedings of the World Conference on Floating Solutions* (pp. 155-171). Springer Singapore.
- Zhang, C., Santo, H., & Magee, A. R. (2022, March). Review and comparative study of methodologies for hydrodynamic analysis of nearshore floating solar farms. In *Offshore Technology Conference Asia* (p. D021S003R001). OTC.
- Zhang, C., Wan, L., Magee, A. R., Han, M., Jin, J., Ang, K. K., & Hellan, Ø. (2019). Experimental and numerical study on the hydrodynamic loads on a single floating hydrocarbon storage tank and its dynamic responses. *Ocean Engineering*, 183, 437-452.
- Zhang, J., Leung, C. K., & Gao, Y. (2011). Simulation of crack propagation of fiber reinforced cementitious composite under direct tension. *Engineering fracture mechanics*, 78(12), 2439-2454.

- Zhang, J., & Li, V. C. (2002). Monotonic and fatigue performance in bending of fiber-reinforced engineered cementitious composite in overlay system. *Cement and Concrete Research*, 32(3), 415-423.
- Zhao, G., Wu, P., & Zhan, W. (1993). Tensile fatigue performance of high-strength concrete.

  China Civil Engineering Journal, 26(6), 13-19. (in Chinese)
- Zhao, J. L., Teng, J. G., Yu, T., & Li, L. J. (2016). Behavior of large-scale hybrid FRP–concrete–steel double-skin tubular beams with shear connectors. *Journal of Composites* for Construction, 20(5), 04016015.
- Zhou, J., Pan, J., & Leung, C. K. (2015). Mechanical behavior of fiber-reinforced engineered cementitious composites in uniaxial compression. *Journal of materials in civil engineering*, 27(1), 04014111.
- Zhou, B., & Uchida, Y. (2017). Influence of flowability, casting time and formwork geometry on fiber orientation and mechanical properties of UHPFRC. *Cement and Concrete Research*, 95, 164-177.
- Zhou, Y., Zhong, Q., Xing, F., Sui, L., Huang, Z., & Guo, M. (2020). Influence of cyclic loading on the tensile fracture characteristics of ultra-high performance engineered cementitious composites. *Construction and Building Materials*, 240, 117937.